Development of Particle Image Velocimetry for *In Vitro* Studies of Arterial Haemodynamics

Nicolas Alexander Buchmann

A thesis presented for the degree of
Doctor of Philosophy
in
Mechanical Engineering
at the
University of Canterbury,
Christchurch, New Zealand.

31 October 2010

to Naomi

Acknowledgements

This thesis would not have been possible without the valuable contributions and support I received from numerous people during the past three years.

In particular I would like to thank my supervisor Dr. Mark Jermy for his guidance and support for this project. His constant commitment and valuable advice have been a great source of encouragement and inspiration to me throughout the time. I would also like to thank my co-supervisor Prof. Tim David for his contributions and expertise and without whom I would never have entered the fascinating field of biomechanical engineering.

I would also like to express my deepest gratitude to Prof. Julio Soria from Monash University for his unconditional support and the interesting discussions and valuable advice. Thank you for hosting me in Melbourne.

Other people directly involved in this project included Dr. Steven Moore, who has provided invaluable discussions and expertise in medical imaging, Dr. Chuong Nguyen and Callum Atkinson with whom I have collaborated on various aspect and Miharu Yamamoto who conducted the numerical simulations.

Also, this work would have not been possible without the technical staff in the Mechanical Engineering workshop, who have spent countless hours in manufacturing experimental equipment. In particular, I would like to thank Eric Cox and Julian Phillips for their support.

The financial support for living, equipment and travel expenses I received by the University of Canterbury International doctoral scholarship, the New

Zealand Ministry of Education, the UC College of Engineering, the Royal Society of NZ Canterbury Branch and the Maurice & Phyllis Paykel Trust is greatly acknowledged.

I would like to thank my colleagues and friends within the research group, in particular Callum Spence, Omid Amilli, Andrew Comerford and Patrick Geoghegan who provided valuable discussions and input into my research. I would also like to thank Sarah Berger and Dr. Jason Wong for proof-reading the early manuscript.

Lastly, I would like to thank my family and friends for their constant encouragement and interest in my work, which has been a great source of motivation throughout this degree. My greatest thanks goes to my partner Naomi without whom it would not have been possible to complete this thesis. Thank you for your enduring love and believe in me and your endless support and patience.

Abstract

Atherosclerosis and related cardiovascular diseases (CVDs) are amongst the largest causes of morbidity and mortality in the developed world, causing considerable monetary pressure on public health systems worldwide. Atherosclerosis is characterised by the build up of vascular plaque in medium and large arteries and is a direct precursor to acute vascular syndromes such a myocardial infarction, stroke or peripheral arterial diseases. The causative factors leading to CVD still remain relatively poorly understood, but are becoming increasingly identifiable as a dysfunction of the endothelial cells that line the arterial wall. It is well known that the endothelium responds to the prevailing fluid mechanic (i.e. haemodynamic) environment, which plays a crucial role in the localised occurrence of atherosclerosis near vessel bends and bifurcations. In these areas, disturbed haemodynamics lead to flow separation and very low wall shear stress (WSS), which directly affects the functionality of the endothelium and impedes the transport of important blood borne agonists and antagonists.

Detailed full field measurements assessing complex haemodynamics are sparse and consequently this thesis aims to address some of the important questions related to arterial haemodynamics and CVD by performing *in vitro* flow measurements in physiologically relevant conditions. In particular, this research develops and uses state-of-the-art Particle Image Velocimetry (PIV) techniques to measure three-dimensional velocity and WSS fields in scaled models of the human carotid artery. For this purpose, the necessary theoretical and experimental concepts are developed and in-depth analyses of the underlying factors affecting the local haemodynamics and their relation to CVD are carried out.

In the first part, a methodology for the construct of transparent hydraulic flow phantoms from medical imaging data is developed. The arterial geometries

are reproduced in optically clear silicone and the flowing blood is modelled with a refractive index matched blood analogue. Subsequently, planar and Stereo-PIV techniques are developed and verified. A novel interfacial PIV (iPIV) technique is introduced to directly measure WSS by inferring the velocity gradient from the recorded particle images. The new technique offers a maximal achievable resolution of 1 pixel and therefore removes the resolution limit near the wall usually associated with PIV. Furthermore, the iPIV performance is assessed on a number of numerical and experimental test cases and iPIV offers a significantly improved measurement accuracy compared to more traditional techniques.

Subsequently, the developed methodologies are applied in three studies to characterise the velocity and WSS fields in the human carotid artery under a number of physiological and experimental conditions. The first study focuses on idealised vessel geometries with and without disease and establishes a general understanding of the haemodynamic environment.

Secondly, a physiological accurate vessel geometry under pulsatile flow conditions is investigated to provide a more realistic representation of the true *in-vivo* flow conditions. The prevailing flow structure in both cases is characterised by flow separation, strong secondary flows and large spatial and temporal variations in WSS. Large spatial and temporal differences exist between the different geometries and flow conditions; spatial variations appear to be more significant than transient events.

Thirdly, the three-dimensional flow structure in the physiological carotid artery model is investigated by means of stereoscopic and tomographic PIV, permitting for the first time the measurement of the full 3D-3C velocity field and shear stress tensor in such geometries. The flow field within the model is complex and three-dimensional and inherently determined by the vessel geometry and the build up of an adverse pressure gradient. The main features include strong heliocoidal flow motions and large spatial variations in WSS.

Lastly, the physiological implications of the current results are discussed in detail and reference to previous work is given.

In summary, the present research develops a novel and versatile PIV methodology for haemodynamic *in vitro* studies and the functionality and accuracy is demonstrated through a number of physiological relevant flow measurements.

Contents

List of Figures

List of Tables

Chapter 1

Introduction

1.1 Background

Atherosclerosis and related cardiovascular diseases (CVD) are the leading cause of morbidity and mortality in the developed world. Atherosclerosis is characterised by the progressive narrowing and hardening of medium and large arteries and, if untreated, can lead to ischemia of the heart, brain or extremities and eventually infarction [Ross, 1999]. The monetary costs associated with cardiovascular disease are considerable and create enormous pressure on public heath systems worldwide. For example, the direct and indirect costs of CVD in the United States for 2008 accumulated to 3% of the total annual GDP[1] (≈$450 billon). Cardiovascular disease causes nearly every fifth death in the United States and more than 40% of all deaths in central Europe[2] and thereby outweighing other major diseases such as cancer or respiratory diseases. Cardiovascular disease predominantly occurs in the older population and affects more females than males, with lifestyle and dietary patterns being a major determinant for disease development. Ethnicity and genetic predisposition is another major determinant as shown in a study in New Zealand [Carter et al., 2006], with the indigenous and Asian pacific population being at a higher risk of stroke and CVD compared to the western/European part of the population.

After coronary heart disease, atherosclerosis of the carotid arteries is the second largest pathological condition and is a direct precursor to acute vascular syndromes such as stroke and transient ischemic attacks. Carotid artery

[1]Heart Disease and Stroke Statistics - Update (2008), *American Heart Association*

[2]European Cardiovascular Disease Statistics (2008), *Department of Public Health, University of Oxford*

atherosclerosis is characterised by the development of arterial plaque and deposition of fatty and calcified tissue on the arterial wall. If untreated, this can lead to thrombus formation or complete vessels occlusion and subsequently to disruption of the blood supply to the brain. Classical treatment methods for carotid artery disease include carotid artery endarterectomy (i.e., surgical removal of plaque) or carotid artery stenting (i.e., expansion of the vessel wall), with the latter method becoming increasingly popular due to its reduced invasiveness.

Due to its severity, the formation and progression of CVD has been the subject of intense research over the past 30 years on a pathological, biological and biomechanical level. From these studies, it has become evident that the fluid dynamic (i.e., haemodynamic) environment in the carotid artery as well as in other major blood vessels is directly linked to the formation of vascular disease, which in turn affects the detailed haemodynamic environment. This is particularly observed in areas of low shear stress, flow separation and prolonged particle residence time such as in arterial bends and bifurcations. Therefore, research investigating the detailed role of the prevailing haemodynamics and its role in CVD is increasingly necessary.

This thesis aims to address some of the critical questions related to this cause-effect relationship. In particular, this research will experimentally investigate the fluid mechanic environment in the human carotid artery using a variety of arterial geometries, flow conditions and Particle Image Velocimetry (PIV) for the non-intrusive and instantaneous assessment of blood flow velocity and shear stress distribution. For this purpose, the research will develop the necessary theoretical and experimental tools required to carry out an in depth analysis of the factors affecting the local flow structure and wall shear stress distribution within the carotid artery.

1.2 Pathology of Cardiovascular Disease

1.2.1 Arterial Wall

The structure of the artery can be broken down into three distinct layers: tunica intima, tunica media and tunica adventitia as illustrated in Figure 1.1. The tunica intima is a thin layer comprising the innermost region of the artery wall, which consists of four parts. In direct contact with the flowing blood is a thin layer of endothelial cells, which acts as an active barrier to the transport of material between the flowing blood and the arterial wall. This layer is surrounded by several layers of connective tissue (i.e., membranes) and an elastic lamina. The middle layer of the arterial wall, which is also the largest layer, is known as the tunica media. This layer consists predominantly of concentrically arranged smooth muscle cells and an elastic and collagen fibrous membrane. The tunica media provides the strength and structural integrity of the artery and its individual composition is highly dependent on the arterial calibre and age [Seeley et al., 2003]. The outermost layer, the tunica adventitia, consists of connective tissue and some collagen and elastic fibre. The adventitia layer also contains smaller blood vessels (i.e., vasa vasorum) that supply the arterial wall with metabolites and nutrients, which are essential for its functioning and survival.

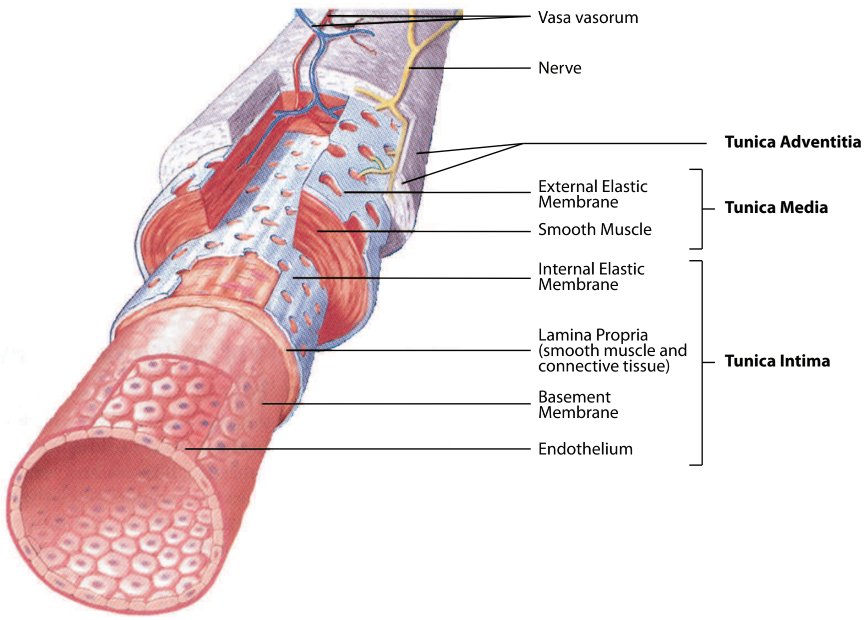

Figure 1.1 Successive layers of the arterial wall. Figure adapted from [Seeley et al., 2003]

1.2.2 Endothelial Biology

A key player in the pathology of atherosclerosis are the endothelial cells, which form a monolayer of cells that line the inner walls of the artery and hence provide an interface between the flowing blood and the arterial wall. Originally, the endothelium was thought to be a passive barrier, but subsequently the converse has been identified [Caro, 2001].

The basic architecture of the endothelial cells is constructed from membranes, organelles and cytosol. The outermost protective coating is called the plasma membrane, which is a semi permeable surface coating that controls the passage of material between the extracellular and intracellular environment. The surface of the membrane contains a variety of integral membrane proteins (or ion channels) to control the permeability of the plasma membrane and to sense the prevailing haemodynamic environment. The region within the cells is composed of further cytosol and organelles surrounded by an internal scaffolding of filaments to provide mechanical strength. These filaments are involved in force transmission (such as shear stress, Section 1.2.3) and re-organisation to allow morphological changes in the structure and orientation of the endothelial cells in response to altered environmental conditions.

The endothelium responds to both the prevailing haemodynamic and biochemical environment, eliciting a number of cellular responses and it has been strongly implicated in the pathology of atherosclerosis through its regulatory functionality [Traub and Berk, 1998; Malek et al., 1999; Resnick et al., 2003].

Homeostasis

Homeostasis refers to the regulatory processes and activities involved in maintaining a normally functioning cardiovascular system and the endothelium, by virtue of its unique location, is a major controller of vascular homeostasis [Gimbrone, 1999; Davies, 2000]. The endothelium responds to external stimuli and is responsible for numerous regulatory processes, which include: coagulation, smooth muscle cells' growth, leucocyte (white blood cells) and low density lipoprotein (LDL) uptake and regulation of vascular tone [Traub and Berk, 1998; Chatzizisis et al., 2007].

Coagulation refers to the process of blood clotting due to platelet aggregation. If coagulation occurs, the healthy endothelium secretes anti-thrombotic agents, which together with certain proteins inhibit the coagulation process and thus keep the blood in a liquid state [Traub and Berk, 1998]. Furthermore, the endothelium actively participates in the breakdown of fibrous clots (i.e., fibrinolysis) through the production of plasminogation activators. In healthy arteries, the endothelium provides a non-adhesive, non-thrombo-genetic surface to prevent leucocytes and other cells, such as platelets and red blood cells from adhering to the endothelium or from migrating into the sub endothelial space [Chatzizisis et al., 2007].

The endothelium is also a source of various vasoactive substances that regulate the local and systemic vascular tone. Vascular tone is the degree of constriction from a basal level and its regulation occurs in response to biochemical stimuli and haemodynamic forces imposed by the flowing blood. Of particular interest here is the activation of the powerful vasodilator nitric oxide (NO), which exhibits many athero-protective characteristics including some of the previously mentioned anti-coagulation agents and the control of vascular adhesion molecules [Libby, 2001]. Furthermore, the endothelium is also an endogenous source of vasoconstrictors (substances that cause constriction of the blood vessel), which have been implicated in the formation of atherogenesis via smooth muscle cell proliferation.

Consequently, the healthy endothelium is responsible for maintaining and balancing many important biochemical processes, which are critical for the normal functioning of the cardiovascular system [Gimbrone et al., 2000].

Endothelial Dysfunction

Endothelial dysfunction refers to a reduced state of homeostatic functionality of the endothelium, which leads to a number of pathogenetic risk factors. The initiation of atherosclerosis was initially thought to be the result of endothelial injury [Ross and Glomset, 1976], but was later discarded after *in vivo* findings revealed that endothelial cells overlying atherosclerosis lesions are morphologically intact [Davies et al., 1976]. From these findings, the concept of endothelial dysfunction has been introduced [Gimbrone et al., 2000].

As described in the previous section, the critical role of the endothelium is to maintain the balance between vasodilators and vasoconstrictors and thereby creating an athero-protective environment [Traub and Berk, 1998]. If this balance is disturbed, many regulatory processes go astray. In this cascade of cellular responses and gene expression, the vasodilator nitric oxide (NO) is of crucial importance as it exhibits key athero-protective characteristics [Barbato and Tzeng, 2004]. A strong relationship between reduced NO activity and endothelial dysfunction has been identified, which includes the up-regulation of vasoconstrictors [Davignon and Ganz, 2004], the promotion of vascular adhesion molecules (which bind leucocytes), the stimulation of growth factors to cause proliferation of the underlying smooth muscle cells [Traub and Berk, 1998] and increased permeability of the endothelium to lipoproteins (LDL), which oxidise within the arterial wall to cause further complications [Chatzizisis et al., 2007]. As a consequence, the surface of the endothelium undergoes a biochemical change turning it into a pro-thrombotic, pro-atherogenetic environment.

The cause of endothelial dysfunction is currently not well defined, but is associated with a number of cardiovascular risk factors such as hypercholesterolemia (i.e., increased blood cholesterol levels), obesity, smoking, alcohol consumption, diabetes and chronic infections as well as hypertension (i.e., high blood pressure) and genetic predisposition.

Additionally, endothelial dysfunction is strongly associated with the prevailing haemodynamic environment, which controls wall shear stress activated NO release [Gimbrone et al., 2000]. Hence, understanding the detailed haemodynamic environment may provide information about predisposed locations for endothelial dysfunction, which can be clinically used to identify potential areas prone to atherosclerosis [Davignon and Ganz, 2004; Chatzizisis et al., 2007].

1.2.3 Mechanisms of Atherosclerosis

This section briefly outlines the processes involved in the initiation and development of atherosclerosis and highlights some of the key mechanisms that are thought to play an important role in the localised occurrence of atherosclerosis at very specific regions in the human vasculature.

Wall Shear Stress

Wall shear stress (WSS) is the force exerted by the flowing blood on the endothelium (Fig. 1.2) and its relation to atherogenesis has been intensely investigated for the past 30 years (e.g., Asakura and Karino [1990]; Friedman et al. [1981]; Zarins et al. [1983]; Ku et al. [1985a]). These studies have established a firm relationship between regions of disturbed flow and locations of intimal thickening, which particularly correlated with regions of low and oscillating WSS. Furthermore, it is well established that atherosclerosis is a site specific disease and is not evenly distributed throughout the human vasculature [DeBakey et al., 1985], occurring preferentially on the lateral walls of vessel bifurcations and inner and outer walls of arterial bends [Asakura and Karino, 1990; Zarins et al., 1983; Gimbrone et al., 2000].

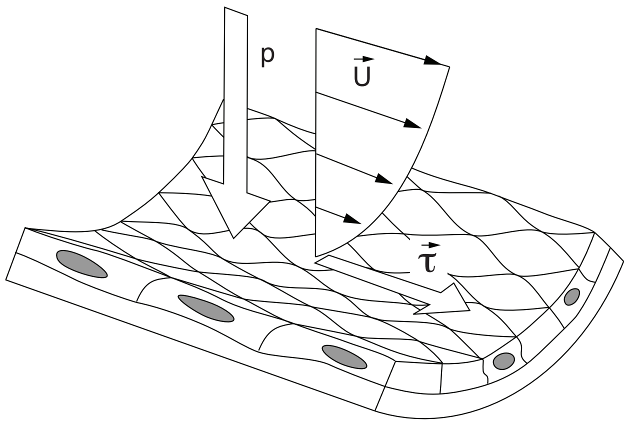

Figure 1.2 Endothelial Shear Stress

For example, Zarins et al. [1983] modelled blood flow in a scaled model using laser-Doppler anemometry and statistically correlated the flow characteristics to intimal thickening obtained from histological sections of an excised human carotid artery. Major findings from this study were that intimal thickening is associated with low WSS, flow separation and non-axially aligned velocity profiles, whilst areas subjected to moderately high WSS and axially aligned flow are not affected. This work was continued by Ku et al. [1985b], who performed unsteady (i.e., pulsatile) flow measurements in the same geometry. Their results confirmed the previous observations and further indicated a positive correlation between oscillatory WSS and intimal wall thickening. Further studies suppoerted the above findings, using artery segments excises from other regions of the human vasculature and thereby firmly establishing a relationship between disturbed haemodynamics and atherosclerosis. Furthermore, the above findings suggest that the arterial geometry, which ultimately determines the haemodynamic environment, plays a major role in the localised occurance of atherosclerosis [Friedman et al., 1983; Thomas et al., 2005].

From a biological point of view, both low and oscillatory WSS is a major regulator of many rapid cell responses, such a vasodilation and NO activation and hence is implicated in the early disease development. In particular, WSS is a major stimulus of endothelial structure and biological function as evidenced by a number of authors (e.g., Chatzizisis et al. [2007]; Malek et al. [1999]; Resnick et al. [2003]; Traub and Berk [1998]). In linear sections of the vasculature with axially aligned flow, the vessel diameter adapts to the local flow environment (via vasodilation and vasoconstriction) to maintain a normal physiological WSS level of approximately 1-2 Pa [Traub and Berk, 1998]. In these regions, the endothelial cells are ellipsoidal in shape and are aligned in an orderly manner with the flow direction [Malek et al., 1999] and exhibit many athero-protective characteristics (as discussed in Section 1.2.2). Consequently, atherosclerosis is rare in these locations. In regions of disturbed flow/low WSS, endothelial cells are poorly aligned and are more susceptible to endothelial dysfunction and potential plaque growth. In these regions (WSS < 0.4 Pa), endothelial cells exhibit pro-atherogenetic characteristics such as impaired NO synthesis, vascular smooth muscle cell proliferation and increased permeability of the endothelium. Furthermore, local mass transfer to and from the arterial wall is inhibited in these regions, leading to an increased aggregation of leucocytes and LDL molecules on the endothelium.

Initiation and Development of Atherosclerosis

The precise mechanisms involved in the early development of atherosclerosis are still disputed, but it has become increasingly evident that atherosclerosis manifests itself as an inflammatory disease that evolves over a considerable number of years [Ross, 1999; Libby et al., 2002]. Atherosclerotic plaque formation involves a complex interaction and structural changes between the arterial wall, the flowing blood and blood borne agonists. The disease is a precursor to well known pathological conditions such as myocardial infarction, stroke and peripheral arterial disease. The inflammation is a response of the body's immune system, resulting in remodelling of the arterial wall via deposition of lipid laden materials in the tunica intima, which eventually protrude into the arterial lumen, narrowing the vessel and causing arterial occlusion or rupture.

In the early stage of atherosclerosis, the endothelial surface exhibits reduced NO production [Libby et al., 2002] and over-expression of vascular adhesion molecules and subsequent leucocyte binding. This is followed by the attachment of leucocytes and LDL molecules, which subsequently penetrate into the intima to cause an inflammatory response. Within the intima, leucocytes differentiate into macrophages and LDL undergoes oxidation resulting in a very atherogenic endothelium and further expression of adhesion molecules. The oxidised LDL is scavenged by macrophages resulting in the formation of 'foam cells' and 'fatty streaks'. Furthermore, reduced NO causes over-expression of growth promoters and under-expression of growth inhibitors, which results in smooth muscle cell migration and proliferation. The proliferating smooth muscle cells also secrete extracellular proteins to form a fibrous cap that is characterised by a relatively high mechanical strength and is thought as a defense mechanism to prevent further thickening and protruding of the plaque.

From here onwards, the individual development of the plaque can vary significantly [Chatzizisis et al., 2007; Libby et al., 2002] as demonstrated in Figure 1.3. Initially, an early fibroatheroma develops in the low WSS environment with no restriction of blood supply occurring due to a dilation of the vessel to accommodate the expansion of the intima (Fig. 1.3(a)). Depending on the vascular response, the fibroatheroma subsequently develops into one of three distinct types: 1) a quiescent plaque; 2) a high risk plaque; and 3) a stenotic plaque.

Quiescent plaques are minimal-stenotic lesions with a thick fibrous cap, a small lipid core and limited inflammation and are caused by local expansive remodelling of the surrounding vascular tissue, normalising the local WSS and hence removing the haemodynamic stimulus for further plaque progression. As a response, the early lesion develops into a quiescent plaque causing no symptoms (i.e., asymptomatic) and low risk of rupture (Fig. 1.3(b)).

However, in the presence of certain haemodynamic, systemic and genetic factors, the local vascular wall may undergo excessive expansive remodelling,

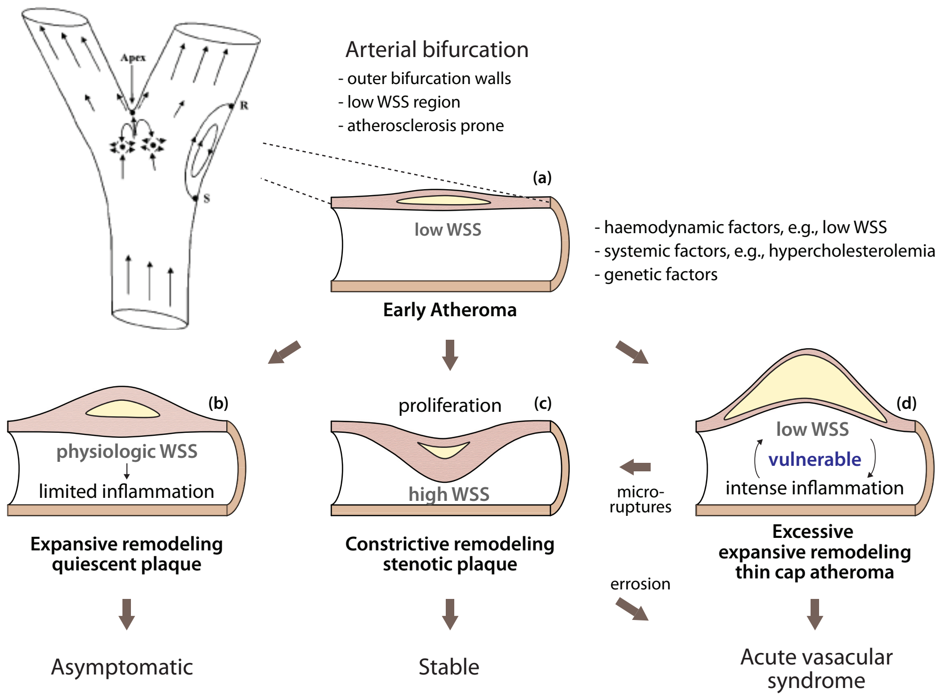

Figure 1.3 Progression of atherosclerosis, adapted from Chatzizisis et al. [2007]:

causing the formation of high risk plaques, which are characterised by a thin fibrous cap, containing significant amount of LDL and inflamed cells (i.e., 'foam cells') (Fig. 1.3(d)). In this case, the local low WSS environment continues to persist, promoting further plaque progression, establishing a self-perpetuating cycle between low WSS, vessel remodelling and plaque inflammation. The resulting plaques are extremely vulnerable and pose significant risk of rupture, which can lead to thrombus formation and associated acute vascular syndromes such as myocardial or ischemic infarction.

Lastly, the early atheroma can evolve into a stenotic plaque (Fig. 1.3(c)) by either fibroproliferation or scaring of prior micro-ruptures of high-risk plaques. Stenotic plaques have a thick fibrous cap and a small lipid core and are associated with constrictive remodelling, which over time leads to vessel occlusion. Typically, stenotic plaques are stable, but pose a moderate risk of rupture due to prolonged exposure to increased mechanical stress imposed by the flowing blood.

The individual plaque development depends primarily on the specific site within the vascular system and systemic and genetic factors. For example, each of the aforementioned plaques can co-exist in the same patient, even in the same artery and factors such as prevailing haemodynamics and local arterial response are critical determinants in the subsequent plaque development [Chatzizisis et al., 2007].

1.3 The Carotid Artery

As discussed in Section 1.2.3, studies have shown that atherosclerosis occurs at particular sites in the human vasculature such as arterial branches and bends. One of the locations particularly predisposed to the formation of chronic atherosclerosis lesion and often leading to acute vascular syndromes, is the carotid artery bifurcation [DeBakey et al., 1985].

The carotid arteries (CAs) are two large blood vessels located in the neck, ascending from the aortic arch and bifurcating into the internal carotid artery (ICA) and external carotid artery (ECA) to supply oxygenated blood to the brain (see Fig. 1.4). The ECA supplies blood to the face and surrounding tissue, while the ICA directly supplies the frontal part of the brain with oxygenated blood, which is distributed via the 'Circle of Willis' (see Guyton and Hall [2000] for more details) to perfuse the entire brain. The total blood flow through the CAs amounts to approximately 20% of the total blood flow within the human circulatory system.

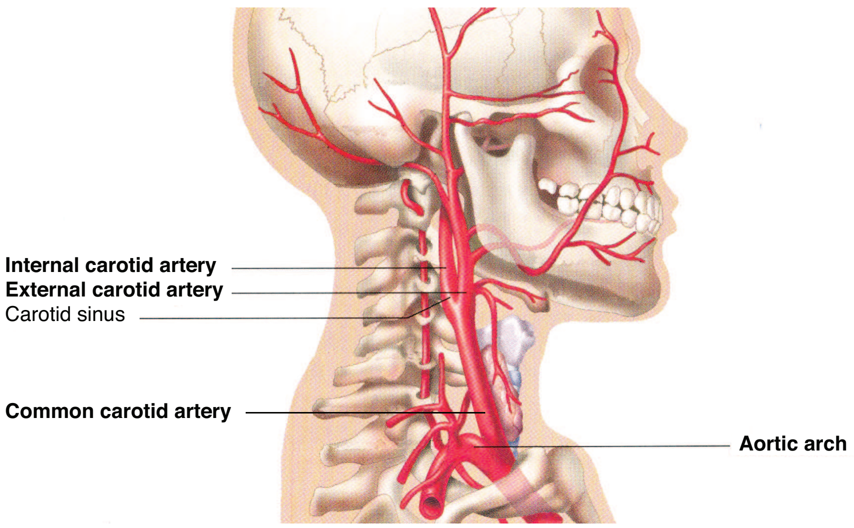

Figure 1.4 Arteries of the head and neck, highlighting the common carotid artery and its bifurcation. Adapted from Guyton and Hall [2000]

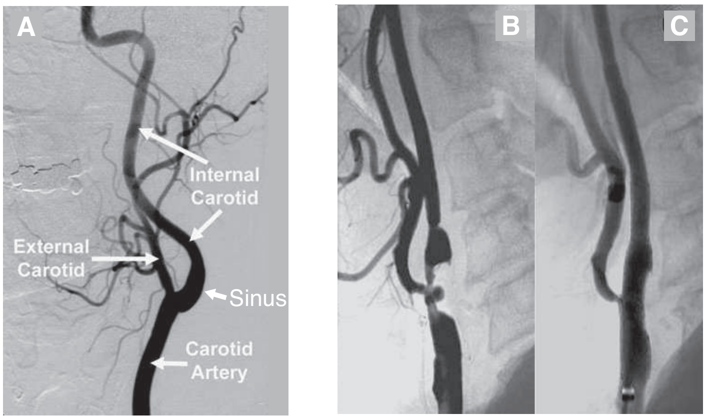

Figure 1.5 Angiogram of the carotid artery (CA); (a) healthy, (b) severe stenosis of the internal CA, (c) after CA stenting of (b)

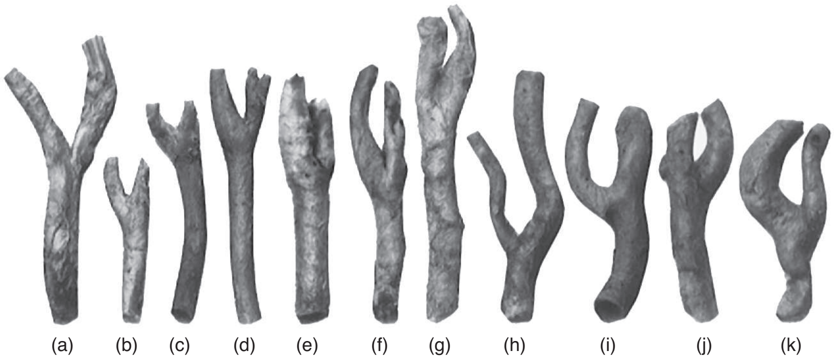

Figure 1.6 Specimens of the human carotid artery bifurcation. Figure adapted from Ding et al. [2001]; y-shaped bifurcation (a-d), tuning fork-shaped bifurcation (e-h), spoon-shaped bifurcation (i-k)

The formation of carotid artery disease has been observed to frequently occur where the common carotid artery (CCA) bifurcates into the ICA and ECA and is considered to be caused by the presence of the carotid sinus located at the origin of the ICA (Fig. 1.5(a)): its dilated, atypical geometry provides a unique haemodynamic environment, giving rise to variations in flow characteristics such as low and oscillating WSS, flow separation and flow turbulence. Furthermore, the vessel wall has strong curvatures in this region, causing the formation of transverse pressure gradients and secondary flow motion. In its most severe form, carotid artery atherosclerosis can lead to complete vessel occlusion and thrombus formation, resulting in disrupted blood supply to the brain and consequently stroke. Classical treatments of carotid artery stenosis include carotid artery endarterectomy to surgically remove the plaque or carotid artery stenting to widen the arterial lumen by inserting a slender metal-mesh tube (Fig. 1.5(b-c)).

Given the significant consequences resulting from atherosclerotic plaque formation in the carotid artery, extensive research has been conducted to correlate the distribution of intimal lesion with the local flow conditions in the carotid sinus. Due to its geometrical variability (see Fig. 1.6), the carotid artery is also of considerable interest for the investigation of the general mechanisms of atherogenesis as similar flow features are often observed in other atherosclerosis-prone regions throughout the human vasculature. Therefore, further investigations of the haemodynamic mechanisms and the localisation of atherosclerotic plaque in the carotid artery is expected to contribute to the general understanding of the pathology of atherosclerosis.

1.4 Carotid Artery Haemodynamics - Experiments and Modelling

The primary techniques used for haemodynamic investigations in the carotid artery and other major blood vessels are *in vivo* investigations and experimental (i.e., *in vitro*) and computational modelling. Until the mid-1980s, traditional engineering flow measurement techniques such as Laser Doppler Velocimetry (LDV) were utilised in early haemodynamic studies, establishing the first links between haemodynamic forces and distribution of atherosclerotic lesions [Friedman et al., 1981; Zarins et al., 1983; Ku et al., 1985b]. These investigations were later complemented by computational studies to provide a higher level of detail hitherto impossible with experimental techniques [Xu and Collins, 1990]. At the same time, medical imaging techniques such as X-ray cine angiography, Doppler ultrasound and magnetic resonance imaging (MRI) emerged, allowing for the first time blood flow measurements *in vivo* [Steinman and Taylor, 2005].

While *in vivo* techniques have the potential to provide the most realistic flow field data, they currently lack the spatial and temporal resolution offered by *in vitro* experimental and computational approaches. However, a major challenge for the latter techniques is the accurate representation of the true physiological boundary conditions such as vessel geometry, blood and tissue properties and inflow/outflow conditions. In order to mitigate these shortcomings, modern modelling approaches utilise vascular geometries and boundary conditions obtained from clinical MRI or computed tomography (CT) data.

The following review of large artery haemodynamic modelling is subdivided into three sections: *in-vivo* techniques, experimental (i.e., *in vitro*) modelling and computational modelling and will primarily focus on the individual techniques and their role in assessing carotid artery haemodynamics. An excellent review of the early numerical and experimental work related to arterial bifurcation in general is given in Lou and Yang [1992] and Ku [1997], while the more recent work in this area is reviewed in Friedman and Giddens [2005]; Taylor and Draney [2004] and Steinman and Taylor [2005].

1.4.1 *In vivo* Techniques

In-vivo measurements of complex blood flow and its interaction with the vessel wall is difficult and various clinical approaches are currently available for diagnosis and treatment. Modern non-invasive techniques dedicated to blood flow measurements include Doppler and ultrasound-based techniques [Vennemann et al., 2007] as well as echo-PIV [Kim et al., 2004; Poelma et al., 2009], a combination of ultrasound imaging and PIV processing. Furthermore, magnetic resonance velocimetry, based on MRI permits the measurement of three-dimensional velocity fields, but is currently limited to mean velocities (i.e., steady flow) or phase-averaged values in periodic flow. The latter is achieved by using an electrocardiogram to trigger the measurement in the case of pulsatile flow. A thorough review of recent developments in MRI velocimetry and its application in physiology and engineering is given by Elkins and Alley [2007].

Common to all *in vivo* techniques is the limited spatial and temporal resolution and relatively large measurement noise due to motion artefacts. Studies of carotid artery haemodynamics involving MRI velocimetry include the likes of Botnar et al. [2000]; Marshall et al. [2004] and Zhao et al. [2003] who used idealised and patient specific boundary conditions. These studies were predominantly used to validate the authors' numerical models, which was mostly done qualitatively due to the limited spatial resolution in MRI [Botnar et al., 2000].

However, for a more detailed quantitative validation of velocity and WSS fields determined by *in vivo* or numerical techniques, instantaneous, high resolution whole-field measurement techniques such as PIV are required.

1.4.2 *In vitro* Techniques

An alternative to *in vivo* measurements is the individual or simultaneous use of laboratory models representing the arterial geometry. Typically, these models are reconstructed from patient specific or population averaged data and are optically transparent. Together with a transparent blood substitute, these models allow the use of nonintrusive, high resolution measurement techniques such as LDV or PIV. The experiments can be of various degrees of complexity, including steady and pulsatile flow conditions, vessel wall compliance or Non-Newtonian blood rheology. Furthermore, some of the previous described *in-vivo* techniques, such as MRI, can also be applied to the laboratory models to verify or improve their accuracy.

Idealised Geometries

Bharadvaj et al. [1982b,a] were amongst the first to study carotid artery haemodynamics in an idealised Y-shaped glass model based on population averaged data. They conducted steady flow measurements to assess the velocity and WSS distributions by means of flow visualisation and LDV. Results from these studies indicated flow separation near the junction between the CCA and ICA and a region of flow recirculation along the outer wall of the carotid sinus. This recirculation region, however, is not a true recirculation zone with particle entrapment as it was later proven by Motomiya and Karino [1984]. Instead, the flow moves laterally approaching a stagnation line to subsequently follow a helical flow trajectory downstream. These helical structures are characteristic for the flow field in the carotid sinus and are a result of the interaction between secondary flows and vessel curvature. These early studies were continued by Zarins et al. [1983] and Ku et al. [1985b] using the same geometry to statistically correlated WSS measurements with histological observations of intimal thickness, establishing for the first time a direct link between arterial WSS and intimal thickening (see Section 1.2.3).

From these observations, the above authors concluded that regions of low WSS, flow separation and departure from axially aligned flow, such as in the carotid sinus, are associated with intimal thickening and the formation of atherosclerosis. On the other hand, in regions of relatively high WSS and unidirectional laminar flow lesion formation was inhibited as concluded by the authors.

Ku et al. [1985a] and Ku and Giddens [1987] extended the above studies by including pulsatile flow characteristics and performing phase-averaged LDV measurements in the same Y-shaped geometry. While many of the general flow characteristics found under steady flow persisted (i.e., flow separation, secondary vortices), new unsteady phenomena appeared to be of important significance. Particularly, flow separation in the carotid sinus did not exist throughout the entire cardiac cycle and the location of the separation and reattachment point migrated along the outer vessel wall.

These observations led to the formulation of the oscillatory shear index (OSI) [Ku et al., 1985a], which is indicative of WSS oscillation and a positive correlation with intimal thickening. Amongst other parameters, OSI is now one of the most commonly used haemodynamic indicators for vascular wall dysfunction [Lee et al., 2009]. In contrast to the observations of Ku et al. [1985a], little quantitative differences between steady and pulsatile flow were reported by LoGerfo et al. [1981], while Friedman et al. [1981] confirmed the negative correlation between intimal thickening and WSS for both steady and pulsatile flow. This disagreement clearly highlights the need for further detailed investigations into the differences of steady and pulsatile flow.

Besides the above cited work, the Y-shaped carotid artery bifurcation geometry was also used by Rindt and Steenhoven [1996] to measure secondary flow characteristics in the carotid sinus and by Gijsen et al. [1999b] to assess the role of Non-Newtonian blood rheology under steady flow conditions.

At the end of the 1990s, the averaged Y-shaped bifurcation had to some extent become a standard in experimental and numerical modelling of carotid artery haemodynamics [Lou and Yang, 1992]. Subsequent work however, revealed that this geometry was not sufficiently accurate to correctly model the physiological flow conditions in the human carotid artery [Ding et al., 2001]. This was particularly observed in relation to the correlation between OSI and locations of intimal thickening, which was strong at the inner and outer sinus walls, but weak at the sidewalls where stronger correlations were expected as suggested by clinical observations. Consequently, Lei et al. [1995] questioned the validity of OSI, while Ding et al. [2001] advised against the use of the Y-shaped bifurcation model. Ultimately, post-mortem studies by Ding et al. [2001] and Goubergrits et al. [2002] revealed that only 8% of the vessels corresponded to a

Y-shaped geometry, while more than 50% of the dissected vessels had a tuning-fork shape (TF-shape) (see Fig. 1.6). As a consequence, Ding et al. [2001] conducted LDV measurements in an idealsied TF-shaped glass model, confirming the hypothesised geometrical differences and demonstrating an improved correlation between OSI and intimal thickening for the TF-shaped model.

Patient Specific Geometries

As mentioned above, the geometry of an individual carotid artery differs markedly from the population average [Ding et al., 2001; Goubergrits et al., 2002; Thomas et al., 2005] and the underlying haemodynamics and hence plaque growth are likely to be influenced by the individual vessel geometry. This causality is referred to as 'geometric risk factor' in the literature [Friedman et al., 1983; Perktold and Resch, 1990; Nguyen et al., 2008b; Thomas et al., 2005]. A number of research groups have requested a greater focus on physiologically realistic geometries to further understand the individual blood flow characteristics and their potential for the development of atherosclerosis [Myers et al., 2001; Perktold et al., 1998]. While this demand is currently well met with numerous numerical studies of carotid artery haemodynamics (see next section), detailed *in-vitro* studies in physiological accurate models are still sparse. This lack of experimental work is mostly due to the increased complexity required to accurately represent the true physiological flow conditions and the herewith associated experimental difficulties. In the past, this has considerably constrained the advancement in these areas, but with the emerge of new measurement technologies such as planar and stereoscopic PIV or MR velocimetry, combined with physiological boundary conditions, experimental *in vitro* studies are still an attractive research tool.

Some of the previous experimental work in such anatomically realistic geometries (healthy and diseased) include the like of Liepsch et al. [1998] and Liepsch [2002], who conducted LDV measurements in rigid and compliant carotid artery models using Newtonian and Non-Newtonian blood rheology and pulsatile inflow conditions. Although, the results from these studies were very instructive in terms of velocity field data, the authors did not measure the WSS, one of the most important haemodynamic parameters. Furthermore, the use of LDV provides only point-wise velocity information, and the measurement of whole field velocity maps, nowadays necessary for a complete haemodynamic assessment, can only be obtained with considerable experimental effort. Unlike in other physiological flow problems, the application of PIV to study, carotid artery haemodynamics in physiological models has received only little attention in the past. Amongst the few studies currently available is the work of Bale-Glickman et al. [2003a,b], who performed planar PIV measurements in adjacent planes in a diseased carotid bifurcation model and more recently stereoscopic PIV measurements in an anatomical carotid artery model by Vétel et al. [2009].

From these studies it can be concluded that the individual flow structure in physiological models broadly resembles that observed in idealised models, but with marked differences in the detailed occurrence of flow separation/recirculation and velocity/shear stress magnitude. Additionally, the latter studies also reported the existence of complex, three-dimensional coherent flow structures and the onset of flow instabilities for higher physiological Reynolds numbers and steady flow conditions, which was not observed in idealised models.

Lastly, non-invasive WSS measurements in such complex geometries are difficult. In doppler ultrasound or MRI measurements, WSS is often inferred by assuming fully developed flow [Reneman et al., 2006], while in *in-vitro* experiments, WSS is often measured by LDV [Ding et al., 2001; Ku and Giddens, 1987]. Common to these techniques are uncertainties in measured WSS due to limited spatial resolution and/or uncertainties in wall normal distance. While for LDV measurements these uncertainties can be relatively low (down to $\pm 1\%$, Durst et al. [1996]), the acquisition of complete WSS maps is rather time consuming and experimentally elaborated. The measurement of detailed WSS maps by means of PIV has been demonstrated by Zhang et al. [2008] for physiological flow in a realistic anastomosis model, yet to the author's best knowledge no such detailed WSS measurements exist in physiological accurate carotid artery models.

In summary, the above review has revealed a lack of experimental work investigating physiological realistic and relevant carotid artery flow cases. Though some attempts have been made, the current experimental assessment of important haemodynamic parameters such as spatial and temporal WSS is still difficult and prone to experimental uncertainties. Furthermore, differences in steady and pulsatile flow were identified and require further investigation, particularly in patient specific modelling. The relevance of flow instabilities and turbulence is also still unclear and their implications in disease development need to be further assessed. Particle Image Velocimetry can overcome some of the current limitations in spatial and temporal resolution and provides instantaneous, three-dimensional and three-component velocity field data, making it an attractive experimental technique for future studies.

1.4.3 Computational Studies

Recently, the biofluid dynamics community has mainly utilised computational fluid dynamics (CFD) as the preferred technique for modelling large artery haemodynamics. Computational fluid dynamics presents itself as a powerful and insightful research tool for the identification of numerous haemodynamic parameters such as WSS (and related indices) that are currently difficult to assess with *in vivo* or *in vitro* techniques.

Wall shear stress remains one of the most intensively researched areas in CFD modelling, primarily due to the strong correlation that has been identified between low WSS and lesion development [Ku et al., 1985b; Zarins et al., 1983]. Early computational models related to WSS were the likes of Perktold and Resch [1990] and Perktold et al. [1991a], who modelled pulsatile flow in a 3D model of the carotid artery bifurcation under different bifurcation angles. They concluded that the most physiologically relevant flow variable is WSS and its temporal variation, which is in agreement with previous *in vitro* results. Following this work, numerous numerical studies investigating WSS were conducted in a variety of arterial models, predominantly bends and bifurcations. These include direct WSS studies [Myers et al., 2001; Perktold et al., 1998] and also WSS related indices such as oscillatory shear index (OSI) [He and Ku, 1996], wall shear stress gradients (WSSG) [Lei et al., 1995; Lee et al., 2009] and particle residence time [Lee et al., 2009], all in an attempt to formulate the underlying characteristics that lead to the onset of atherosclerosis.

Obviously, WSS is directly affected by the prevailing haemodynamics, but also by other factors such as the shear thinning properties of blood and vessel wall compliance. In large arteries, Non-Newtonian rheology is negligible, as the essential flow characteristics are captured by Newtonian flows due to the generally high shear environment [Gijsen et al., 1999b; Perktold et al., 1991b] and the assumption of Newtonian blood properties are now generally accepted for large to medium arteries.

More recently, the investigation of geometric variations as a potential risk factor has seen increased attention not at least due to the increased availability of medical imaging data [Friedman et al., 1983; Perktold and Resch, 1990; Nguyen et al., 2008b; Karner et al., 1999; Lee et al., 2009; Milner et al., 1998; Tan et al., 2008; Zhao et al., 2000], highlighting the role of the inter-individual variation of arterial geometry in the localised occurrence of atherosclerosis. However, to establish a firm relationship between individual geometrical markers and the localised development of atherosclerotic lesions, further systematic studies are required [Thomas et al., 2005], both numerically and experimentally.

The simulation of vessel wall motion and fluid structure interaction has also received an increased interest [Karner et al., 1999; Zhao et al., 2000; Tang et al., 2008], though the mechanical properties of the arterial wall are not yet well known, and the numerical implementation of complex fluid structure interaction is currently still immature and requires experimental validation.

Lastly and probably most limiting to the accurate numerical simulation of arterial blood flow, is the common assumption of laminar flow conditions [Friedman and Giddens, 2005]. While this assumption is mostly valid in healthy carotid arteries, in the presence of complex geometries or chronically diseased arteries, the flow can become unstable and undergo transition to low Reynolds number (weak) turbulence [Vétel et al., 2009; Lee et al., 2007; Bale-Glickman et al., 2003a], rendering the laminar flow assumption invalid. Although simulations can be carried out for transitional and turbulent flows, the associated increase in numerical complexity and turbulence modelling still requires thorough experimental validation on an almost case by case basis [Friedman and Giddens, 2005]. For example, recent direct numerical simulations by Fischer et al. [2007] in a diseased CA model revealed the existence of time-dependent small-scale turbulent structures and velocity fluctuations, resulting in high-frequency flow variations in the post-stenotic region. Similar observations were reported by Rayz et al. [2007] and confirmed with experiments using the same geometry and boundary conditions by Bale-Glickman et al. [2003a]. The significance of flow turbulence in the pathology of vascular diseases is also still unclear and requires further investigation on a biochemical and biomechanical level.

1.5 Summary and Thesis Aims

In summary, for 'routine' investigations of large artery haemodynamics, and in particular parametric studies, CFD is the preferred research tool. This is mainly because of its relative flexibility and the easy accessibility of the full three-dimensional velocity field, WSS and spatial and temporal gradients, which are difficult to obtain experimentally.

Nevertheless, experimental techniques and particularly *in vitro* methods continue to play a key role in arterial modelling, especially in applications where CFD remains relatively immature including models with moving walls, embedded devices, such as vascular stents, and in cases of developing flow instabilities and turbulence in diseased vessels. Therefore, to further our knowledge in cardiovascular fluid dynamics the current experimental techniques need to be advanced and new techniques have to be developed and tested.

The goal of this research is to develop a new experimental procedure to accurately measure velocity and WSS fields *in vitro*. The technique will be based on PIV and readily applicable to patient specific vascular models to provide full spatial and temporal velocity and WSS data, suitable for comparison with numerical predictions. Furthermore, the research will perform full-field flow measurements in idealised and patient specific models of the human carotid artery to verify the newly developed methodology and to gain further insight into the interplay between local haemodynamics and disease development.

In particular, the specific aims of this research are:

1. To develop a methodology for the construction of patient specific vascular *in vitro* models suitable for optical nonintrusive flow measurements.

2. To develop the necessary soft- and hardware components to perform Particle Image Velocimetry measurements of the three-dimensional flow structure in complex arterial models developed in (1).

3. To develop a PIV based WSS measurement technique to provide full field, high fidelity WSS data.

4. To employ (1) - (3) to investigate carotid artery haemodynamics and to

study the effect of inflow conditions (i.e., steady vs. pulsatile) and differences between idealised and patient specific geometries.

5. To investigate and establish the precision and uncertainties of the measurement techniques developed in (1) -(3).

6. To analyse the results from (4) to extract spatial and dynamic velocity and WSS characteristics. Particular attention will be given to the analysis of the three-dimensional flow structure and the associated WSS distribution.

7. To provide technology and expertise for subsequent experimental research projects utilising Particle Image Velocimetry and/or vascular modelling.

1.6 Thesis Outline

In the following, a brief overview of the individual thesis chapters is given:

Chapter 2 introduces the applied haemodynamic modelling assumptions and presents the development of vascular flow phantom representative of the human carotid artery (aim 1). The appropriate literature is reviewed and several key aspects are discussed systematically. The result of this chapter is a transparent silicon phantom with a refractive index matched blood substitute suitable for optical flow measurements.

Chapter 3 presents the newly developed Particle Image Velocimetry algorithm with stereoscopic reconstruction. The individual components of the PIV analysis are reviewed and discussed and an assessment of the measurement uncertainty is provided using synthetically generated test cases (aims 2 & 5).

Chapter 4 develops a novel, PIV based methodology for the accurate measurement of WSS along curved surfaces (aim 3). The problem of near-wall PIV is described and solutions to overcome these limitations and methods to improve the PIV measurement accuracy are introduced. The WSS method is verified and validated using numerical and experimental test cases (aim 5).

Chapter 5 analyses the flow field and WSS distribution in an idealised carotid artery model under steady flow conditions. Results are compared with numerical predictions and the influence of carotid artery stenosis on the flow field, WSS and flow turbulence is discussed (aims 4 & 6).

Chapter 6 applies the previously developed measurement techniques to the study of a patient specific carotid artery model with physiological boundary conditions. The differences between steady and pulsatile flow are discussed and reference to the idealised model is given (aims 4 & 6).

Chapter 7 presents an investigation in the three-dimensional flow structure within the carotid sinus. Stereoscopic PIV and full three-dimensional tomographic PIV measurements in the idealised and patient specific model are presented for steady inflow conditions. The three-dimensional flow topology and WSS distribution is discussed and the techniques are further characterised with regard to their measurement uncertainty (aims 4, 5 & 6).

Chapters 8 summarises the key aspects of this thesis and presents possible future improvements and applications for this research.

Chapter 2

Blood Flow Modelling and Experimental Materials

2.1 Introduction

The first part of this chapter describes the basic blood modelling assumptions and techniques for the reconstruction of anatomically accurate vessel geometries employed in this research. The second part of this chapter will introduces techniques to reproduce such geometries in a transparent flow phantom with rigid walls. Lastly, the development of a dynamically similar and refractive index matching blood analogue liquid is described.

2.2 Arterial Modelling Considerations

Blood is a suspension of blood cells (haematocrit) in blood plasma and its primary function is the transport of nutrients and waste products. The suspended particles are red blood cells, white blood cells and platelets, which account for approximately 42% of the blood volume [Guyton and Hall, 2000]. Blood plasma accounts for the remainder and is composed of about 92% water and 8% proteins. In order to model such a complex fluid, a number of considerations and assumptions are made to achieve physically plausible results in an experimental *in-vitro* approach. The following three sections outline the basic model assumptions, governing equations and similarity analysis relevant to this work.

2.2.1 Modelling Assumptions

Generally, blood can be assumed to be homogeneous and incompressible, which allows it to be treated as a piecewise continuous medium in space and time. Strictly speaking, as mentioned earlier, blood is a suspension of particles in plasma, but in large and medium sized vessels a macroscopic view can be taken. For example, the common carotid artery diameter is about 6-8mm, whereas the largest particles suspended within the plasma are in the order of 7.5μm. This provides at least three orders of magnitude difference and hence allows blood to be treated as homogenous within the scope of this work. The incompressible assumption is valid for all liquids that undergo relatively small pressure variation, as it is the case within the human vasculature. Furthermore, blood is assumed to be an isothermal fluid.

An interesting factor of blood is that it exhibits a shear thinning non-Newtonian rheology, meaning that the relationship between stress in the fluid is not proportional to its rate of deformation. The blood viscosity depends largely on shear stress and haematocrit level [Guyton and Hall, 2000] and in general, the higher the haematocrit, the higher the viscosity. Neglecting non-Newtonian rheology is a common practice in arterial modelling and is based on the argument that in large to medium sized arteries, the shear rates are predominantly

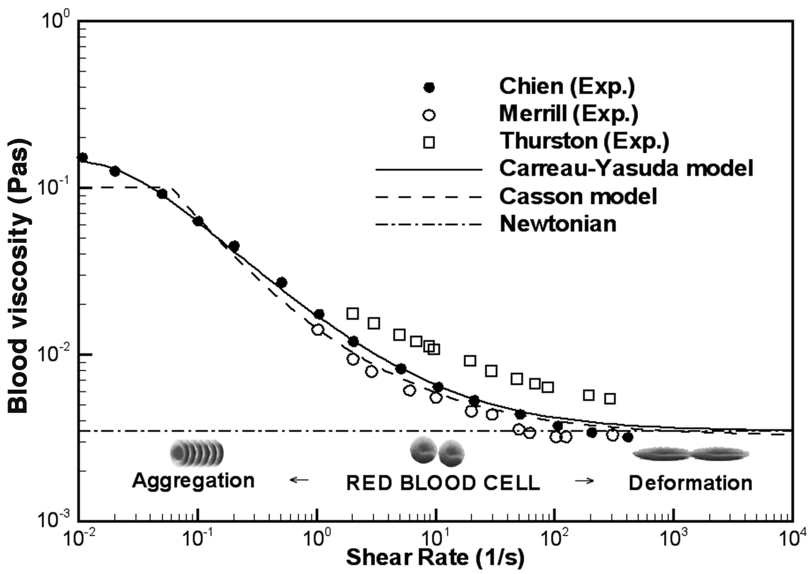

Figure 2.1 Variation of blood viscosity with shear rate [Moore, 2008]

high (>100s^{-1}), and hence, blood viscosity approaches its Newtonian high shear rate limit viscosity (μ_∞) as shown in Figure 2.1. For example, Perktold et al. [1991b] computed unsteady flow in a three-dimensional model of the human carotid artery to investigate the effects of Newtonian versus non-Newtonian blood rheology. Their findings indicated very similar large scale flow characteristics between the two rheologies and differences in wall shear stress (WSS) magnitude were less than 10%. Some studies supported these findings [Cho and Kensey, 1991; Lee and Steinman, 2007], whilst others contradicted them [Gijsen et al., 1999b; Liepsch and Moravac, 1984]. Other studies utilised rescaled Newtonian liquids based on a characteristic shear rate and obtained remarkably good agreement in comparison to non-Newtonian blood rheology [Ballyk et al., 1994; Gijsen et al., 1999a; Thurston, 1979].

Considering the momentum equation for steady, axisymmetric flow in a straight pipe, a characteristic shear rate ($\dot{\gamma}_c$) can be defined as the following:

$$\dot{\gamma}_c = \frac{4Q}{\pi a^3} \tag{2.1}$$

which is equivalent to that introduced by Hoeks et al. [1995]. For a typical mean flow rate of Q = 10ml/s in the carotid artery and a radius of a=3.3mm, the shear rate is calculated as 354s^{-1}, which is greater than the given threshold of 100s^{-1}. Hoeks et al. [1995] conducted *in-vivo* ultrasound measurements in common carotid arteries and found peak and mean shear rates of 1104s^{-1} and 342s^{-1}, respectively. These findings were later confirmed by Samijo et al. [1998] who additionally measured whole blood viscosity, which in average ranged between $2.89 - 3.22 \times 10^{-3}$Pa·s, depending on the subjects' sex and age.
Based on this evidence, blood is assumed as a Newtonian fluid in this research with a high shear rate limit viscosity of $\mu_\infty = 3.5 \times 10^{-3}$Pa·s and density $\rho = 1.025$g/cm^3 [Gijsen et al., 1999b].

It is well known that *in-vivo*, arteries are distensible and their walls move during the cardiac cycle in response to pressure induced by the flowing blood. In this research, the effects of distensibility are neglected and the arterial walls are assumed to be rigid. Previous studies [Karner et al., 1999; Perktold and Rappitsch, 1995] used computational methods to model the flow within a distensible carotid bifurcation. Their results indicated a reduction in flow separation and recirculation with an accompanied reduction in WSS of up to 25%, but concluded that the global flow structure and stress pattern remained relatively unchanged. Another reason for neglecting wall distensibility is due to the difficulties and complexity in constructing flexible flow models that are suitable for non-invasive optical measurements. Therefore, the arterial walls are assumed to be rigid in this work. It should be noted that this assumption does not diminish the importance of wall distensibility in arterial modelling, nor its role in atherosclerosis, and that the issue should be addressed in future studies.

2.2.2 Governing Equations

Following the above assumptions, blood flow can be described with the Navier-Stokes equation, which in its general form reads:

$$\rho \frac{D\mathbf{u}}{Dt} = \rho \mathbf{k} + \nabla \cdot \mathbf{T} \tag{2.2}$$

$$\nabla \cdot \rho \mathbf{u} = 0 \tag{2.3}$$

where $\mathbf{u}$ is the velocity vector, $\frac{D}{Dt}$ the material derivative, $\mathbf{k}$ the body forces per unit mass, ∇ the gradient operator and $\mathbf{T}$ the Cauchy stress tensor. A constitutive equation is required to couple the Cauchy stress tensors to the rate of deformation and/or the deformation of the fluid. For an incompressible Newtonian fluid with a constant dynamic viscosity μ, the Cauchy stress tensor can be written as:

$$\mathbf{T} = -p\mathbf{I} + 2\mu \mathbf{E} \tag{2.4}$$

$$\mathbf{E} = \frac{1}{2}[\nabla \mathbf{u} + (\nabla \mathbf{u})^T] \tag{2.5}$$

where p is the hydrostatic pressure and $\mathbf{E}$ the rate of deformation tensor. In the case of non-Newtonian fluid models, the constitutive equations can be rewritten to incorporate the non-linear and time-dependent properties of blood (see Gijsen et al. [1999b]).

2.2.3 Dimensionless Parameters in Blood Flow

Experimental scaling based on dynamical similarity (i.e., dimensional analysis) is a well established concept in experimental fluid mechanics and permits the use of models to investigate full-scale conditions that are difficult to replicate in a laboratory environment. Typically, dynamical similarity is used to down-scale large scale problems, but in the study of blood flow in small arteries, models larger than life-scale are often required. This section describes the fundamental scaling requirements of blood flow under the above mentioned assumptions.

As described in Chapter 1, the shear stress acting on the endothelial wall (τ_w) is an important haemodynamic parameter and can be seen as a function of

$$\tau_w = f[U, D, \rho, \mu, \omega, \hat{u}] \tag{2.6}$$

where U represents the spatial and temporal mean velocity, D the artery diameter and ρ the fluid density. In addition, blood flow is of pulsatile nature, which is characterised by the frequency of pulsation ω and the velocity range $\hat{u} = (u_{max} - u_{min})$. Applying the Buckingham Π-theorem to Equation 2.6 yields the following relation:

$$\frac{\tau_w}{\frac{1}{2}\rho U^2} = f\left[\frac{UD\rho}{\mu}, \frac{\omega D}{U}, \frac{\hat{u}}{U}\right] \tag{2.7}$$

which describes the dependency of WSS on the above parameters in three non-dimensional groups. Namely, the Reynolds number, Re the Strouhal number, St and the pulsatility index, $\frac{\hat{u}}{U}$.

In haemodynamic studies, the Womersley parameter α is often preferred over the Strouhal number and can be obtained by combining the latter with the Reynolds number to $\alpha = \frac{1}{2}\sqrt{ReSt}$. The Womersley number is a quantification of quasi-steadiness and represents the ratio of the fully developed viscous boundary layer thickness ($\frac{D}{2}$, for Poiseuille flow) relative to the oscillating boundary layer thickness. If the oscillatory viscous layer does not re-establish at each cycle, its thickness will be smaller than the vessel radius; consequently, α is larger than unity and quasi-steadiness cannot be assumed. The quasi-steadiness hypothesis supposes that the fluid responds instantaneously to pressure gradient variations. For small Womersley numbers, viscous forces dominate and velocity profiles are parabolic in shape with the centerline velocity oscillating in phase with the driving pressure gradient [Womersley, 1955]. For high Womersley numbers (>10), unsteady inertial forces dominate, and velocity profiles are flat. The flow amplitude decreases at higher frequencies, and the phase difference between pressure gradient and flow increases [Ku, 1997]. The Reynolds number describes the relative importance of viscous forces to inertial forces and the pulsatility index is a measure of peak velocity to mean velocity.

Therefore, any experimental design should aim to match the following three dimensionless groups to maintain dynamical similarity between the laboratory measurements and *in-vivo* flow conditions.

$$\mathrm{Re} = \frac{UD\rho}{\mu} \quad : \quad \text{Reynolds number} \tag{2.8}$$

$$\alpha = \frac{D}{2}\sqrt{\frac{\omega\rho}{\mu}} \quad : \quad \text{Womersley number} \tag{2.9}$$

$$\frac{\hat{u}}{U} \quad : \quad \text{pulsatility index} \tag{2.10}$$

Within the human vasculature, typical Reynolds numbers range between 1 in small arterioles to approximately 4000 in the largest arteries such as the aorta. Likewise, Womersley numbers vary between 1 to approximately 10 in the large arteries. In the carotid artery, mean Reynolds numbers are approximately 300 (peak, 900) and the Womersley number falls in the range of about 4-5 [Ku, 1997].

To include the non-Newtonian properties of blood, the above dimensional analysis can be extended by including a power-law model for the dynamic viscosity as detailed by Gray et al. [2007]. The results of this analysis are an additional non-dimensional parameter and a modified 'power-law' Reynolds number. Alternatively, rescaling of a Newtonian liquid can be performed as proposed by Gijsen et al. [1999a]. In this case, the viscosity of the rescaled Newtonian liquid is based on the characteristic shear rate (Eq. 2.1) and is typically smaller than the high shear rate viscosity. Hence, the Reynolds and Womersley number reduce accordingly.

2.3 Arterial Geometries

As illustrated in Chapter 1, the carotid artery bifurcation is a complex three-dimensional structure, which varies greatly among the general population. In order to simulate blood flow within the carotid bifurcation, three important questions arise in the development of a geometric model:

- What anatomical data should the model be based on?
- How much of the vascular tree should be included in the model?
- Should the model be generic, based on population averaged dimensions or is a patient specific model required?

The first and second questions are intimately linked and depend on the quality and availability of anatomical data and the scope of the investigation. Anatomical data can either be obtained from autopsy studies or medical imaging such as Magnetic Resonance Imaging (MRI) or Computed Tomography (CT). While autopsy data usually provides population averaged information such as length, diameter and bifurcation angles, they lack information regarding the complex 3D structure and surface topology. Hence, the use of population averaged data ultimately implies the development of generic models. Medical imaging data can overcome these limitation, but suffers from limited spatial resolution. For example, for a 1.5T MRI scanner, the typical resolution limit is 0.5mm. This resolution limit does not pose a great problem in the reconstruction of medium to large arteries, but limits the reconstruction of small arteries and other fine topological details. The use of medical image data also requires image segmentation techniques to create a 3D surface mesh of the arteries.

The following sections describe three different techniques for the construction of idealised and patient specific models of the carotid artery bifurcation utilised in this research.

2.3.1 Idealised Geometries

The geometry of an idealised carotid artery bifurcation is developed in SolidWorks (SolidWorks, Concord, MA, USA). The dimensions of the bifurcation correspond to a population average and details are given in Chapter 5. In the following section, only the procedure for developing the 3D computer model is outlined.

The idealised bifurcation geometry is axisymmetric and the branching plane is the symmetry plane. An initial 2D sketch comprising the basic geometry is created on a planar surface, with the required branching angle specified. Orthogonal planes with their normals defining the axis direction of the artery are created at the end of the 2D line sketches as shown in Figure 2.2(a). On each plane, the corresponding vessel diameters are specified via a circular sketch and subsequently joined with 3D lines to create the final skeleton of the idealised vessel bifurcation (Figure 2.2(b)).

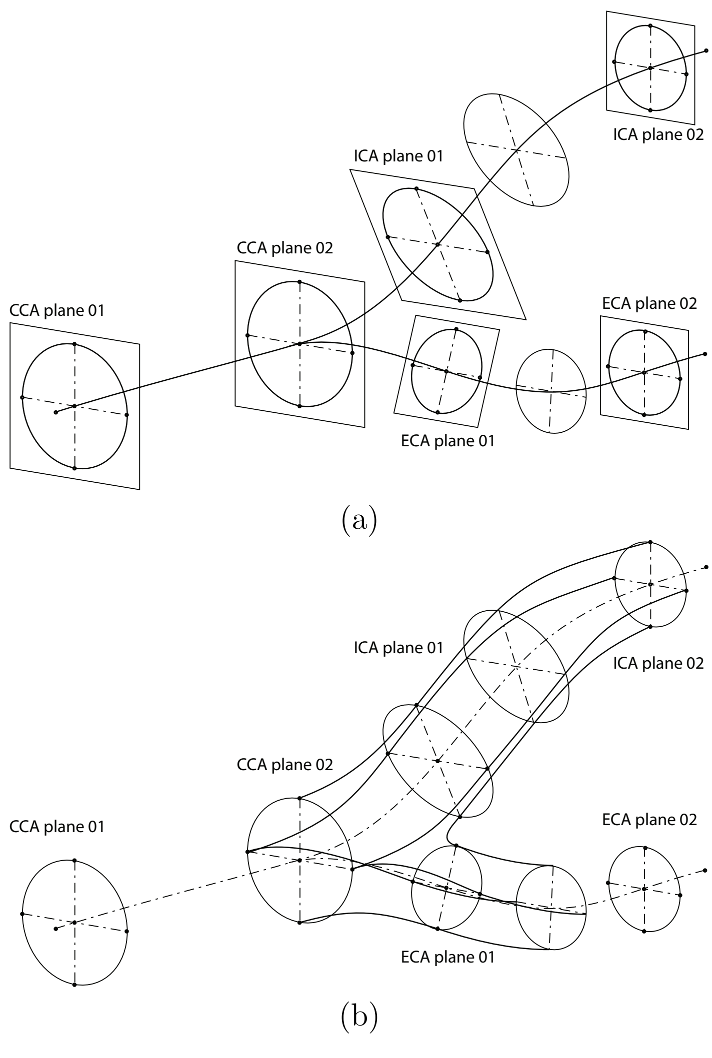

Figure 2.2 Procedure for developing the idealised model: (a) underlying geometry with representative artery diameters and centerline (b) 3D skeleton used for surface lofting

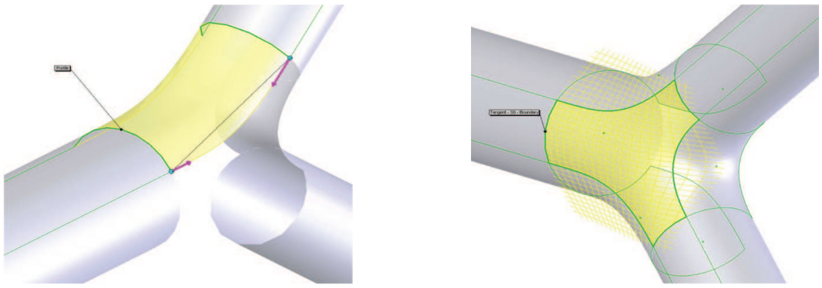

(a) (b)

Figure 2.3 Development of 3D surface: (a) lofting of outer bifurcation wall (b) filling of upper and lower surface with tangent conditions at each edge

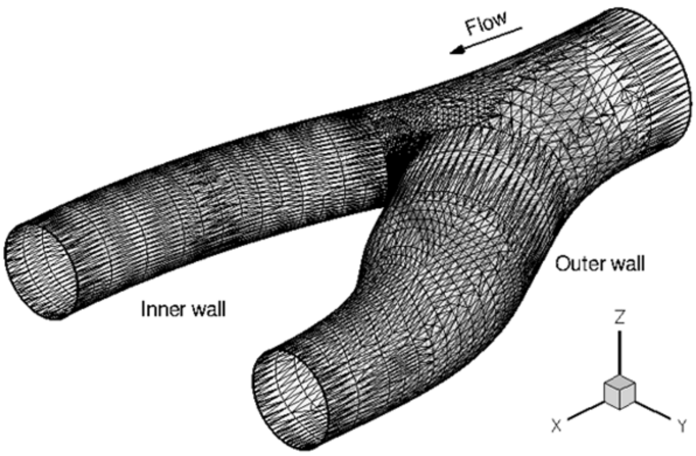

Figure 2.4 Surface mesh of the idealised carotid artery geometry

The sketches on two corresponding planes are connected with a B-spline interpolation (lofting) to form a hollow surface of the individual vessel segments as demonstrated in Figure 2.3(a). The surface is created tangential to the 3D lines and the arrows indicate the direction of the surface and the tangency to the adjoining surfaces. The remaining hollow sections on the upper and lower surface in the bifurcation region is then filled with a tangential fill condition. This applies surface tangency at each adjoining face and is indicated by the mesh overlaid in Figure 2.3(b). The final result is an idealised artery model with smooth surfaces and curvature. The final model is solidified and exported into stereolithography (STL[1]) format. Figure 2.4 illustrates an example of the final bifurcation geometry with the surface mesh overlain.

[1]**STL** is a widely used file format for rapid prototyping and computer-aided design. It describes the unstructured triangulated surface by the unit normal and vertices of the triangles.

2.3.2 Patient Specific Geometries

While generic models are relatively simple to construct and can be parameter driven, they are useful for examining the general flow topology and WSS distribution, but do not permit a detailed study of anatomical variations and their influence on haemodynamic factors. In these cases, anatomically accurate geometries are required and techniques for a rapid generation of such models from MRI and surface point data are described in the following section.

MRI data reconstruction

MRI uses a spatially varying magnetic field and radio-frequency electromagnetic radiation to generate the phenomena of *nuclear magnetic resonance* within hydrogen molecules in the various tissues present in the human body. The complex MR signal generated during resonance is converted into an induced voltage signal by the principle of Faraday and can be used to reconstruct an image of the tissue. For a detailed explanation of MRI see Bushberg et al. [2001]. One particular angiographic MRI technique is *Time of Flight* (TOF), where the MR signal from stationary tissue is suppressed and the signal from moving tissue such as blood is enhanced. TOF scans are routinely used in the imaging of the vascular structure and produce scaled images of resolution and quality sufficient for clinical diagnosis.

During this work, the TOF scans used to acquire the raw MRI data are performed on a General Electric 1.5T scanner. Some of the scanning parameters are listed in Table 2.1. Scans are performed in axial planes across the neck and the lower part of the brain and are available as a series of 2D gray-scale images, i.e., DICOM[2] format. The individual pixel intensities within the images correspond to different tissue properties and are organised in a 3D array of the form $I(i, j, k)$, where i, j, k corresponds to the voxel locations along an axis normal to the sagittal, coronal and axial planes, respectively. An example of a data set is shown in Figure 2.5 showing a maximum intensity projection (MIP) of the carotid arteries and the cerebral arteries located in the neck and the base of the brain.

[2]**D**igital **I**maging and **Co**mmunications in **M**edicine (DICOM) is a standard for handling, storing, printing and transmitting information in medical imaging.

The approach utilised in this study for the segmentation of the arterial lumen from the TOF dataset uses a *marching cube* algorithm, implemented in an in-house software package. While the principle of the segmentation algorithm is detailed in Moore [2008], here only a brief description relevant to the current work is given. The basic idea is that a given 3D intensity array $I(i, j, k)$ is 'marched' through by a hypothetical cube. By comparing the intensity values at the vertices of the cube to a user defined isosurface value, cases arise where vertices are above or below this threshold and hence a surface corresponding to the arterial wall will pass through the cube. As the cube is marched through the 3D array, the arterial wall is described by a surface triangulation of all the resulting surface triangles. Lastly, the spatial coordinates of the resulting surface vertices are multiplied by the respective pixel and slice spacing (Table 2.1) to yield the final scaled surface triangulation (Figure 2.6).

Table 2.1 Time of Flight parameters used for MRI data acquisition

Matrix Size	512×512 pixel^2
Pixel Spacing	0.47mm
Slice Spacing	1.2mm

Due to the limited resolution of the MRI data and the presence of noise, the segmented arterial geometry often appears coarse with surface irregularities (Fig. 2.6(a)). In these cases, Gaussian smoothing is used to flatten the surface (Fig. 2.6(b)) and interpolation algorithms are applied to increase spatial reso-

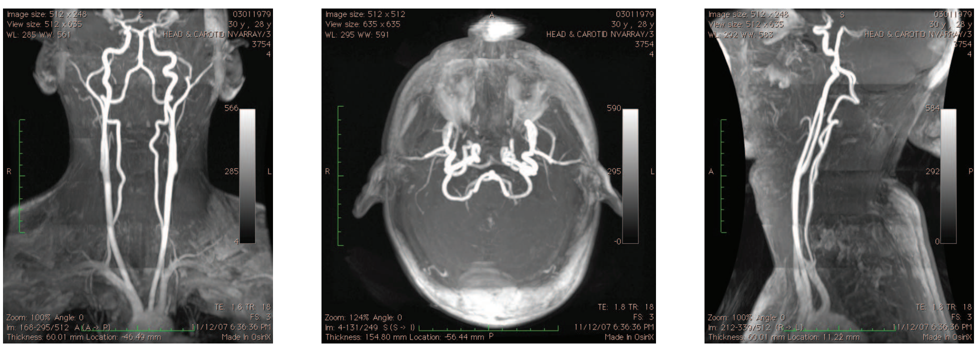

(a) (b) (c)

Figure 2.5 Maximum intensity projection (MIP) image of the carotid arteries and the cerebral vasculature: (a) coronal view (b) axial view (c) sagittal view

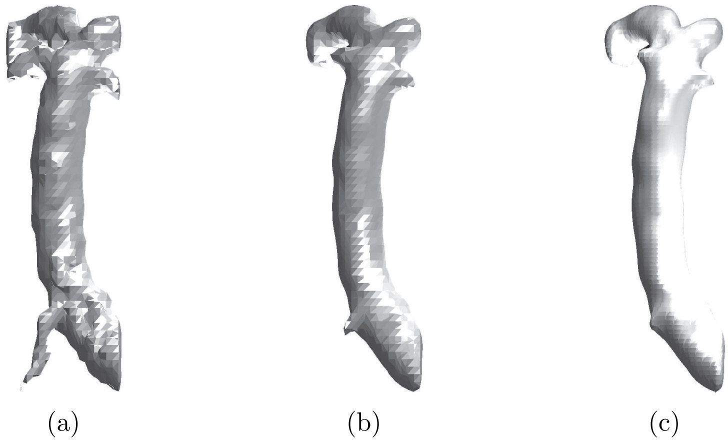

Figure 2.6 3D surface illustration of a vessel segment reconstructed from MRI data: (a) Irregularities and coarseness of the vessel wall surface resulting from limited spatial resolution and image noise (b) smoothing of the dataset to remove lumps and noise (c) interpolated surface with increased resolution. Images reproduced from Moore [2008] with consent

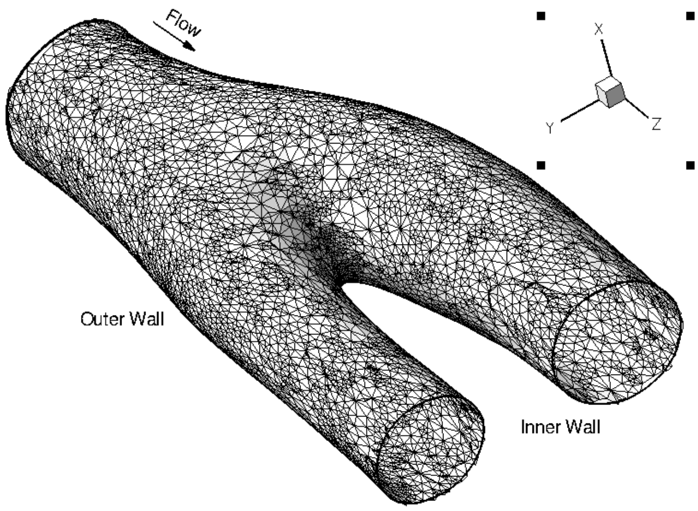

Figure 2.7 Surface mesh of the anatomically realistic carotid artery bifurcation

lution and to produce a fine surface topology (Fig. 2.6(c)). An example of a reconstructed carotid artery bifurcation from the dataset in Figure 2.5 is shown in Figure 2.7.

Surface point reconstruction

Another technique for the reconstruction of patient specific geometries is the use of digitised post-mortem data. Typically, the vessel of interest is excised by autopsy and its shape and appearance is conserved by a casting procedure. The resulting vessel cast can then be digitised and reconstruction techniques can be used to create a 3D computer model. Unlike MRI, this technique is rather simple and inexpensive, while offering a similar degree of detail and accuracy.

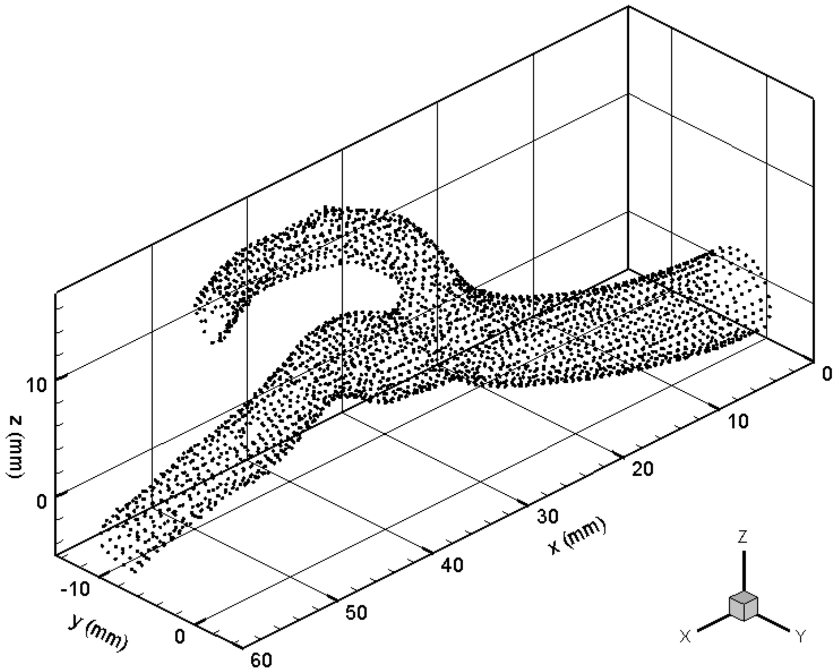

Figure 2.8 Surface point cloud of a post-mortem carotid artery vessel cast used for surface reconstruction. Note, only every second surface point is shown for clarity, $N \sim 10^4$

In this research, digitised data of a carotid artery[3] cast are used to obtain a corresponding 3D surface description. The vessel cast is obtained by autopsy and injected with a polymer resin under a physiological pressure of 80mm Hg. After hardening of the polymer, the arterial wall is removed leaving an exact replica of the arterial lumen. The surface geometry is subsequently digitised to create a point cloud of approximately 10^4 points, which is shown in Figure 2.8. Details on the vessel cast preparation and digitisation can be found in Goubergrits et al. [2002, 2009].

[3]The digitised raw data used in this study were kindly provided by L. Goubergrits, Biofluid Mechanics Laboratory, Charité - Universitätsmedizin Berlin, Germany

For a given set of N points $\mathbf{x}_i$ and their values f_i, a 3D surface $s(\mathbf{x})$ can be reconstructed via radial basis functions (RBFs) In the present case, N is the number of vertices in the point cloud and f_i their functional value indicating whether the point lies below, above or on the surface. Radial basis functions provide an analytical description of $s(\mathbf{x})$ and are functions of the following form:

$$s(\mathbf{x}) = p(\mathbf{x}) + \sum_{i=1}^{N} d_i \phi(\|\mathbf{x} - \mathbf{x}_i\|) \tag{2.11}$$

with p being a low order polynomial and $\phi(\|\mathbf{x} - \mathbf{x}_i\|)$ the 'basis function', which is the Euclidian norm shifted by the position of its center $\mathbf{x}_i$. The solution of Equation 2.11 is obtained by fitting and evaluating the RBFs to the above point cloud with a MATLAB toolbox developed by FarField Technology [2004].

Although there are various other reconstruction algorithms [Dey, 2007], RBFs often give the most accurate surface approximation for unstructured data, while maintaining a high degree of surface smoothness. Furthermore, RBFs give an analytical description of the fitted surface, which can be sampled at any density. Therefore, it is possible to create a surface mesh of the artery segment with a reasonable level of discretisation, which is independent of resolution and spacing of the initial point cloud. Figure 2.9 shows an example of the reconstructed surface mesh from the point cloud shown in Figure 2.8.

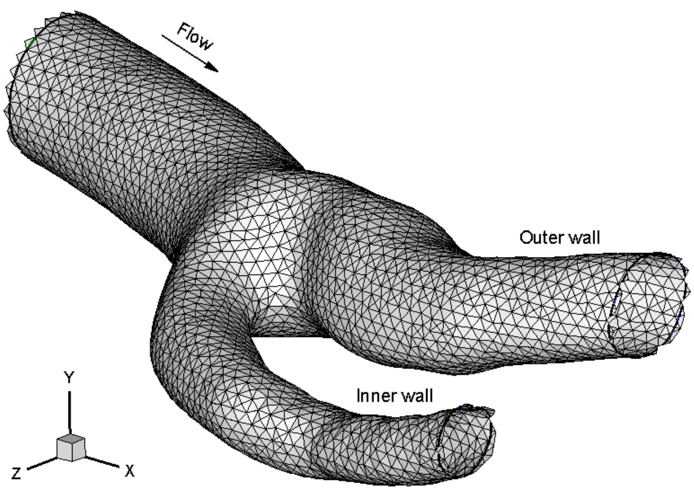

Figure 2.9 Reconstructed surface mesh of a post-mortem vessel cast using radial basis functions (RBF)

2.4 Flow Phantom Construction

Having laid out the fluid flow modelling assumptions and surface reconstruction methods, the following section covers the development of a hydraulic flow phantom, which is suitable for non-invasive optical flow measurements. First, a short review of the relevant literature is given before the phantom construction process developed and utilised in this work is described. Lastly, an assessment of the process accuracy and fidelity is presented.

2.4.1 Background

Experimental blood flow studies in hydraulic flow phantoms are often conducted using optical measurement techniques such as flow visualisation, Laser Doppler velocimetry (LDV) and more recently, Particle Image Velocimetry (PIV). A difficulty common to all techniques is the refraction of light passing through the liquid-solid interface at the flow phantom and/or test section walls. In LDV, refraction can lead to rotation and distortion of the measurement volume or to misalignment of the laser beam [Budwig, 1994]. In PIV, refraction becomes even more important due to the combination of optical and laser measurements. Lowe and Kutt [1992] showed that refraction through a circular pipe wall can cause hidden regions and multiple images in PIV. Moreover, refraction causes particle image distortion and can lead to erroneous velocity estimates.

Refraction occurs when light travels from one medium with a given refractive index to a medium of different refractive index. At the media interface, the light wave's velocity is altered and consequently a change in direction (and wavelength) occurs. The index of refraction n for a given material is defined as the ratio of the speed of light in vacuum to the speed of light in the material. The relation between the refractive index of two materials and the associated refraction angle is given by *Snell's Law*.

In vascular flow, modelling the problem of refraction is twofold. Under the most general case, refraction occurs at the air/model interface and the model/liquid interface. Whilst the first one can be eliminated by viewing the flow model from directions perpendicular to the model, the second usually requires a more elaborate method of refractive index matching.

When constructing an optical flow passage with curved walls, a number of methods are applicable. The flow passage can be reproduced by CNC milling in a block of transparent perspex [Bharadvaj et al., 1982b; Frayne et al., 1992; Gijsen et al., 1999b] or in a block of optically clear resin using a casting technique [Chong et al., 1999; Friedman et al., 1995; Yedavalli et al., 2001]. Both techniques yield a flow phantom with planar outside walls. Alternatively, a box with flat walls can be constructed around a tubular model [Ding et al., 2001; Gray et al., 2007] and filled with a refractive index matching liquid [Durst et al., 1996]. In any case, the flow passage can be viewed without refraction errors at the air/model interface. However, refraction errors due to refractive index differences between the model material and the working liquid may still occur. To alleviate this problem, different methods exist and are discussed in Section 2.5.

A second challenge arises from the fact that the flow geometries are of complex 3D shape with convoluted surfaces and topologies (see Section 2.3). Reproducing this shape in a transparent flow phantom faithfully, while at the same time considering the problem of optical refraction is a difficult task. A number of different methods have been published over the last two decades, some of which are reviewed here.

Early studies used borosilicate glass [Ding et al., 2001; Gray et al., 2007; Ku and Giddens, 1983; Walburn and Stein, 1981] and acrylic models [Bharadvaj et al., 1982b; Frayne et al., 1992; Gijsen et al., 1999b], which were typically produced by glass blowing or computer controlled milling. Although these techniques are easy to use, their applicability is usually limited to idealised model studies, due to their inability to produce complex surfaces. A common approach is to use casting methods. Liepsch et al. [1998] used a post-mortem vessel cast to produce a wax duplicate, which was then cast into silicone and subsequently dissolved. The use of vessel casts has also been reported by Motomiya and Karino [1984]; Friedman et al. [1995], however this method only permits the construction of 1:1 scale models. To produce models other than life-size usually requires a computer model of the vessel geometry. Bale-Glickman et al. [2003a] acquired the geometry of a dissected carotid artery via MRI scanning and others used *in-vivo* MRI [Yedavalli et al., 2001] or CT data [Doyle et al.,

Table 2.2 A selection of material and their properties suitable for the construction of vascular prototypes and transparent flow phantoms

Materials	Model construction	n	Comments
Prototyping			
Low melting point alloy	casting		melts at $> 65^o$
wax	manual, casting		shrinkage
plaster, starch	3D printing		dissolves in water
ABS	stereolithography		dissolves in acid
Glass			
borosilicate (Pyrex)	glassblowing, fusing	1.47-1.49	available in tubes and rods
optical glass	grinding, polishing	1.45-1.96	expensive and difficult to work
Plastic			
acrylic (Plexiglas, Perspex)	all plastics: machining, bonding polishing	1.49	available in tubes, sheets and rods
polychlorotrifluoro-ethylene (PCTFE)		1.435	
tenite butyrate		1.47	
Casting resin			
silicone elastomer		1.43	flexible and most commonly used
epoxy based	machinable after curing (except. silicone)	1.59	
acrylic based		1.49-1.53	
urethane based		1.49	

n, refractive index

2008; Hopkins et al., 2000; Tateshima et al., 2001]. In any case, a computer model of the vessel was constructed using similar techniques to those described in Section 2.3. Using rapid prototyping techniques such as stereolithography or 3D printing, the arterial geometry can then be reproduced as a physical model and at any scale. To create the final flow phantom, a combination of rapid prototyping and casting techniques are most commonly used, and a review of these methods, relevant to the current work is presented in the following.

- In a four step process for example, stereolithography is used to create a negative of the vessel segment, (i.e., flow passage) from which a positive rubber mould is produced [Tateshima et al., 2001]. This mould is filled with a low melting point alloy or wax [Adler and Bruecker, 2007; Cieslicki and Ciesla, 2005] to create a sacrificial duplicate of the vessel (negative) and is subsequently embedded in a clear casting resin. The final flow phantom is obtained after curing and dissolving of the metal or wax cast. While this process requires four steps, which decreases accuracy, it offers the advantage of producing a permanent positive mould, which allows the rapid production of multiple phantoms. On the other hand, low melting point alloys and wax exhibit considerable shrinkage (up to 6% for wax), which has to be taken into account when producing the initial male cast.

- A variation of the above routine is to create a positive mould directly via stereolithography [Goubergrits et al., 2009] and then to proceed as above. While stereolithography techniques are fairly expensive (particularly for large scale models) their advantage lies in the fact that the positive moulds can be produced with a high accuracy (±0.05mm, Yedavalli et al. [2001]). In the case of very complex 3D shapes, the construction of simple split moulds may not suffice and the female cast has to be constructed from several segments, which in turn increases the complexity of the process.

- Lastly and probably the most straight forward process, is to directly prototype a sacrificial model (negative) from materials such as plaster, starch or ABS[4] [Hopkins et al., 2000; Yedavalli et al., 2001]. These materials are easy to dissolve and can be cast directly into a clear resin to produce the final flow phantom. These models are fairly inexpensive compared to resin models produced by stereolithography, but are usually fragile and delicate to work with. Furthermore, some form of coating is required to make their surface impermeable to the casting resin.

Aside from the above techniques, a multitude of variations and combinations exist. There is also some interest in creating vascular phantoms with thin walls

[4]**ABS**, acrylonitrile butadiene styrene

to study the effects of distensibility. Doyle et al. [2008] used similar casting techniques to the ones mentioned earlier to produce a distensible model of an abdominal aortic aneurysm and a coating techniques was used by Liepsch et al. [1998] to create a thin wall carotid artery model.

Finally, the issue of choosing an appropriate casting material for the transparent flow phantom has to be addressed. While the transparency of the model material is a necessity, factors regarding the ease of use, index of refraction, elasticity or price also have to be considered. Table 2.2 shows common materials that can be used to construct the models and test sections. The data are collected from the afore mentioned studies in addition to those given by Budwig [1994] and Nguyen et al. [2004].

2.4.2 Casting Procedure

The previous section provided an introduction and review of model making techniques, aspects on optical refraction and the reproduction of complex 3D shapes. With this information on hand, the next section will cover the details of the flow phantom construction procedure that has been developed and employed in this study. To aid in justifying the selected model making procedure, it is worth clearly summarising the requirements and objectives for such a technique again.

- The hydraulic flow phantom has to be optically transparent, it should have flat external walls and should allow for a matching of the refractive index between the phantom material and the blood analogue liquid.
- Complex 3D flow geometries have to be reproduced with a high degree of anatomical detail and surface topology. The technique should utilise the flow geometries developed in Chapter 2.3 and should enable the production of scaled models.
- Accuracy and reproducibility has to be high and readily available technologies should be used. Furthermore, the technique has to be cost and time efficient.

During the course of this research, several different techniques and materials were developed, some of which had shortcomings and were rejected, while others were developed further. Some of the techniques investigated include the use of wax or low melting point alloys, stereolithography techniques and flow phantoms cast from acrylic resin. Here, only the final procedure for constructing the flow phantom is summarised and described below.

1. Create a solid computer model of the flow passage geometry
2. Obtain a water-soluble negative of the flow passage by rapid prototyping
3. Cast the negative in transparent silicone
4. Dissolve the negative to obtain the final flow phantom

In the following, each step of the procedure is described in greater detail

3D computer model The starting point for the creation of the flow phantom is a solid computer model (STL format) that defines the *in-vivo* flow geometry (see Section 2.3). The model is scaled larger than life-size to increase the spatial accuracy during the rapid prototyping process. Scaling factors typically vary between 2.5-3 times life-size and depend on the initial *in-vivo* size. In the case of the patient specific geometries, the inlet and outlet diameters are extended to create circular cross-sections and to fit standard-sized plastic pipes.

Rapid prototyping[5] 3D printing (ZPrinter 310, Z Corporation) is used to create a negative of the flow passages from the scaled computer model. The model is built up from a water-soluble plaster powder (ZP 130) with a layer thickness of 0.1mm. The maximum dimensions of the prototype can be up to $200 \times 254 \times 200$mm and can be produced at a cost of about NZ\$0.4/cm^3. The resulting prototype is brittle and porous and is typically filled with wax or epoxy to increase their strength. This however renders them insoluble.

Prototype preparation For this application, the prototypes are produced without any treatment so that the acquired parts are water-soluble. In this state, the plaster prototype is fragile and porous and needs to be handled with great care. The prototype is then coated with several layers of

[5]The rapid prototyping was carried out by Creative Industries Research Institute, Faculty of Design & Creative Technologies, Auckland University of Technology, NZ

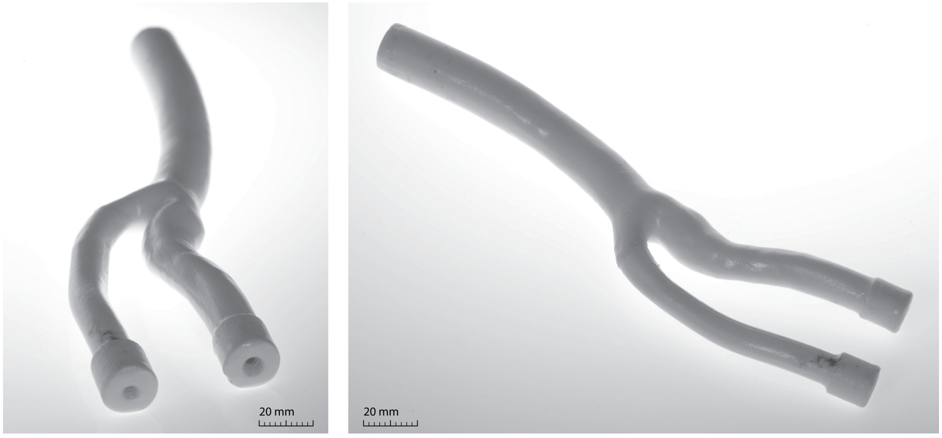

Figure 2.10 Larger than life-size plaster prototype of an anatomically realistic carotid artery bifurcation in front and side view

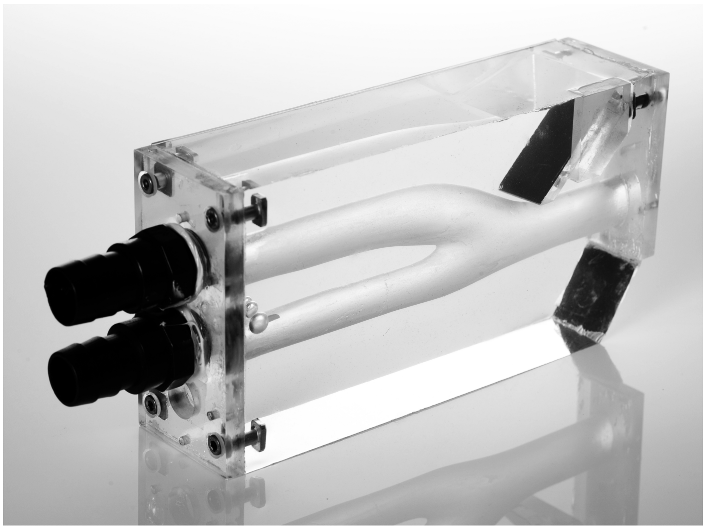

Figure 2.11 Transparent silicone flow phantom of an anatomically realistic carotid artery bifurcation

polyvinyl acetate (PVA), making them impermeable to the liquid casting resin. This also improves the strength of the prototype and provides a physiologically realistic smooth surface to the model. An example of a final prototype is shown in Figure 2.10.

Model casting The final prototype is placed inside an acrylic casting box, which has flat external walls to reduce optical distortions. The flow phantom is then created by embedding the prototype in an optically transparent silicone elastomer (Sylgard 184, Dow Corning), which has a refractive index of approximately $n = 1.43$. After the silicone has cured, the model is immersed in water to dissolve the plaster prototype and the PVA coating. Finally, the casting box is removed, yielding a replica of the flow passages in a block of clear silicone. Barbed connectors are inserted at the outlet of the phantom to provide connectivity to the later flow circuitry. The final flow phantom is shown in Figure 2.11.

The overall time required to manufacture the flow phantoms is in the order of 8-10 days including the computer model preparation and curing time of the silicone ($\sim$48 hours). Full mechanical strength of the silicone models is obtained after 7 days. The costs for one phantom depend on the final size and are approximately NZ$ 250.00 for one phantom of $100 \times 50 \times 250$mm.

2.4.3 Model Fidelity Assessment

To assess the fidelity of the above model manufacturing process, a CT scan of each silicone phantom was conducted. A total of 930 slices per phantom were obtained at a resolution of approximately 400μm (see Table 2.3). The air within the phantoms provided excellent contrast and a very low noise level. The images were segmented using the in-house software described in Section 2.3.2 to obtain a surface mesh of the flow passage. Since the model was scaled up, the effective resolution is correspondingly increased and thus, the uncertainty in determining the fabricated geometry is relatively small.

Table 2.3 Spatial resolution of the CT scan to asses phantom fidelity

Matrix Size	512×512 pixel^2
Pixel Spacing	312.5μm
Slice Spacing	400μm

To compare the reconstructed geometry to that of the original STL file, both geometries were manually aligned along their major axes. The alignment was done iteratively to achieve the best overlap. From this, the vessel cross-sectional area and hydraulic diameter were calculated at various locations along the major axis and plotted in Figure 2.12 as percentage errors. Compared to the original computer model, the respective averaged variations in vessel diameter and cross-sectional area are approximately 3% and 5%.

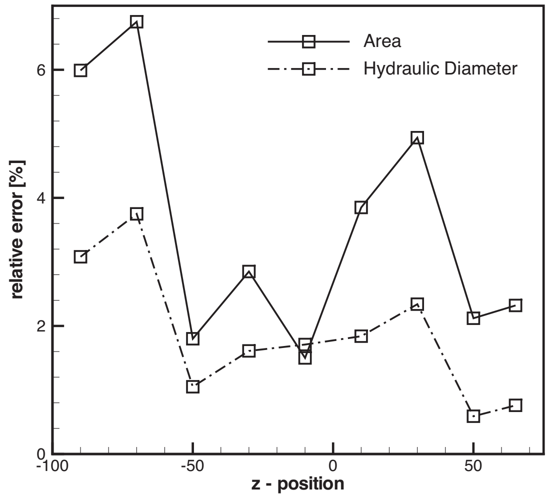

Figure 2.12 Geometric differences between the original STL and reconstructed flow geometry at selected cross-sections

The differences between two surface meshes can be expressed using the so-called Hausdorff distance, which is the maximum distance of one surface to the nearest point at the other surface [Aspert et al., 2002]. The Hausdorff distance is calculated as

$$h(S, S') = \max_{p \in S} \left\{ \min_{p' \in S'} \{\|p - p'\|\} \right\} \tag{2.12}$$

where p and p' are points on surface S and S' and $\|p - p'\|$ the Euclidian norm. Strictly speaking, Eq. 2.12 is the *forward* Hausdorff distance and typically $h(S, S') \neq h(S', S)$.

The comparison is performed at model scale, and Figure 2.13 shows the distribution of $\|p - p'\|$ between the original STL geometry (S) and the reconstructed fabricated geometry (S'). The mean surface distance with standard deviation evaluated for the whole surface is 0.277mm ± 0.207mm. These values are scaled to model size, which is about three times larger than *in-vivo* size. The analysis shows that the largest deviations occur at the daughter branches. Also observed is a slightly larger surface distance in the bifurcation region, whilst differences along the parent branch are small. The distribution of the surface

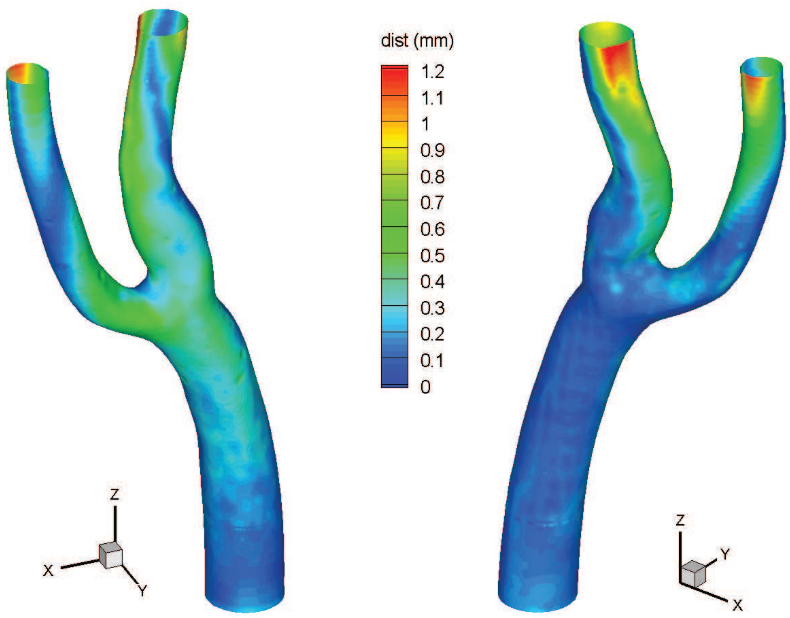

Figure 2.13 Distribution of the surface distance $\|p - p'\|$ between the reconstructed and the original geometry

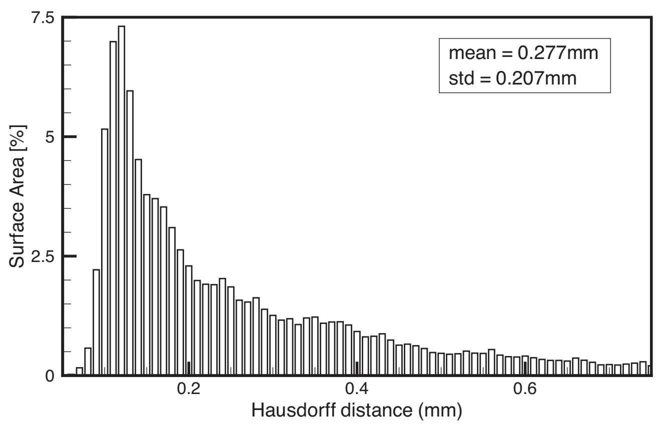

Figure 2.14 Histogram of the surface distance distribution $\|p - p'\|$ normalised by surface area for the reconstructed geometry

distance normalised by the total wall surface is shown in Figure 2.14. The analysis shows that 86.9% of the surface mesh have a surface distance error equal or less than 0.5mm and 98.8% of the surface are below a 1mm error. These errors are in the range of the resolution of the CT scan and if translated to *in-vivo* size, are in the order of 100-300μm.

2.4.4 Discussion of the Flow Phantom

This section has presented a method for creating scaled and optically clear flow phantoms, which can be used for PIV, LDV or MRI flow experiments. An important aspect of the technique is that it allows the construction of physiologically realistic flow phantoms. The use of scaled models allows for a higher effective spatial resolution of the velocity and WSS measurements and greater accuracy that could not be obtained otherwise. Scaling also allows flow modeling in vessels which are too small to be reproduced in 1:1 scales or are too small for the optical flow diagnostic.

Rapid prototyping techniques have become an important tool in the construction of vascular flow phantoms [Goubergrits et al., 2009; Hopkins et al., 2000; Tateshima et al., 2001; Yedavalli et al., 2001] and some advantages over CNC machining [Chong et al., 1999; Doorly et al., 2008] or post-mortem casting [Motomiya and Karino, 1984; Friedman et al., 1995] techniques exist. Rapid prototyping offers large geometric flexibility and freedom in obtainable shapes and sizes, while utilising different materials (soluble or chemically inert) and surface qualities. Moreover, rapid prototyping offers an accuracy in the order of $\pm$0.05mm, [Yedavalli et al., 2001] and has become increasingly time and cost efficient.

In this work, rapid prototyping is used to create a water soluble plaster model of the flow passage that is subsequently cast into an optically clear silicone elastomer and dissolved to create a transparent flow phantom. The accuracy and fidelity of this procedure is directly linked to the accuracy of the rapid prototyping and casting technique. For the current method, the variation in vessel diameter and cross-sectional area compared to the original computer model are less than 3% and 5%, respectively. The surface distance (Hausdorff distance) between the original and the reconstructed geometry is on average 0.277 ± 0.207mm (Mean $\pm SD$). This corresponds to a difference in vessel diameter of about 2.8%. When translated to *in-vivo* size, the surface distance error amounts to approximately 90μm, which is significantly smaller than that reported by Goubergrits et al. [2009] (232μm) or Doorly et al. [2008] (290μm). Overall, the systematic error is small and can primarily be attributed to additional thickness of the PVA coating. In the case of phantoms constructed from medical image data, the quality of the lumen geometry additionally depends upon the quality and resolution of the imaging modality and segmentation technique. For example, when using MR images, Yedavalli et al. [2001] reported mean errors in reconstructed vessel diameters between 1.4% to 3.3% depending on the smoothing and reconstruction technique used.

Although the current technique is developed for models with essentially rigid walls and planar surfaces, the technique can easily be extended to create elastic wall models. For silicone models for example, Doyle et al. [2008] used two moulds of different sizes to create a thin wall model, whereas Liepsch et al. [1998] used a coating technique and Große et al. [2008] centrifugal spinning. In the case of the rigid wall model, some dilation is observed for large static pressures [Ruwet et al., 2008] and under pulsatile flow conditions. Additionally, it should be noted that an increase in stiffness and slight discolouration of the silicone elastomer occurs over time due to aging.

Lastly, there is also some interest to use the reconstructed flow phantom geometry for mesh generation in Computational Fluid Dynamic (CFD) simulations. This allows for detailed comparison between CFD and experimental measurements with closely matched three-dimensional geometries. For physicians, three-dimensional flow models are particularly helpful when dealing with complex vascular geometries. They could enhance the understanding of the local vascular anatomy and are useful in the testing of various therapeutic techniques, e.g., stents, shunts and bypass crafts.

In summary, the developed method allows the reproduction of physiologically realistic geometries in a scaled and optically clear flow phantom with rigid walls. The method uses commercially available technology, is cost efficient and models can be produced within ten days.

2.5 Blood Analogue Liquid

As mentioned in the previous section, optical refraction also occurs at the model/liquid interface due to mismatches in refractive index between the flow phantom and working liquid. In the case of simple geometries, refraction might be corrected analytically [Lowe and Kutt, 1992] or by performing some form of image calibration [Soloff et al., 1997]. However, in situations where the flow geometry is of complex 3D shape with convoluted surfaces, the above methods are inadequate and/or require substantial experimental effort. In these cases, the use of working liquids with similar or equal refractive index to that of the flow phantom are the most appropriate solution.

This section describes the development of such a refractive index matching liquid as used in the present work. First, the necessary literature is reviewed and some considerations regarding the choice of an appropriate liquid are outlined. Next, a mathematical description for the refractive index and viscosity of the blood analogue liquid is derived. Lastly, a technique is introduced that allows for the adjustment of the refractive index under experimental conditions and the mathematical predictions are verified.

2.5.1 Background

Typically, the refractive index of a liquid can be adjusted with the use of chemical additives such as Sodium Iodide (NaI), Sodium Thiocyanate (NaSCN), Potassium Thiocyanate (KSCN) or Zinc Iodide (ZI). Some of the above substances however, are potentially hazardous (toxic, flammable or reactive) and/or are too expensive making their application in flow experiments limited.

Narrow et al. [2000] developed a model to predict the refractive index of aqueous Sodium Iodide solutions as a function of temperature, NaI concentration and wavelength to match the refractive index of pyrex ($n = 1.47$). A polynomial regression to determine the concentration of a sucrose-water solution was derived by Budwig [1994]. Finally, Nguyen et al. [2004] proposed an analytical expression for the refractive index and the viscosity of liquid mixtures and showed how these values can be altered by adjusting the concentration and temperature of the mixture.

Table 2.4 Properties of refractive index matching fluids at 20^oC. μ_0 is the dynamic viscosity of water. (w=water, al=alcohol, gly=glycerin, eth=ether). Data are primarily taken from Weast [1988]; Budwig [1994]; Nguyen et al. [2004]

	n	μ/μ_0	Solubility	Comments
water	1.33	1		
Aqueous solutions				
zinc iodide	1.33-1.62	n.a.	w,al	ν/ν_0 = 1-10
sodium iodide	1.33-1.487 1.5	n.a.	w,al,gly	0-60%, 20-40^oC 60% by wt.
sodium thiocyanate	1.479	7.55	w,al	0-56% by wt.
sodium chloride	1.38	1.99		0-26% by wt.
potassium thiocyanate	1.475	2.43	w,al	0-64% by wt.
ammonium thiocyanate	1.33-1.50	1-2.1	w,al	
sucrose	1.501	∼2000		0-84% by wt.
Organic liquids				
glycerin	1.47	∼1500	w,al	
ethanol	1.361	1.20	w,eth	
diethyl phthalate	1.504	12.0	al	
d-limonene	1.472		sparingly	ν/ν_0 ∼1.28
methyl salicylate	1.526	4.09	al	
mineral oil	1.46	25	al	
olive oil	1.47	84		
silicone oil	1.4-1.5	50-1000	al	various types

n, refractive index

A comprehensive summary on refractive index matching in vascular models for both Newtonian and Non-Newtonian blood analogue liquids is given by Nguyen et al. [2004]. One of the most commonly used Newtonian blood analogue liquids is a mixture of water and glycerin, which allows a range of viscosities and refractive indices (n =1.33 to 1.47) to be matched. Alternatively, Palmen et al. [1993] used an aqueous solution of potassium thiocyanate (KSCN) and

Tateshima et al. [2001] used a saturated aqueous solution of Sodium Iodide to match the refractive index of their acrylic models ($n = 1.47$). Other studies developed non-Newtonian blood analogues for optical measurements such as aqueous solutions of KSCN and Xanthan gum [Gijsen et al., 1999b; Gray et al., 2007] or polyacrylamide [Liepsch, 2002] to match both, the shear thinning behavior of blood and the refractive index.

Besides being refractive index matching, blood analogue liquids also have to be dynamically similar to satisfy the similarity considerations outlined in Section 2.2.3. Studies in 1:1 scale models typically use a dynamic viscosity equal to that of blood, i.e., 3.5×10^{-3}Pa·s, whereas studies with larger than life-size models applied liquids with higher viscosity. Generally, when choosing the liquid's viscosity, practical constraints such as the measurable range of flow rates or the achievable time periods in pulsatile flow experiments also have to be considered.

In this study, the hydraulic flow phantoms are constructed from silicone elastomers ($n \sim 1.43$) and are built as rectangular blocks with planar outer surfaces, thus minimising refraction errors at the air/model interface. Furthermore, to preserve dynamical similarity in scaled modelling, a higher kinematic viscosity is desired to compensate for the increase in vessel diameter. A list of liquids that are excellent candidates for matching in experimental flow studies is given in Table (2.4), which lists index of refraction and dynamic viscosity at 20^oC. Another extensive list of refractive index matching liquids used in vascular modeling and other applications is given by Miller et al. [2006]. There are a number of considerations for the successful choice of matching liquids such as index of refraction, optical clarity, density, viscosity, material compatibility, chemical stability, safety and price. In some cases, bio-compatibility must also be considered. In the present study, the requirements for the blood analogue liquid are the following:

- Optically clear liquid with a refractive index identical to that of the silicone flow phantom

- Newtonian behavior with a high shear viscosity of approximately three times that of blood to compensate for the increased model size and to keep the experimental flow rates within measurable ranges

- Non-toxic, chemically stable, compatible with common flow circuit materials and low cost

It has been shown that the refractive index of a blood analogue fluid can be matched with that of the hydraulic flow phantom by mixing two clear and miscible liquids [Nguyen et al., 2004]. One liquid with a refractive index lower than the target value and the other with a respective higher refractive index. The rationale is that the target value can be obtained by estimating the mixture proportion and temperature. Using Table 2.4, a water-glycerin mixture is chosen for the refractive index matching liquid. Glycerin is a clear liquid with a high refractive index and viscosity. Moreover, glycerin is inexpensive as it is commonly used in the food industry and it is non-toxic with good material compatibility.

The following two sections give a mathematical and experimental derivation to estimate the optimal proportions and temperature of the aqueous glycerin mixture, which will fulfill the refractive index and viscosity requirements outlined above.

2.5.2 Mathematical Formulation

Common to most liquids is their temperature dependency of the refractive index and its correlation to the liquid's density. An empirical relation between the change in refractive index and the liquid density exists as: $\triangle n \approx 0.6 \triangle \rho$ [Perry and Chilton, 1973]. As temperature increases, the liquid's density decreases and consequently the index of refraction decreases proportionally. The temperature dependency of the refractive index of organic liquids can be modeled with the following linear relation [Nguyen et al., 2004]:

$$n(T) = a + bT \tag{2.13}$$

where, n is the index of refraction, a and b are material constants and T is the absolute temperature. The refractive index of a mixture of two liquids in proportions P and $(1 - P)$ can be derived by the following linear interpolation:

$$n_{mix} = n_1 P + n_2 (1 - P) \tag{2.14}$$

where the subscript refers to the two different liquids and their refractive indices can be calculated from Equation 2.13.

Similar to the refractive index, the temperature dependency of the dynamic viscosity can be estimated with a Vogel-Fulcher-Tamman (VFT) model [Shelby, 2005] and that of the density with an empirical relation [Nguyen et al., 2004] of the following forms:

$$\mu(T) = \mu_o exp\left(\frac{f}{g+T}\right) \tag{2.15}$$

$$\rho(T) = \rho_o\left(\frac{T_o}{T}\right)^s \tag{2.16}$$

where f, g and s are material constants of the individual liquids and $T_0 = 20^o$C the reference temperature. Furthermore, the temperature dependency of the mixture's viscosity is described with a semi empirical model and the mixture's density is assumed to follow the volume additive rule.

From Equation 2.14, the mixture proportion P, which is required to match a given refractive index n$_{target}$ can be derived as follows:

$$P = \frac{n_{target} - a_2 + b_2 T}{a_1 - a_2 + (b_1 - b_2)T} \tag{2.17}$$

The temperature dependency of the kinematic viscosity for a given proportion P of the mixture can then be expressed as the ratio of dynamic viscosity and density

$$\nu_{mix} = \frac{exp\left[P\left(e_1 + \frac{f_1}{g_1+T}\right) + (1-P)\left(e_2 + \frac{f_2}{g_2+T}\right) + W_0 + \frac{W_{12}}{T}\right]}{P\left(g_1\left(\frac{T_0}{T}\right)^{s_1}\right) + (1-P)\left(g_2\left(\frac{T_0}{T}\right)^{s_2}\right)} \tag{2.18}$$

where W_0 and W_{12} are adjustable parameters related to the activation energy.

2.5.3 Experimental Verification

The physical properties (viscosity, refractive index and density) of water and glycerin are fully characterised as a function of temperature during this research. The temperature dependency of the dynamic viscosity is measured with a rotary rheometer and that of the refractive index with a benchtop refractometer. For all measurements, the temperature is controlled with a water bath circulator and measurements are performed at temperature intervals between $10-30^{o}$C. The density is measured manually using a 25ml flask and a digital scale. For each substance, a minimum of two measurements is performed for each temperature and their average is recorded. The error of the refractometer measurements is ± 0.001, that of the density measurements is ± 4.6kg/m^3 and the accuracy of the rheometer is calibrated to better than $\pm 4\%$. The material parameters in the above Equations (2.13, 2.15, 2.16) are determined via least squares fitting of the experimental data points and are listed in Table A.1. Also given are some physical properties of additional liquids selected from Table 2.4, which are obtained from literature.

The refractive index of the silicone elastomer (Sylgard 184, Dow Corning) used to cast the flow phantoms is specified by the manufacturer as 1.43. However, due to inherent differences in mixing and curing of the elastomer, the actual index varies from model to model. In this study, the refractive index of the silicone elastomer is measured to 1.415 ± 0.005, which differs from the specified index by about 0.015 or 1.06%. Although this difference appears relatively small, it has a significant effect on the mixture proportion of the refractive index liquid. For example, at 20^{o}C and for an index of 1.43, Eq. 2.17 returns a mixture proportion of 69.1% glycerin b.w. in water, whilst for a refractive index of 1.415 the glycerin proportion reduced to 58.1%. To unambiguously match the mixtures refractive index to an individual flow phantom, an iterative experimental technique is developed similar to that proposed by Hopkins et al. [2000]. A grid of lines is placed behind the flow model and a mixture with excess glycerin is circulated through the flow phantom. The distortion of the grid lines are recorded and water is added to the mixture gradually. As the target refractive index is approached, the distortion in the grid lines begin to disappear and at the matching mixture the distortion disappear completely. The technique allows for an accurate match of indices and used in this way the

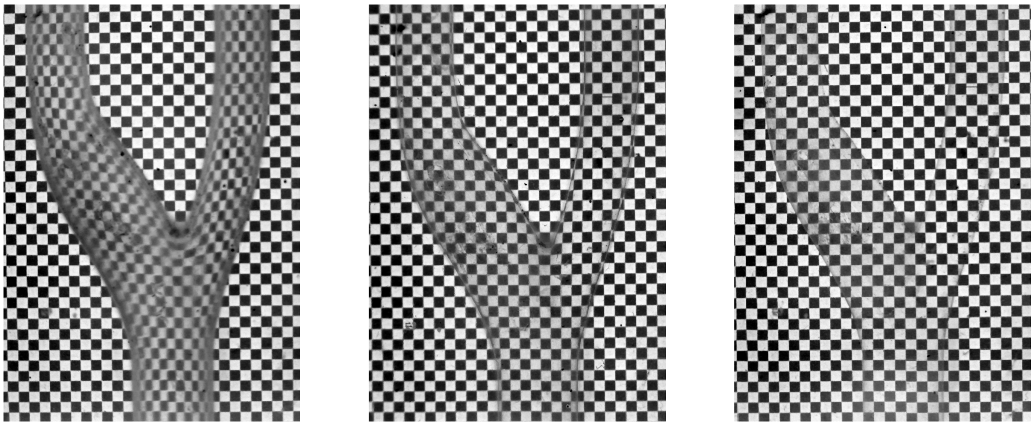

(a) (b) (c)

Figure 2.15 Distortion of the grid lines as seen through the flow phantom when filled with (a) air, (b) water, and (c) the optimal 39:61 water-glycerin mixture.

optimal mixture proportions are found to be 39% water and 61% glycerin by weight. Figure 2.15 shows the distortion of the gridlines as seen through the model when filled with air, water and the optimal mixture of 61% glycerin.

The mixture's physical properties are fully characterised under the above measurement protocol and compared to those predicted by the mathematical model for $P = 61\%$. A good agreement between the measurements and the predicted values is achieved and is shown in Figure 2.16 for the dynamic viscosity, refractive index and density, respectively. For a typical operating temperature of 20^{o}C, the present results yield a measured mean refractive index of 1.417 compared to the predicted 1.419 ($\epsilon = 0.14\%$) and a mean kinematic viscosity of 10.2×10^{-6}m^2/s compared to the predicted 10.51×10^{-6}m^2/s ($\epsilon = 3.04\%$).

Both, water and glycerin are Newtonian liquids and consequently the mixture of the two liquids is also expected to be Newtonian. Figure 2.16(d) shows the shear stress versus rate of strain relation, which for a Newtonian liquid is a linear relation. As it is evident from the power-law fit, the aqueous glycerin mixture does not behave perfectly linearly and a 7.5% increase in apparent viscosity is observed over the range of investigated shear rates. Overall, the water-glycerin mixture exhibits only minor shear thickening behavior and therefore can safely be assumed to be a Newtonian liquid.

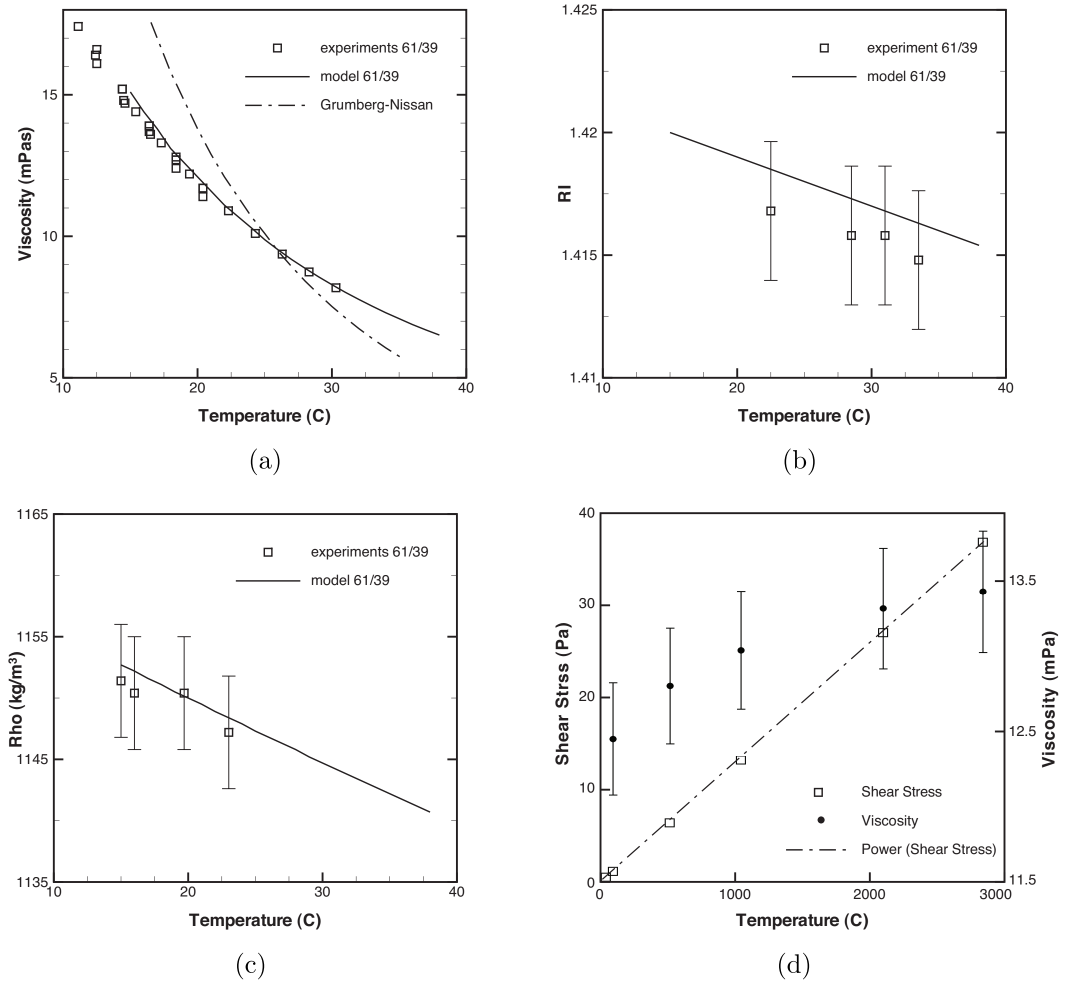

Figure 2.16 Physical properties of the 39:61 water-glycerin mixture, comparison between measurement and model prediction (a) temperature dependency of the dynamic viscosity, (b) temperature dependency of the refractive index, (c) temperature dependency of the density, (d) shear stress and dynamic viscosity versus shear rate

2.5.4 Discussion of the Blood Analogue Liquid

This section has presented a simple empirical method to extrapolate the proportion and physical properties of a binary liquid mixture from the characterisation of single liquid properties to obtain a given refractive index. A glycerin-water mixture is chosen as an appropriate liquid and the single liquid properties (dynamic viscosity, refractive index, density) are fully characterised as a function of temperature. The refractive index of the silicone flow phantom is found to differ from the manufacturers specification and between different flow phantoms. It is shown that the mixture proportions can be determined in two different ways. One, by simply measuring the index of the cast silicone elastomer and solving Eq. 2.17, and secondly, by noting the image distortion and manually adjusting the mixture proportion to obtain the target index.

The resulting working liquid is a water-glycerin mixture of ratio 39:61 (volume ratio) with a refractive index of 1.417 and kinematic viscosity of $10.2 \times 10^{-6}\mathrm{m}^2/\mathrm{s}$ at 20^oC, which is about three times that of blood. A comparison between the measured and predicted physical properties showes an excellent agreement with respective errors of 0.14% and 3% for refractive index and kinematic viscosity. Similar water-glycerin compositions were used by Adler and Bruecker [2007] (45:55), Hopkins et al. [2000] (41:59), Boutsianis et al. [2009] (40:60) and Burgmann et al. [2009] (39.3:60.7).

The strength of the mathematical models lies in the fact that if the exact target index is known *a priori*, the mixture proportions and physical properties can be predicted with good accuracy. Under practical conditions however, it is often more appropriate to derive the mixture proportions experimentally as the target refractive index varies between flow phantoms and elastomer compositions. The analytical model can then be used to predict the mixture's viscosity. This approach enables the refractive index and viscosity to be determined *in-situ* and eliminates the need for extensive viscometric measurements, each time the working liquid is adjusted.

It should be stressed that the viscosity is strongly dependent on temperature as can be seen from the highly non-linear model (Eq. 2.15) and that the refractive index is much less dependent on temperature (linear relation, Eq. 2.13). Indeed, it is this property that allows the adjustment of the final viscosity without affecting the refractive index significantly. The developed method is flexible enough to give the user the choice of a suitable kinematic viscosity and/or refractive index depending on the temperature at which the experiments are conducted. Given the strong dependency of the liquid's viscosity ($\sim 3\%$ per ^{o}C), a temperature control system is required to maintain the temperature at a constant level to ensure that Reynolds number and other non-dimensional parameters (Section 2.2.3) remain constant between experiments.

In this work, the viscosity of the liquid mixture was modelled with a two parameter empirical model as derived in Appendix A. This choice was made based on the observation that the activation energy is dependent on the temperature and independent of the mixture proportions. In contrast, Nguyen et al. [2004] used a one parameter Grunberg-Nissan model, which takes into account the mixture proportions but neglects temperature dependency. This model performs poorly under the current conditions as demonstrated in Figure 2.16(a) and Appendix A. Likewise, the temperature dependency of the viscosity was modeled with a Vogel-Fulcher-Tamman relation, which is commonly used for melts and polymeric systems. Other models, such as the Arrhenius relation [Nguyen et al., 2004] are also applicable and their implementation in the current model is straight forward. In the case of non-Newtonian liquids, Helleloid [2001] derived a viscosity temperature dependence model for a single non-Newtonian liquid. But there are no readily available models in the literature for predicting the viscosity of a binary mixture of two non-Newtonian liquids.

The refractive index matching method is illustrated for the case of a low refractive index ($n \sim 1.43$) and a water-glycerin mixture. Consequently, the same liquid combination can also be applied for flow phantom materials of a similar refractive index (see Table 2.2). For materials with a higher refractive index, i.e., acrylic or glass), liquids with a higher refractive index are required as listed in Table 2.4. Finally, it should be mentioned that the above analysis is only required when the fluid is in motion. In the case of a viewing box, the quiescent liquid only needs to reproduce the refractive index.

Chapter 3

Particle Image Velocimetry (PIV) Techniques

3.1 Introduction

Particle Image Velocimetry (PIV), also referred to as 'PIV' is a commonly used, non-intrusive and instantaneous whole-field measurement technique. PIV is based on the association of the displacement of small tracer particles with the fluid motion. The flow is illuminated with a laser light sheet and the scattered light distribution of the tracer particles are recorded with digital cameras at two time instances. Subsequent data processing is used to determine the average displacement of the particles and knowledge of the separation time between the two recordings permits the computation of the fluid velocity.

The early development of PIV goes back to the pioneering work of Meynart [1983] who described velocity measurements by speckle velocimetry and was complemented by the work of Adrian and Yao [1984]. Later, the technique was extended to digital PIV by Willert and Gharib [1991] and Westerweel [1993]. During theses years, substantial advancements in digital PIV correlation were achieved such as the window-shifting technique [Soria, 1996; Westerweel et al., 1997] or image distortion method [Scarano, 2002; Lecordier and Trinite, 2004]. Also, further advancement in hardware development (e.g., Laser, CCD Camera) have made PIV a widely used measurement technique in fluid mechanics, which is routinely applied to air and water flow investigations.

The advancement in the development of PIV during the past 25 years enables a nearly complete description of the technical aspects of PIV today [Adrian, 2005]. An excellent summary of the PIV technique and a good reference is the work by Raffel et al. [1998], which is often referred to as the handbook for Particle Image Velocimetry. This book contains more than 450 references and examples of a variety of PIV applications. Yet, as PIV further develops new applications such as in biology, turbomachinery or compressible flows require special implementations of the technique, of which some are summarised in Schröder and Willert [2008] and Stanislas et al. [2000, 2004].

In this chapter, some of the key developments in PIV are reviewed, which are used to develop a new cross-correlation analysis algorithm for the purpose of this research. In the first part, some fundamental aspects of PIV recording are discussed before the mathematical background and digital image evaluation method are outlined. In the second part, the developed PIV cross-correlation (PIVCC) algorithm is described, including a description of the multigrid interrogation and image deformation method as well as several strategies for robust processing. The third part of this chapter provides a performance assessment of the PIVCC algorithm by means of simulated synthetic particle images and characterises the influence of various experimental and processing parameters. The last part of this chapter contains a short description of the stereoscopic PIV technique and its implementation into the developed cross-correlation algorithm.

3.2 Physical and Technical Background

A typical PIV setup consists of a light source (i.e., double pulsed laser) for illumination, a recording medium (i.e., digital camera) and hard- and software for data acquisition and analysis and is illustrated schematically in Figure 3.1. The laser light is shaped into a thin light sheet (≈1mm) by a set of spherical and cylindrical lenses and spread over a region of interest. The light scattered by the tracer particles is recorded with a digital camera (i.e., CCD) equipped with an object lens of focal length f. The magnification factor of the optical recording system is expressed as:

$$M = \frac{z_o}{Zo} = \frac{f}{Zo - f} \tag{3.1}$$

where Zo is the distance between the object and lens plane and zo the distance between the lens and image plane.

Both, light source and camera are synchronised and two sequential images are recorded at times t and $t + \Delta t$. The particle displacement $\Delta\mathbf{x}$ between the two recordings is determined via local cross-correlation from which the measured local in-plane velocity $\mathbf{V}$ is obtained as following:

$$\mathbf{V} = \frac{\Delta\mathbf{x}}{\Delta t} = \frac{1}{\Delta t}\int_{\Delta t}\mathbf{V}(t)dt \tag{3.2}$$

where $V(t)$ is the velocity of the particle ensemble. It can be seen that the measured velocity represents a temporal and spatial averaging over the pulse separation Δt and the particle ensemble within the recording domain.

Since PIV flow measurements are performed by the direct association of the tracer velocity, some fluid mechanical and imaging properties of the tracer particles need to be considered first. Ideal tracer particles follow the surrounding fluid flow faithfully with no or little velocity lag and are assumed to not interfere with the flow field. Furthermore, ideal tracer particles should scatter sufficient laser light to create good image contrast and detectability.

In order to optimise the performance of the PIV system as described above, a number of parameters can be estimated beforehand. In the following section, the most important parameters regarding tracer particle selection and imaging properties are briefly discussed. Furthermore, a short description of the utilised laser illumination and digital imaging recording system is provided.

3.2.1 Tracer Particles

The dynamic behavior of small particles and their application as tracer particles in flow measurements is discussed extensively in the literature (i.e., Dring [1982]; Melling [1997]). The motion of small particles is commonly assumed as Stokes flow around a sphere and can be described by the Basset-Bousinesq-Oseen (BBO) Equation [Maxey and Riley, 1983].

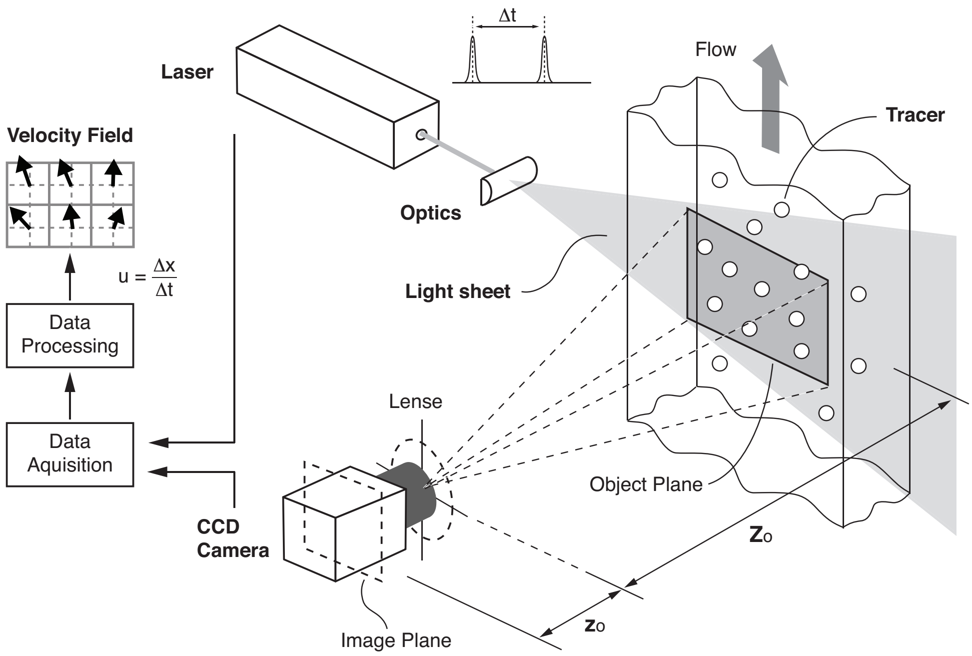

Figure 3.1 Principle of a Particle Image Velocimetry setup

The relative velocity (or slip velocity), $\mathbf{U}_s$ between the particle and the flow can be expressed as follos:

$$\mathbf{U}_s = \mathbf{U}_p - \mathbf{U} = d_p^2 \frac{(\rho_p - \rho)}{18\mu} \mathbf{a} \tag{3.3}$$

where $\mathbf{U}_p$ is the particle velocity and ρ_p the particle density. The acceleration term $\mathbf{a}$ contains the local fluid acceleration as well as gravitational acceleration. Considering the case $\rho_p/\rho \gg 1$, the particles step response follows an exponential law with its characteristic response time [Raffel et al., 1998]:

$$\tau_p = d_p^2 \frac{\rho_p}{18\mu} \tag{3.4}$$

τ_p is also called relaxation time and is a convenient measure for the tendency of the particles to retain velocity equilibrium with the fluid, (i.e., to follow the fluid acceleration).

As it can be seen from Equation 3.3, the condition of neutrally buoyant particles ($\rho_p = \rho$) is desirable to ensure a faithful tracking of the velocity field. While this condition can be satisfied for liquid flows, it presents a major obstacle in gas flow applications [Melling, 1997; Raffel et al., 1998]. Furthermore, the tracer particles should be very small in order to satisfy Equation 3.4. This is particularly important in oscillating flow as studied in Chapter 5.

Contrarily, the dynamic conditions are conflicting with the requirements for the particle to scatter sufficient light. The total amount of scattered light is proportional to the particle diameter and the differences in refractive index between the particle and the fluid. In liquid flows, a lower scattering efficiency is encountered due to reduced differences in refractive index and larger particles ($d_p = 10 - 10^2 \mu$m) should be used. However, when the particle size increases, the interaction with the flow becomes no longer negligible.

It is clear from this that ideal conditions cannot be achieved in any experiments and a compromise has to be found. This problem is discussed extensively in the literature, which also provides recommendations for commonly used seeding particles, in both, liquid and gas flow applications [Melling, 1997; Meyers, 1991; Raffel et al., 1998].

The particles used in this research are hollow glass spheres of nominal diameter, $d_p = 10\mu$m and density, $\rho_p = 1.1$g/cm^3. To achieve a highly homogeneous distribution, the seeding particles are continuously added to the flow to account for particle deposition and sedimentation in the hydraulic system. The suspended particles are almost neutrally buoyant[1] and exhibit excellent flow tracking and light scattering properties. Figure B.2 shows the particle size distribution with an estimated 99% of the particles ranging between 1 and 40μm and a mean particle diameter of approximately 16.2μm. The particle response time is estimated to $\tau_p = 13 \times 10^{-6}$s, which is considerably smaller than the typical time scale of the mean flow (i.e., oscillation frequency $\geq$ 1Hz).

3.2.2 Particle Imaging

This section provides a brief description of the diffraction limited imaging, which is of particular significance in PIV recording. A more complete review of the particle aspects of image recording in PIV is given by Stanislas and Monnier

[1] the density of the working liquid is $\rho = 1.15$g/cm^3 at $20^o C$.

[1997] and Raffel et al. [1998] and omitted here as it would extend the scope of this introduction.

The recorded tracer particles are typically very small ($d_p = 1 - 10^2 \mu$m) and the size of their image is limited by lens diffraction. This results in a Fraunhofer diffraction pattern, which is also known as Airy disk [Stanislas and Monnier, 1997]. The Airy disk or point spread function is described by the square of the first order Bessel function and represents the impulse response of the optical system. For infinitely small particles and an aberration free, well focused lens the point spread function is commonly approximated with a normalised Gaussian distribution.

The diffraction limited minimum diameter (i.e., diameter of the first Airy disk) of the recorded particles is then defined as follows:

$$d_{diff} = 2.44(M+1)\frac{f}{2\sigma}\lambda \tag{3.5}$$

where M is the magnification factor, f the focal length of the lens, 2σ the lens aperture and λ the wavelength of the scattered light (i.e, 532nm for Nd:YAG laser). The factor $f/2\sigma$ is also referred to as the f-number, $f^{\#}$.

As it can be seen from Equation 3.5, diffraction diminishes for increasing apertures and increases vice versa. In PIV, the minimum diffraction limited diameter, d_{diff} is only obtained for very small particles (in the order of the wavelength), large f-numbers and small magnifications. For larger particles and/or larger magnifications, geometric imaging effects will dominate. The total particle image diameter is expressed as:

$$d_\tau = \sqrt{(Md_p)^2 + d_{diff}^2} \tag{3.6}$$

The capability of the imaging system to produce clear and focused particles is expressed by the depth-of-field [Stanislas and Monnier, 1997], which is a measure for the thickness of the region containing in-focus particles:

$$\delta_z = \pm\frac{(M+1)}{M^2} f^{\#} d_{diff} \tag{3.7}$$

It can be seen from Equation 3.7 that the depth of field, δ_z and hence the region of in-focus particles, can be increased by either increasing the f-number or decreasing the magnification. Furthermore, it can be concluded that a larger aperture (small $f^{\#}$) is required to record sufficient light from each particle and to reduce the diffraction limited diameter (i.e., sharp particles). On the other hand, large apertures yield a small depth of field and an increase in lens aberration.

For example, for a typical f-number of $f^{\#} = 8$, a magnification of $M = 1/4$ and a 10μm particle, the diffraction limited diameter is $d_{diff} = 13\mu$m, the recorded image diameter is $d_\tau = 13.2\mu$m and the resulting depth of field is $\delta_z = \pm 2.08$mm. Depending on the particular experimental condition, usually a compromise between sufficient light and depth of field is required.

It should also be stated that the above equations are only valid for a single, ideal lens. Obviously, the optical system in PIV does not act as an ideal lens and to accurately predict the performance of the imaging system, one needs to determine the modulation transfer function of each optical component. Since this is not feasible, the equations above are only thought to be a rough estimate.

3.2.3 Digital Image Recording

The continuous light distribution described in Equation D.5 is captured by a digital pixel sensor typically of a CCD (Charged Couple Device) or CMOS (Complementary metaloxidesemiconductor) architecture. The sensor is composed of several light sensitive elements (i.e., pixel) arranged over a rectangular array. The pixels have a typical size of approximately 7μm $\times$ 7μm and standard CCD arrays contain between 1000 $\times$ 1000 up to 2000 $\times$ 4000 pixels for high resolution measurements.

The light distribution impinges on the sensor surface and is spatially discretised over the pixel array. The latter acts as a transducer to convert the incoming light photons into charged electrons, which can be read as a voltage signal during the pixel read out process. The analogue signal containing the pixel intensities is converted into a digital signal through a sampling and quantisation process. The recorded images are transferred to computer via a frame

Table 3.1 Full frame interline transfer CCD recording devices

Manufacture	KODAK Megaplus 1.0	DANTEC Flow Sense 2M	PCO Pixelfly
Sensor type	CCD	CCD	CCD
Pixel linear size [μm]	9.7	7.4	4.65
Spatial resolution [$pixel$]	1008×1018	1600×1200	1248×1024
Quantum efficiency @ 532nm [%]	42	-	43
Frame rate [Hz] (double exposure)	15	15	7.5
Frame separation [μs]	1.0	0.2	5
Quantisation [$bits$]	8	8 or 10	8 or 12

grabber and stored for later processing. Modern digital CCD cameras used in PIV experiments are typically capable of frame rates in the order of 10-15Hz in double exposure mode with minimum frame separations time of approximately 1μs. Typical quantisation levels are 8 or 12bits.

In the design of a PIV experiments, it is crucial to evaluate the important characteristics of the recording device. Some of these parameters are presented in Table 3.1 for the three different CCD sensors used in this research.

3.2.4 Light Source

The standard method used for illumination of the tracer particles is by means of pulsed or continuous lasers. Lasers are capable of emitting high intensity and monochromatic light, so that any chromatic aberrations of the imaging system are avoided [Raffel et al., 1998]. Using a number of spherical and cylindrical lenses, the emitted laser beam is converged into a thin light sheet, which illuminates the measurement volume.

To eliminate motion blur of the tracer particles at higher flow velocities, pulsed lasers with short pulse durations are usually preferred to 'freeze' the flow during the image acquisition. Furthermore, as most PIV systems record pairs of images with very short interval times, double cavity (i.e., 'double-pulsed') lasers are most commonly used.

Table 3.2 Specification of the Nd:YAG PIV lasers

Manufacture	New Wave SoloPIV 120XT	Spectra Phys. PIV-400-10
Repetition rate (per cavity) [Hz]	1-15	1-10
Max. pulse energy [mJ]	120	400
Pulse width [ns]	3-5	5-10
Energy stability [%]	< 4	< 5
Beam diameter at laser output [mm]	5	9
Divergency [mrad]	< 3	< 0.5
Beam pointing stability [μrad]	< 100	< 100

Most PIV applications use dual cavity solid state Nd:YAG lasers[2], which provide short pulse width (5-10ns), high instantaneous pulse energies (of up to 400mJ) and good beam characteristics. Traditional dual cavity Nd:YAG lasers allow very short interval times at repetition rates of up to 30Hz, while for time-resolved measurements, high-speed Nd:YAG lasers are required with repetition rates of up to 10kHz, however only at a comparably lower pulse energy.

Nd:YAG lasers are optically pumped using a flash-lamp or laser diode and typically emit light in the infrared at a wavelength of 1064nm. Pulsed lasers are usually operated in the so called Q-switching mode with an optical switch inserted into the laser cavity. The pulse energy is controlled by adjusting the delay time between the flash-lamp and the relaxation of the neodymium ions via the Q-switch (i.e., Q-switch delay). For PIV applications, the high-intensity pulses are frequency doubled with a harmonic generator to generate visible laser light at 532nm (green light). Typical operating characteristics of the two different Nd:YAG lasers used in this research are summarised in Table 3.2.

The timing and synchronisation of the laser and recording equipment is illustrated in Figure 3.2. The lasers are operated in Q-switch mode, whereby the flash-lamps and Q-switch delays are triggered with TTL signals and synchronised to the camera acquisition via a digital 4 channel delay generator (BNC-

[2] Nd:YAG - Neodymium-doped Yttrium Aluminum Garnet; Nd:$Y_3Al_5O_{12}$ is a crystal that is used as a lasing medium for solid-state lasers.

500, Berkeley Nucleonics Corporation, USA). The typical acquisition times of the PIV cameras are 1-999μs for the first exposure and up to 33ms for the second exposure. Inter-frame times are typically 5-10μs and readout times are about 30ms. In traditional single exposure, double pulse PIV, the lasers are triggered so that the first pulse occurs towards the end of the first exposure and the second pulse during the exposure of the second image. In this way pulse separation times (Δt) between 10μs to 33ms can easily be realised permitting a large range of flow velocities.

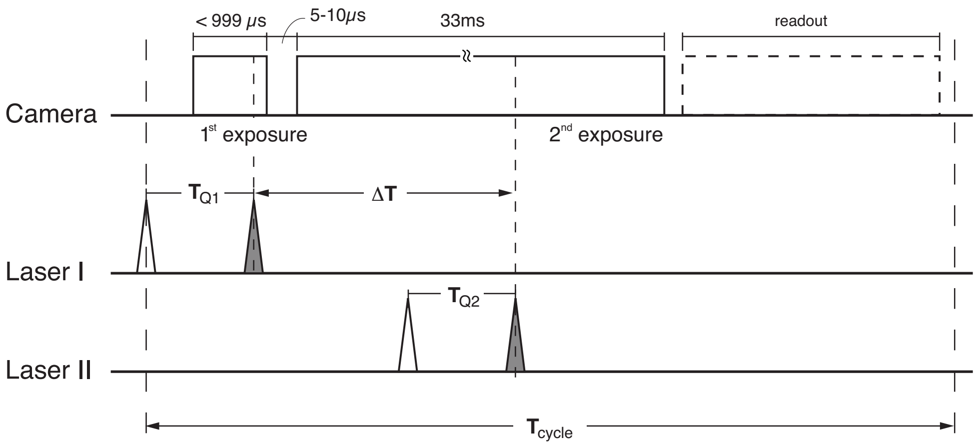

Figure 3.2 Schematic illustration of the timing and synchronisation sequence in single exposure, double-pulsed PIV

3.3 Digital Image Evaluation Method

This section describes the numerical interrogation technique for the digital evaluation of the tracer particle displacement. The discussion is limited to the case of the cross-correlation method applied to a pair of single exposed particle image recordings, which can be described through a well established theoretical process. Relevant aspects of the discrete cross-correlation functions and its implementation via the Fast Fourier Transform are presented and aspects of sub-pixel fitting and data validation are discussed.

3.3.1 Mathematical Background

As mentioned earlier, PIV recordings are typically evaluated by local cross-correlation of two single exposed image frames. A detailed analysis of the statistical PIV method is given by Keane and Adrian [1993] and Westerweel [1997] who provide a detailed mathematical formulation and point out some key properties of the cross-correlation operation. Furthermore, the work of Raffel et al. [1998] provides a comprehensive review of the mathematical background related to the statistical evaluation of the tracer image pattern for a wide range of recording techniques. Optimisation techniques for the single exposed particle image evaluation are provided by Keane and Adrian [1990] on a theoretical basis. Here, only the main aspects of digital image evaluation with relevance to the current work are summarised.

The recorded image of a single particle can be described mathematically as the convolution of the geometric particle image and the impulse response of the imaging system. Hence, the intensity distribution of the tracer ensemble $I(x, y)$ is obtained by superposition of the individual particle images at locations $\mathbf{x}_i$.

$$I(x, y) = \sum_{i=1}^{N} I_o(i) \cdot \delta(\mathbf{x} - \mathbf{x}_i) \tag{3.8}$$

where $I_o(i)$ is the peak intensity of the i^{th} particle and $\delta(\mathbf{x} - \mathbf{x}_i)$ the convolution between the geometric image and the point spread function applied to a rectangular window.

In the following it is assumed that the particles belonging to an interrogation area are subjected to a uniform displacement $\mathbf{d}$ between the two exposures at times t and $t + \Delta t$ so that $\mathbf{x}' = \mathbf{x} + \mathbf{d}$ and $\mathbf{d} = [d_x, d_y]^T$. Thus, considering the image intensity distribution in Equation 3.8, the resulting intensity field for the second exposure $I'(x, y)$ is given as:

$$I'(x,y) = \sum_{j=1}^{M} I_o(j) \cdot \delta(\mathbf{x} - \mathbf{x}_j - \mathbf{d}) \tag{3.9}$$

Note that M and j differ from N and i in Equation 3.8 due to the number of particles entering and leaving the interrogation area during the two exposures.

The cross-correlation function $R_{II}(\mathbf{s})$ of the two intensity fields can then be written as:

$$R_{II}(\mathbf{s}) = \frac{1}{W} \sum_{i,j} I_o(i) I_o(j) \int_W \delta(\mathbf{x} - \mathbf{x}_i)\delta(\mathbf{x} - \mathbf{x}_j + \mathbf{s} - \mathbf{d}) d\mathbf{x} \tag{3.10}$$

where $\mathbf{s}$ is the separation vector in the correlation plane and W the interrogation area. If the contribution of the corresponding particle pairs ($i = j$) are separated from those due to spurious correlation ($i \neq j$), the left hand side of Equation 3.10 can be re-written as follows:

$$R_{II}(\mathbf{s}) = R_C(\mathbf{s}) + R_F(\mathbf{s}) + R_D(\mathbf{s}) \tag{3.11}$$

where $R_C(\mathbf{s})$ corresponds to the mean intensity convolution and equals zero if the mean intensity is subtracted. The term $R_F(\mathbf{s})$ corresponds to the correlation noise due to randomly distributed particles and image noise. $R_D(\mathbf{s})$ corresponds to the convolution of matching particle pairs ($i = j$), which can further be expressed as:

$$R_D(\mathbf{s}) = \delta(\mathbf{s} - \mathbf{d}) \sum_{i=1}^{N} I_o(i) I_o(j) \tag{3.12}$$

The components of the spatial cross-correlation function (3.10) for a pair of single exposed interrogation areas is illustrated in Figure 3.3 with randomly located particles and a constant in-plane displacement $\mathbf{d}$.

Consequently, for a given distribution of particles, the correlation function $R_{II}(\mathbf{s})$ exhibits a maximum for $\mathbf{s} = \mathbf{d}$. Hence, the cross-correlation matching process becomes an optimisation procedure [Scarano, 2000], which restates the issue of particle image displacement evaluation as the minimisation of distance between two successive tracer images.

3.3.2 Discrete Spatial Correlation

In PIV image processing, the cross-correlation approach is applied to the light intensity distribution recorded by the CCD pixel array. The spatial discrete cross-correlation function for two $N \times M$ pixel interrogation images I and I' is given by Westerweel [1997] as:

$$R_{II}(x, y) = \sum_{i=1}^{N} \sum_{j=1}^{M} I(i, j) I'(i + x, j + y) \tag{3.13}$$

where $1 \leq x \leq N$ and $1 \leq y \leq M$. In the present analysis algorithm, the normalised spatial cross-correlation is used and defined as follows [Westerweel, 1997]:

$$R_{II}(x, y) = \frac{\displaystyle\sum_{i=1}^{N} \sum_{j=1}^{M} (I(i, j) - \overline{I})(I'(i + x, j + y) - \overline{I}')}{\left[\displaystyle\sum_{i=1}^{N} \sum_{j=1}^{M} (I(i, j) - \overline{I})^2 \sum_{i=1}^{N} \sum_{j=1}^{M} (I'(i, j) - \overline{I}')^2\right]^{1/2}} \tag{3.14}$$

where $\overline{I}$ and $\overline{I}'$ are the mean image intensities subtracted from the images to remove the mean convolution term $R_C(\mathbf{s})$. Equation 3.14 is normalised by the auto-correlation coefficient and $0 \leq R_{II} \leq 1$, because $I \geq 0$ and $I' \geq 0$. Furthermore, the advantage of Equation 3.14 over 3.13 lies in the reduction of a displacement bias due to clipped particle images [Anandarajah et al., 2006].

Typically, the recorded images are divided with a uniform grid into windows, which are interrogated separately. Most commonly, Equation 3.13 and 3.14 are

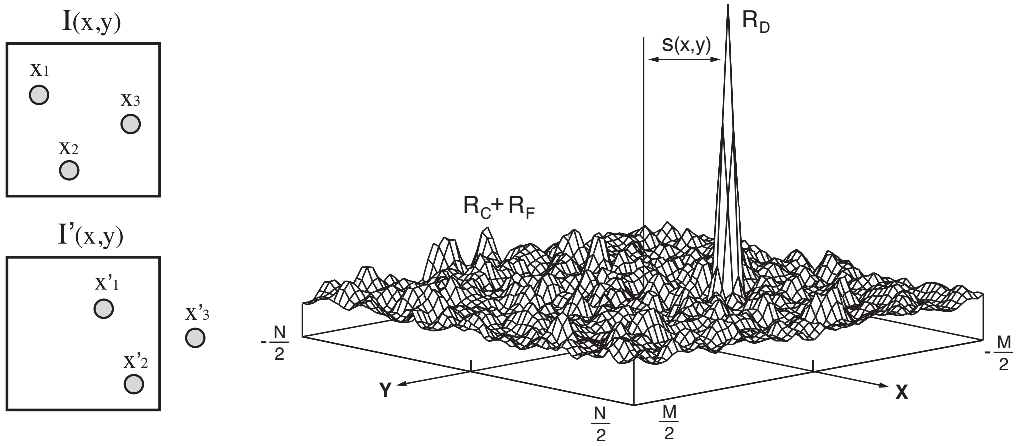

Figure 3.3 Cross-correlation function R_{II} between two single exposed image frames I and I', $N_I = 15$ and $|\mathbf{d}|/\sqrt{N^2 + M^2} = 0.125$

computed in the frequency domain using the fast Fourier transform (FFT) as it enables a significant reduction in computation time.

$$I(i,j) \otimes I'(i,j) \Leftrightarrow FFT^{-1}\left\{\hat{I}(\xi,\eta) \times \hat{I}'^{*}(\xi,\eta)\right\} \tag{3.15}$$

where $\hat{I}(\xi,\eta)$ denotes the Fourier transform of $I(i,j)$ and $\hat{I}'^{*}(\xi,\eta)$ the complex conjugate of the Fourier transform of $I'(i,j)$ (see also Figure 3.4). It should also be noted that the computation of the cross-correlation via the FFT suffers from wrap-around effects due to the assumed periodicity of the FFT signal. This error is minimised by the use of zero-padding [Raffel et al., 1998] and Equation 3.15 becomes a very good approximation of the cross-correlation in Equation 3.14.

The discrete spatial normalised cross-correlation operation yields the area averaged tracer displacement within the interrogation window. The location of the correlation maximum provides the displacement vector of the seed particles and the local average velocity follows readily by taking into account the optical magnification, M and the time separation Δt between the two exposures. Equation 3.14 is computed at discrete locations and the global displacement field is composed of the individual local displacement vectors located at the interrogation window centre.

Lastly, it is noted that the application of the fast Fourier transform is not essential to the evaluation of the cross-correlation. It however, constitutes a

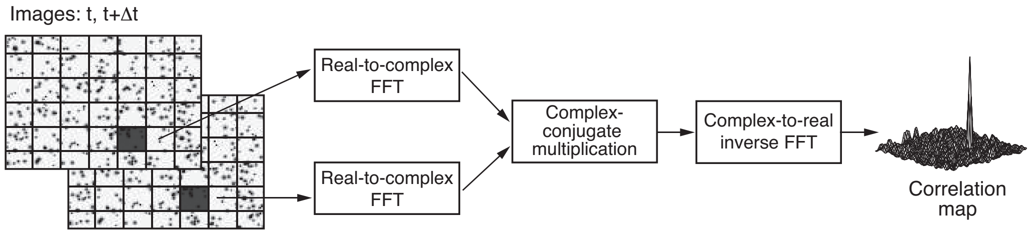

Figure 3.4 Analysis of single exposed image frames: Implementation of the cross-correlation function via the fast Fourier transform (FFT)

faster and computationally more efficient alternative to the direct computation of the cross-correlation sum in Equation 3.14.

Peak Detection

The displacement $\mathbf{d} = [d_x, d_y]^T$ is given by the position of the correlation peak in the correlation map. Since the correlation function is evaluated at discrete points i, j (i.e., pixel intensity locations), the displacement is initially obtained at discrete locations, $\delta \mathbf{x}_c$ to an accuracy of ± 0.5pixel.

To improve the measurement precision, the sub-pixel location of the correlation peak is most commonly approximated by means of interpolation functions, which are based on the peak neighbouring values. Amongst the most common choices are centroid methods and parabolic and Gaussian fits, which are widely discussed in the literature (i.e., Nobach and Honkanen [2005]; Scarano and Riethmuller [2000]; Willert and Gharib [1991]).

In this work, the expression for a two-dimensional (elliptical) Gaussian regression [Nobach and Honkanen, 2005] is used to estimate the sub-pixel location of the correlation peak such that:

$$\rho(x, y) = exp(c_{00} + c_{10}x + c_{20}x^2 + c_{11}xy + c_{01}y + c_{02}y^2) \tag{3.16}$$

This function has six coefficients $c_{n,m}$ which are evaluated from the correlation maximum ρ_0 and the eight neighbouring correlation values $\rho_{x+i,y+j}$, $i, j \in [-1, 1]$ with a L_2 norm [Nobach and Honkanen, 2005]. The sub-pixel coordinates of the correlation peak are then derived as:

$$\Delta x = \frac{c_{11}c_{01} - 2c_{10}c_{02}}{4c_{20}c_{02} - c_{11}^2} \tag{3.17}$$

$$\Delta y = \frac{c_{11}c_{01} - 2c_{01}c_{20}}{4c_{20}c_{02} - c_{11}^2} \tag{3.18}$$

and the true location of the correlation peak is given as the sum of the discrete and sub-pixel (fractional) location, $\delta\mathbf{x}_{pk} = \delta\mathbf{c}_d + \Delta\mathbf{x}$.

Nobach and Honkanen [2005] have shown significant improvements in estimation accuracy of the above two-dimensional Gaussian regression compared to the traditional one-dimensional, three-point interpolations [Raffel et al., 1998]. This was particularly pronounced in the case of non-axially orientated or elliptically shaped correlation peaks as they often occur in regions with strong velocity gradients [Soria, 2006].

As it will be demonstrated in the following, the sub-pixel interpolation significantly enhances the performance of the cross-correlation estimation. Nevertheless, imperfect correlation peak shapes cause a displacement bias, which can only be mitigated, but not removed with the above procedure.

3.3.3 Data Validation

After the evaluation of the displacement field, a certain number of vectors is incorrect, due to the failure of the cross-correlation algorithm (i.e., spurious correlation peaks). The causes for the correlation algorithm to fail are several; for example, locally low seeding density, high image noise due to light reflections, CCD noise, high velocity gradients, ect., all of which can lead to degraded correlation peaks.

The purpose of the data validation is to increase the confidence level of the measurement and to provide a complete data set for post-processing (i.e., instantaneous and ensemble averaged flow properties and statistics). The data validation procedure can be distinguished into two tasks: first, detection of the erroneous or ambiguous data, and second, removal and appropriate substitution of the spurious data.

In order to detect incorrect data, the raw displacement field has to be validated and several methods are proposed in the literature (i.e., Shinneeb et al. [2004]; Westerweel [1994]; Hart [1999]; Raffel et al. [1998]; Westerweel and Scarano [2005]). For example, the detectability, D_0 of the correlation peak is defined by Keane and Adrian [1990] as the ratio of the highest and second highest peak in the correlation map $R_{II}(\mathbf{s})$, which assesses the measurement reliability based on the correlation map topology. The detection probably increases with image density, N_I (i.e., number of particles per interrogation window, ppw). Based on their numerical analysis, Keane and Adrian [1990] quote an optimal value of $N_I \geq 15$ to obtain a 95% detection probability.

There are however, some practical limitations with D_0 as the only detection criterion [Westerweel, 1994] and alternatively, statistical criteria based on the computed displacement distribution are often used. Such methods include global mean or histogram operators [Raffel et al., 1998] and local mean and median operators [Westerweel, 1994; Westerweel and Scarano, 2005].

In the present work, it is proposed to use a combined application of a correlation base and a statistical criterion. The first one is adapted from Keane and Adrian [1990] and modified to suit the current application. It expresses the detectability, D_0 as the ratio of the correlation peak height to the mean correlation value (averaged over the interrogation area) and is referred to as the signal-to-mean ratio (SMR) in the remainder of this work.

$$D_0 = \frac{max\{R_{II}(x,y)\}}{\frac{1}{W}\int_W R_{II}(x,y)d\mathbf{x}} \tag{3.19}$$

The advantage of this criterion compared to Keane and Adrian [1990] is that it also returns a valid detection in the absence of a second correlation maxima as it occurs during ensemble correlation averaging. Typically, values of the SMR criterion are between 1.5 and 2.0.

The second detection criterion used in this work is the normalised median test (NMT) developed by Westerweel and Scarano [2005] and defined as:

$$r_0 = \frac{|U_0 - U_m|}{r_m + \epsilon} \tag{3.20}$$

where r_0 is a normalised displacement residual, r_m the median of the displacement residual $r_i = |U_i - U_m|$, U_m the median displacement, ϵ the acceptable fluctuation level due to cross-correlation and U_0 the displacement vector under consideration. Equation 3.20 is evaluated in a 3×3 neighbourhood and constitutes a 'universal' detection criterion independent of the vector field's spatial resolution [Westerweel and Scarano, 2005]. Typical threshold values for NMT are between $2 - 3$, meaning that vectors with NMT values above the threshold are rejected.

Once the displacement field is validated, erroneous vectors are substituted using various replacement schemes. This is necessary, as most post-processing operations (i.e., vector statistics, vector operators) require complete data fields without gaps or data-drop-outs. Replacement schemes used in this work include bilinear and binomial interpolation [Westerweel, 1994] and a mean value and moving average scheme [Raffel et al., 1998].

Furthermore, some post-processing methods also require smoothing of the vector field to suppress random noise typically present in experimental data. This is generally performed with a simple convolution of the data with a 3×3 or larger smoothing kernel of equal weight. Note that by choosing a kernel size with spatial dimensions smaller than the effective interrogation window size, the effects of lowpass filtering of the vector field are minimised.

3.4 PIV Cross-Correlation (PIVCC) Algorithm

3.4.1 Multigrid Interrogation Method

The following section presents the iterative, multigrid, window shifting cross-correlation procedure adopted in this research. Similar iterative multigrid algorithms have been developed by Soria [1996], Westerweel et al. [1997], Scarano and Riethmuller [1999], Scarano [2002] and Lecordier and Trinite [2004] and are common practice in modern PIV analysis.

Dynamic Range and Measurement Uncertainty

The performance analysis and improvement of the cross-correlation operator is an ongoing subject within the PIV community. In the past, the above mentioned authors amongst others have significantly contributed to the understanding of the cross-correlation analysis and while some arguments are still subjected to discussion, there is a general agreement on some key aspects:

- The velocity dynamic spatial range (DSR) is limited by the in-plane *loss-of-particles*
- The finite extend of the interrogation window introduces a displacement bias
- A periodic bias occurs in the fractional displacement (*peak locking* effect)

The problem of in-plane *loss-of-particles* [Adrian, 1997] limits the size of the smallest possible interrogation window, IW with respect to the largest in-plane displacement, d_{max}. Keane and Adrian [1990] give the *one-quarter rule* that limits the maximum in-plane displacement to 25% of the IW to ensure an adequate number of matched particle pairs in the correlation sum (3.14). From Adrian [1997] the dynamic spatial range follows immediately to:

$$DSR = \frac{d_{max}}{\sigma_u} = \frac{c \cdot IW}{\sigma_u} \tag{3.21}$$

where σ_u is the minimum resolvable length scale (i.e., measurement uncertainty) and the $c = 0.25$ is derived from the *one-quarter rule*. Expression 3.21 reads as the trade off between accuracy and spatial resolution and DSR can be enlarged by increasing IW; however, at the same time the spatial resolution is decreased. Typically, the measurement uncertainty is in the order of 0.1 pixel [Willert and Gharib, 1991], which leads to a dynamic range of approximately two orders of magnitude for a 32×32 pixel^2 window. The numerical simulation in the remainder of the chapter will assess the measurement uncertainty for the current analysis algorithm in more detail (Section 3.5).

A systematic bias error arises due to FFT cross-correlation procedure (which assumes a periodic signal) and the finite interrogation window size as detailed by Westerweel [1997] and Raffel et al. [1998]. The convolution of two uniformly weighted interrogation areas produces a triangular weighting in the correlation plane with values close to the centre being weighted higher than correlation values at the edges. As a consequence, the correlation peak is distorted, which leads to a bias in the peak position towards the origin of the correlation map (i.e., smaller displacements). This displacement bias is proportional to the width of the correlation peak (i.e., particle image diameter, velocity gradients) and the interrogation window size.

This effect is more pronounced for smaller interrogation windows and therefore somewhat constrains the trade off between spatial resolution and measurement accuracy. Methods to remove this bias error exist and rely upon a proper normalisation of the correlation function [Westerweel, 1997]. Alternatively, adaptive window offset schemes can be used to compensate for the in-plane loss of particle pairs and constitute a viable option to obtain an accurate displacement estimate. Furthermore, these algorithms can effectively reduce the bias error as it will be demonstrated later on.

Additionally to the main bias term, the displacement estimate contains another systematic error in the fractional displacement. This error is commonly referred to as *peak locking* (or *pixel locking*) and describes the bias of the sub-pixel peak interpolator [Raffel et al., 1998; Gui and Wereley, 2002]. This error has a periodic behaviour with respect to the displacement and a wavelength of one pixel. A detailed discussion of this tracking error is given in Scarano and Riethmuller [2000] and Westerweel [1997] amongst others. The effect of the *peak* *locking* is a periodic over- or under-estimation of the fractional displacement, which leads to a bias towards zero (or the closest integer) displacement. Currently, the Gaussian peak estimator is commonly accepted to provide the lowest peak locking effect [Raffel et al., 1998].

Window Offset

The discrete window offset method initially introduced by Soria [1996] and Westerweel et al. [1997] consists of a relative integer shift between the origins of interrogation windows, which follows the motion of the tracer particles. As a result, parts of the correlation operation are anticipated with a predictor (from a previous interrogation) and the relative displacement between the interrogation windows is reduced to its fractional part. Hence, the method compensates for the in-plane *loss-of-particles* due to the translation of the interrogation windows. The local displacement predictor is obtained from a previous interrogation at a larger spatial resolution.

The multigrid window shift technique is demonstrated more clearly in Figures 3.5 and 3.6. Initially, the predictor is set to zero (no offset) and the interrogation window size is chosen in accordance with the *one quarter rule* (solid line in Figure 3.5). After the first interrogation, the result is used as the predictor and interpolated onto a finer grid resolution (dashed lines). The window size is consequently reduced (by a factor of two) and the interrogation windows are offset by the integer value of the displacement predictor. In the present case, the widow offset is applied symmetrically to both interrogation windows (Figure 3.6(a)) and corresponds to a central difference interrogation, which is second-order accurate in time [Raffel et al., 1998].

The displacement field at the next iteration is then obtained as the sum of the predicted displacement $\delta_p(x, y)$ and the measured fractional correction $\delta_c(x, y)$

$$\delta^{k+1}(x, y) = \delta_p^k(x, y) + \delta_c^{k+1}(x, y) \tag{3.22}$$

where the predictor is given by the relation $\delta_p = \text{integer}(\delta^k)$. The iterative structure of the multigrid analysis algorithm is illustrated in Figure 3.8.

As a consequence, the interrogation window size in the subsequent steps is no longer limited by the *one quarter rule* and the recorded particle images can be interrogated with a progressively higher resolution. Accordingly to Scarano and Riethmuller [2000], the dynamic spatial range for the multigrid window shift method is given as:

$$DSR = \frac{c \cdot R \cdot W_k}{\sigma_u} \tag{3.23}$$

where W_k is the size of the k^{th} interrogation window and R the refinement ratio defined as: $R(k) = W_0/W_k$. The DSR can now be extended in proportion with the refinement ratio and is independent of the initial interrogation window size (i.e., maximal in-plane displacement).

The advantage of the multigrid window shift technique is the de-coupling of the dynamic range and the spatial resolution as detailed above. Moreover, the interrogation window offset increases the signal-to-noise ratio of the correlation peak due to a higher number of matched particles, which increases the valid data yield. Furthermore, the measurement uncertainty σ_u of the fractional displacement is significantly reduced as it will be shown later and hence, the dynamic range is extended on both ends.

A straight forward extension of the discrete window offset is the application of a fractional window shift. If the exact displacement is applied between the interrogation windows prior to the cross-correlation operation, the resulting fractional displacement is zero and as a consequence, the displacement bias also approaches zero [Scarano and Riethmuller, 2000]. This additional gain in accuracy arises from the fact that the correlation peak is now centred on the correlation plane, which significantly reduces the bias effect due to the finite window size and the sub-pixel peak estimator. This behaviour is further validated in Section 3.5.

Window distortion

In PIV, the particle displacement is measured under the assumption that the motion of the tracer particles within the interrogation window is approximately

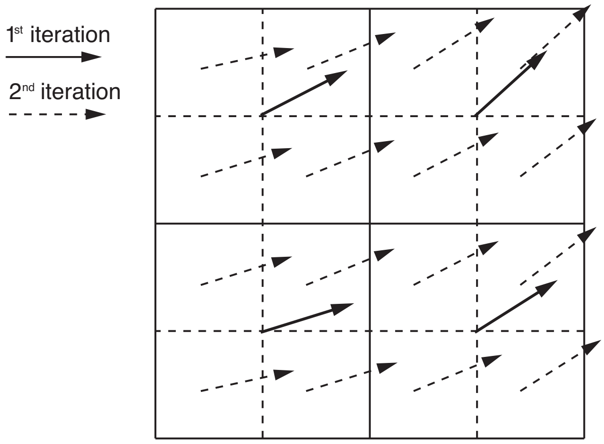

Figure 3.5 Schematic of the multigrid interrogation method; (solid lines) coarse grid for 1^{st} iteration, (dashed lines) 2^{nd} iteration on a refined grid

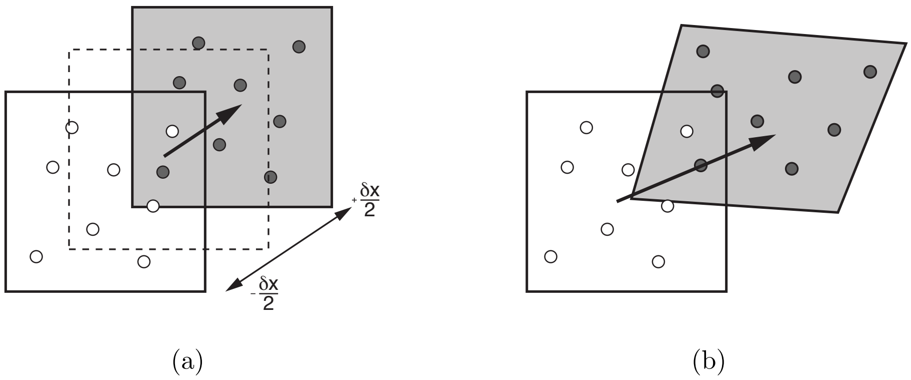

Figure 3.6 Principle of the window offset method: (a) central difference window shift, (b) window deformation; Second exposure in grey, solid circle indicate tracer particles correlated with the first exposure. Figure adapted from Scarano [2002]

uniform. In practice however, this hypothesis is almost never true and the cross-correlation performance is affected by local velocity gradients. While the effects of low to moderate gradients (up to 3% of the interrogation window size) are rather negligible [Keane and Adrian, 1990], strong velocity gradients lead to a significant reduction of the signal to noise ratio and broadening or splitting of the correlation peak [Raffel et al., 1998; Soria, 2006; Westerweel, 2008]. As a result, the displacement measurement in the presence of strong velocity gradients is affected by large uncertainties and high vector rejection rates [Raffel et al., 1998].

In these cases, the iterative window distortion technique [Huang et al., 1993;

Scarano, 2002; Scarano and Riethmuller, 2000] is conceived for the compensation of the in-plane velocity gradient by iteratively deforming the interrogation windows. As discussed by Huang et al. [1993], it is therefore possible to significantly enlarge the measurable range of velocity gradients in high shear and wall bounded flows as they for example occur in the carotid artery (see result Chapters 5 and 6).

The basic principle of this method is illustrated in Figure 3.6(b). In analogy to the iterative window shift technique, the interrogation windows are translated and transformed according to a previously calculated predictor field (i.e., deformation field). Rather than performing the deformation for each individual interrogation area, the procedure is implemented based on the deformation of the entire PIV recording so that:

$$\tilde{I}(i,j) = I\left(i - \frac{\delta x}{2}, j - \frac{\delta y}{2}\right) \tag{3.24}$$

$$\tilde{I}'(i,j) = I'\left(i + \frac{\delta x}{2}, j + \frac{\delta y}{2}\right) \tag{3.25}$$

where $\delta x, \delta y$ is the image deformation displacement at location (x, y) and is obtained via a bi-linear interpolation of the predictor displacement $\delta_p^k(x, y)$ onto a pixel grid. The deformed images $\tilde{I}(i,j), \tilde{I}'(i,j)$ are then substituted into Equation 3.14 and the interrogation is performed with a single step FFT cross-correlation.

The implementation of the window (or image) deformation technique into the existing iterative multigrid structure is straightforward. The deformation field is calculated from the previous displacement and Equation 3.22 is iterated until the desired spatial resolution and convergency is obtained (Figure 3.8).

If the image distortion is repeated over several iterations (with or without grid refinement), the distance between the two image pairs will be minimised and $\tilde{I}(i,j)$ and $\tilde{I}'(i,j)$ approach a close match. In analogy to the fractional window shift method, the correlation peak will then be symmetrical and centred on the correlation plane. This reduces the measurement uncertainties due to a distorted peak shape and/or inaccurate peak reconstruction (see error discussion above).

On the downside, the iterative interrogation method tends to oscillate, which results in the selective amplification of wavelength smaller than the interrogation window size as mentioned by Schrijer and Scarano [2006, 2008]. Stability of the iterative process is obtained in the present algorithm by a low-pass filtering of the predictor displacement $\delta_p^k(x, y)$ [Schrijer and Scarano, 2008].

Image Interpolation

In order to apply the fractional window offset or image deformation method, the particle image intensities have to be interpolated at non-integer pixel locations. The topic of image interpolation in PIV is extensively reviewed by Astarita and Cardone [2005]; Nobach et al. [2005] and Roesgen [2003]. Additionally, Thevenaz et al. [2000] provide a discussion of image interpolation in medical image processing.

PIV images mainly consist of discontinuous and short wavelength data (close to the sampling size) and as such, an image interpolation procedure should be able to properly reconstruct these discontinuous signals [Raffel et al., 1998]. Therefore, to achieve high accuracy and to avoid loss of information, higher order reconstruction schemes, such as biquatratic or bicubic, B-spline functions or Gaussian and FFT based schemes should be preferred [Astarita and Cardone, 2005; Nobach et al., 2005]. Also, the bilinear interpolation is widely used as it offers a good compromise between accuracy and computational efficiency [Lecordier et al., 1999; Gui and Wereley, 2002].

In the current work, the cardinal function interpolation (also referred to as Whittaker or *sinc* function interpolation) is implemented. According to Scarano [2000], the cardinal function interpolation respects the sampling theorem and allows the complete reconstruction of the image signal, if it is sampled according to the Nyquist criterion. The cardinal function interpolation is defined as:

$$F_{x,y} = \sum_{i=-\infty}^{i=\infty} \sum_{j=-\infty}^{j=\infty} f_{i,j} \cdot \frac{\sin \pi(i-x)}{\pi(i-x)} \frac{\sin \pi(j-y)}{\pi(j-y)} \tag{3.26}$$

and Expression 3.26 is evaluated on an interpolation grid of 11×11 pixel (or larger). Astarita and Cardone [2005] report a total measurement error of less than 0.005 pixel for the cardinal interpolation, while for the bilinear and bicubic interpolations they report errors in the range of 0.03 and 0.01 pixel, respectively. However, the computational expense increases by more than one order of magnitude (i.e., $\sim 10^0$ sec for 16×16 pixel^2) for the cardinal interpolation. Nevertheless, image interpolation via Equation 3.26 is preferred in this work as the gain in accuracy outweighs the computational expense.

3.4.2 Correlation Enhancement

Image Pre-Processing

The signal to noise ratio is strongly affected by the particle image intensity, image background noise and light reflections. Particles with high image intensities dominate the correlation signal whilst low intensities and stationary light reflections cause a bias towards lower displacements. Furthermore, non-uniform illumination resulting from light sheet non-uniformities, pulse to pulse laser variations, irregular particle shapes and out-of-plane motion also significantly influence the correlation signal. For this reason, image enhancement methods prior to image processing are often applied. The main goal of these methods is to enhance the particle image contrast and to reduce image noise. Some of these methods include *background subtraction*, *low-* or *high-pass filtering*, *intensity clipping* or *stretching* and *image thresholding* and *binarisation* [Honkanen and Nobach, 2005; Stitou and Riethmuller, 2001; Raffel et al., 1998; Westerweel, 1993].

Image pre-proceesing techniques for the current set of experiments include *background subtraction*, *dynamic histogram filtering* and image *smoothing* and are described in greater detail in Appendix C together with some representative examples. The background subtraction technique is also used to extract a image mask of the no-flow region, which is then applied during the PIV processing. A further discussion of the background subtraction and masking technique is also provided in Chapter 4.

Ensemble Correlation

When evaluating single exposed image recordings with the conventional cross-correlation technique, a sufficiently large number of particle images per interrogation window are required to obtain a valid velocity estimate ($N_I \geq 15$, Section 3.3.2). However, in some applications or under certain experimental conditions, the particle image density N_I is too low, which results in a weak correlation peak and consequently a reduced vector detection rate.

In these cases, a common procedure to enhance the quality of the measured displacement is to average the spatial correlation functions of corresponding interrogation windows in successive image pairs [Delnoij et al., 1999; Meinhart et al., 2000; Westerweel et al., 2004]. This *ensemble correlation averaging* can be expressed as follows:

$$\overline{R_{II}}(x, y) = \frac{1}{N} \sum_{k=1}^{N} R_{II}^{k}(x, y) \tag{3.27}$$

where $R_{II}^{k}(x, y)$ is the correlation function of a single image pair and $\overline{R_{II}}(x, y)$ the average (or ensemble) correlation function for N image pairs [Wereley et al., 2002].

Another technique to increase the detection probability consists of averaging the individual image recordings (*average image*) to produce an average image of the first and second exposure [Meinhart et al., 2000]. The resulting image pair is then evaluated using the above cross-correlation method. Both of the above techniques were originally intended for micro-PIV applications, but have now also been widely used for macro-PIV applications [Raffel et al., 1998; Buchmann, 2005; Delnoij et al., 1999]. Note that these methods only allow the computation of time-averaged velocity fields and information relating to the unsteadiness of the flow is lost. In this sense, one can say that both techniques are primarily suitable for steady flows or periodic flows with phase averaging as analysed in the following chapters.

Lastly, a third averaging method and probably the most common one is the computation of the time-averaged velocity field by averaging the instantaneous velocity maps (*average velocity*).

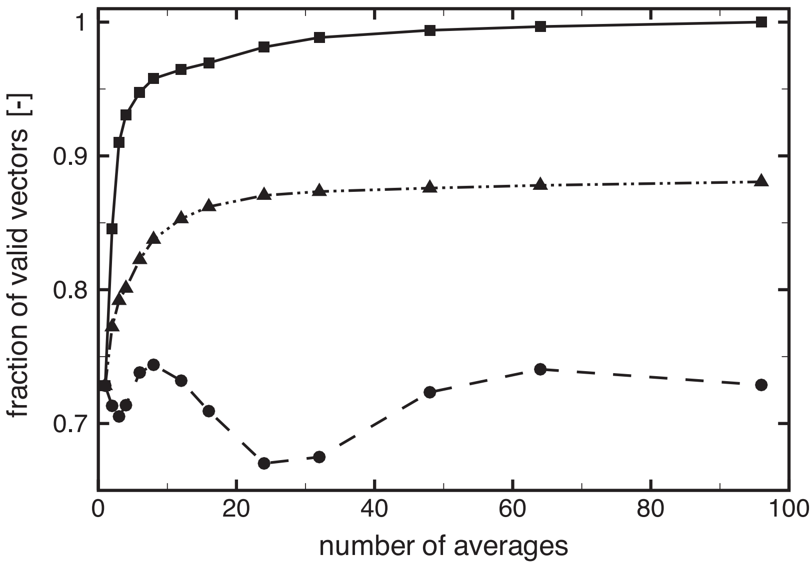

Figure 3.7 Comparison of the performance of the three averaging techniques: ensemble correlation (square), average image (circle) and average velocity (triangle)

To demonstrate the relative performance of the different averaging algorithms, an analysis similar to that of Meinhart et al. [2000] is carried out. For this the flow field shown in Figure 3.9 is interrogated with a window size of 32×32 pixel^2 and the three different averaging techniques. The average number of particles per interrogation window is approximately 6.8. The fraction of valid vectors is determined by identifying the number of velocity vectors that deviate by more than 10% from the known solution. The known solution is estimated by applying the ensemble correlation technique to 96 realisations.

The result of this analysis is shown in Figure 3.7. The ensemble correlation method performs superior and produces less than 1% erroneous vectors after averaging 32 realisations, while the average vector method only reaches 87% after the same number of averages. The average image method produces 74% reliable vectors for 8 averages. A further increase in realisations used for the average image method decreases the measurement reliability due to random correlations between non-paired particle images [Meinhart et al., 2000]. Overall, the obtained results are similar to those reported in Meinhart et al. [2000] with the exception of the average image method, which shows a weaker performance for the present data.

3.4.3 Algorithm Outline

Based on the previous discussion of PIV processing modalities, this section presents an overview of the developed PIV cross-correlation (PIVCC) algorithm. Parts of the algorithm are developed in C++ language (i.e., cross-correlation, image interpolation) and the overall implementation is done in MATLAB (Mathworks Inc., 2008). The iterative multigrid structure of the current algorithm is illustrated in Figure 3.8 and briefly described below.

The first part of the iterative multigrid analysis consists of a single FFT cross-correlation pass as follows:

1. The pre-processed particle images (Appendix C) are sampled at discrete locations and the intensity values for each interrogation window are extracted. The interrogation windows coincide spatially and are of equal size following the *one-quarter-rule*. Typically, an overlapping factor of 0.5 or 0.75 between the interrogation windows is applied to further increase the spatial sampling.

2. For each interrogation area, the cross-correlation is evaluated between the two exposures at time t and $t + \Delta t$ following the procedure illustrated in Figure 3.4. At this stage, no bias correction is applied.

3. The correlation peaks are interpolated with the two-dimensional peak estimator (Equation 3.16) and the displacement field is composed.

4. Optional correlation enhancement methods, such as the correlation based correction [Hart, 1999] or ensemble correlation averaging are applied.

5. Finally, the resulting displacement field is validated using the signal to mean and normalised median test (typically $SMR \geq 1.5$, $NMT \geq 2$). Erroneous vectors are subsequently replaced using a bilinear interpolation and the resulting velocity field is low-pass filtered with a 3×3 kernel.

The first interrogation pass is then followed by the iterative multigrid analysis, which can then be decomposed into two parts. The first part is the multigrid analysis, where the interrogation window size (and spacing) is progressively reduced. This process eliminates the constraint of the *one-quarter-rule* and increases spatial resolution and is usually terminated when the required level of resolution is reached. The second part consists of the iterative analysis at a fixed window size (and grid spacing). This process allows to further improve the accuracy and is particularly useful during the image deformation procedure. Typically, three iterations at the final grid size suffice [Scarano, 2002].

The iterative multigrid procedure is outlined below:

6. Following the first iteration, the predictor field is obtained by bilinear interpolation of the estimated displacement field onto the next higher resolution level. For the window shift method, the interrogation windows are offset (discrete or fractional), while for the window deformation, the recorded particle images are deformed according to Equation 3.24 and 3.25. Image interpolation at sub-pixel locations is performed via the cardinal interpolation function (Equation 3.26).

7. The next cross-correlation pass is performed and the predictor field is updated with the current result (Equation 3.22). The iteration pass then continues with correlation enhancement, vector validation and low pass-filtering (steps 2-5).

8. The resolution level is incremented and steps 6 and 7 are repeated until the final image resolution is reached.

9. Finally, several iterations are performed at the final interrogation window size and sampling distance. As a result, the fractional displacement will further decrease with each iteration and the solution typically converges after two or three iterations.

The window offset (or deformation) generally converges to less than ± 1 pixel in the final interrogation pass, which ensures that the PIV recordings are evaluated at an optimal level. However, the final interrogation window size depends on the particle image density. Below a certain number of matched particles ($N_I < 15$, [Keane and Adrian, 1990]) the detection probability will decrease rapidly and the measurement noise increases regardless. An illustration of the resulting displacement field at several iterative refinement steps is shown in Figure 3.9.

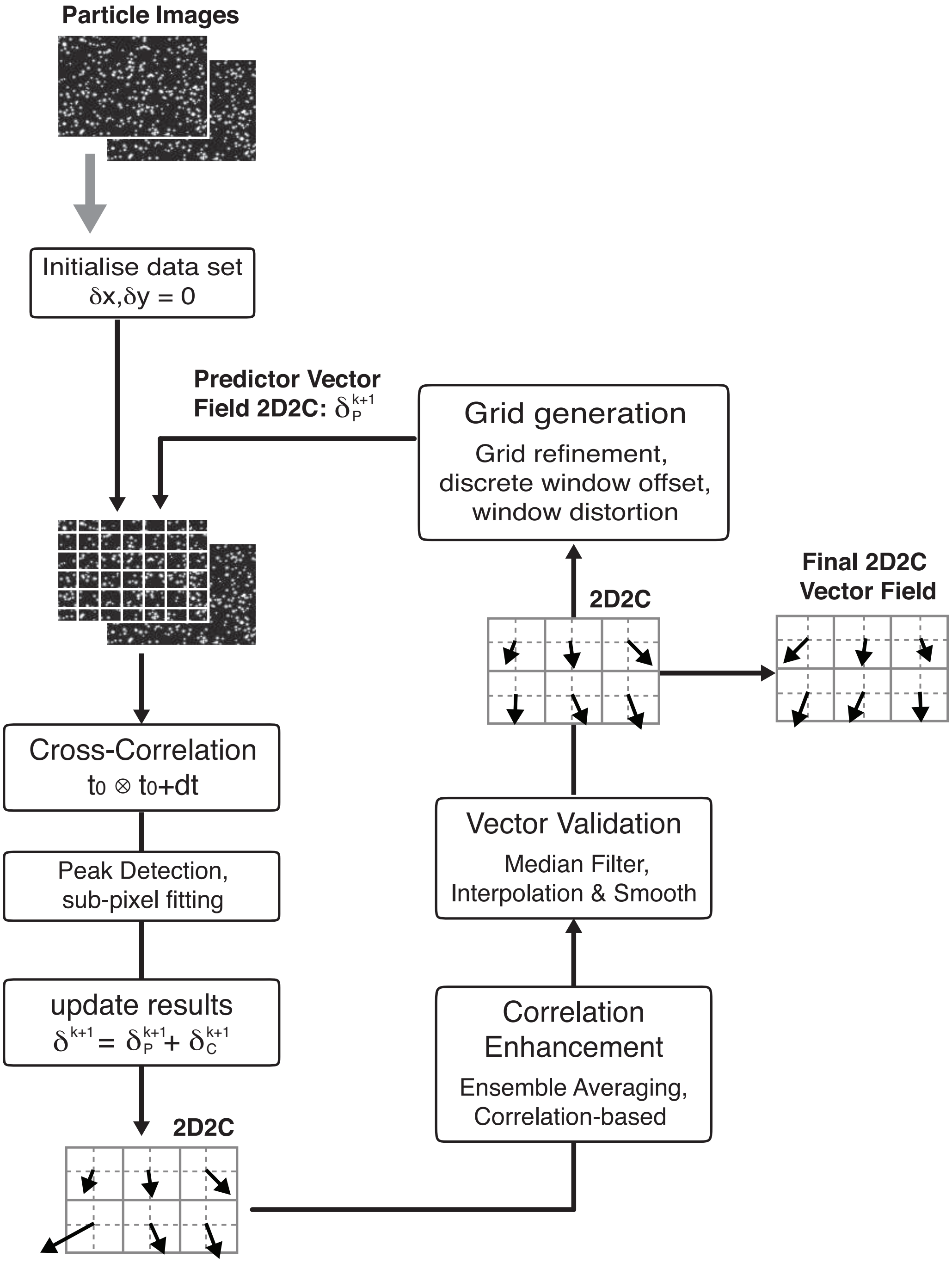

Figure 3.8 PIVCC algorithm: Flow chart for planar PIV vector calculation

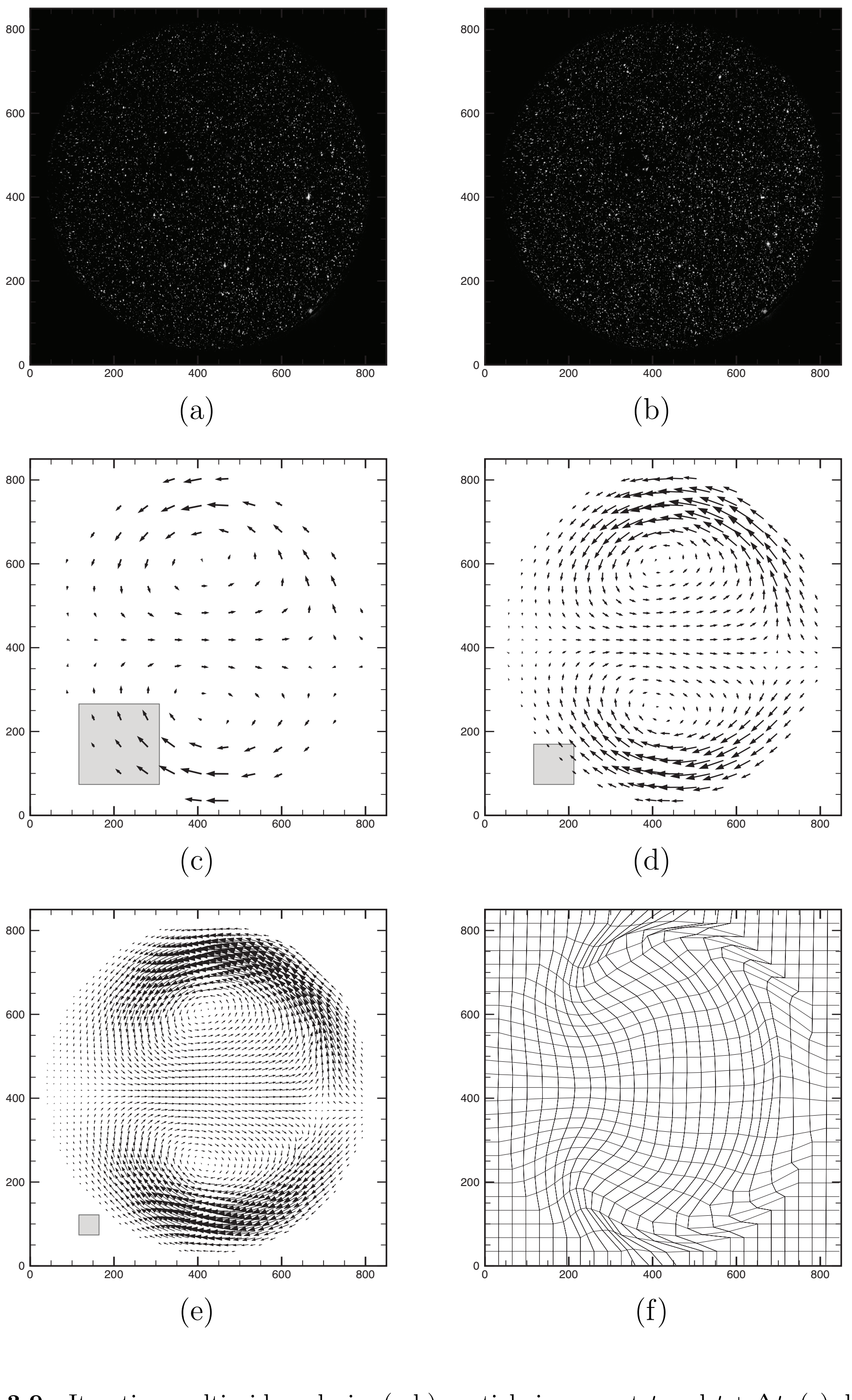

Figure 3.9 Iterative multigrid analysis: (a-b) particle images at t and $t + \Delta t$, (c) displacement field at initial resolution, (d) first iteration, (e) final iteration and resolution and (f) interrogation windows (IW) during the image deformation step. Grey squares indicate the IW size.

3.5 Simulation

In the following, a systematic analysis is performed to assess the performance of the proposed cross-correlation algorithm on the basis of computer simulated particle images. For this, synthetic particle images are generated and the systematic and random errors are assessed by means of Monte Carlo simulations. The particle images are uniformly displaced (or under shear) and a high number of simulations, O(1000) are carried out per test parameter. The results are quantified using the mean bias error and the RMS measurement uncertainty as detailed in Appendix D.

Although this approach includes idealised conditions that differ from *real* experiments, it allows a performance assessment within a controlled environment. For a discussion of the errors under experimental conditions, the interested reader may be referred to the experimental error section in Appendix F.

3.5.1 Synthetic Images

Particle images with a Gaussian light intensity distribution are artificially created at random x, y, z locations within a virtual top-hat light sheet. The particles are of constant diameter, d_τ and the pixel intensity distribution (8 bits) is obtained by integrating the Gaussian light intensity over a virtual sensor with a pixel fill factor of 1.0. The generated particle images are of type I with a zero image background intensity level. A more detailed description of the synthetic image generation is given in Appendix D.2.

The particle density, C is varied between $1/64 - 1/16$ ppp (particle per pixel), the displacement range covers U = [0:0.1:3] pixel and the range of analysed displacement gradients is $\partial U/\partial m$ = [0:0.02:0.2] pixel/pixel. The generated particle images are interrogated with 32×32 and 16×16 pixel^2 windows using the discrete spatial cross-correlation (FFT-CC) and the discrete (DWS) or continuous (CWS) window shifting method. In the case of displacement gradients, the images are interrogated with the continuous window deformation (CWD) technique.

3.5.2 Results

Dislacement error

Figure 3.10(a) shows the mean displacement error (bias error) for the imposed particle image shift and different interrogation procedures. A systematic underestimation occurs for the conventional single step FFT-CC, while the DWS method exhibits a periodic behaviour (i.e., peak locking) with a one pixel wavelength and zero bias for integer displacements. For displacements less than 0.5

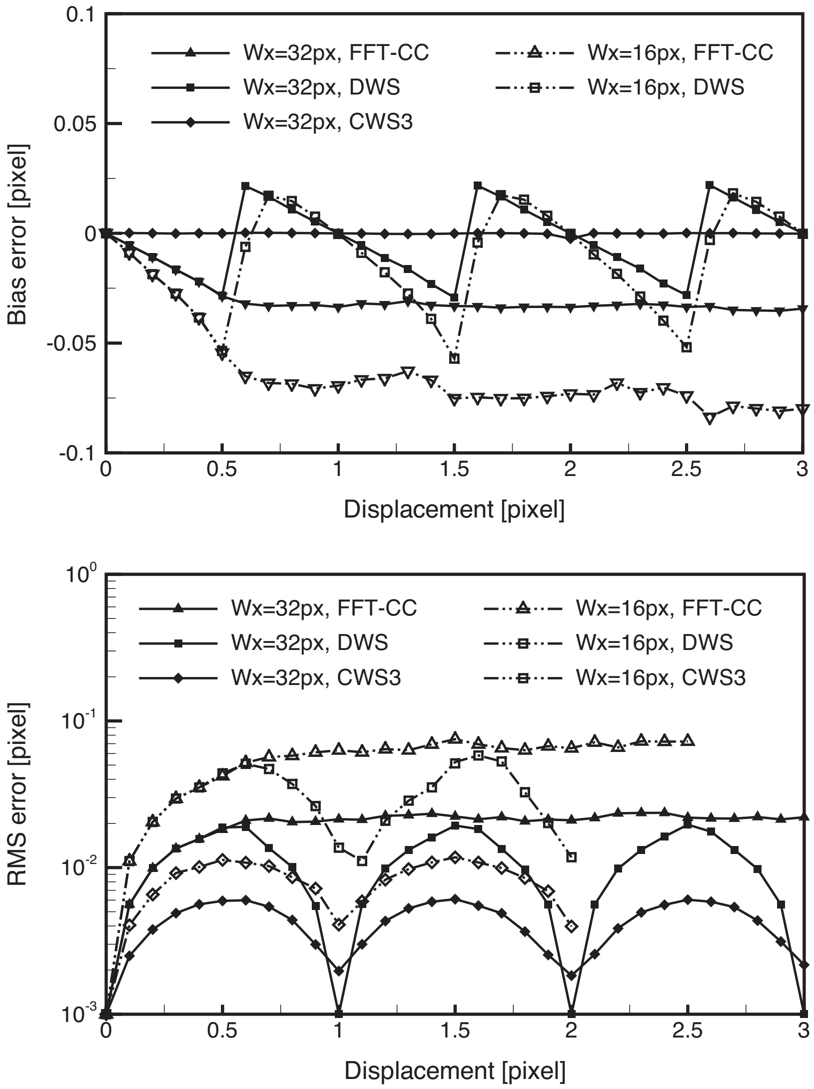

Figure 3.10 Mean displacement error (bias) and measurement uncertainty (RMS) as a function of the particle displacement for different window sizes and interrogation procedures. Simulation parameters: $d_p = 2$ pixel, $C = 1/32$ ppp

pixel the DWS method follows the classical FFT-CC method before it introduces a discontinuity at fractional displacements of 0.5 pixel. The CWS method reduces the tracking error to less than 10^{-3} pixel after three iterations (indicted by the number, i.e., CWS3). As a result, the displacement bias is practically removed and the CWS method oscillates with a period of two pixel (due to the symmetric window shift, [Astarita and Cardone, 2005]).

The corresponding RMS measurement uncertainty is shown in Figure 3.10(b). The RMS error related with the single step FFT-CC is zero for zero displacement, increases linearly for displacements below 0.5 pixel and remains fairly constant for increasing displacements. Again, the DWS method closely tracks the FFT-CC for displacements below 0.5 pixel, but produces a zero error at integer displacements. For the CWS method the measurement uncertainty reduces further to values below 0.005 pixel.

The present results are in very good agreement with previous studies of Gui and Wereley [2002]; Scarano and Riethmuller [2000] and Westerweel [1997] with the bias error being even smaller than that reported by Scarano and Riethmuller [2000] for a very similar FFT-CC and DWS algorithm. Also note that for the same seeding density (i.e., 1/32ppp), both bias and RMS error increase for smaller interrogation windows due to the reduced number of particle pairs contributing to the cross-correlation sum.

Optimal Particle Image Diameter

It is well known that the particle image diameter significantly influences the performance on the PIV analysis [Raffel et al., 1998]. This is evidenced more clearly in Figure 3.11, which plots the total measurement error, ϵ_{tot} (Equation D.1) averaged over the displacement from 0 to 1 pixel as a function of the particle image diameter. The optimal particle image diameter for the DWS method is found to be approximately $d_p = 1.6$ pixel. This is smaller than the 2 pixel given by Raffel et al. [1998], which is based on the RMS error. In fact, when analysing the RMS error alone, the present results are consistent with the numerical simulations of Raffel et al. [1998] and the theoretical analysis of Westerweel [1997]. The differences in optimal particle image diameter are most likely due to the different choice of the sub-pixel peak interpolator, e.g., Raffel et al. [1998] used a 1-D Gaussian interpolation.

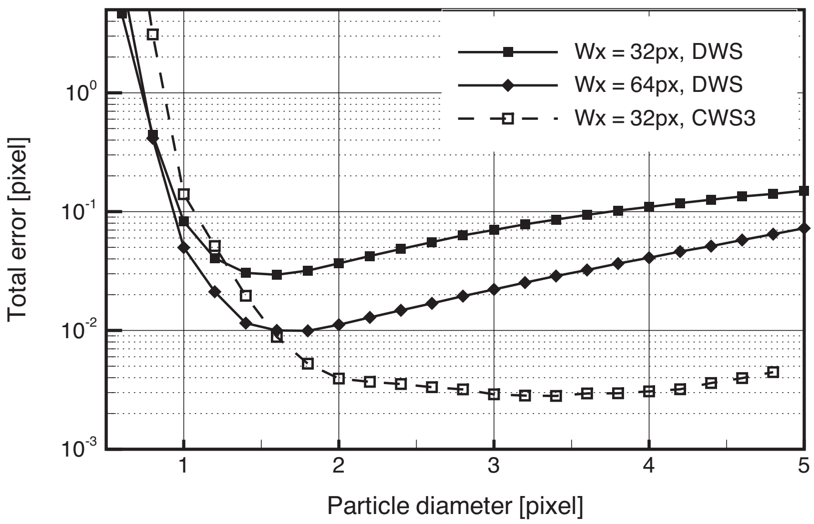

Figure 3.11 Total measurement error, ϵ_{tot} versus particle image diameter for different window shifting methods; $C = 1/32$ppp

For smaller particle images, bias and RMS error increase significantly, while for larger particle images, only the bias error increases (Figure D.3).

Figure 3.11 also shows the total error for the CWS method. The results clearly demonstrate that the optimal diameter differs for the CWS compared with the FFT-CC method. This can be attributed to the use of the cardinal function interpolation scheme for which the total measurement error is approximately one order of magnitude lower (as shown before). The optimal particle image diameter for the CWS method ranges between 3 to 4 pixel and is consistent with previous observations by Astarita and Cardone [2005] and Nobach et al. [2005]. For particle image diameters smaller than 1.5 pixel no significant error reduction occurs and it is better to use the DWS method, which is also computationally more efficient.

Effect of Background Noise

Figure D.4 illustrates the bias error and measurement uncertainty due to simulated image (or background) noise. The noise intensity is varied as a fraction of the image dynamic range ($I_b \pm \sigma$) and added linearly to each pixel. Although this simulation may not be very realistic, it shows the effect of image noise in comparison to the correlation noise and corresponds well with data from Foucaut et al. [2004]. For example, at a noise level of $10 \pm 5\%$ ($\approx$ 5bit/pixel), both RMS and bias error increase significantly to values of up to 0.1pixel. Note that if a background subtraction is applied prior to the cross-correlation, the errors are reduced again to the reference case of 0% background noise (i.e., correlation noise).

Effect of Particle Image Density

As shown by Raffel et al. [1998], the particle image density N_I directly affects the RMS error, which increases when the number of particles per interrogation window increases. Furthermore, the probability of a valid displacement measurement increases (detection probability) for higher particle image density and an optimal value of $N_I \geq 15$ ppw is given by Keane and Adrian [1990]. As shown in Figure D.5, if N_I increases, more particles contribute to the correlation, which strengthens the correlation peak and consequently the RMS error decreases. Conversely, the bias error remains unchanged, regardless of particle image density. For the present algorithm, a particle image density of $N_I \geq 16$ ppw (or $C = 1/64$ppp) yields RMS values below 0.03 pixel and appears to be a good compromise.

Effect of Displacement Gradients

Lastly, the performance of the analysis algorithm is assessed in the presence of velocity gradients. For this, a constant gradient (zero mean) is added to the particle displacement and the average error is calculated over a displacement range from -1 to 1 pixel. In Figure 3.12 the measurement uncertainty is plotted as a function of the velocity gradient and for the DWS and CWD method. The results demonstrate that the velocity gradient rapidly affects the measurement uncertainty with variations of up to two orders of magnitude ($0.01 - 2$pixel). For increasing shear rates, the first order CWD method provides significantly lower uncertainty levels compared to the DWS method and is consequently better suited for flows with strong velocity gradients. Furthermore, it should be noted that in the presence of velocity gradients the RMS uncertainty at integer locations is no longer zero as shown in Figure D.6.

One interesting observation is that for the same particle image density, smaller interrogation windows can tolerate larger velocity gradients. This in fact is consistent with Keane and Adrian [1990] who showed that the effects of velocity gradients is proportional to the total shear ($\partial U/\partial y M$) across the interrogation window, which reduces for small windows. As a consequence, for flows with strong velocity gradients, the CWD method together with small interrogation windows should be the preferred choice. However, considerations regarding particle image density and an adequate particle image diameter should not be ignored in these cases.

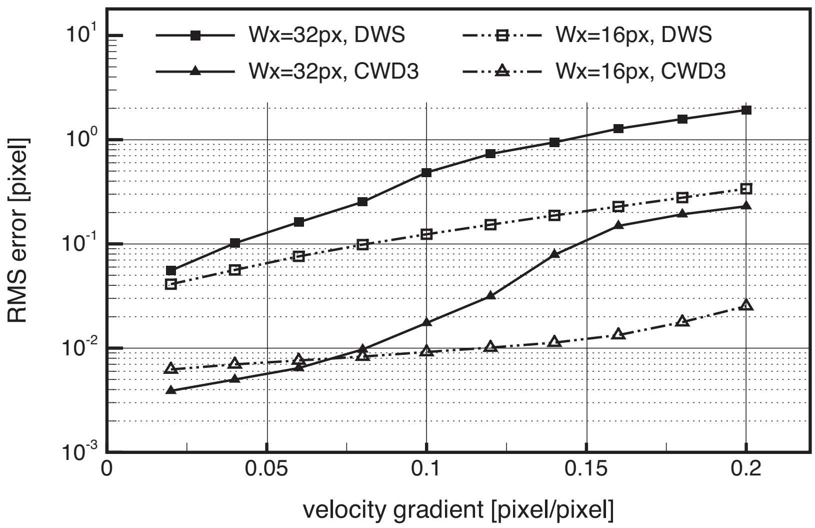

Figure 3.12 Measurement uncertainty (RMS) as a function of the velocity gradient for different window sizes and interrogation procedures. Simulation parameters: $d_p = 2$ pixel, $N_I = 16$ ppw

In conclusion, the developed cross-correlation algorithm has been assessed on the basis of computer generated particle images and the results from the Monte Carlo simulations are in correspondence with those reported in the literature. For typical imaging and processing conditions with $d_p = 2$ pixel, $C = 1/32$ ppp, 10% background noise, moderate velocity gradient, 32×32 pixel^2 interrogation window and discrete window shifting, the expected total measurement uncertainty, ϵ_{tot} is approximately $0.05 - 0.1$ pixel.

3.6 Stereoscopic PIV Processing

Having presented the fundamentals and implementation of the current PIV processing technique, this section addresses an extension of the method to stereoscopic PIV system imaging. In highly three-dimensional flows, conventional 2D, two component PIV (2D-2C) suffers from two distinct deficiencies:

- The resolved two velocity components, u and v are a 2D projection of the true three component velocity field. Thus, the out-of-plane component, w is lost [Raffel et al., 1998].
- The in-plane-velocity components suffer from a perspective error due to the local out-of-plane velocity component. This error is proportional to the ratio of the magnitude of the in-plane to the out-of-plane components [Prasad, 2000].

Within the carotid artery, strong three-dimensional flows occur in the bifurcation and the carotid sinus region as described in the latter chapters. Consequently, the resulting perspective error due to out-of-plane flow can be estimated to approximately 5% for the current experimental investigations.

This inherent limitation of the 2D-2C PIV method can be overcome through the use of a second camera to create a stereoscopic PIV (SPIV) system. Stereo-Optic reconstruction of the 2D information from each camera can then remove the perspective distortion and resolve the out-of-plane velocity component. Several variations of the stereo-camera system are available and their inherent advantages and disadvantages are reviewed extensively by Lawson and Wu [1997b]; Prasad [2000] and Willert [1997].

For the final experimental campaign of this thesis, stereo-PIV measurements were conducted and are presented in Chapter 7. For this purpose, the 2D-2C PIVCC technique was extended to an stereo-PIV system to resolve the full 3D velocity information of the flow (i.e., 2D-3C). A more complete description of the developed stereo-PIV methodology and apparatus is given in Appendix E. In the following, only a short discussion to the stereo-PIV technique is given and its implementation in the current analysis algorithm is described.

3.6.1 Principle

There are two basic stereo-PIV configurations. The translation method, which is omitted here, and the angular offset method, which is used in this work. The angular offset configuration is shown in Figure 3.13 and consists of two cameras orientated under an angle θ of typically 30-45 degrees.

Viewing the object plane under an angle creates a perspective distortion and difficulties arise to uniformly focus over the entire plane. To alleviate this problem, a larger depth-of-field (i.e., large $f^{\#}$) should be used and the camera arrangement should satisfy the so-called Scheimpflug condition. The Scheimpflug condition occurs when the lens plane, image plane and object plane intersect at a common point in the object plane. This is illustrated in Figure 3.13 and further discussed in Appendix E.

Furthermore, significant radial distortions occur in liquid flow applications due to the mis-match in refractive index between the surrounding air and the

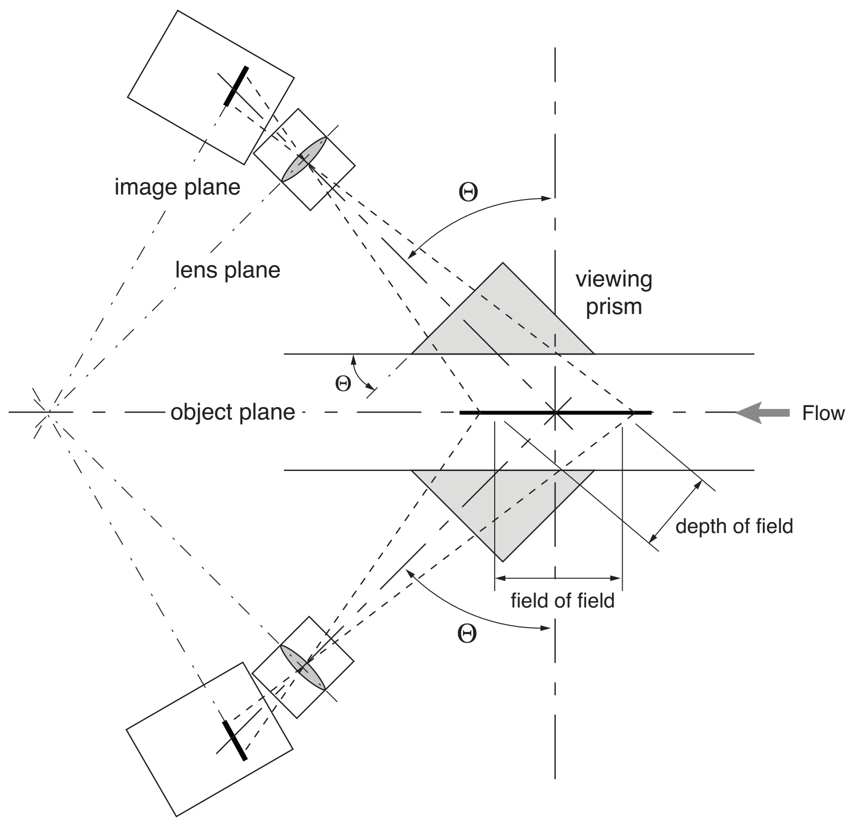

Figure 3.13 Schematic of the angular offset stereo-PIV method showing the camera arrangement, Scheimpflug condition and viewing prisms

silicone model [Prasad and Jensen, 1995]. This causes an astigmatism and adversely affects the ability to satisfy the Scheimpflug conditions and hence severely contaminates any subsequent image correlations. To overcome this problem, viewing prisms as shown in Figure 3.13 are used to enable orthogonal viewing at the refractive index boundary. This corrects radial distortions and allows the Scheimpflug condition to be satisfied.

3.6.2 Processing and 3C Reconstruction

The ability of the stereo-PIV method to accurately determine the in-plane and out-of-plane particle displacement is primarily dependent on

1. the quality of the measured in-plane component of the individual 2D recordings and
2. the accuracy of the mapping of the distorted 2D image space to the undistorted 3D object space.

While the former has been discussed in the previous sections, the latter is primarily dependent on the chosen camera calibration and vector reconstruction method.

Several calibration and reconstruction techniques exist for stereo-PIV and are for example summarised in Lin et al. [2008]; Prasad [2000] and Willert [2006]. Generally, these techniques can be categorised as two-dimensional calibration-based reconstruction, three-dimensional calibration-based reconstruction and geometric reconstruction techniques [Prasad, 2000].

An in-situ three-dimensional calibration-based reconstruction method similar to that described by Soloff et al. [1997] is implemented in this work. This technique does not rely on an accurate knowledge of the geometry of the stereo-camera setup and is able to account for any known and unknown distortion encountered in the real experiment. The cameras are calibrated on a rectangular calibration grid, which is traversed through the measurement volume. The locations of the calibration markers are identified via a local pattern matching (i.e., cross-correlation) and used to calculate the object to image space mapping function, F, described in Equation E.2. According to Soloff et al. [1997], a third order polynomial mapping function is sufficient to account for linear distortions. This is confirmed in Figure E.1, which gives an indication of the typical distortion for a rectangular grid encountered in the current measurement campaign.

The stereo-PIV data analysis involves the simultaneous acquisition of the particle images from each stereo-camera with a similar procedure to the 2D-PIV acquisition described in Section 3.2. From this, the three-component velocity field is obtained by first computing the 2D-2C vector fields for each camera view and subsequent stereo-reconstruction. The complete flow chart for the stereo-PIV processing (SPIVCC) is shown in Figure 3.14. The 2D-2C vector fields are separately computed for each camera using the multigrid scheme. A user defined regular grid in the object space is projected onto each camera such that the resulting vectors are already located at the correct object position. The individual 2D-2C vector fields are validated and filtered. Both cameras are interrogated until the final resolution is achieved. The 2D-3C reconstruction is performed via the system of linear Equations (E.4) in Appendix E, which relates the three-component velocity field (u, v, w) in object space to the measured velocity field (u_1, v_1) and (u_2, v_2) in image space. Equation E.4 is solved in a least squares sense and the resulting 2D-3C vector field represents the three components of the velocity in object coordinates measured on a single 2D plane.

The reconstruction method described above assumes that the calibration target is aligned with the centre of the light sheet plane. In practice, however, this alignment is difficult and a slight out-of-plane shift or rotation can introduce significant errors in the image to object mapping [Willert, 1997; Wieneke, 2005]. A method for the alignment correction as proposed by Wieneke [2005] is also implemented into the current stereo-PIV procedure. This is generally referred to as self-calibration and shown in Figure 3.14 as disparity correction.

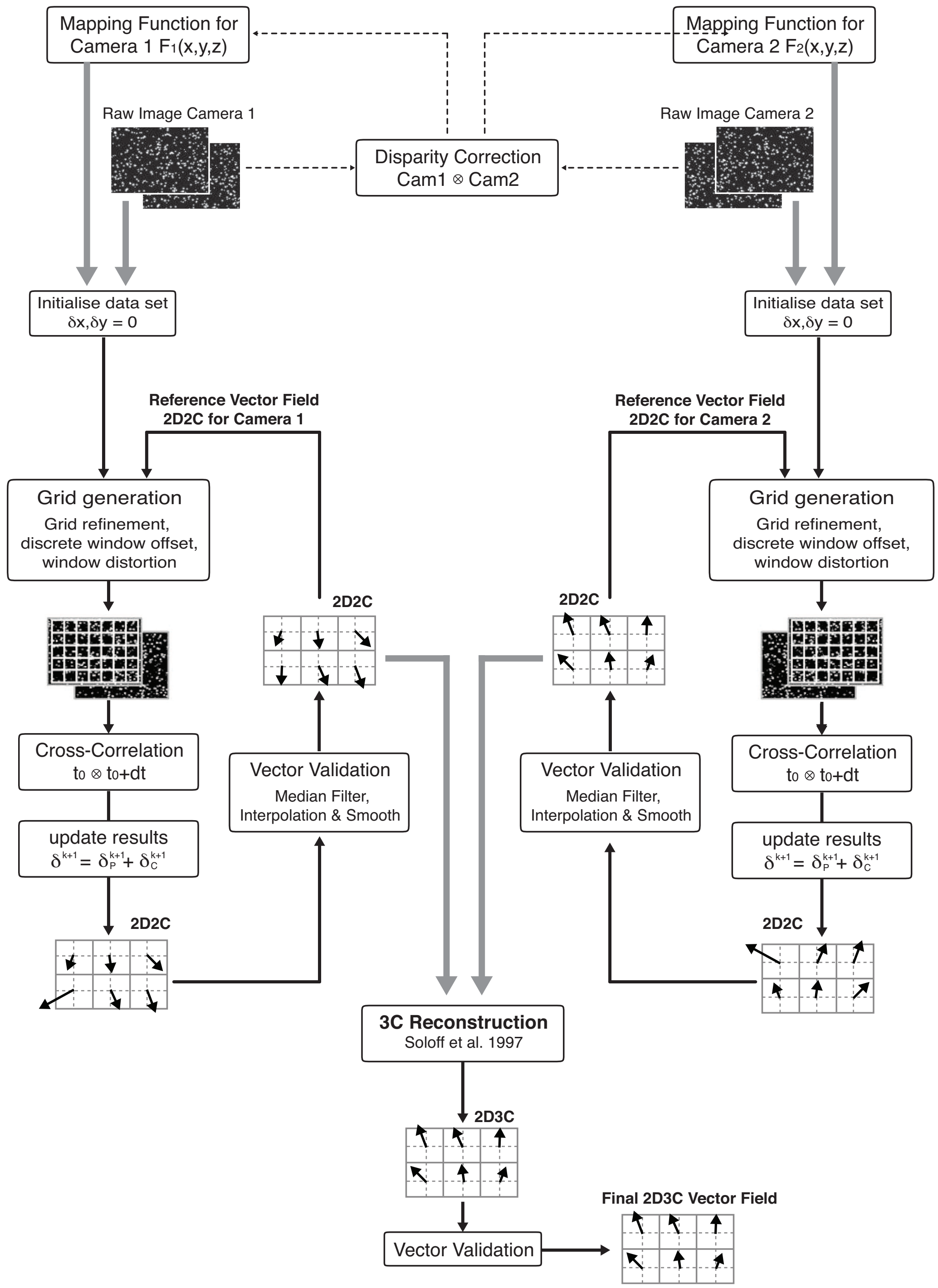

Figure 3.14 SPIVCC algorithm: Flow chart for stereo PIV vector calculation

3.6.3 Validation and Errors

Since the development and application of the PIV and stereo-PIV technique is new to the University of Canterbury, a rigorous validation of the techniques is necessary. A validation based on synthetic data has already been presented in Section 3.5 and was used to verify the accuracy of the PIVCC algorithm.

A validation of the stereo-PIV methodology under more realistic conditions is presented in Appendix F. The measurement accuracy is dependent on the direction of motion and the error analysis indicates absolute errors of 0.4% and 0.5% due to in-plane and out-of-plane motion, respectively. Since the out-of-plane component is dependent on the accuracy of the in-plane component, it typically experiences a larger error. Additionally, the accuracy of the out-of-plane component depends on the camera angle. For the present analysis, the camera angles are ±45 degrees, for which the two errors are of similar magnitude [Lawson and Wu, 1997a].

The accuracy of the object to image mapping function can be estimated by the mapping error. The largest RMS mapping error is measured at 0.21 pixel, which corresponds to a nominal error[3] of 0.0156mm in the object plane.

[3]Note that the nominal error in object space is dependent on the camera magnification, which varies across the image. In image space the error remains constant at 0.21 pixel

Chapter 4

Wall Shear Stress Measurement Techniques

The role of wall shear stress (WSS) in the pathology of cardiovascular disease has been discussed in Chapter 1 and while its significance as an important haemodynamic indicator is well accepted, it is a notoriously difficult quantity to determine experimentally [Poelma et al., 2008]. Therefore, this chapter deals with the experimental determination of WSS in complex physiological models using planar digital PIV. A short review of commonly used techniques is provided in the first part before the problem of near-wall PIV is introduced and discussed. In the second part, a novel interfacial PIV technique is developed to overcome some of the inherent shortcomings of the previous techniques and to enable the accurate measurement of WSS along curved surfaces. The chapter concludes with a numerical assessment of the measurement uncertainties of the new technique and provides some recommendation for the optimal design of future experiments.

4.1 Introduction

Conventionally, *in vivo* wall shear stress (WSS), τ_w is estimated on the basis of a Poiseuille flow assumption by measuring the blood flow rate Q, the lumen radius a and the whole-blood viscosity μ^* [Reneman et al., 2006].

$$\tau_w = \mu^* \frac{4Q}{\pi a^3} \tag{4.1}$$

Obviously, expression (4.1) constitutes a significant simplification of the true WSS and its validity in cardiovascular flows can be debated, particularly in cases of pulsatile flow and vessel curvature. Therefore, the shear stress, τ can be expressed in more general terms as a function of shear rate, $\dot{\gamma}$ and blood viscosity, $\mu(\dot{\gamma})$, which in turn depends on shear rate itself (see Section 2.2).

$$\tau = \mu(\dot{\gamma})\dot{\gamma} \tag{4.2}$$

In Cartesian coordinates, the shear rate at a given point in the flow is derived from the rate of deformation tensor $\mathbf{E}$

$$\mathbf{E} = \frac{1}{2}[(\nabla\mathbf{u}) + (\nabla\mathbf{u})^T] \tag{4.3}$$

with $\nabla\mathbf{u}$ representing the velocity gradient tensor

$$\nabla\mathbf{u} = \frac{\partial u_{ij}}{\partial x_{i,j}} \tag{4.4}$$

The physical coordinates and velocities are defined as $\mathbf{x} = (x, y, z)$ and $\mathbf{u} = (u, v, w)$, with (x, z) being the wall-parallel directions and y the wall normal direction. For incompressible flow with no-slip, the deformation tensor $\mathbf{E}$ significantly simplifies and the local wall shear rate (WSR) can be expressed as:

$$\dot{\gamma}_w = \left[\left(\frac{\partial u}{\partial y}\right)^2 + \left(\frac{\partial w}{\partial y}\right)^2\right]^{\frac{1}{2}}\Bigg|_{y=0} \tag{4.5}$$

with the local WSS following readily from Equation 4.2. Not that Equation 4.5 eliminates the assumptions of Poiseuille flow, however, requires detailed velocity information close to the wall in order to estimate the spatial derivatives in streamwise and spanwise direction.

The measured *in vitro* WSS can be related to *in vivo* values by using the Buckingham Pi Theorem and Reynolds number scaling (Chapter 2.2.3).

$$\tau_{w,b} = \frac{\rho_b}{\rho_f}\left(\frac{\mu_b D_f}{\mu_f D_b}\right)^2 \tau_{w,f} \tag{4.6}$$

The subscripts b and f refer to the respective blood and working fluid properties, and D to the vessel diameter.

Estimating WSR from PIV data is difficult, particularly in complex geometries such as in the carotid artery, and often only the streamwise component can be resolved (i.e., planar PIV). The complete WSR tensor can only be measured with dual-plane stereoscopic or volumetric PIV techniques. In principle, the field of velocity gradients can be obtained by discrete or analytical differentiation of the measured velocity field. To determine WSR (and subsequently WSS), it is necessary to compute Equation 4.5 in the vicinity of the wall. However, imaging errors (optical distortions, light reflections and low tracer density near the wall) and systematic errors (peak fitting algorithm, image interpolation, etc.) can cause signal truncation and greatly affect the performance of conventional PIV near interfaces. These errors are further compounded when computing velocity derivatives and even for well-executed PIV experiments this can lead to substantial uncertainties in the velocity derivatives [Luff et al., 1999]. Understanding these limitations is imperative for accurate velocity and velocity gradient measurements near stationary walls. Therefore, the first part of this chapter provides a discussion of near-wall PIV velocity error together with an assessment of some conventional discrete and analytical derivative operators.

To overcome the aforementioned limitations in near-wall PIV, the current literature proposes several strategies including adaptive correlation schemes [Theunissen et al., 2008] or interface treatment via image parity exchange [Tsuei and Savas, 2000]. Also, direct techniques, which do not rely on the prior estimation of the velocity field for WSR estimation, exist and include shear stress sensitive films [Amili et al., 2009] and micro-pillars [Große et al., 2008], long-distance micro-PIV imaging [Kähler et al., 2006] and PIV interface Gradiometry [Nguyen and Wells, 2006a].

To further expand the capacity of WSR estimation using PIV, the second part of this chapter introduces a new interfacial PIV (iPIV) technique to directly evaluate the near wall velocity gradient from the recorded particle images. This method readily facilitates WSS measurements along curved walls and does not require prior estimates of the velocity field and hence propagation of the velocity error. The iPIV technique is particularly well suited for the investigation of arterial WSS and its performance and uncertainty under the current experimental conditions will be assessed.

4.2 PIV near Interfaces

4.2.1 Problem Statement

When performing PIV measurements near interfaces, one is confronted with a number of difficulties including non-uniform image properties in wall-normal direction and strong light reflections, which are often more intense than the individual particle images. Under these circumstances, the velocity estimation via cross-correlation is adversely affected, leading to increased measurement uncertainty and systematic bias. Additionally, the presence of strong velocity gradients at no-slip interfaces and a lack of seeding particles in the near wall region further degrade the cross-correlation operation.

An example of the resulting distortion in the correlation map due to the presence of an interface is shown in Figure 4.1 using a synthetic image pair of type III. The interface delimits the region where particles are present from the background or no-flow region. The correlation map is dominated by the auto-correlation of the interface with the true displacement peak embedded within the rim and surrounded by additional high-intensity noise. This decreases the peak detection probability and can lead to erroneous displacement estimates near the wall, either biased towards the origin or even via false peak detection.

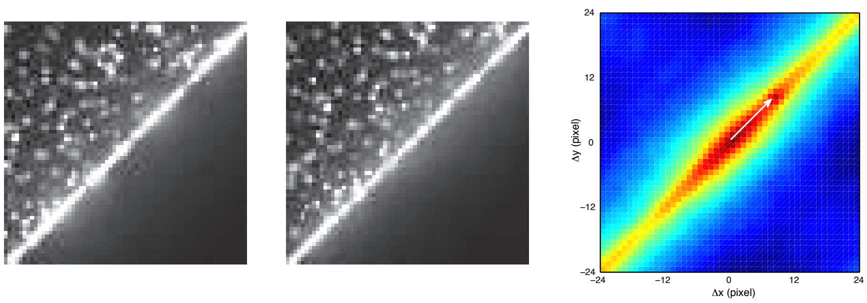

(a) (b) (c)

Figure 4.1 Synthetic particle image pair of type III (a,b) with corresponding correlation map (c). White arrow indicates true tracer displacement of $\Delta x = \Delta y = 8$ pixels

In typical PIV experiments, the interface region is either characterised by an opaque-diffusive or reflective surface (e.g., metallic surfaces, glass or silicone model, ect.). In the first case, the image intensity across the interface drops, causing a step-like discontinuity, while in the latter case, differences in refractive index between the fluid and interface cause strong light reflections and image flare. Following Theunissen et al. [2008], this signal truncation and reflection across the interface can be modelled with a step, S and a top-hat function T, respectively.

Using this model and recalling the expression for the particle intensity distribution (Eq. 3.8), the recorded image intensity, I, affected by truncation and reflection can be decomposed as following:

$$I \approx (I^o \cdot S) + k_B \cdot S + k_R \cdot T \tag{4.7}$$

where the first term models the truncation of the particle images due to the interface and the last two terms represent the truncation in background noise, k_B and the presence of reflections, k_R. Additionally, the scaling parameters k_B and k_R can be time-dependent if the reflections and background intensities vary between the individual recordings.

With the above expression, the cross-correlation between the two exposures I_a and I_b can be estimated as the correlation of each individual term in Equation 4.7 and its respective cross-terms, i.e.,

$$\begin{aligned} I_a * I_b \approx & \underbrace{(I_a^o \cdot S) * (I_b^o \cdot S)}_{cross-correlation} + \underbrace{k_B^2 \cdot (S * S) + k_R^2 \cdot (T * T)}_{auto-correlation} \\ & + \underbrace{k_B \cdot ((I_a^o + I_b^o) \cdot S) * S + k_R \cdot ((I_a^o + I_b^o) \cdot S) * T + 2 \cdot k_B k_R \cdot (S * T)}_{cross-terms} \end{aligned} \tag{4.8}$$

The distortion in the correlation map is caused by the cross-correlation of the truncated signal $(I^o \cdot S)$ and the auto-correlation of the DC components (i.e., S and T). The extent of the distortion depends on the prominence of the signal truncation, which has its maximal amplitude at the origin of the interrogation window. Hence, the measured displacement will be biased towards zero and in its worst case will be severely in error due to a false peak detection. See Theunissen et al. [2008] for more details on this aspect and for a graphical presentation of Equations 4.7 and 4.8.

If the coefficients k_B, k_R and the extend of the interface are estimated prior to the cross-correlation, the influence of reflections and background truncation could be minimised, correcting the cross-correlation operation to

$$I_a * I_b \approx (I_a^o \cdot S) * (I_b^o \cdot S) \tag{4.9}$$

Possible means to estimate the coefficients and interface location are background intensity characterisations, such as image subtraction and manual or morphological operations (i.e., edge detection, moving contours, ect.). However, the signal truncation $(I^o \cdot S)$ cannot be corrected by simple image pre-processing operations, but must instead be dealt with by adequate cross-correlation methods such as mask exclusion techniques [Gui et al., 2003; Theunissen et al., 2008].

Additionally, the interface also introduces a positional error in the vector location. When the interrogation windows overlap with the interface, the centroid of the measurement area is shifted away from the centre of the interrogation window into the flow domain. Therefore, attributing the vector origin to the centre of the interrogation window is no longer suitable, introducing further biasing [Hochareon et al., 2004; Buchmann and Jermy, 2007].

In summary, the following problems are identified as crucial for PIV measurements and subsequent WSR estimation near stationary and moving interfaces:

(a) signal truncation and spurious light reflections at the interface
(b) velocity bias and positional errors
(c) increased measurement uncertainty
(d) insufficient wall-normal resolution due to the window averaging effect

In order to obtain a reliable estimate of the velocity field and velocity derivative near interfaces, it is crucial to minimise the velocity bias and increase the measurement certainty through proper signal processing operations. Thus, the remainder of this first section will address point (a) and (b) by means of image pre-processing and the vector-relocation technique. Furthermore, the propagation of the random velocity error, σ_u and the effect of insufficient wall normal resolution (i.e., point (d)) during WSR calculation by means of conventional velocity field differentiation is discussed.

4.2.2 Velocity Bias and Correction Methods

In the following, two different processing options will be evaluated regarding their effectiveness in enhancing the velocity estimation near interfaces. For this purpose, Monte Carlo simulations are carried out using synthetic particle images of type III (see Appendix D.2), with a mean particle diameter of 2 pixel, a seeding density $C = 0.08$ ppp and mean background noise of 5%.

Image Pre-Processing

Assuming no temporal fluctuation in image intensities (except tracer particle movement), time-averaged image subtraction (see Appendix C) is in principle sufficient to remove the truncation and reflection terms k_B and k_R in Equation 4.7. This results in an almost complete removal of the reflection and noise truncation with the remaining intensity distribution containing only the signal truncation as shown in Figure 4.2(b,e) for the case of minimal background subtraction. However, in the case of time-depended coefficients k_B and k_R, minimum background subtraction is unable to completely remove the interface noise, resulting in only a marginal reduction of the auto-correlation terms (Fig. 4.2(c,f)). Conversely, mean background subtraction almost completely removes the auto-correlation terms, even in the case of time-varying noise terms as demonstrated in Figure 4.2(g,h).

A similar behaviour is observed for real particle images as illustrated in Figure 4.3, which is similar to that reported by Theunissen et al. [2008], but with the mean background subtraction being more effective in the present study. A comparison of the resulting bias error and RMS uncertainty is shown in Table 4.1 for both, synthetic and real images.

Vector Relocation

Traditionally, the obtained displacement vectors are attributed to the centre of the interrogation windows. However, if the centre of the interrogation window (IW) coincides with the interface, the obtained non-zero displacement estimate (located at the IW centre) is erroneous. This problem is of particular concern in the case of no-slip boundaries and has been discussed previously by Tsuei and Savas [2000] who proposed a reflection of the original particle image

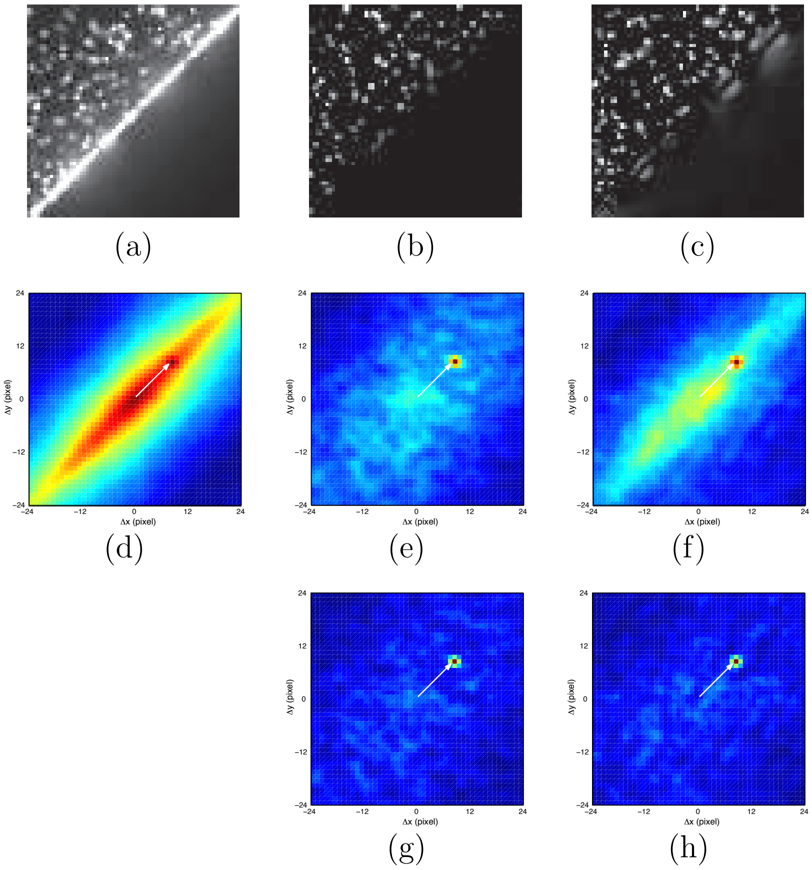

Figure 4.2 Typical correlation maps for type III images with inclined interfaces at 45^o and constant (*middle*) and varying reflection and flare (*right*). (a-c) raw and pre-processed images; (d) correlation map without pre-processing; (e-f) minimum background subtraction; (g-h) mean background subtraction. True displacement peak indicated by arrows

across the interface to artificially extend the image and thereby removing the signal truncation. If the direction of the reflected images is also reversed, an additional no-slip condition is imposed. While this approach is rather computationally intensive, an alternative approach, particularly for irregular boundaries, is to simply relocate the displacement vector to the centroid of the interrogation window contained within the flow region [Hochareon et al., 2004; Buchmann and Jermy, 2007; Theunissen et al., 2008]. Thus, the problem reduces to a proper repositioning of the vector representing the particles' ensemble displacement.

In order to assess the effects of vector relocation and wall-normal resolution, a simulated Womersley velocity profile, typical for oscillating flow in straight pipes and arterial bifurcations, is investigated. The profile is defined in Equation 4.10, where ζ and Λ are complex variables related to the wall-normal coordinate and the non-dimensional frequency Ω, respectively. J_0 is the zero-order Bessel-function, U_0 the maximum velocity of 10 pixels, $t/T = 0.525$ and $\Omega = 7$.

$$u_\phi(y,t) = -\frac{4}{\Lambda^2} U_0 \left(1 - \frac{J_0(\zeta)}{J_0(\Lambda)}\right) e^{i\omega t} \tag{4.10}$$

A single cross-correlation pass is performed using a 32 pixel interrogation window and the effect of overlapping windows is studied by progressively varying the wall overlap ratio (WOR) between -1 to +1. Results are shown in Figure 4.4 together with the reference response of a moving average (MA) filter of equal size and overlap. Without vector relocation, the maximal attainable overlap between interrogation window and interface is 50%. For higher WORs, the geometric centre of the window lies outside the flow domain, in which case the displacement is set to zero to satisfy the no-slip condition. This causes a

Table 4.1 Displacement and RMS error after application of different background subtraction schemes for type III synthetic images shown in Figure 4.2 with 8 pixel imposed displacement and 45^o interface inclination and real images shown in Figure 4.2. Images processed with single cross-correlation pass and 65 pixels interrogation window

Pre-Processing method	Type III		Real Image	
	bias	*rms*	*mean*	*rms*
none	1.157	3.246	1.079	1.253
minimum back.	0.048	0.030	2.486	0.956
mean back.	0.015	0.022	2.804	0.812

values in [pixels]

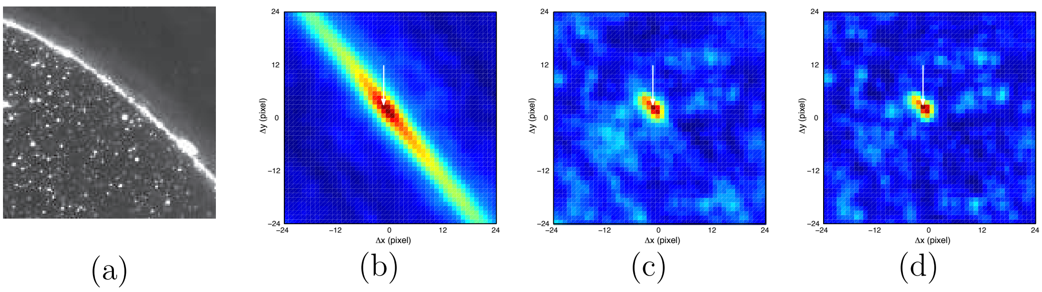

Figure 4.3 Correlation maps for a real image recoding with an interface inclination of approx. 45^o. (a) original particle image; (b) no pre-processing; (c) minimum background subtraction; (d) mean background subtraction

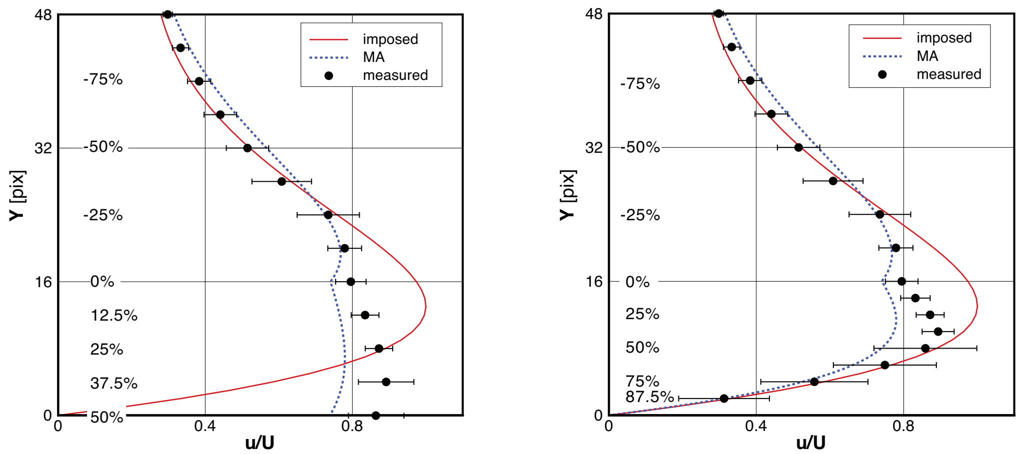

(a) (b)

Figure 4.4 Measured displacements for an imposed Womersley velocity profile applied to a synthetic image of type II. Single cross-correlation step with a 32 pixels interrogation window and different wall overlapping ratios (WOR). (a) Vector position in the geometric centre of the interrogation window; (b) relocation of the vector to the centroid of the seeded area. Horizontal bars correspond to a 95% confidence interval

strong discontinuity in the near-wall velocity profile, which is also depicted by the MA response. More accurate displacement estimates are obtained when the displacement vector is relocated to the centroid of the window containing the flow information. This permits WOR exceeding 50%, however, only at the expense of increased measurement uncertainty due to the reduced number of particles contributing to the correlation sum. Nevertheless, the obtained values follow the imposed velocity profile more closely and the discontinuity near the wall is resolved.

4.2.3 Wall Shear Rate Estimation using Velocity Derivatives

In order to obtain the velocity derivatives in Equation 4.5 from PIV velocity field data, the current literature proposes several techniques. The first one, and probably most commonly used technique, is based on discrete differential operators applied to neighbouring grid points. These include first-order forward/backward differences [Hochareon et al., 2004], second- and higher-order centred differences [Foucaut and Stanislas, 2002], Richardson extrapolation [Lourenco and Krothapalli, 1995], least-squares methods [Raffel et al., 1998] as well as eight-point circulation approaches [Luff et al., 1999]. A comprehensive summary of these methods is for example provided by Foucaut and Stanislas [2002].

An alternative technique to the above methods is based on fitting an analytical function to the discrete velocity field and subsequent analytical differentiation to obtain the local velocity derivative. This approach is often used for LDV data [Durst et al., 1996; Fatemi and Rittgers, 1994], but can also be applied in PIV by means of quadratic [Buchmann and Jermy, 2007] or bi-quadratic [Fouras and Soria, 1998; Elsinga et al., 2007] polynomial least-squares fits.

A third group of techniques used for estimating velocity derivatives are radial basis functions, which provide a robust method for estimating near-wall velocity gradients particularly for noisy velocity field data [Karri et al., 2009].

However, the use of the above derivative operators requires an accurate determination of the velocity field, which for example can be achieved by improving the sub-pixel displacement measurement using advanced interrogation techniques such as window shifting, window deformation or ensemble correlation (see Section 3.4 for more detail). Nevertheless, the numerical velocity field differentiation suffers from error propagation and numerical truncation errors. Common to all methods is their sensitivity to the random velocity error, velocity field sampling resolution and correlation window size (i.e., spatial resolution) and the truncation of the velocity field curvatures to linear displacement approximation in PIV [Raffel et al., 1998].

In the following section, the noise amplification, resolution sensitivity and amplitude responses of some discrete and analytical differential operators are investigated. The operators under consideration are the discrete forward differences (FD), second and sixth order centred differences (CD), fourth order Richardson extrapolation (RE) with and without noise optimisation, least square operator and third and fifth order polynomial least-squares fit. The following analytical concept is illustrated for the centred difference scheme only, but is applicable to all differential operators and is outlined in full in Appendix G.

The velocity derivative at the wall ($j = 1$) estimated with a centred difference scheme of order n is expressed as follows:

$$\left.\frac{\partial u}{\partial x}\right|_{j=1} = \frac{1}{a\Delta x}\sum_{i=1}^{n/2} 2a_i u_{j+1} + \sum_{i=n+1}^{\infty} \alpha_i \frac{\Delta x^{i-1}}{i!}\left.\frac{\partial^i u}{\partial x^i}\right|_j + \epsilon\frac{\sigma_u}{\Delta x} \tag{4.11}$$

where the velocity field has been extended across the interface by reflecting reversing its direction to impose the no-slip condition, i.e., $u_{j+1} = -u_{j-1}$ [Tsuei and Savas, 2000]. The grid spacing of the velocity field is denoted with Δx and the values of a and α_i, obtained from Foucaut and Stanislas [2002] are summarised in Table G.1. The second term on the right hand side of Equation 4.11 is the numerical truncation error and the last term is the noise term $\sigma_{\dot{\gamma}}$. This term represents the propagation of the velocity measurement noise σ_u in terms of the noise amplification coefficient ϵ, which is obtained via Monte Carlo simulation and also listed in Table G.1.

Following Fouras and Soria [1998], a dimensionless noise transmission factor λ_0, describing the propagation of the random velocity error in the shear rate measurement can be defined as follows:

$$\lambda_0 = \frac{\sigma_{\dot{\gamma}}\Lambda}{U_{ref}} \cdot \frac{U_{ref}}{\sigma_u} = \Lambda\frac{\sigma_{\dot{\gamma}}}{\sigma_u} \tag{4.12}$$

where U_{ref} is a characteristic velocity and Λ the characteristic spatial wavelength. Substituting the expression for $\sigma_{\dot{\gamma}}$ into Equation 4.12, the dimensionless noise transmission factor is expressed as:

$$\lambda_0 = \epsilon\frac{\Lambda}{\Delta x} \tag{4.13}$$

In order to validate this theoretical analysis, the velocity profile in Figure 4.4 is contaminated with random noise of 0.1 pixel (mean value) and the dimensionless noise amplification factor (Eq. 4.12) is calculated via Monte Carlo simulation for the various differential operators and compared with the theoretical prediction from Equation 4.13. Furthermore, the signal truncation (or fitting error for the analytical operators) is also assessed by analysing the individual amplitude responses using a noise-free simulation.

The results are summarised in Figure 4.5 as a function of the dimensionless spatial resolution $\Delta x/\Lambda$. For the discrete differential operators, the truncation error decreases for higher order approximations, while conversely, the noise amplification decreases for lower order operators. For example, the sixth order CD exhibits the best amplitude response but also a 52% larger noise amplification compared with the second order CD. Low noise amplification is obtained by the least squares approach and the noise optimised Richardson extrapolation (RE) yielding approximately 55% lower noise amplification compared to the second order CD. However, the amplitude response is also low. Note that the fourth order CD is mathematically identical to the fourth order RE and is therefore omitted here.

The analytical polynomial operators provide a significantly improved amplitude response over a wider range of spatial resolutions. Contrarily, the polynomial operators suffer from significant noise amplification, which is approximately one order of magnitude larger than that of the differential operators.

Characteristic for all operators is the increase in amplitude response for increasing spatial resolutions and conversely the decrease in noise amplification for decreasing resolutions. This means that a high amplitude response and low

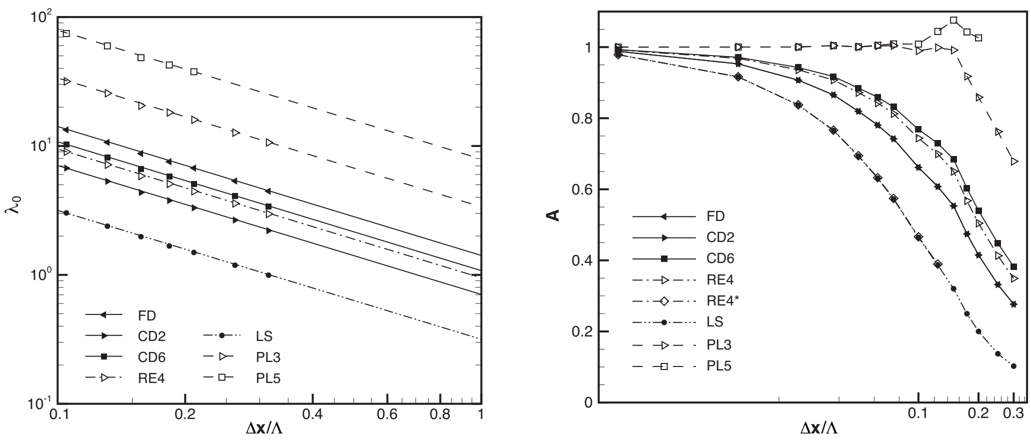

Figure 4.5 (a) Dimensionless noise transmission, λ_0 as a function of $\Delta x/\Lambda$ for various discrete and analytical derivative operators. The solid lines indicate the theoretical prediction of Equation 4.13. Symbols correspond to the numerical experiment of the velocity profile shown in Figure 4.4, contaminated with 0.1 pixel random noise. (b) Amplitude response using noise-free data for the same velocity profile. FD = forward differences, CD2 and CD6 = second and sixth order centred differences, RE4 = fourth order Richardson extrapolation, RE4* = RE4 with noise optimisation, LS = least squares, PL3 and PL5 = third and fifth order polynomial fit

measurement noise can only be obtained for velocity fields with high spatial resolution and low noise levels. The latter however, is difficult to achieve, as the random velocity error in PIV inevitably increases for smaller sampling sizes and higher grid resolutions (see Chapter 3.5).

4.2.4 Section Summary

Summarising the previous results, image pre-processing enables a substantial attenuation of interface reflections and consequently an increase in peak detection probability. Using appropriate vector relocation, the bias error can be further compensated, though only at the expense of increased measurement noise. It is the latter that is further propagated into the gradient estimation, increasing the measurement uncertainties in the WSR estimation proportionally.

However, these problems continue to remain if reflections and signal truncations cannot be accounted for properly and/or when the interface is not aligned with the pixel grid. Furthermore, reduced spatial resolution close to the wall remains the limiting factor in both velocity and gradient estimation and as such new approaches have to be thought of.

For example, to increase spatial resolution, Westerweel et al. [2004] proposed a single pixel resolution PIV technique based on ensemble correlation averaging (Section 3.4.2) and Theunissen et al. [2006, 2008] introduced an adaptive concept in which the interrogation window size varies according to interface proximity and seeding density. Alternatively, Nguyen and Wells [2006a] proposed a PIV interface Gradiometry method to directly measure the wall velocity gradient by shearing the interrogation windows parallel to the boundary, whereas Ruan et al. [2001] directly measured vorticity by using a pattern matching technique and particle image deformation. The latter two methods do not require pre-computation of the velocity field and therefore achieve higher measurement accuracy compared to velocity differentiation. Furthermore, these techniques can easily be extended to curved interfaces by, for example, using conformal transformation of the recorded particle images [Nguyen et al., 2006].

4.3 Interfacial PIV (iPIV)

This section describes a new technique, similar to PIV interface Gradiometry, to accurately measure the near wall velocity field and particularly WSR along no-slip interfaces. The technique uses a single pixel line cross-correlation approach to increase spatial resolution and conformal image transformation to facilitate measurements along curved interfaces.

4.3.1 Single Line Cross-Correlation

In the proximity of stationary interfaces, the flow can be assumed to closely follow the wall contours and thus the problem of near wall flow can be reduced to a 'quasi' one-dimensional problem. Furthermore, if the interface is horizontal and aligned with the CCD array, the tracer displacement in wall proximity can in principle be resolved by performing a one-dimensional cross-correlation between the two exposures and along horizontal pixel lines. The result of this operation is the wall parallel velocity profile with single pixel resolution in wall normal direction, i.e., no averaging in normal direction. In the following, the implementation of such a procedure is described in detail.

Denoting the pixel coordinates by (i, j) and recalling Equation 3.13, the cross-correlation between the image intensities along a horizontal line, i at a constant height, j can be expressed as:

$$C_{II}(x) = \sum_{i=1}^{M} I_a(i,j) I_b(i+x,j) \tag{4.14}$$

and normalised by the auto-correlation coefficients as:

$$\hat{C}_{II}(x) = \frac{\displaystyle\sum_{i=1}^{M}(I_a(i,j) - \overline{I}_a)(I_b(i+x,j) - \overline{I_b})}{\left[\displaystyle\sum_{i=1}^{M}(I_a(i,j) - \overline{I}_a)^2 \sum_{i=1}^{M}(I_b(i,j) - \overline{I_b})^2\right]^{1/2}} \tag{4.15}$$

where $\overline{I}_a$ and $\overline{I_b}$ are the mean intensities on each pixel line for the first and second exposure. The 1D, wall parallel correlation function $C_{II}(x)$ is evaluated at each horizontal pixel line and subsequently grouped to produce a correlation map $R_{U,y}$ on axes of the horizontal (i.e., wall parallel) displacement U and the vertical (i.e., wall normal) coordinate y. Correlation peaks in $R_{U,y}$ occur at heights y with strong tracer signals and lie at horizontal positions that correspond to the tracer displacement. Figure 4.6 summarises this procedure applied to a synthetic particle image pair with an imposed velocity profile given in Equation 4.10.

Using the normalised correlation function (Eq. 4.15) will increase the correlation signal of weaker particles and produce a more consistent correlation peak profile as shown in Figure 4.6(d). However, this will also amplify the measurement noise, which is particularly crucial in cases of low signal-to-noise (e.g., low seeding density). Prior to the cross-correlation, the particle images are also interpolated to sub-pixel resolution to reduce the peak locking effect [Raffel et al., 1998], which can be significant for small particle displacement. Multigrid and multipass operations (Section 3.4.1) can also be applied during the cross-correlation operation, but their effect is small due to the already relatively small displacement encountered in the wall proximity.

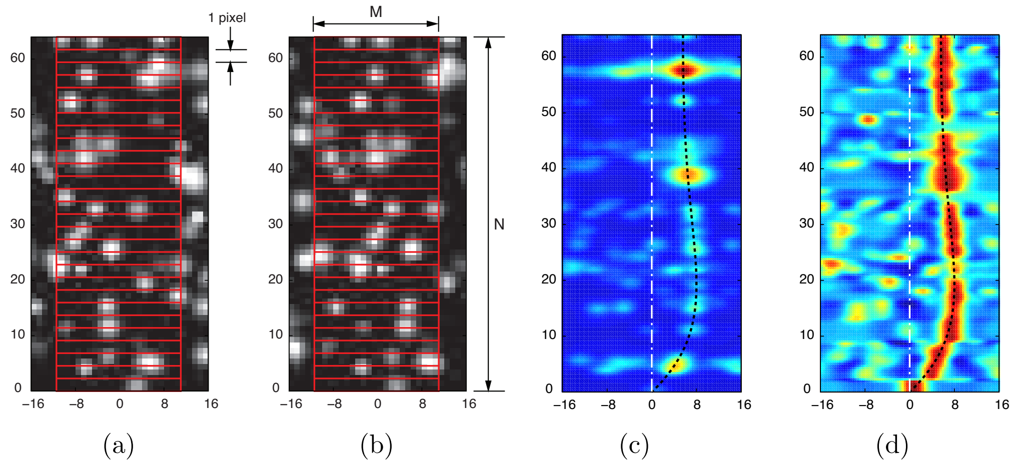

Figure 4.6 Line correlation, (a-b) interrogation windows/lines for the 1^{st} and 2^{nd} exposure; (c) instantaneous correlation map, $R_{U,y}$ composed from individual 1D cross-correlation functions. Note, peaks lie on the same position as the displacement profile (solid line); (d) normalised correlation map

Lastly, it should be noted that the above approach is only valid if the wall-normal displacement of tracer particles is less than their particle diameter. For larger displacements, the tracer particles leave the pixel line in the second exposure, resulting in loss of signal. In this sense, very similar considerations to those in traditional 2D PIV should be made, particularly with regards to the maximum tracer displacement (i.e., time separation) and seeding density.

4.3.2 Wall Shear Rate Estimation

This section describes the direct extraction of WSR and tangential velocity profiles from the computed correlation map. While this procedure is demonstrated here for the normalised correlation map (Eq. 4.15) $\hat{R}_{U,y}$ only, the same procedure can also be applied for the non-normalised cross-correlation function, $R_{U,y}$ or its ensemble time average, $\overline{R}_{U,y}$ [Buchmann et al., 2008].

Assuming no-slip, $U(0) = 0$, the velocity gradient at the wall can be extracted by fitting a straight line through the correlation peaks as shown in Figure 4.7(a). The fit is obtained by 'sweeping' the line L through the correlation map and computing the Gaussian weighted sum of correlation values to:

$$F(grad(y)) \equiv \frac{\sum_{y=-N}^{N} \hat{R}_{U,y} \cdot \Omega(y)}{\sum_{y=-N}^{N} \Omega(y)} \tag{4.16}$$

where the correlation map has been reflected around $(U = 0, y = 0)$ to impose the no-slip condition. The Gaussian weighting function $\Omega(y)$ is centred at the current wall normal position, n and given as:

$$\Omega(y) = exp\left[-\frac{(y-n)^2}{2\sigma^2}\right] \tag{4.17}$$

where $2\sigma^2$ is the spread of the Gaussian function. Weighting the correlation peaks as a function of wall normal distance acts like a filter to reduce the measurement uncertainty and to increase robustness by preventing detection of spurious or very strong peaks further away. Subsequently, the velocity gradient at the wall $\partial u/\partial y$ is found as the slope of the line for which the functional $F(grad(y))$ is maximal. Hence, the WSR is given as:

$$\left(\frac{\partial u}{\partial y}\right)\Bigg|_{y=0} = max\{F(grad(0))\} \tag{4.18}$$

Compared to the conventional PIV method with subsequent differential gradient estimation, the iPIV provides a direct estimate of the WSR, which is independent of the spatial resolution of the velocity field and its uncertainty.

Using the above gradient estimation, the wall parallel velocity profile can also be found via integration of the velocity gradient in wall normal direction.

$$u(n+1) = u(n) + \left(\frac{\partial u}{\partial y}\right)\Bigg|_{n} \tag{4.19}$$

Equation 4.19 is computed at one pixel increments, yielding the best possible spatial resolution in wall normal direction. At each step n, the velocity gradient is estimated according to Equations 4.16 to 4.18 and the incremental velocity profile is computed as shown in Figure 4.7(b). This incremental approach provides a more robust estimation of the velocity profile compared to other line-fitting procedures such as weighted Gaussians or least-squares [Nguyen and Wells, 2006a].

The fitted velocity profile is shown in Figure 4.7(c) as well as a comparison of velocity profiles computed for different weighting parameters σ. As can be seen in Figure 4.7(d-e), small values of σ introduce small-scale noise, while large weighting values provide a smoother velocity profile, but tend to underestimate the large gradient. The optimal choice for σ depends primarily on the seeding density and the spatial wavelength (i.e., shape) of the velocity profile and will be discussed in more detail in the next sections.

If the no-slip condition is not satisfied, the velocity integration can start from the top of the correlation map towards the slip interface, or for a known interface velocity, Equation 4.19 can be modified to take an initial velocity at $y = 0$ into account.

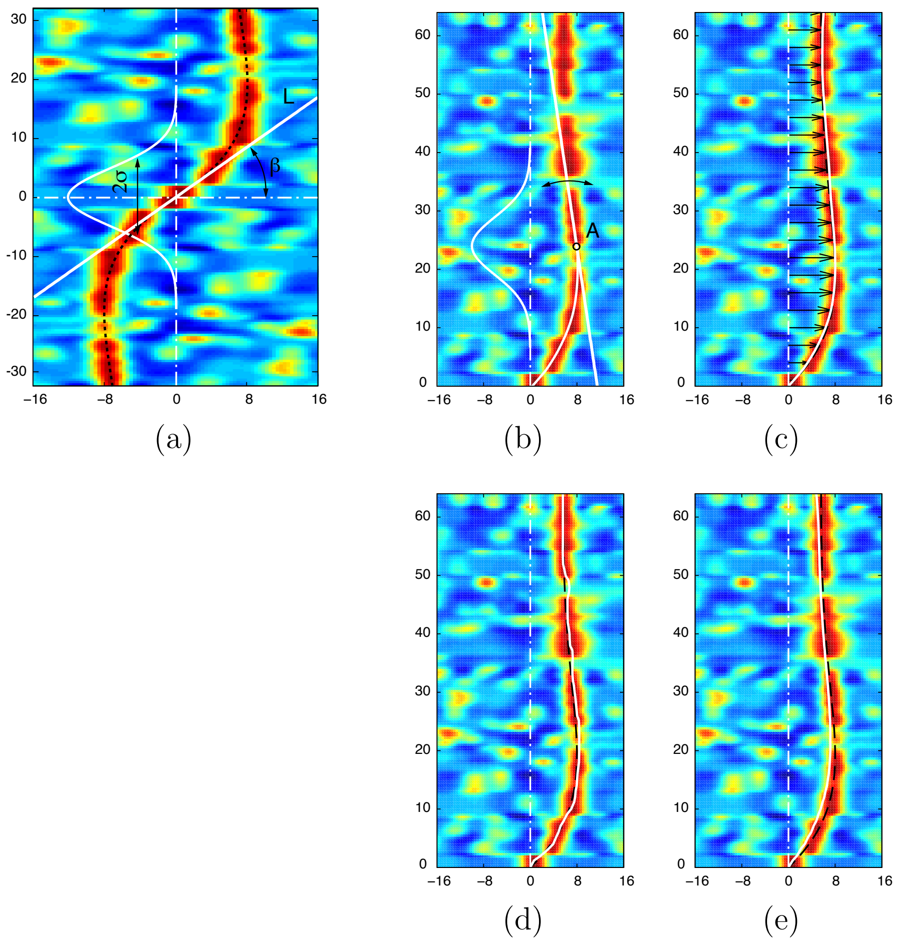

Figure 4.7 Wall shear rate (WSR) and velocity profile estimation using the normalised 1D correlation map, $\hat{R}_{U,y}$: (a) original and inverted correlation map for WSR estimation. The line L is swept through the domain and the Gaussian weighted sum of correlation values is computed for each angle, β; (b) velocity profile integration by repeating the previous step to find the local velocity gradient; (c) fitted velocity profile (white) compared with the imposed velocity distribution (black arrows), $\sigma = 5$; Comparison of Gaussian weighting parameter (d) $\sigma = 1.5$ and (e) $\sigma = 10$

4.3.3 Application to Curved, No-Slip Interfaces

In the case of horizontal interfaces, the application of the 1D wall parallel cross-correlation function is straight forward and can be achieved by aligning the pixel rows (or columns) of the digital camera with the interface. However, for curved or irregular shaped interfaces (as used in the current study) this approach is not possible. In these cases, a detailed knowledge of the interface location is necessary to transform the data from the measurement coordinate system to a coordinate system aligned with the interface.

This is typically achieved by defining a local coordinate system, $(\tilde{x}, \tilde{y})$ aligned with the wall and decomposing the velocity field into its wall parallel and wall normal components to compute the local WSR via velocity differentiation [Poelma et al., 2008; Buchmann and Jermy, 2007]. However, as the local coordinate system can vary along the interface, it is sometimes more convenient to compute local flow properties on a Cartesian grid. This can be achieved by transforming the curved domain to a regular domain and subsequent reverse transformation of the computed variables. Such a procedure for the WSR computation via iPIV on curved or irregular shaped interfaces is outlined in the following and consists of four steps:

1. Identification of the interface location
2. Transformation of the curved, irregular domain into a rectangular domain via conformal transformation and image interpolation
3. Estimation of the WSR (and velocity profiles) in the rectangular domain via iPIV (see previous section)
4. Reverse transformation of measured WSR into the physical domain (i.e., curved interface)

Interface Identification

The interface can be identified using appropriate manual or morphological operations such as proposed in Nguyen et al. [2008a] and Burgmann et al. [2009]. To identify the wall interface in the present study, the recorded images are averaged to yield the time average background image of the flow domain. Individual tracer images are averaged out, while the wall interface becomes clearly visible due to light reflections along the interface. The wall interface is assumed to lie in the centre of the reflections and is tracked by manually fitting a piecewise spline. The fitted points are subsequently smoothed and resampled to yield the final interface coordinates. Note that an automated procedure based on the same principle is also possible, but not necessary. Figure 4.8(a) gives an example of the time averaged background image and the detected interface from experimental data of the flow through the internal carotid artery. The 95% confidence interval of the interface fit (i.e., ≈1 pixel) is indicated in the figure insert.

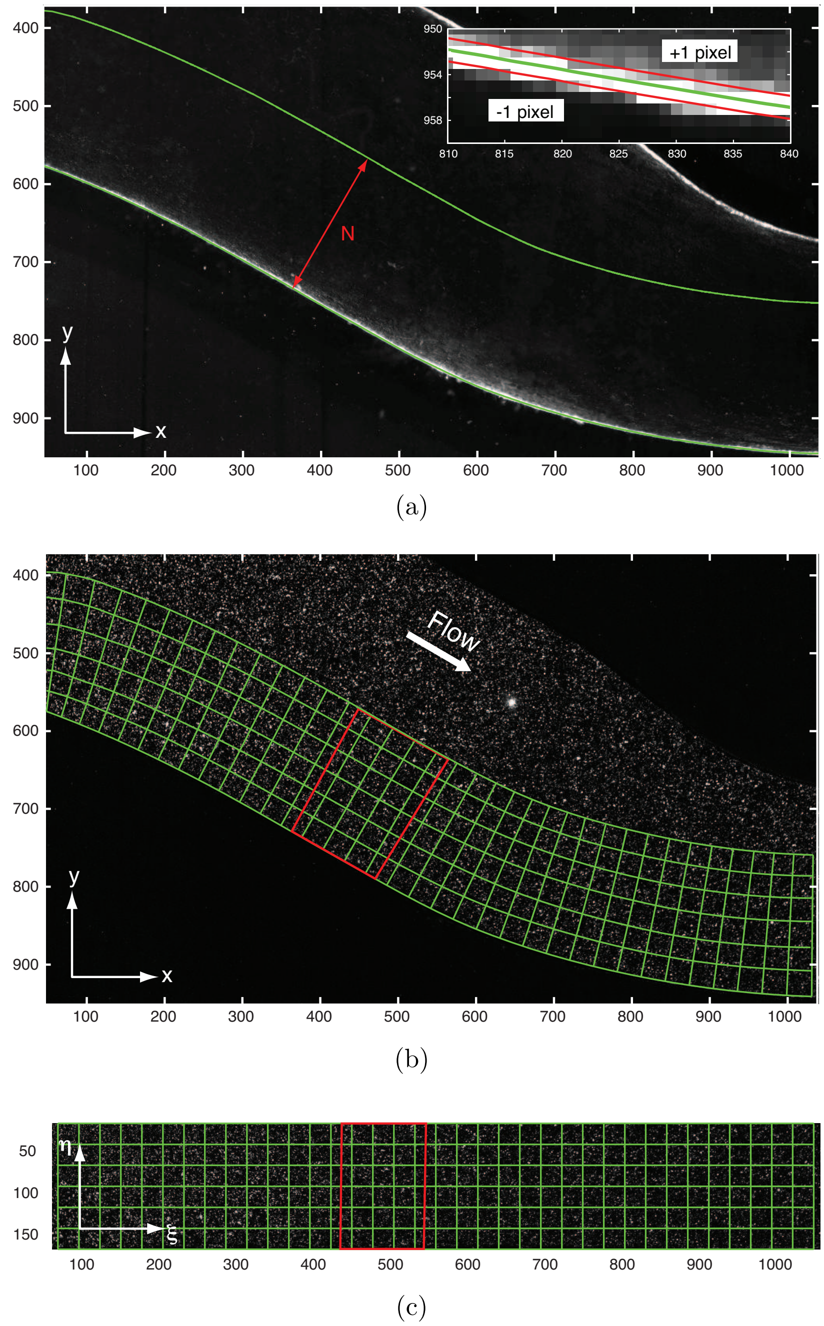

Figure 4.8 Conformal image transformation. (a) time-averaged background image with detected wall interface and near-wall region of height N. Figure insert indicates 95% confidence interval for wall detection; (b) orthogonal curvilinear grid in (x,y) space and interrogation window of size (M, N); (c) re-sampled near-wall image in transformed space (ξ, η)

Conformal Transformation of the Near Wall Region

Next, a wall region of constant wall normal height N (typically 80 pixels) is specified in physical coordinates (x, y) and conformal transformation is used to convert the near wall region to a rectangular image in transformed coordinates (ξ, η). The advantage of conformal transformation is that the orthogonality of the fluid domain is preserved during the mapping, which drastically simplifies the reverse transformation of the measured WSR into the physical domain.

The conformal transformation implemented in this work is based on a conformal mapping and grid generation algorithm developed by Ives and Zacharias [1987] and described in more detail in Nguyen et al. [2010]. In brief, the x and y coordinates of the flow domain are given by the solution of the following Laplace's equations:

$$\frac{\partial^2 x}{\partial \xi^2} + \frac{\partial^2 x}{\partial \eta^2} = 0 \tag{4.20}$$

$$\frac{\partial^2 y}{\partial \xi^2} + \frac{\partial^2 y}{\partial \eta^2} = 0 \tag{4.21}$$

which are solved with an iterative Poisson solver implemented in MATLAB to produce the orthogonal curvilinear grid shown in Figure 4.8(b).

The pixel intensities at the resulting grid points are interpolated at sub pixel locations using the previously described cardinal interpolation routine (Section 3.4.1). The result is a rectangular image in mapped coordinates as shown in Figure 4.8(c), which can be processed with the iPIV technique or conventional PIV and subsequent velocity differentiation to obtain the WSR in the transformed domain.

Reverse Transformation

The relationship between displacement in the image (or physical) domain (u, v) and the corresponding displacement in the conformal transformed domain (U, V) can be expressed as:

$$u = \frac{\partial x}{\partial \xi} U + \frac{\partial x}{\partial \eta} V \tag{4.22}$$

$$v = \frac{\partial y}{\partial \xi} U + \frac{\partial y}{\partial \eta} V \tag{4.23}$$

from which the coefficients characterising the coordinate transformation can be derived as:

$$g_\xi = \sqrt{\left(\frac{\partial x}{\partial \xi}\right)^2 + \left(\frac{\partial y}{\partial \xi}\right)^2} \tag{4.24}$$

$$g_\eta = \sqrt{\left(\frac{\partial x}{\partial \eta}\right)^2 + \left(\frac{\partial y}{\partial \eta}\right)^2} \tag{4.25}$$

For the current iPIV method, only the horizontal displacement component U is measured in the transformed domain (i.e., $V = 0$), which, in physical space, corresponds to the local wall parallel displacement $\tilde{u}$ in a coordinate system $(\tilde{x}, \tilde{y})$ aligned with the interface. Hence, the magnitude of the wall parallel displacement is expressed as:

$$\tilde{u} = U g_\xi \tag{4.26}$$

and consequently, the WSR in physical coordinates is obtained as:

$$\frac{\partial \tilde{u}}{\partial \tilde{y}} = \frac{\partial U}{\partial \eta} \frac{g_\xi}{g_\eta} \tag{4.27}$$

where $\partial U / \partial \eta$ is the WSR measured in the transformed domain.

4.4 Numerical Assessment of iPIV

In order to evaluate the interfacial PIV (iPIV) measurement accuracy, Monte Carlo simulations with synthetically generated particle images of fully developed steady and oscillatory pipe flow are carried out. The generated image pairs are of type III with the interface located at the bottom of the image, a mean particle image diameter of 2 pixels (0.5 pixel variance), seeding density of C=0.08 ppp and background noise of 8% ± 4%. Error statistics (Appendix D.1) are computed from 1000 individual realisations by systematically varying the wall shear gradient to assess the effects of Gaussian weighting, interrogation size (i.e., M) and sensitivity to errors in interface location.

4.4.1 Wall Shear Rate

Bias and RMS Error

As already illustrated in Figure 4.7(d-e), the width of the Gaussian weighting kernel, σ in Equation 4.17 directly affects the accuracy and robustness of the iPIV method and should be specified according to the seeding density and the desired resolution. Figure 4.9 illustrates the bias and RMS error for different values of σ and interrogation sizes M. Note that for a uniform flow such as here, changing the interrogation size has a similar effect as changing the seeding density. By changing the linear interrogation size M = [16, 32] pixel, the effective number of particles contributing to the 1D cross correlation are 1.3 and 2.6, respectively.

The bias error in estimated WSR shown in Figure 4.9(a) is between 0.01 to 0.2 pixel/pixel for a range of medium to high shear rates and processing parameters. For a given interrogation size M, the bias error increases nearly proportional with WSR and Gaussian weight σ. For shear rates larger than 1 pixel/pixel, the bias error flattens and tends to decrease again for smaller interrogation sizes, while for shear rates below 0.5 pixel/pixel, the bias error appears to be independent of the linear interrogation size.

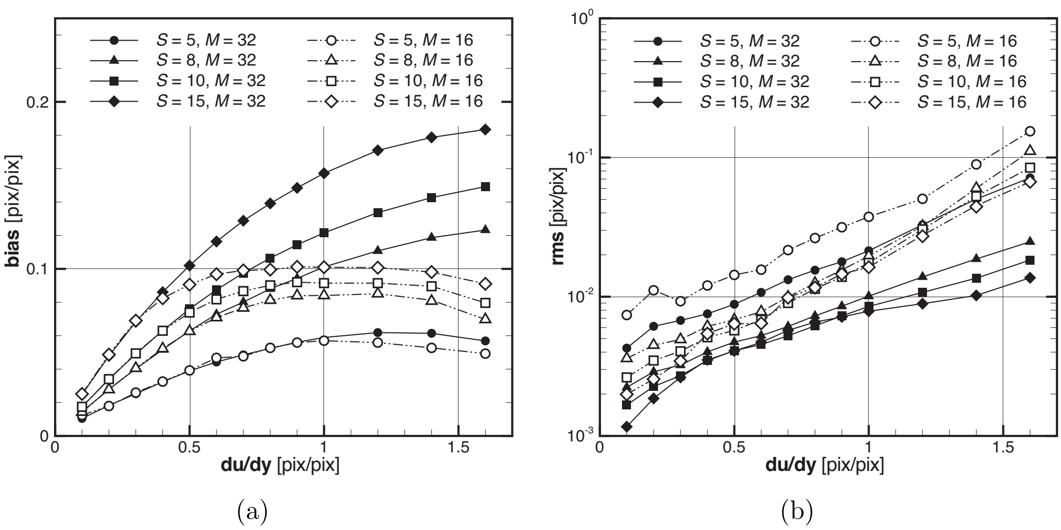

Figure 4.9 iPIV measurement uncertainty assessed by means of synthetic, type II particle images of a parabolic velocity profile ($\Lambda = 65$ pixel): (a) Bias error; (b) RMS error for different Gaussian weighting parameters S and linear interrogation size M

The RMS error varies between 10^{-3} and 10^{-1} pixel/pixel and exhibits very similar characteristics to those observed in conventional 2D PIV interrogation. This is an exponential increase in measurement uncertainty for large shear rates and a decrease for increasing sampling sizes M (due to the increased number of tracer particles). The effect of the Gaussian weighting on the RMS error is only minor and for larger values (i.e., $\sigma > 5$) the RMS error is nearly a function of shear rate and interrogation size only.

Single Wavelength Amplitude Response

The responses of the Gaussian weighting during the gradient estimation can be seen as a low pass filter that suppresses measurement noise on the one hand, but on the other hand attenuates higher frequency contents (i.e., high shear gradients). The latter can be compensated to some extent by choosing a smaller interrogation size, however only at the expense of increased measurement uncertainty. Due to the low pass filtering characteristics, the iPIV amplitude response and thus the optimal weighting is depended on the velocities' spatial wavelength Λ, similar to the differential operators in Section 4.2.3.

Therefore, to evaluate the response of the iPIV method to velocity distributions with a single wavelength, the WSR amplitude response for a one-dimensional sinusoidal displacement is studied. For this, a sinusoidal displacement amplitude $U_0 = [2, 4]$ pixels with several values of the spatial wavelength is considered $\Lambda = [8, 12, 16, 24, 32, 48, 64, 128]$ pixels. By varying the Gaussian weighting $\sigma = [5, 8, 10, 15, 20]$ and the spatial wavelength, the amplitude response diagram is obtained as a function of the normalised weighting parameter $\sigma^* = \sigma/\Lambda$ and shown in Figure 4.4.1.

The continuous line represents the best fit to the data points obtained for different linear interrogation sizes $M = [16, 32, 64]$ pixels. For values of $\sigma^* \gg 0.1$, the measurement is attenuated due to the low pass filtering and iPIV behaves similarly to the differential operators in Figure 4.5(b). However, the iPIV amplitude response is improved over a wider range of wavelengths. For large σ^*, the measurement is influenced by strong correlation peaks further away from the wall and consequently the estimated WSR is biased towards lower values. Contrarily, for small σ^*, the measurement is affected by outliers due to reduced tracer signal and additional wall noise closest to the wall (i.e., reflections, flares,

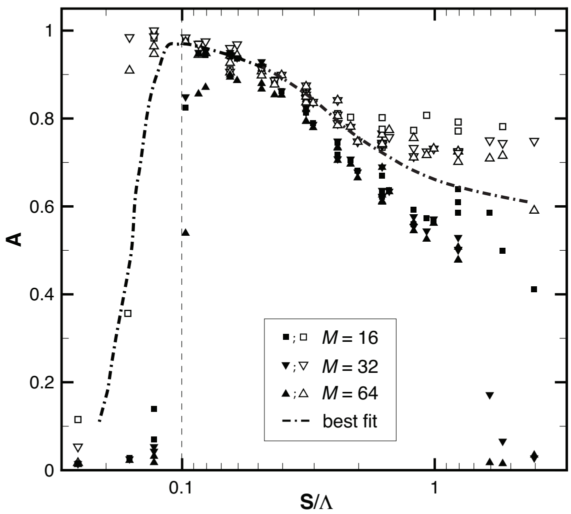

Figure 4.10 iPIV amplitude response as a function of the normalised Gaussian weight, $\sigma^* = \sigma/\Lambda$ and different linear interrogation sizes M

ect.). This effect can clearly be seen in the amplitude response, which drops markedly for $\sigma^* \ll 0.1$. The optimal amplitude response is obtained for normalised weights in the order of $\sigma^* = 0.1$, where the measured signal reaches almost 100% of the original signal.

Wall Sensitivity

The accuracy and sensitivity of iPIV with regards to an erroneous wall location is investigated by systematically varying the location of the wall interface by y_w = [-1:1] pixel. All simulations are carried out for a parabolic velocity profile with $\Lambda = 100$ pixel, $\sigma = 10$ and $M = 32$ pixel if not indicated otherwise, constituting nearly optimal iPIV conditions.

A summary of the bias error as a function of the WSR and the Gaussian weighting is given in Figure 4.11(a), while the bias error for different values of y_w is shown in Figure 4.11(b). Similarly to changing σ, the bias error also increases with shear rates and departure from the optimal wall location. This is particularly evident for wall location errors in excess of $\pm$ 1 pixel. As the wall is moved *into* the flow domain (+ values), the velocity profile is truncated near the wall and no longer fulfills the no-slip condition. As a consequence, the velocity at the wall is non zero resulting in an overestimation of the velocity gradient at the wall. Likewise, if the wall is moved *away* from the flow domain ($-$), the velocity gradient is underestimated.

Following an analysis from Nguyen et al. [2006], a normalised sensitivity $\tilde{S}$ of the estimated WSR to errors in wall location can be calculated as follows:

$$\tilde{S} = \frac{\Delta\left(\dfrac{\partial U}{\partial y}\right)\cdot\sigma}{\dfrac{\partial U}{\partial y}\cdot\Delta y_w} \tag{4.28}$$

where $\Delta(\partial U/\partial y)$ is the change in measured WSR caused by a change in wall position Δy_w over an interval of [-1;1] pixel and normalised by the imposed shear rate and Gaussian weight σ.

Normalised wall sensitivity is plotted in Figure 4.11(c) and shows an almost linear increase for increasing shear rates, but is nearly constant for different

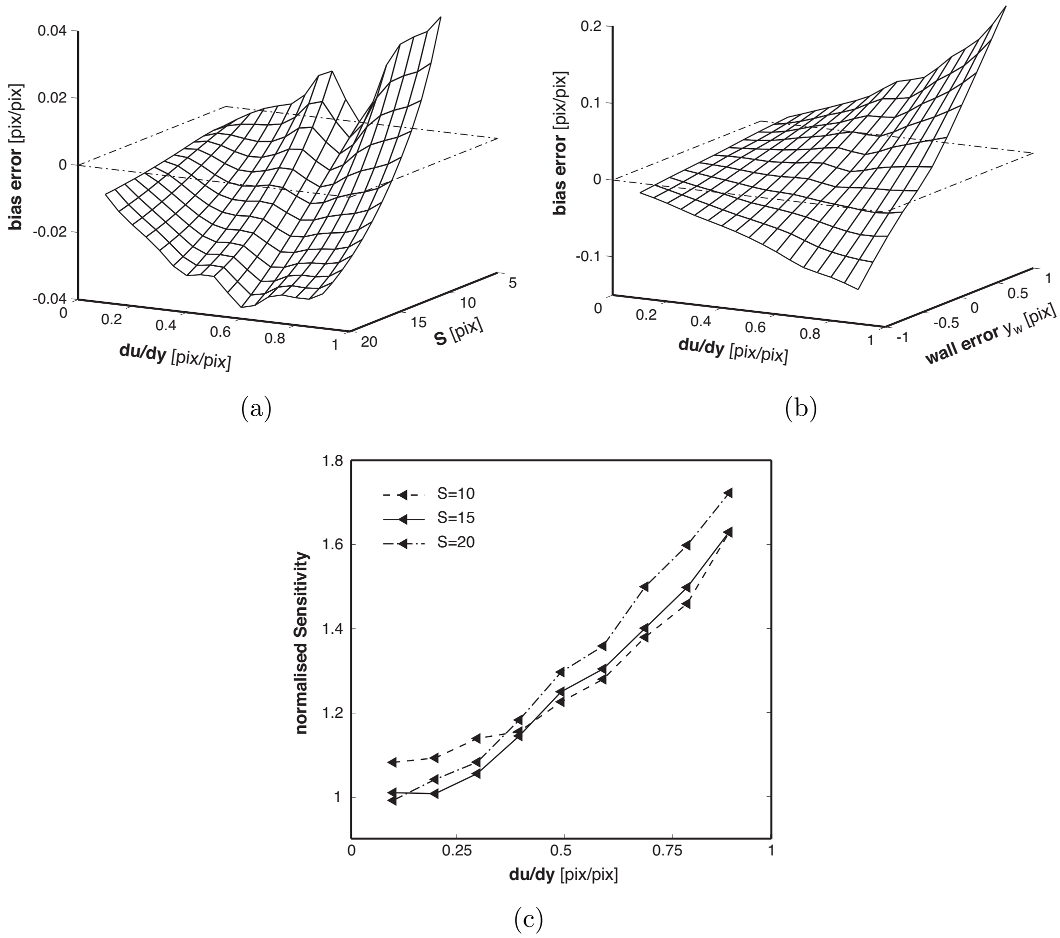

Figure 4.11 iPIV wall sensitivity: (a-b) Bias error as a function of the velocity gradient, Gaussian weighting and wall detection error; (c) Normalised wall sensitivity for different Gaussian weights. S = Gaussian weighting parameter, y_w = wall detection error

values of σ, suggesting an independency of the Gaussian weighting. However, dimensional wall sensitivity $S = \Delta(\partial U/\partial y)/\Delta y_w$ is inversely proportional to σ and will be lower for increasing values of σ, confirming the low pass filtering of the velocity gradient. Normalised sensitivity values are in the order of 1-1.7 and are similar to those reported by Nguyen et al. [2006] for the interface Gradiometry technique. A further discussion of the wall sensitivity under experimental conditions is given in Buchmann et al. [2008].

4.4.2 Velocity Profiles

Figure 4.12(a) analyses the perviously introduced Womersley velocity profile (Fig. 4.4) with the iPIV technique. The spatial wavelength is approximately $\Lambda = 48$ pixel and the images are interrogated with nearly optimal parameters of $\sigma = 5$ pixel and $M = 32$ pixel. The analysis clearly shows the advantage of the iPIV method in providing an accurate and robust estimate of the near wall velocity profile with single pixel resolution and low measurement uncertainty (note error bars in figure). The corresponding bias error and RMS measurement uncertainty are plotted in Figure 4.12(b) and compared to the 2D PIV interrogation with vector relocation. Overall, the iPIV method exhibits a lower bias error compared to the 2D PIV interrogation, though a slightly larger under-

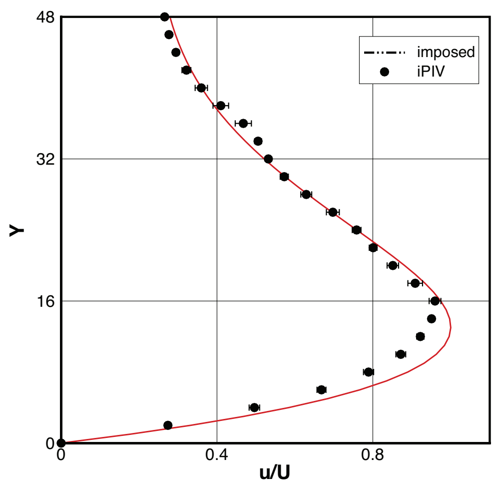

(a)

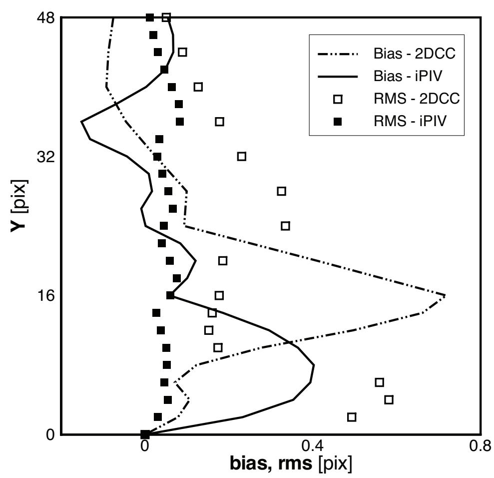

(b)

Figure 4.12 iPIV measurement (σ=5 pixel) of an imposed Womersley velocity profile applied to a synthetic image of type II. (a) mean velocity profile, N=1000, (b) Bias and RMS errors. Note, only every second data point is shown for clarity estimation of the velocities closest to the wall occurs. Most remarkably though, the RMS uncertainty in iPIV is significantly lower ($\epsilon < 0.1$ pixel), compared to the 2D PIV interrogation, which suffers from large measurement uncertainty ($\epsilon > 0.4$ pixel) due to the low seeding density closest to the wall. Moreover, the measurement uncertainty in iPIV remains fairly constant in wall normal direction, while the latter method exhibits an increase in uncertainty towards the wall (also see Section 4.2.2).

4.5 Discussion and Conclusion

The measurement accuracy in PIV near moving and stationary interfaces is greatly influenced by imaging and systematic errors that cause signal truncation and lead to erroneous velocity measurements. Methods such as image pre-processing and vector relocation are in principle able to nearly completely remove the velocity bias and to increase spatial resolution, but also cause an increase in measurement noise. It is the latter that is propagated during the near wall velocity gradient estimation when using discrete or analytical differentiation of the measured velocity fields. The extent of the error amplification and amplitude response of the differential operators depends primarily on the order of the derivative scheme and the spatial resolution of the velocity field. For example, the second order central difference scheme, one of the most frequently used operators [Foucaut and Stanislas, 2002], provides an acceptable tradeoff between spatial resolution and RMS uncertainty. Higher order schemes provide better spatial resolution and amplitude response, but also suffer from significantly greater error amplification.

To circumvent some of the difficulties in near wall PIV, a new interfacial PIV (iPIV) technique has been developed to accurately measure WSR and velocity profiles along curved and irregular shaped interfaces. Interfacial PIV directly estimates the velocity gradient from the recorded particle images and therefore eliminates the necessity for prior velocity field calculation and consequently error propagation. The flow is assumed to predominantly move parallel to the interface contour (i.e., wall normal displacement is smaller than one particle diameter), permitting a 'quasi' one-dimensional approach. The tracer displacement normal to the wall is determined by one-dimensional cross correlation and the subsequent WSR and wall parallel velocity profiles are estimated via an incremental linear fit of the correlation peaks. Furthermore, to facilitate measurements along curved interfaces, the recorded particle images are mapped to rectangular coordinates by means of conformal transformation. The transformed images can also be analysed with conventional 2D cross-correlation, if for example, the wall normal velocity field is required, which is currently not available with iPIV.

Compared to velocity field differentiation, iPIV has a significantly lower measurement uncertainty and a maximum possible spatial resolution of 1 pixel in wall normal direction. Similar to the differential operators, iPIV exhibits a low pass filtering behaviour, which is optimised by adjusting the linear interrogation size and the Gaussian weighting in normal direction. For shear rates in the order of 1 pixel/pixel, RMS errors of $1 - 2 \cdot 10^{-2}$ pixel/pixel are possible, which is an improvement in measurement certainty by more than order of magnitude. The amplitude response is dependent on the spatial velocity wavelength and the dimensionless weighting parameter $\sigma^* = \sigma/\Lambda$. An optimal response is obtained for $\sigma \approx 0.1$, while the measurement at respectively lower and larger values is affected by signal truncation and low pass filtering.

In conventional 2D PIV with velocity differentiation, the RMS uncertainty and amplitude response are inevitably coupled, requiring a tradeoff between spatial resolution and measurement uncertainty. In iPIV however, this coupling is only weak, with the RMS uncertainty being nearly independent of the Gaussian weighting, allowing the spatial response to be adjusted independently of the measurement noise.

Considering the velocity profile in Figure 4.12(a) with an imposed wall velocity gradient of $\dot{\gamma} = 0.3766$ pixel/pixel and a spatial wavelength $\Lambda = 48$ pixel, the expected measurement uncertainties can be estimated using the analysis presented in Sections 4.2.3 and 4.4.1. For the traditional PIV interrogation with vector relocation (32 pixel^2, $\Delta x/\Lambda = 0.083$, $\sigma_u \approx 0.4$) and second order centred difference WSR estimation ($\lambda_0 = 8.52$), the expected WSR measurement uncertainty is $\sigma_{\dot{\gamma}} \approx 18.9\%$ (0.071 pixel/pixel) at an amplitude response of $A = 0.72$. Decreasing the spatial resolution by a factor of two (i.e., $\Delta x/\Lambda = 0.167$), the respective RMS uncertainty and amplitude response also decreases to $\sigma_{\dot{\gamma}} \approx 9.4\%$

and $A = 0.5$. In comparison, for optimal processing parameters of $\sigma^* = 0.104$ and $M = 32$ pixel, the expected WSR errors with iPIV are only $\sigma_{\dot{\gamma}} \approx 0.8\%$ ($3 \cdot 10^{-3}$ pixel/pixel) and $A = 0.98$ for the random error and amplitude response, respectively.

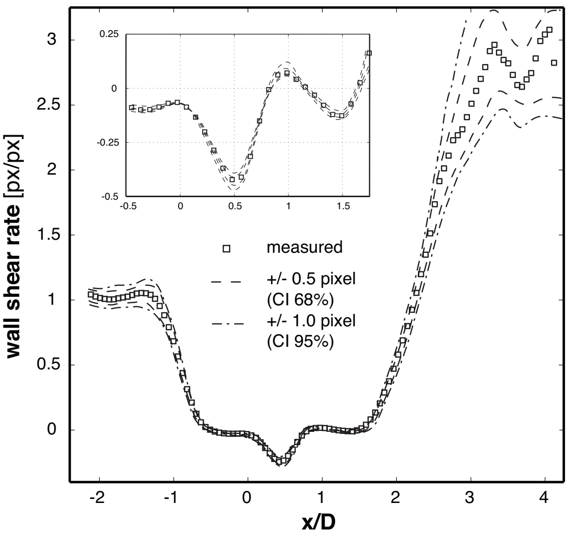

Figure 4.13 Measured wall shear rate and associated uncertainty due to errors in wall detection of 0.5 pixel (broken line) and 1 pixel (dashed line)

Errors in wall location considerably affect the accuracy of the iPIV technique as well as that of the differential operators. In iPIV, the sensitivity of measured WSR to an erroneous wall location is inversely proportional to the Gaussian weighting and proportional to the shear gradient. In the present study, the wall coordinates are identified manually, which can be achieved to a good accuracy for horizontal interfaces. However, in the case of curved walls, interface identification is less certain. Figure 4.13 shows the measured WSR for the image illustrated in Figure 4.8(a) together with the estimated WSR for interface errors of $\pm$ 0.5 and $\pm$ 1 pixel. The actual error in wall position is assumed to be normally distributed with a standard deviation of 0.5 pixel[1]. Hence, the envelopes in Figure 4.13 mark the respective 68% and 95% confidence intervals in measured WSR with manual interface identification. The results are sensitive to errors in wall location, particularly in cases of no-slip conditions. Thus, great care should be taken when locating the wall interface.

[1] ± 0.5 pixels seem to be a reasonable estimate for the interface location error and has been determined by repetitively identifying the same interface

In conclusion, iPIV provides two significant advantages compared to traditional velocity field differentiation. Firstly, a significantly lower measurement uncertainty and de-coupling of aptitude response and measurement noise is achieved and secondly. Secondly, when used together with conformal transformation, iPIV immediately facilitates WSR measurements along curved interfaces.

Chapter 5

Steady Flow in Idealised Carotid Artery Bifurcations[1]

This chapter provides detailed insight into the haemodynamic environment within a model of a healthy and a stenosed carotid artery bifurcation under steady flow conditions. In the first part, the experimental apparatus and methodology are detailed and the primary and secondary velocity fields in a population averaged carotid artery bifurcation are investigated. An interpretation of the three-dimensional flow structure is provided by means of a critical point theory to provide a general understanding of the complex flow environment within the carotid artery. The experimental results are accompanied by numerical simulations in an identical geometry to validate the experimental methodology and in particular the wall shear stress measurements. The flow field in a stenosed carotid bifurcation is investigated in the second part of this chapter. Wall shear stress results are presented for both geometries and reveal further details of the flow structure. In conjunction with the 'low-WSS' hypothesis (see Chapter 1.2.3), the current results can be used to identify areas subjected to low WSS and reduced cell signaling, and can be extended to endothelial dysfunction and disease. In the case of diseased vessels, high WSS is an important contributor in thrombus formation and plaque rupture.

[1] The content of this chapter has in part been published in *J. of Biomechanical Science and Engineering*, 2010, Vol. 5, No. 4, pp. 421-436, under the title:

Particle Image Velocimetry and Computational Fluid Dynamics Modelling of Carotid Artery Haemodynamics under Steady Flow: A Validation Study

N.A. Buchmann, M. Yamamoto, M.C. Jermy and T. David

5.1 Introduction

Atherosclerosis is a systemic proliferation and inflammatory vascular disease, which leads to arterial wall remodelling and narrowing (stenosis) due to intima thickening and vascular plaque formation. In its most severe form, atherosclerosis leads to complete vessel occlusion through thrombosis and is a major cause of stroke and ischemic infarction. The causative factors that contribute to the formation of atherosclerosis have been discussed in Chapter 1.2 and haemodynamic factors are identified as an important determinant in the localised development of atherosclerosis and vascular plaques. The pathology of atherogenesis involves the endothelial cells and vascular smooth muscle layer and their response to low and oscillating wall shear stress (WSS), flow separation and departure from unidirectional flow.

One of the predominant sites of chronic atherosclerotic lesion is the carotid artery. The most important haemodynamic phenomena are observed where the vessel branches into the internal and external carotid artery and the carotid sinus. The vessel wall has strong curvatures in these areas and a transverse pressure gradient develops due to centripetal forces, which favours flow separation, secondary flow vorticity and spatially and temporally varying WSS. Due to the severe consequences of atherosclerotic plaque formation, carotid artery haemodynamics has been the subject of intense research in the past (see Chapter 1.4 for a detailed review). While for the healthy carotid artery, plaque growth predominantly occurs in areas of low and oscillating WSS, haemodynamic factors such as high WSS are important contributors to thrombus formation and embolisation in diseased arteries.

High shear stress initiates platelet activation and aggregation, which plays a key role in thrombosis. High shear stress on the fibrous cap results in increased mechanical stress and ultimately plaque rupture. Furthermore, *in-vitro* studies using pulsatile and steady flow [Young and Tsai, 1973] indicate that vessel stenosis increases turbulent intensity and pressure losses. A comprehensive review on flow in stenotic vessels is given by Berger and Jou [2000]. Although the carotid bifurcation has been the focus of many haemodynamic studies, there are only few experimental studies on moderately and severely stenosed bifurcations, some of which include LDA measurements by Palmen et al. [1993]; Gijsen et al. [1996]; Lesniak et al. [2002], MRI measurements by Marshall et al. [2004] and a comparison between CFD and PIV by Steinman et al. [2000].

Steady State Assumption

A major simplification for the work considered in this chapter is the assumption of steady blood flow and hence neglecting the effects of flow pulsatility. This simplification of realistic blood flow is deemed reasonable, since the time scale of one cardiac cycle (approx. 1 sec.) is considerably shorter than that of physiological processes that influence mass transport and cellular reactions relevant to atherogenesis. For example, Rappitsch and Perktold [1996] investigated pulsatile flow for low diffusion coefficient species such as ATP and reported only moderate differences between steady flow and time-averaged concentrations. Comerford et al. [2008] reported insignificant species concentration variations in transient simulations and concluded that mass transport phenomena are dominated by spatial variations caused by flow geometry, rather than temporal variations. Furthermore, they noted that the species distribution was highly dependent on the secondary flow structure. In addition, the time scale of endothelial cell dynamics is one or two orders of magnitude larger than the cardiac cycle [Wiesner et al., 1997] and hence the effect of pulsatility on endothelial signaling may be neglected compared to the spatial variation of haemodynamic stimuli [Plank et al., 2006]. Furthermore, the study of steady flow conditions is relevant to patients with chronic heart failure that rely on continuous, i.e., steady flow ventricular assisted devices. The study of arterial haemodynamics under these conditions is important to understand long term effects of the implantation of these devices [Ootaki et al., 2005; Thalmann et al., 2005]. Nevertheless, it remains important to test the effects of pulsatility and to the assess the relation between time-averaged and steady flow haemodynamic metrics. An investigation in the pulsatile nature of blood flow will be presented in Chapter 6.

5.2 Methodology

5.2.1 Arterial Geometry

The most commonly used idealised carotid artery geometry is the averaged human carotid bifurcation (AHCB) first developed by Bharadvaj et al. [1982a]. This geometry was derived from systematic angiogram studies of 22 adults and comprises the common carotid artery (CCA) and the internal (ICA) and external (ECA) carotid arteries forming a Y-shaped bifurcation. Due to its relative simplicity, the Y-AHCB has to some extent become a standard in experimental and numerical investigations [Lou and Yang, 1992] and has been used by many researchers in the past [Gijsen et al., 1996; Ku et al., 1985b; Perktold et al., 1991c; Zarins et al., 1983]. More recently, it emerged that this geometry is not sufficiently accurate to entirely model the physiological flow conditions in the carotid bifurcation [Ding et al., 2001], particularly in relation to the correlation between the oscillatory shear index (OSI) and the location of intimal thickness. Systematic studies of 148 post-mortem specimens by Ding et al. [2001] revealed that in more than 50% of all cases the internal and external carotid arteries were bent inwards, forming a tuning-fork like shape (TF-shape) and only 8% of the dissected vessels corresponded to a Y-shape configuration. Goubergrits et al.

Table 5.1 Mean geometric parameters of the human carotid artery collected from literature. Parameters are non-dimensionalised by the common carotid diameter. Locations A-E are indicated in Fig. 5.1(a)

	N	Dimensionless Geometric Parameter				
		D	A	C	E	α
Bharadvaj et al. [1982a]	22	1	1.04	0.72	0.69	50.5^o
Zarins et al. [1983]	12	1	0.98	0.57	0.66	46^o
Ding et al. [2001]	148	1	1.04	0.72	0.69	44.3^o
Goubergrits et al. [2002]	86	1	1.06	0.79	0.68	61.6^o
Thomas et al. [2005]	50	1		0.81	0.81	48.5^o
Mean		1	1.03	0.72	0.7	50.2^o
Dimensional values this study (mm)		6.2	6.39	4.46	4.34	50.2^o
SD		(0.15)	(0.19)	(0.56)	(0.37)	(6.8^o)

[2002] and Thomas et al. [2005] reinforced the preference for tuning-fork models, especially in young adults who exhibit significantly less inter-individual variations compared to older subjects. A summary of the most relevant dimensions (i.e., diameter and bifurcation angles) from the above studies are given in Table 5.1. Also shown are the dimensions of the average human carotid bifurcation used in this work, which has a common carotid diameter of 6.2mm ($\pm$0.15mm) and a bifurcation angle of 50.2^o ($\pm$6.8^o).

Based on these findings, the average human tuning-fork shaped carotid artery bifurcation (TF-AHCB) is adopted in this work. The three-dimensional geometry is described as a parametric STL model (Chapter 2.3) and consists of the common carotid artery and the bifurcation into the internal and external carotid branches. The model is scaled to approximately 3.2 time life size. The model is axi-symmetric with a common carotid diameter of D=20mm and a bifurcation angle of α=50^o (CCA:ICA=30^o, CCA:ECA=20^o). The TF-AHCB geometry is illustrated in Figure 5.1(a) and the respective model dimensions are summarised in Table 5.2. Also shown are the proportionally scaled dimensions for the Y-shaped AHCB model from Bharadvaj et al. [1982a] and the tuning fork model from Ding et al. [2001].

From this model, a stenosed model is constructed by gradually reducing the carotid sinus diameter. Pathological measurements by Stary et al. [1995] indicated that the cross-sectional shape created by arterial plaques is essentially circular and thus the stenosis contours can be assumed to be relatively smooth. In the current model, the changes in vessel diameter are described with a cosine function to create an axi-symmetric stenosis with a 63% reduction in cross-sectional area (i.e., 63% stenosis). The resulting stenosed averaged human carotid bifurcation (ST-AHCB) is depicted in Figure 5.1(a) (dashed line) and described in Table 5.2 and is similar to that used by Steinman et al. [2000].

The transparent flow phantoms are constructed using the process described in Chapter 2.4. Physical prototypes of the bifurcation models are reproduced in a water soluble plaster by three-dimensional computer controlled printing and subsequently embedded in clear silicone. The transparent flow phantoms of the TF-AHCB and ST-AHCB are then obtained after curing of the silicone and removal of the plaster prototype and are shown in Figure 5.1(b) and (c).

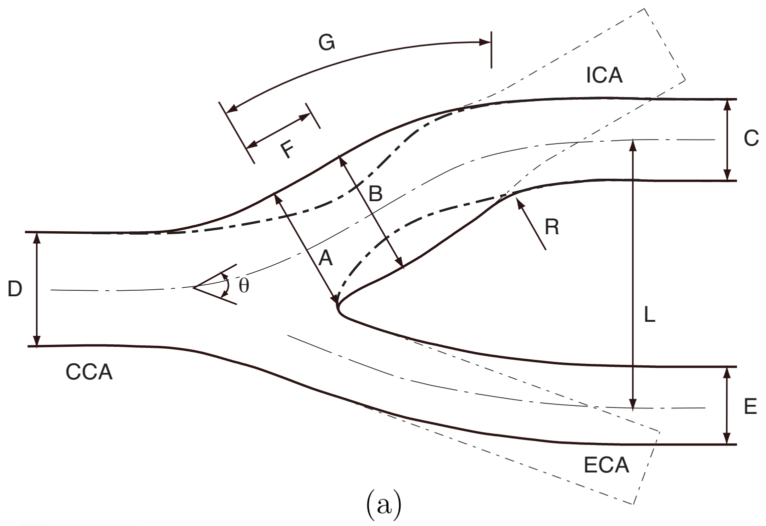

(a)

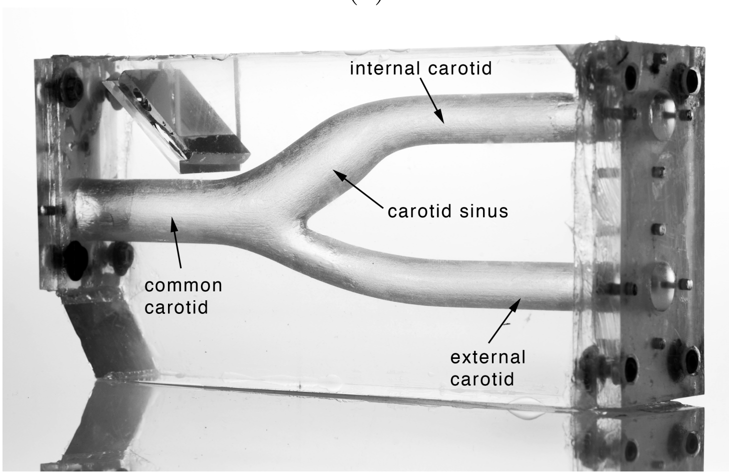

(b)

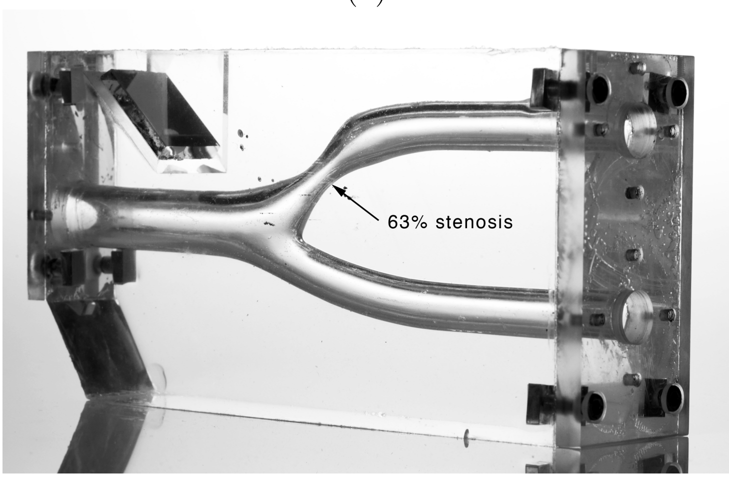

(c)

Figure 5.1 Carotid artery models: (a) schematic representation of the model geometry, solid line: tuning-fork shaped average human carotid bifurcation (TF-AHCB), dash-dotted line: stenosed average human carotid bifurcation (ST-AHCB), also shown is the Y-shaped AHCB. Dimensions are listed in Tab. 5.2; (b) TF-AHCB silicone phantom with connector plates and mirror for cross-sectional imaging; (c) ST-AHCB silicone flow phantom

Table 5.2 Dimensions of the average human tuning-fork shaped carotid artery bifurcation model. Locations A-R as indicated in Fig. 5.1(a)

	Location in Fig. 5.1(a)								
	D	A	B	C	E	F	G	L	R
This study									
Dimensionless values	1.0	1.04	1.11	0.72	0.69	0.9	3.0	2.4	4.1
Idealised carotid artery	20	20.8	22.2	14.4	13.8	18.0	60	48	82
63% stenosed model	20	16.8	8.8	14.4	13.8	18.0	60	48	82
Values proportional to									
Ding et al. [2001]	20	21.3	22.7	14.0	11.3	18.7	42.7	48	48
Bharadvaj et al. [1982a]	20	20.8	22.2	14.4	13.8	18.2	42.8		

Dimensions in (mm), $\alpha = 50^o$ for all models

5.2.2 Experimental Setup

Flow Circuit

A schematic representation of the experimental setup is given in Figure 5.2. The system provides a steady flow between an upper and lower fluid reservoir with a constant fluid level. Fluid from the upper reservoir is passed through a series of flow straighteners and a settling chamber to reduce flow vorticity and to provide stable flow at the inlet pipe. A straight pipe of length $L = 75D$ (D=20mm) is placed ahead of the test section to ensure fully developed flow at the entrance to the flow phantom. The flow is monitored with an inline electromagnetic flow sensor (Flowmaster FXE4000, ABB) just ahead of the test section and with rotameters in the two daughter branches. The flow rates between the two daughter branches are adjusted with gate valves located downstream of the test section. Fluid is collected in a lower tank from which the upper reservoir is refilled via a centrifugal pump. To ensure stable operating conditions, a temperature feedback controlled system is installed, which maintains the temperature of the working liquid to within $\pm 0.5^o$C.

To match the refractive index of the silicone flow phantom (n=1.141) a working fluid composed of 39% water and 61% glycerin b.w. is used. At 20^{o}C, the liq-

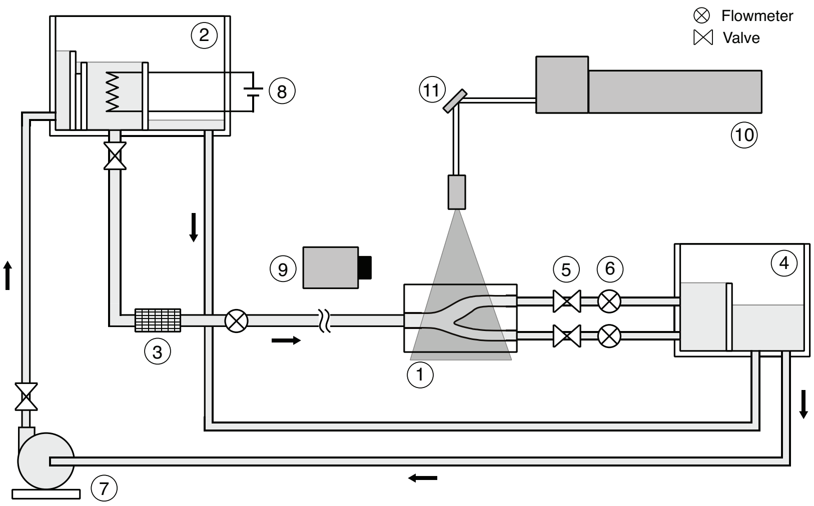

Figure 5.2 Schematic representation of the experimental facility showing the test section (1), upper (2) and lower (4) reservoir, flow straightener and settling chamber (3), valves (5) and flow meters (6), centrifugal pump (7) and temperature feedback control (8); The optical arrangement consists of a CCD camera (9), dual cavity Nd:YAG laser (10) and light sheet optics (11)

uid has a kinematic viscosity of $\nu = 10.2 \cdot 10^{-6}\mathrm{m}^2/\mathrm{s}$ and density of $\rho = 1.15\mathrm{g/cm}^3$ and allows distortion-free viewing of the three-dimensional flow passage. Detailed information regarding the selection of the blood analogue working liquid and the refractive index matching is provided in Chapter 2.5.

Particle Image Velocimetry

Planar digital PIV is used to measure blood flow velocities and WSS distribution in the carotid bifurcation models. The basic principle of this technique and details of the analysis algorithm are described in Chapter 3. In this section, only a description of PIV equipment relevant to the current study is provided, while a schematic of the optical arrangement is shown in Figure 5.2.

The working liquid is uniformly seeded with hollow glass spheres (Dantec Dynamics) of 10μm nominal diameter and density $1.1\mathrm{g/cm}^3$. The suspended particles are nearly neutrally buoyant and exhibit excellent flow tracking[2] and light scattering properties. A digital CCD camera (Kodak Megaplus 1.0), with an array size of 1008×1018 pixel^2 is used to record sequential particle images at a rate of 14Hz. The camera is fitted with a 55mm lens (Micro Nikkor Nikon) at an aperture of $f^{\#}$=8 and magnification $0.055-0.250$ depending on the measure-

[2]response time, $\tau_p \approx 0.5\mu$s, see Chapter 3.2

ment location. With these settings, the estimated depth of field for the experiments is approximately 2mm and the diffraction limited particle size is 13μm. The suspended particles are illuminated with a dual-cavity Nd:YAG laser (New Wave, Solo PIV 120) with a wavelength of 532nm and a pulse energy of 120mJ and 5ns duration. The laser beam is shaped into an approximately 1.2mm thick laser sheet using a series of spherical and cylindrical lenses. The approximate height of the laser sheet is 120mm. Both, camera and light sheet optics are mounted on 2-axis railing systems to facilitate translation. Depending on the measurement locations and flow conditions, the time delay between the two laser pulses varies between $500 - 2600\mu$s. This is to ensure a maximum particle displacement of approximately 25% (or 16 pixels) of the sampling window used in the PIV image analysis. Some of the image acquisition parameters are listed in Table 5.3.

Table 5.3 PIV image acquisition parameters

Parameter	Value
FoV	120×120 mm^2
$f\#$	8
M	$0.025 - 0.25$
dof	2mm
Δt	$500 - 2600\mu$s

A total of 100 image pairs are recorded per measurement and are preprocessed to remove background intensities and image noise. This involves background subtraction, followed by Gaussian smoothing (3×3), and intensity normalisation (see Appendix C). The resulting particle images are analysed using the adaptive multi-grid PIVCC algorithm with an initial interrogation window size IW_0 and two iterative refinement steps with discrete window shift. Furthermore, ensemble correlation averaging is used and the data are validated using the signal-to-mean ratio (SMR) and a normalised median test (NMT) as described in Chapter 3. The spacing between velocity vectors Δ corresponds to 4 pixels or approximately 40 vectors across the model diameter. A summary of the relevant interrogation parameters is given in Table 5.4.

Wall shear stress is analysed with the iPIV technique described in Chapter 4 and the interrogation parameters in Table 5.4. The vessel walls are identified

Table 5.4 PIV and iPIV image analysis parameters

Parameter	Value
# images	100
PIV	
IW_0	64 px
IW_1	16 px
SMR	1.5
NMT	2
Δ	4 px
iPIV	
IW_0	32 px
H	80 px
σ	10 px
Δ	8 px

from the pixel averaged background image and the recorded particle images are mapped onto the orthogonal grid of height, H by means of cardinal function interpolation. The velocity gradient at the wall is estimated from the time-averaged, normalised correlation maps using a Gaussian weight of $\sigma = 10$ pixel.

The uncertainties and errors associated with the velocity and WSS measurements are discussed in detail in Appendix F and Chapter 4. The experimental or hydraulic uncertainties due to variations in operating temperature, flow rate, fluid viscosity and light sheet alignment are estimated to approximately 2.3%, while the digital PIV displacement error is ≈ 0.1 pixel amounting to a velocity error of approximately 1.3%. The iPIV error depends on the WSS magnitude, velocity wavelength and wall detection accuracy and is estimated between $1 - 12\%$.

5.2.3 Numerical Modeling

For the numerical simulations, the inlet and outlets of the TF-AHCB model are extended and positioned approximately $7D$ and $20D$ away from the bifurcation. This is to ensure fully developed flow at both, the inlet and outlets, as well as that the flow through the region of interest is unaffected by the flow conditions at the boundaries. All other model dimensions remain unchanged.

The volume mesh is created with the automatic mesh generation package Harpoon (Sharc, Manchester, UK). The initial meshes consisted of 2.58-4.6 million hex-dominant elements and included a structured boundary layer along the wall to accurately capture the near-wall velocity gradients. Preliminary simulations are carried out using these meshes in order to ensure that the solutions are independent of the mesh size and obtained efficiently. The mesh independence is verified by comparing WSS along the sinus outer wall for the different meshes as shown in Fig.5.3(a). The final mesh shown in Figure 5.3(b) contains 2.58 million elements with no further improvements observed for finer meshes.

The flow field in the bifurcation model is solved with the commercial finite-volume CFD package FLUENT (Fluent Inc., Lebanon, USA). The blood flow is modeled as an incompressible, Newtonian fluid with identical density and dynamic viscosity to that used in the experiments. The steady-state flow field is solved iteratively via the continuity (Eq. 2.3) and momentum (Eq. 2.2) equation using a SIMPLE algorithm for the pressure-velocity coupling and a second-order

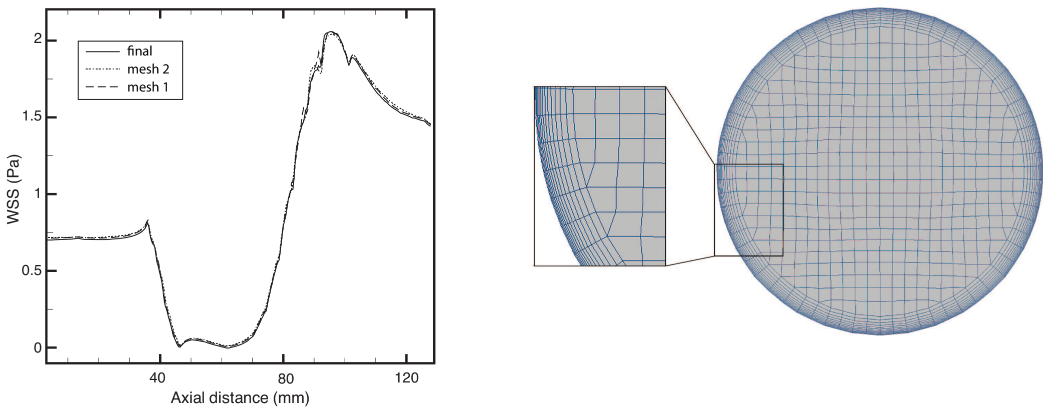

(a) (b)

Figure 5.3 (a) WSS along the outer ICA wall to test mesh convergence; (b) Cross section of the CFD carotid artery mesh, showing the hex-dominant grid structure and the boundary layer applied along the wall upwind scheme for the convection terms. Based on preliminary measurements and the range of investigated Reynolds numbers, the flow is assumed to be laminar and no turbulence model is included in the simulations.

As in the experiments, the wall of the bifurcation model is assumed to be rigid and with a no-slip boundary condition and a fully developed, i.e., parabolic, flow profile at the model inlet. The outlet boundary conditions are defined as zero-diffusive flux in the streamwise direction for all variables, for which the extended vessel outlets ensure fully developed flow at the model outlets. Further details on the numerical simulations and implementation can be found in Buchmann et al. [2010] and Comerford et al. [2008].

5.2.4 Description of the Measurement

Velocity and wall shear stress measurements are performed under steady flow conditions. The dimensionless parameters describing the flow, Re and γ are defined in Chapter 2.2.3.

Measurements are performed for $Re = 400$, 800 and 1200. This is to provide an understanding of how different inlet conditions affect the formation of flow recirculation, secondary flows and WSS distribution. The selected Reynolds numbers are expected to be representative of mean and peak systolic flow con-

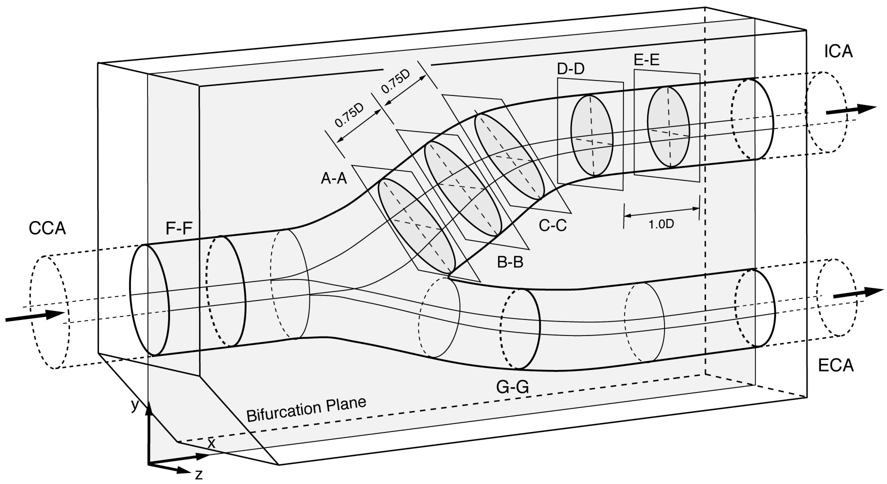

Figure 5.4 Locations for velocity measurements in the bifurcation plane and cross-sectional planes A-A to E-E; WSS is measured in the bifurcation plane along the inner and outer walls

ditions and a period of mild exercise. Although it has been reported that the division of flow in the two daughter branches varies during one cardiac cycle, the time averaged flow division in the carotid artery is approximately $\gamma = 0.7$ [Ku and Giddens, 1987]. Physiologically, changes in flow division arise from luminal area changes of the external carotid artery due to pulse pressure. To account for this variation and to assess its effect on flow circulation and WSS under steady flow conditions, different flow division ratios ($\gamma = 0.6 - 0.8$) are investigated in this study. The numerical validation is performed for $Re = 400$ and 800 and $\gamma = 0.7$.

The velocity field is investigated in the bifurcation plane (or symmetry plane) and cross-sectional planes as indicated in Figure 5.4. In the internal carotid artery, the velocity distribution is mapped in five spanwise planes (A-D) separated by a distance $0.75D$ along the streamwise direction. This is to observe the mean flow characteristics as well as the secondary flow structures induced by the branching and curvature of the vessel.

5.3 Idealised Carotid Artery Bifurcation

5.3.1 Flow Characteristics

Axial Velocity Fields

The flow features in the idealised carotid model are characteristic of bifurcating flow and are similar to previous studies. Figure 5.5 and 5.6 detail the axial velocity profiles in the bifurcation plane for different flow division ratios γ and Reynolds numbers Re. In the common carotid artery, flow is fully developed and exhibits a nearly perfect parabolic flow profile. At the bifurcation, the high momentum fluid is split into the internal and external branch and following the flow divide, the velocity profiles are skewed, thereby creating high shear stress along the inner walls of the bifurcation. On the outer wall, a large region of low momentum fluid and consequently low WSS exists. The central part of the low velocity region occupies approximately 50% of the vessel lumen. For larger Re, the same skewing of the velocity profiles occur and the low velocity region increases and flow separation and flow reversal at the proximal sinus strengthen. Moreover, the velocity gradient along the inner wall increases for larger Re and high WSS in this region is maintained for high Reynolds numbers. Similar trends are observed for different flow division ratios with the velocity magnitude in the daughter branches increasing or decreasing according to γ.

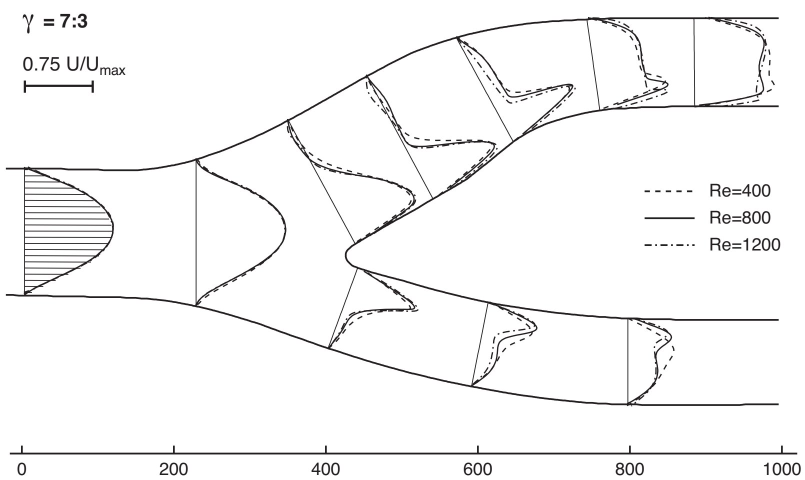

Figure 5.5 Axial velocity profiles in the branching plane for different Reynolds numbers, $Re = 400, 800, 1200$. Data are normalised by the maximum velocity in the common carotid artery

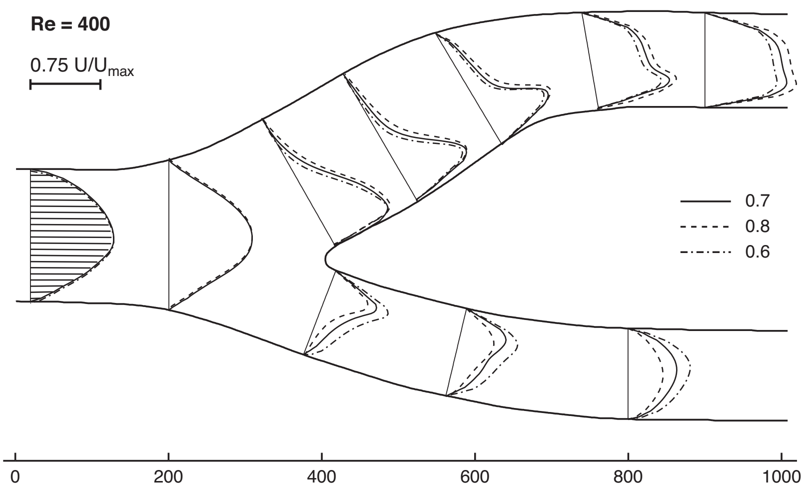

Figure 5.6 Axial velocity profiles in the branching plane for different flow devision ratios, $\gamma = 0.6 - 0.8$. Data are normalised by the maximum velocity in the common carotid artery

Secondary Velocity Fields

The branching and curvature of the outer wall produce complex secondary flow patterns that are known as Dean type flow [Dean, 1928] and are shown in Figure 5.7 and 5.8. The flow consists of a pair of counter-rotating helical vortices that are located almost symmetrically on either side of the bifurcation plane.

Secondary flow arises because of a lateral (centripetal) acceleration u^2/R, which causes a radial pressure gradient that drives slower moving fluid near the vessel wall towards the center, while faster moving fluid in the vessel core is swept outwards. The strength of the secondary flow is characterised by the Dean number κ and the ratio of the vessel radius to the radius of curvature $\delta = a/R$, where a and R are the vessel radius and curvature, respectively. For a uniformly curved vessel (i.e., δ = const.) with slight curvature ($\delta \ll 1$) the Dean number is defined as [Berger et al., 1983]:

$$\kappa = \frac{2a\overline{U}}{\nu}\left(\frac{a}{R}\right)^{1/2} = 2\delta^{1/2}Re \tag{5.1}$$

where $\overline{U}$ is the mean axial velocity in the vessel. The Dean number is the ratio of the square root of the product of the inertial and centrifugal forces to the viscous forces and equals the Reynolds number modified by the vessel curvature. There are many different definitions of the Dean number in the literature and one has to be careful in interpreting different formulations. One of the most commonly used definition is that of McConalogue and Srivastava [1968]:

$$Dn = \frac{Ga^2}{\mu}\left(\frac{2a^3}{\nu^2 R}\right)^{1/2} \tag{5.2}$$

where $G = -\partial p/\partial x$ is the axial pressure gradient. However, definitions of the Dean number based on the mean axial velocity (i.e., Expression 5.1) are generally preferred by experimentalists as $\overline{U}$ is readily measured and provides a more convenient characterisation of the flow than the more difficult to measure pressure gradient.

For fully developed flow, small curvatures ($\delta \ll 1$) and small Dean numbers, there is little difference between κ and Dn and the pressure gradient may be estimated from the solution of fully developed flow in a straight pipe of equal diameter [Berger et al., 1983]. In this case, κ and Dn are related by $Dn = 2^{5/2}\kappa$. For larger Dean numbers however, the relationship between κ and Dn is more complex and one must consider the flux ratio, which for a given G is lower in a curved pipe than in a straight pipe of equal diameter [van Dyke, 1978]. It should also be noted that the original definition of the Dean number, K introduced by Dean [1928] is related to Dn by $Dn = 4K^{1/2}$.

A summary of characteristic Dean numbers in the internal carotid artery is given in Table 5.5 for different Reynolds numbers.

Table 5.5 Values of different Dean numbers in the internal carotid artery

Re	δ	κ	Dn	K
400	0.104	258	1461	$1.33 \cdot 10^5$
800	0.104	516	2921	$5.33 \cdot 10^5$
1200	0.104	775	4382	$1.20 \cdot 10^6$

Although the carotid artery geometry is much more complex than a uniformly bent pipe with complex and multiple curvatures (c.f., Fig. 1.6) some conclusions regarding the secondary flow motion can be drawn using the above concept. For example, in the idealised model, the internal carotid artery exhibits two distinct curvatures of similar magnitude, but of opposite direction. The secondary flow topology in the internal carotid artery at various cross-sections is depicted in Figure 5.7 and 5.8 for Re = 400 and 800, respectively.

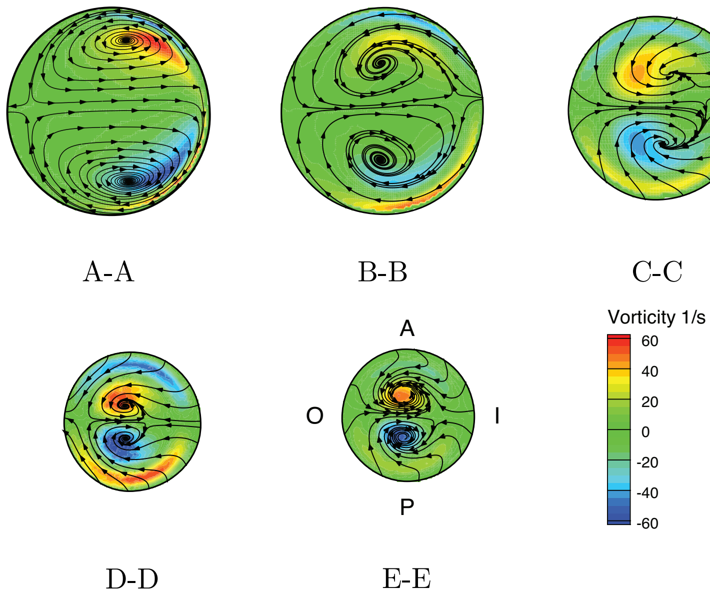

Figure 5.7 Secondary flow streamlines at Re=400 in the carotid sinus at the distal internal carotid branch. (I) inner, (O) outer, (A) anterior and (P) posterior wall

At the proximal sinus (A-A), the Dean number is large (Tab. 5.5) and the fluid experiences a strong radial acceleration, which pushes the symmetric pair of counter-rotating vortices towards the flow divider wall (i.e., outer wall of the bend). At mid- and distal sinus (B-B, C-C) the vessel straightens slightly and the Dean number reduces with the vortex pair moving towards the vessel center. At the distal locations (D-D), the vessel curvature changes direction and the flow again experiences a strong acceleration. The Dean number is large in

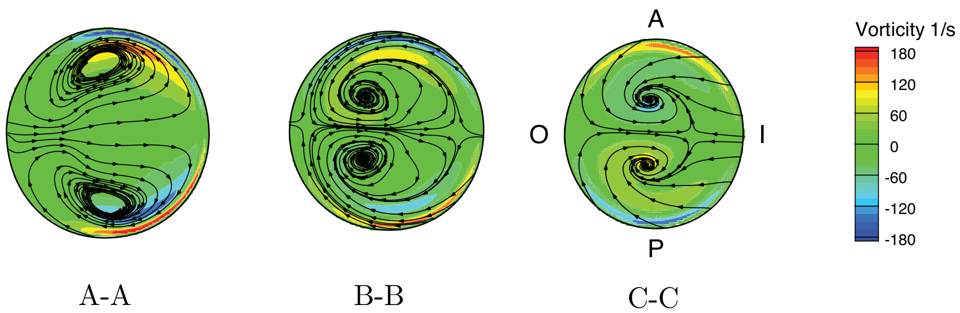

Figure 5.8 Secondary flow streamlines at Re=800 in the carotid sinus at the proximal, mid- and distal location. (I) inner, (O) outer, (A) anterior and (P) posterior wall

this region and this time the vortices are pushed towards the outer bifurcation wall (i.e., outer wall of the bend). Finally, at position E-E, the vessel straightens and the secondary vortices move back to the vessel center and eventually decay further downstream ($Dn = 0$).

At this point it is useful to briefly describe the evolution of the general secondary flow pattern in terms of Dean number. For small Dean numbers ($Dn < 96$), the secondary vortices are located close to the vessel center and the maximum circumferential velocity is attained in the center of the vessel as seen in cross-section C-C and E-E. Additionally, at small Dn the flow stabilises and the critical Reynolds number for which turbulent transition occurs increases (c.f., Berger et al. [1983] for more details). At intermediate Dean numbers ($96 < Dn \lesssim 600$), a secondary or circumferential boundary develops with fluid entering the boundary layer near the outer bend and leaving near the inner bend as observed in cross-section A-A. Further increase in $Dn \gtrsim 600$ and hence large centripetal force, increases the circumferential velocity (and vorticity) and causes more fluid to enter the secondary boundary layer as observed in Figure 5.8. Simultaneously, the secondary vortices are pushed away from the center towards the outer wall and are skewed to adjust for the increase in boundary layer thickness. The growth in the boundary layer thickness causes a reductions in flux, which at high Dn constricts the flow through the vessel considerably compared to a straight pipe with equal pressure gradient. Likewise, the skin friction and energy dissipation increase with increasing Dn and approximately scales with $\kappa^{1/2}$ [van Dyke, 1978; Berger et al., 1983].

Interpretation of the Three-Dimensional Flow Structure

The flow field in the carotid sinus is detailed in Figure 5.9 in the form of time-averaged sectional streamlines[3]. The topology of the velocity fields and the sectional streamlines are described with the critical point theory [Perry and Chong, 1987], which are points in the flow field where the velocity is zero and the streamline slope is indeterminate. Critical points are divided into three different types: saddle, nodes and foci and can either be stable (attracting) or unstable (repelling). The basic pattern of critical points reveals information

[3]Sectional streamlines are defined as lines tangential to the in-plane velocity vector

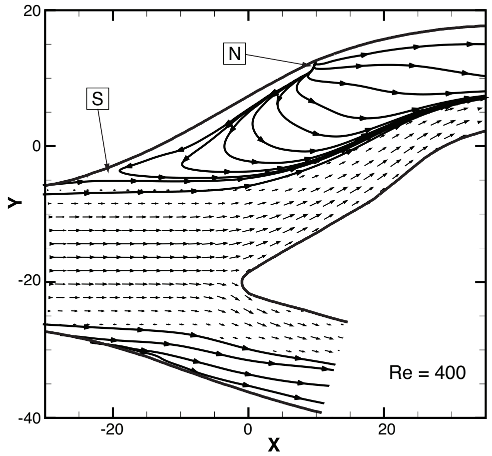

(a)

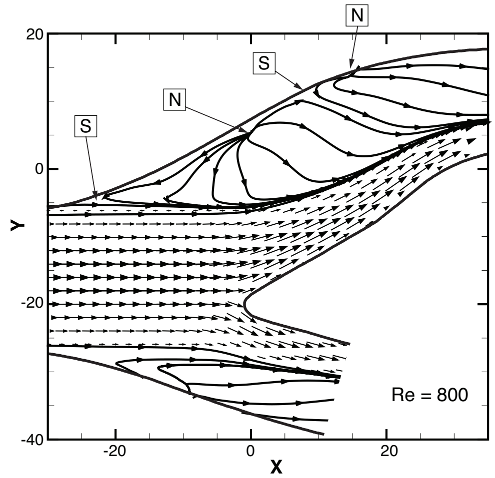

(b)

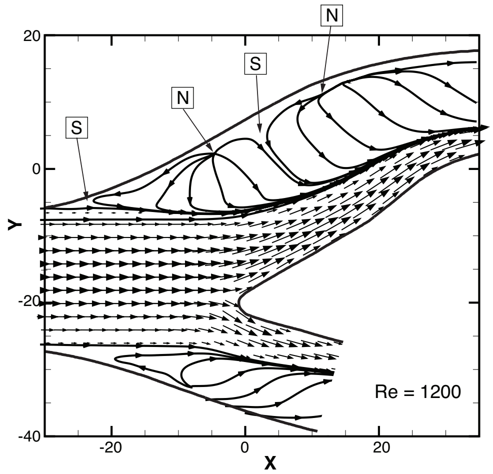

(c)

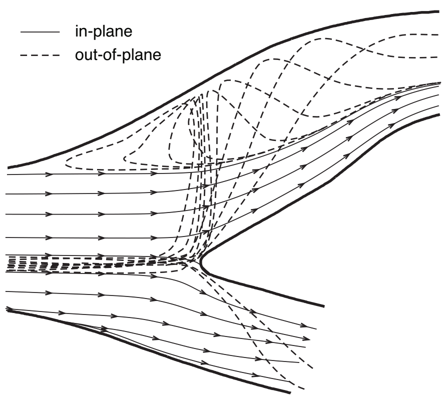

(d)

Figure 5.9 (a)-(c) Detailed flow pattern in the carotid artery bifurcation for different Reynolds numbers, $Re = 400, 800, 1200$, showing the formation of a reversed flow region and critical points, S = saddle point, N = node point; (d) Schematic representation of the vortical flow structure in the carotid sinus similar to Motomiya and Karino [1984]. Solid lines are sectional streamlines in the bifurcation plane, dashed lines are particle paths, which are far away from the median plane (projection of the particle paths on the common median plane)

regarding the three-dimensional flow topology, such as vortex formation [Perry and Chong, 1994].

In the carotid sinus, the low momentum flow region is separated from the mean flow by a dividing streamline, which originates from the proximal sinus where the main flow separates from the outer wall, i.e., saddle point. For low Re, a single repelling node exists at the distal sinus, whilst for larger Re two repelling nodes, separated by a saddle point emerge at the mid and distal sinus location. At the nodal points, the in-plane velocities are zero and by definition, i.e., continuity, an out-of plane velocity component must exist in order for the sectional streamlines to emanate from this point.

From the current data, the following conclusion can be drawn regarding the three-dimensional flow topology within the carotid sinus. The interaction between the main axial and secondary flow creates a helicoidal flow structure. High momentum fluid in the symmetry plane flows through the bifurcation region and subsequently through the internal and external daughter branches with little disturbance. On the other hand, fluid far away from the median plane is deflected at the bifurcation apex and moves laterally along the anterior and posterior walls of the bifurcation as illustrated in Figure 5.9(d). In the internal carotid artery, the deflected flow travels almost perpendicularly to the axial main flow and impinges on the sinus outer wall where it meets the symmetry plane. At the point of impingement, a repelling node forms. From here some portion of the flow is convected downstream, while the remainder moves upstream to form a reversed axial velocity region along the outer sinus wall (Figure 5.9(a)-(c)). The deflected flow joins again the main flow at the proximal sinus (i.e., saddle point) and is convected downstream along the counter rotating helicoidal flow through the carotid sinus. For larger Re, several deflected fluid streams exist, each impinging on the bifurcation plane at the location of the nodal points.

The phenomena of deflected transverse flow at the proximal sinus under steady flow conditions has also been reported by Motomiya and Karino [1984] and Ding et al. [2001] in flow visualisation experiments. Furthermore, it is important to note that the separated flow region is not a recirculation region in its classical sense where fluid particles become entrapped and streamlines form closed loops. This part of the flow is progressively restored to streamwise flow and regarded as reversed low-momentum flow region within the context of this work. The formation and size of the reversed low-momentum region as well as the helicoidal flow structure depends on the flow division, γ, the vessel curvature, δ and the Reynolds number, Re.

Finally, a three-dimensional illustration of the individual planar velocity fields is presented in Figure 5.10. Note the high velocity region near the flow divider wall and the low momentum flow region along the outer wall. Secondary velocities are approximately one order of magnitude smaller than the stream-wise velocities. An additional discussion of the three-dimensional flow structure in the carotid artery is presented in Chapter 7 on the bases of stereo and volumetric PIV measurements.

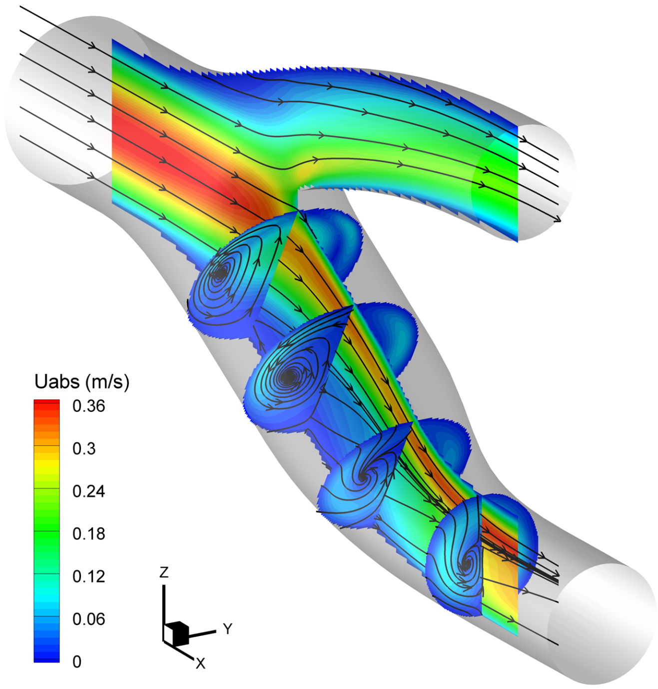

Figure 5.10 Illustration of the heliocoidal flow structure in the carotid sinus by means of individual planar velocity fields, $Re = 400$

5.3.2 Wall Shear Stress

A detailed examination of WSS under various flow split ratios is presented in Figure 5.11(a). At the bifurcation, the flow experiences a sudden increase in cross-sectional area, which leads to a rapid decrease in WSS to values close to or below zero at the proximal sinus. Wall shear stress remains low across the majority of the sinus region before it increases again at the distal sinus due to the reduction in vessel cross-section and adverse vessel curvature. Overall, a proportional relationship between flow split and WSS exists as it has already been established for the axial velocity fields.

In significant contrast are the effects of changing Re as demonstrated in Figure 5.11(b). For low Re, i.e., 400, a single detached flow region exists along the carotid sinus outer wall with flow separation and reattachment occurring proximally and distally. This trend persists for larger Re, yet the magnitude of negative WSS increases for increasing Re. Additionally, the formation of a second detached flow region, located at the distal sinus can be observed and is shown in Figure 5.12(a) in greater detail. Note that WSS is normalised by its corresponding value in the common carotid artery $\text{WSS}_{CCA} = 8Re\rho\nu^2/D^2$. The respective *in-vivo* values are 1.0, 2.0 and 3.0 Pa for Re = 400, 800 and 1200. The spatial WSS distribution and magnitude in the carotid sinus varies significantly between Re and in the distal branch, WSS is significantly increased for larger inlet velocities.

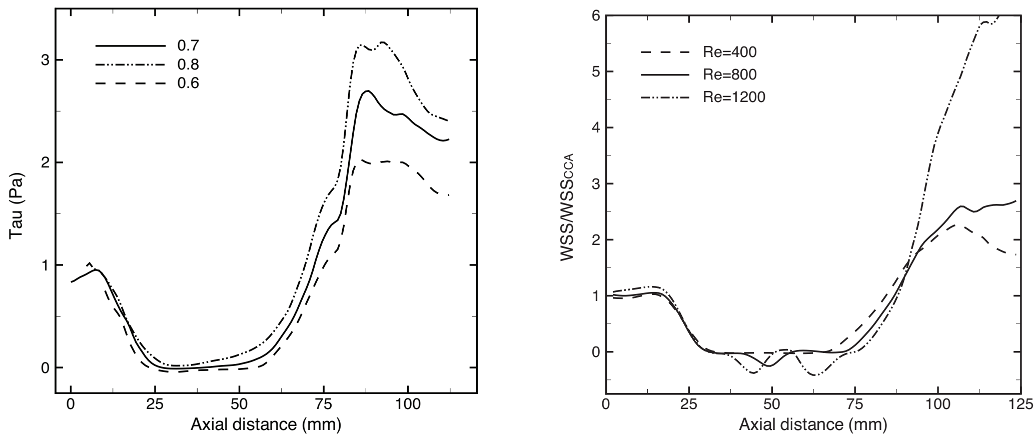

(a) (b)

Figure 5.11 WSS plotted along the outer sinus wall for (a) different flow division ratios, $\gamma = 0.6 - 0.8$ and (b) Reynolds numbers, $Re = 400, 800, 1200$. Data are normalised by their corresponding value in the common carotid artery $\text{WSS}_{CCA} = 8Re\rho\nu^2/D^2$

The increase in flow recirculation and hence negative WSS is directly related to the amplification of secondary flows, helicity, and the growth of the low momentum flow region. There is a strong correlation between flow separation, re-attachment and the three-dimensional flow structure as demonstrated in Figure 5.12(b). In general, flow separation occurs at the outer proximal sinus wall (first saddle point), regardless of flow division or Re. Depending on vortical strength, the flow re-attaches again approximately at the impingement point (first node) of the transverse flow deflected at the bifurcation apex. For larger Re, flow separates again at the second saddle point and subsequently re-attaches at the second node. WSS along the outer sinus wall undergoes significant spatial variations with values ranging between $0 - 1.6$ Pa.

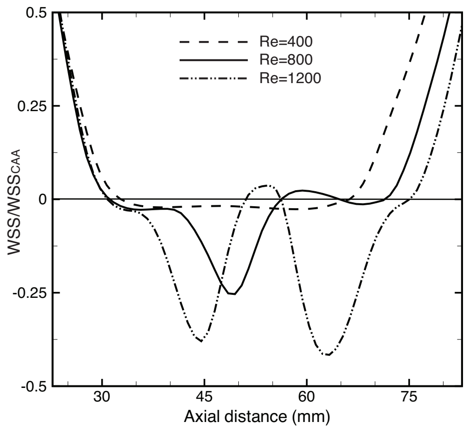

(b)

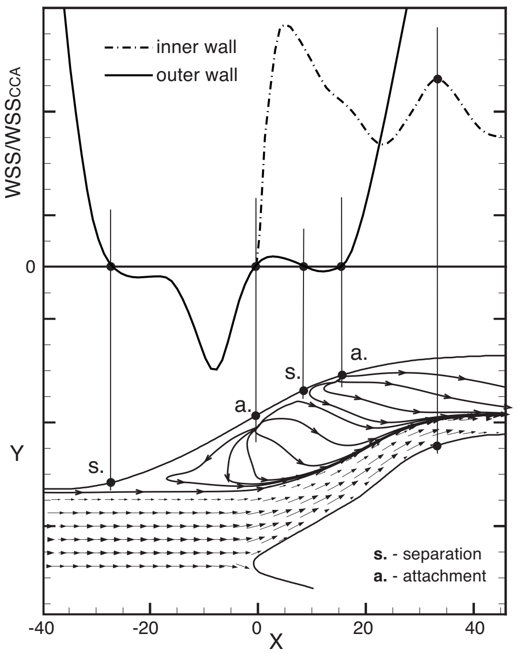

(a)

Figure 5.12 WSS in the carotid sinus; (a) along the outer wall and for different Re, detail from Figure 5.11(b). (b) Correspondence between spatial WSS variation and three-dimensional flow structure

In the external carotid artery and along the outer wall, shear stresses are low at the proximal sinus and flow separation only occurs for larger Re (Figure 5.13(a)). Wall shear stress in the external carotid artery exhibits a similar behaviour to that observed in the carotid sinus, but with less spatial variation

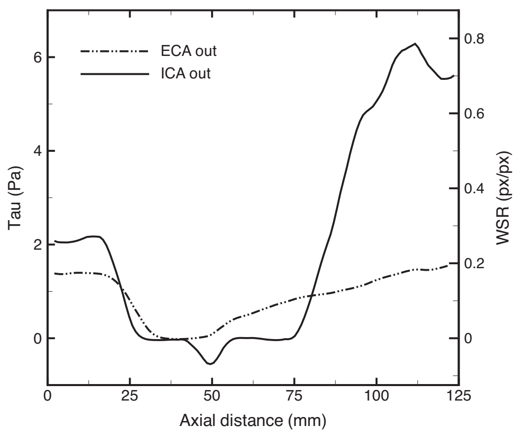

(a)

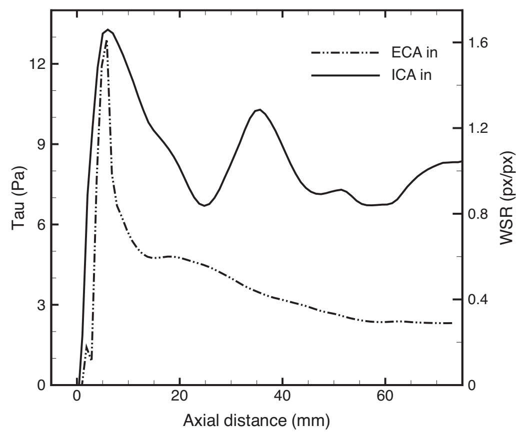

(b)

Figure 5.13 WSS at $Re = 800$ plotted along the (a) outer and (b) inner walls of the carotid bifurcation and lower magnitudes. At the inner walls, a stagnation point forms at the bifurcation apex and WSS peaks to approximately $6-7$ times to that in the common carotid artery, i.e.,$\sim$13.5 Pa. Further downstream WSS reduces again regardless of Re, but remains at an elevated level compared to the outer walls, Figure 5.13(b). In the internal carotid artery, WSS peaks a second time at the distal sinus where the vessel cross-section reduces and vessel curvature increases.

Clearly the Reynolds number plays a vital role in steady WSS magnitude, which increases nearly proportionally with Re. It is however, the *spatial* variation in WSS that is of primary interest in this context. The key observations are firstly, that the outer wall of the bifurcation is subjected to relatively low or negative WSS irrespective of Reynolds number and flow division. Secondly, WSS along the outer wall undergoes strong spatial variations brought about by the three dimensional characteristics of carotid artery flow and the strengthening of secondary flow for increasing Reynolds numbers.

5.3.3 Comparison with Numerical Results[4]

This section presents a quantitative comparison between the experimental data and numerical simulation. This is to validate the experimental procedure and in particular the WSS measurement performed with iPIV. To assess the differences between the observed and predicted velocities and spatial WSS data, a relative error ϵ_{rel} and a normalised error ϵ_{norm} are introduced.

$$\epsilon_{rel} = \left| \frac{f_N - f_E}{f_N} \right| \tag{5.3}$$

and

$$\epsilon_{norm} = \left| \frac{f_N - f_E}{f_{C,N}} \right| \tag{5.4}$$

where f_N and f_E are the numerical and experimental data points, and $f_{C,N}$ is the observed numerical value in the common carotid artery.

[4]Ms. Miharu Yamamoto is greatly acknowledged for carrying out the numerical simulations presented in this section and her stimulating discussions on the topic

Both, numerical and experimental axial velocity profiles are shown in Figure 5.14. The velocity profiles are sampled at seven spanwise locations in the bifurcation pane and plotted against the normalised radius r/D. As already discussed, the branching and vessel curvature introduce a radial pressure gradient. This causes the axial velocity profiles to be skewed towards the inner bifurcation wall, and consequently creating a low and reversed flow region along the outer wall. A satisfying data match between the CFD prediction and the experimental data is obtained for $Re = 400$ with a maximum relative error of $\epsilon_{rel} = 11.3\%$ at section H-H. Larger discrepancies occur for $Re = 800$ in the carotid sinus and the distal external carotid branch. Particularly at the mid-sinus location (B-B), large differences occur along the outer wall (r/D=-0.5) with a maximal error of $\epsilon_{rel} = 43\%$. The respective averaged maximal errors $\overline{\epsilon_{rel}}$ for the selected profiles are 6.1% and 13.7% for $Re = 400$ and 800, respectively. The overall difference in peak velocity is 1.23%.

The secondary flow structure obtained from the numerical simulation is illustrated in Figure 5.15 for $Re = 800$ and a good agreement is obtained when compared with the experimental results from Figure 5.8. Both techniques reproduce very similar secondary flow structures and the size and location of the vortex cores as well as streamwise vorticity magnitude are matched closely. Maximal errors in vorticity are observed in the vortex center at the proximal sinus (A-A) and are $\epsilon_{rel} = 9.5\%$ and $\epsilon_{rel} = 20.5\%$ for $Re = 400$ and 800, respectively.

Experimental and numerical WSS are compared for the inner and outer bifurcation walls. Some differences exist, particularly within the reversed low momentum flow region along the outer internal and external artery wall as shown in Figure 5.16(a) and (b). While the size of the reversed flow region is predicted correctly by both techniques, there are some differences in reversed flow magnitude and location of the second separation and reattachment point, i.e., saddle and node point, in the carotid sinus. This is consistent with the discrepancies seen in the velocity profile at mid-sinus and indicative of some differences in the three-dimensional flow structure. There is also significant under-prediction of the high shear stress regions by the iPIV technique (Figure 5.16(c)). This is possibly due to the limited spatial resolution and low pass characteristics of

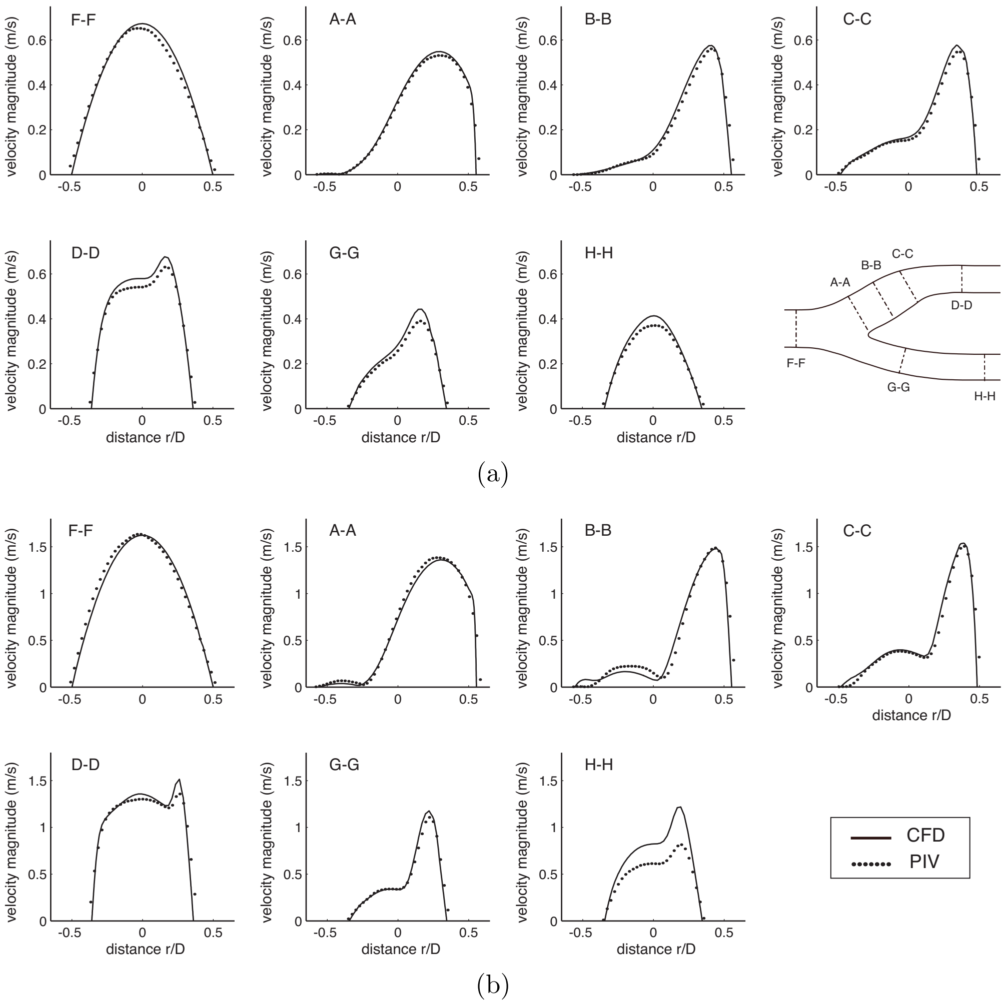

Figure 5.14 Comparison of axial velocity profiles at selected locations in the common, internal, and external carotid artery; (solid lines) CFD data, (points) PIV measurements. (a) $Re = 400$, (b) $Re = 800$

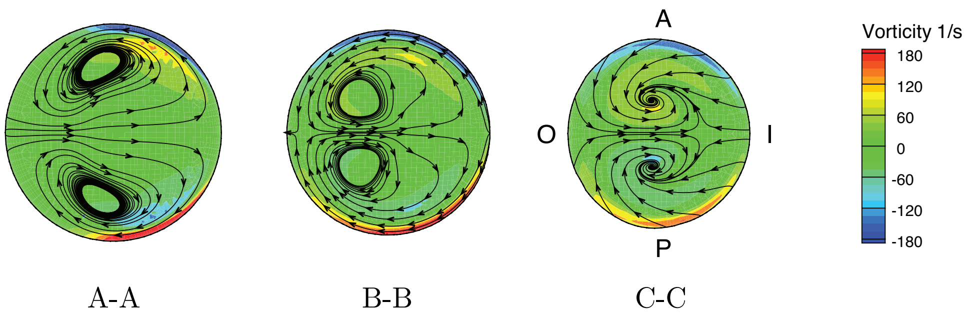

Figure 5.15 Numerical Data: Sectional streamlines and streamwise vorticity magnitude at Re=800 in the carotid sinus at the proximal, mid- and distal location. (I) inner, (O) outer, (A) anterior and (P) posterior wall

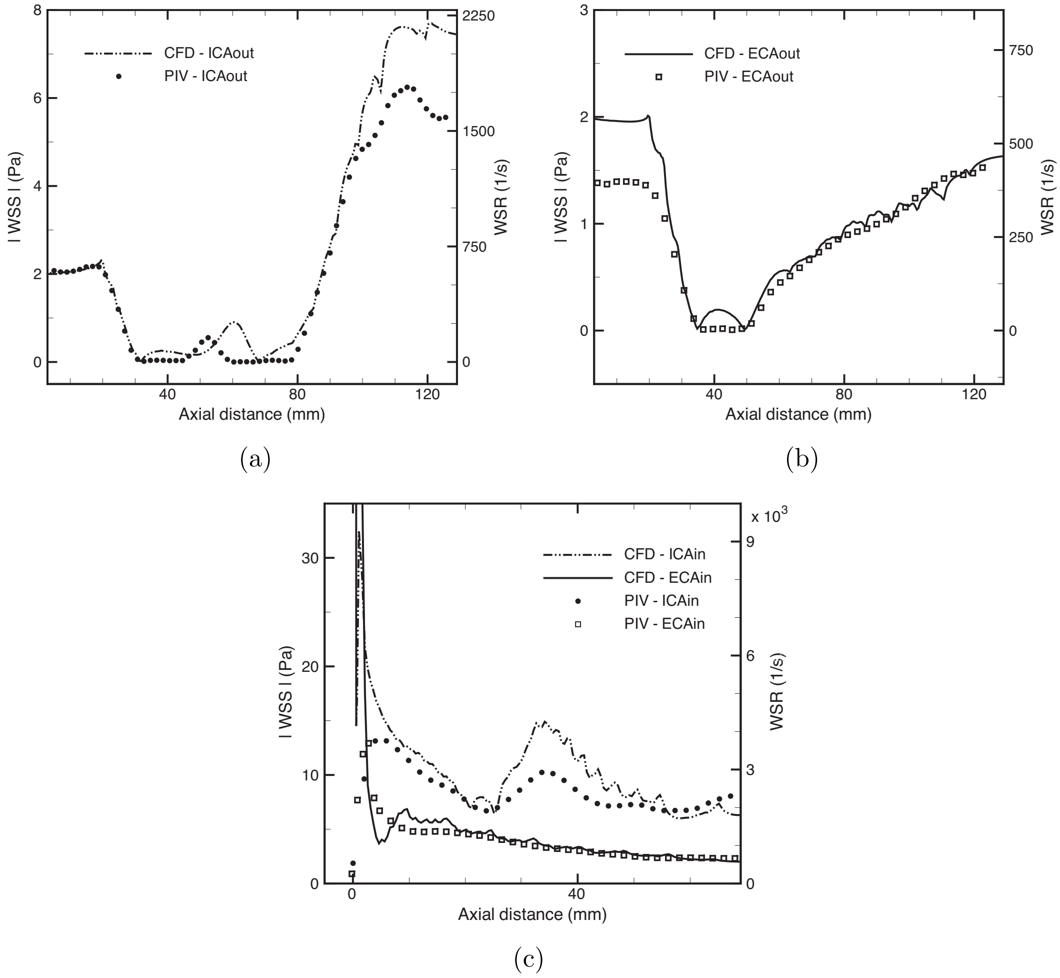

Figure 5.16 WSS magnitude for Re = 800 along (a) the outer internal and (b) outer external carotid artery wall, (c) inner bifurcation walls. Solid lines and symbols indicate CFD and PIV data, respectively

the iPIV technique as it has been discussed already in Chapter 4.4. Overall however, a good qualitative data match is obtained between the two techniques, particularly for medium shear rates and in the proximal and distal parts of the bifurcation.

A summary of absolute and percentage WSS errors is given in Table 5.6 for the outer wall of the common and internal carotid artery. A very good agreement between PIV and numerical WSS data is achieved in the common carotid artery with absolute errors of about 0.02 Pa and ϵ_{rel} = 1.0-1.5%. In the carotid sinus, errors vary greatly between $\epsilon_{rel} = 4.3 - 95.7\%$ and ϵ_{norm} = 0.9-9.8%, depending on Re and location within the sinus. Absolute errors in this area

Table 5.6 Absolute error $f_N - f_E$ and percentage errors ϵ_{rel}, ϵ_{norm} between experimental and numerical wall shear stress. Data are sampled at selected locations along the outer common and internal carotid artery wall.

Section	$Re = 400$			$Re = 800$		
	$f_N - f_E$	ϵ_{rel}	ϵ_{norm}	$f_N - f_E$	ϵ_{rel}	ϵ_{norm}
F-F	0.02	1.5	1.5	0.02	1.0	1.0
A-A	0.05	71.4	5.1	0.2	86.9	9.8
B-B	0.01	95.7	1.0	0.19	42.2	9.3
C-C	0.01	4.3	0.9	0.09	69.2	4.4
D-D	0.29	12.9	29.7	0.78	13.7	38.0

absolute error in Pa

however, are low and only between 0.01-0.2 Pa. Downstream of the carotid sinus, the discrepancies increase to $\epsilon_{rel} = 12.9$-13.7% and $\epsilon_{norm} = 29.7$-38.0% due to the higher shear rates in this region. Note that variations in ϵ_{rel} are always larger than in ϵ_{norm} and that the largest relative errors always occur in areas of low WSS, i.e., carotid sinus. The corresponding normalised error is usually small in these cases. In contrast, large ϵ_{norm} occur for higher shear rates and are of the same magnitude as the relative errors.

5.4 Stenosed Idealised Carotid Artery Bifurcation

Diseased carotid bifurcations are also subjected to disturbed flow conditions, such as detachment and recirculation. In addition to low WSS, areas of high WSS and turbulence are expected to form at the stenosis throat and the post-stenotic region. Steady flow experiments in the 63% stenosed averaged human carotid bifurcation are performed at Reynolds numbers of 400 and 800. The flow characteristics and shear stress distributions are analysed and comparisons are made with the *healthy* idealised model.

5.4.1 Flow Characteristics

The flow in the stenosed carotid artery, as expected, exhibits skewed velocity profiles and secondary flows (Dean vortices) due to centripetal acceleration. At the stenosis throat, axial velocities are accelerated to approximately twice the velocity in the common carotid artery and a jet forms, which impinges on the outer carotid sinus wall. Irrespective of Reynolds number, velocity profiles are skewed towards the outer sinus wall and flow reversal is evident along the inner wall as shown in Figure 5.17. Flow in the external carotid artery appears unaffected by the stenosis and is similar to that in the idealised carotid model.

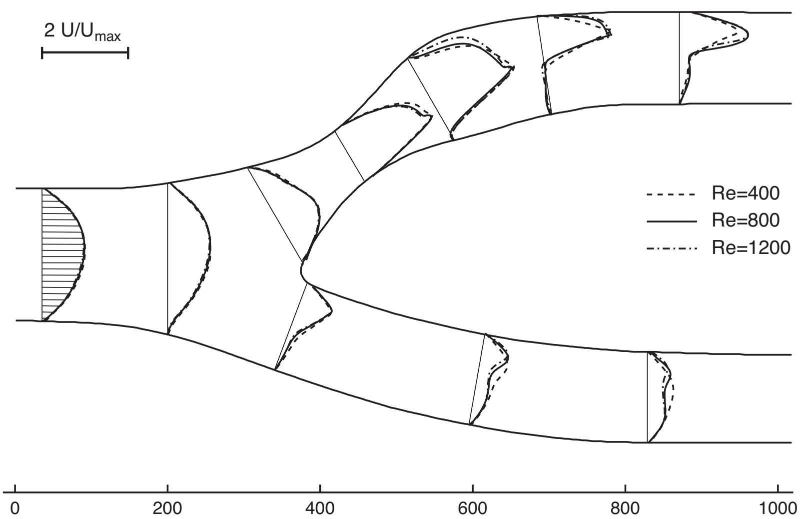

Figure 5.17 Axial velocity profiles in the branching plane of the 63% stenosed carotid bifurcation model at different Reynolds numbers, $Re = 400$ and 800. Data are normalised by the maximum velocity in the common carotid artery

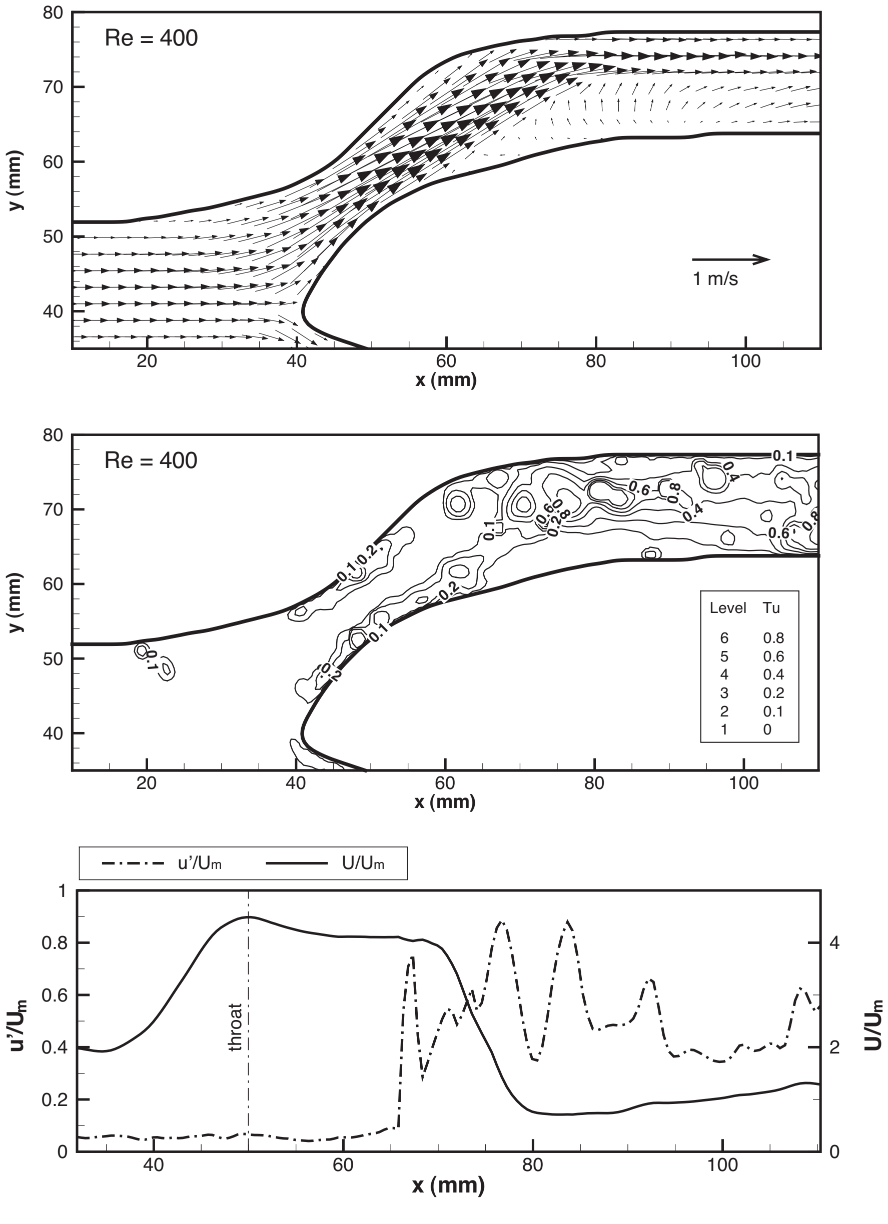

Figure 5.18 Flow patterns in the stenosed carotid artery bifurcation for $Re = 800$; (top) velocity field showing the formation of a stenotic jet and a reversed low velocity region (every 4^{th} vector shown); (center) Turbulence Intensity, $Tu = \sqrt{\frac{1}{2}(u'^2 + v'^2)}/U_m$; (bottom) mean velocity and velocity fluctuation along the vessel centerline

Flow separation occurs immediately after the throat and a large detached flow region exists along the inner bifurcation wall (Figure 5.18(a)). This low flow region is very similar to the one observed in the *healthy* idealised model, yet it occurs along the inner bifurcation wall. The essential characteristics of the helicoidal flow structure are a saddle point at the post-stenotic expansion and a nodal point at the distal sinus. There is also some evidence for a detached flow region along the outer wall, but less pronounced.

The presence of the severe stenosis introduces flow turbulence in the post-stenotic region as illustrated in Figure 5.18(b) by means of turbulence intensity contours. Turbulence intensity, Tu is defined as the ratio of the root-mean-square velocity fluctuation, u', v' to the mean free-stream velocity in the common carotid artery, U_m. Furthermore, no flow disturbance u'/U_m is present prior to the stenosis, but increases rapidly at the post-stenotic expansion as shown in Figure 5.18(c). The velocity fluctuations occur at discrete spatial frequencies and are associated with vortex shedding.

Figures 5.19 and 5.20 present profiles of the velocity and disturbance intensity. Flow through the throat is nearly uniform and a strong shear layer and subsequent flow separation are observed in the post-stenotic region. Turbulence intensity, Tu and axial (u') and circumferential (v') velocity fluctuations

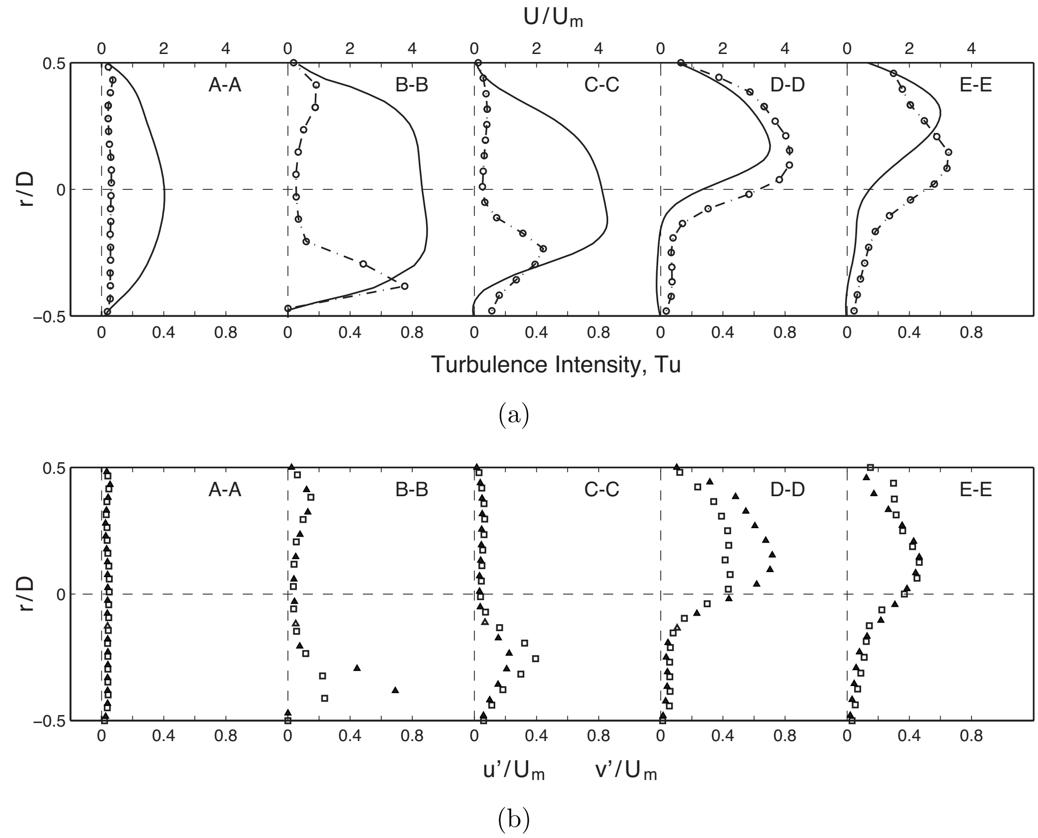

Figure 5.19 Velocity fluctuation at selected axial positions for $Re = 400$; (a) Turbulence intensity (circles) and velocity profiles (solid lines), (b) velocity fluctuation u'/U_m (square) and v'/U_m (triangle)

increase near the wall at the throat (B-B) and in the post-stenotic expansion (C-C). Upstream turbulence levels are low and within the range of measurement noise. Very intense fluctuations occur within the shear layer, reaching values as high 64% in turbulence intensity at section C-C. Turbulence transition occurs in the post-stenotic region and for both Reynolds numbers, velocity fluctuations are in excess of 60% at the distal locations.

Figure 5.21 shows that, for both Reynolds number investigated, the secondary flow pattern in the carotid sinus differ significantly from those in the *healthy* geometry. A strong circumferential flow component exists at the proximal sinus (A-A), due to a reduction in vessel cross-section. Sectional streamlines in this plane converge to a single bifurcation line in the vessel center. At the stenosis throat, the vessel cross-section reduces to about 16% of its original size and the formation of a symmetric pair of counter-rotating vortices can be ob-

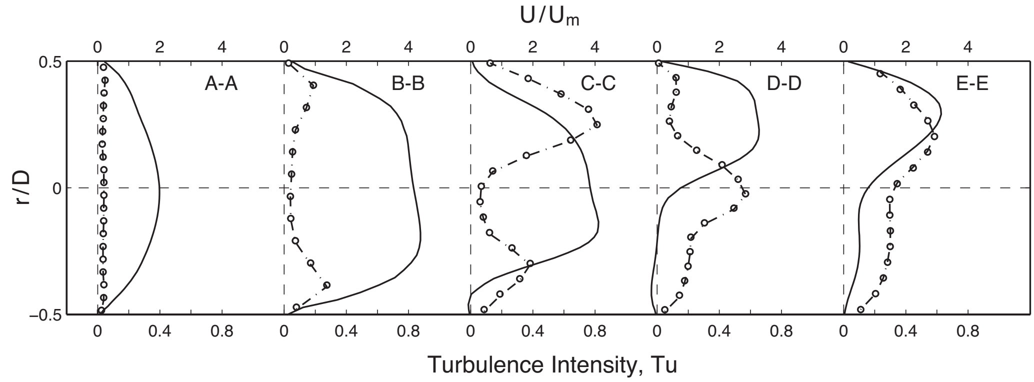

(a)

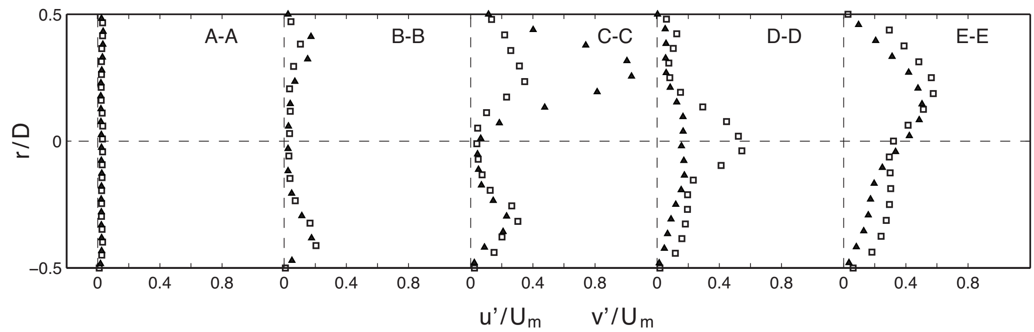

(b)

Figure 5.20 Velocity fluctuation at selected axial positions for $Re = 800$; (a) Turbulence intensity (circles) and velocity profiles (solid lines), (b) velocity fluctuation u'/U_m (square) and v'/U_m (triangle)

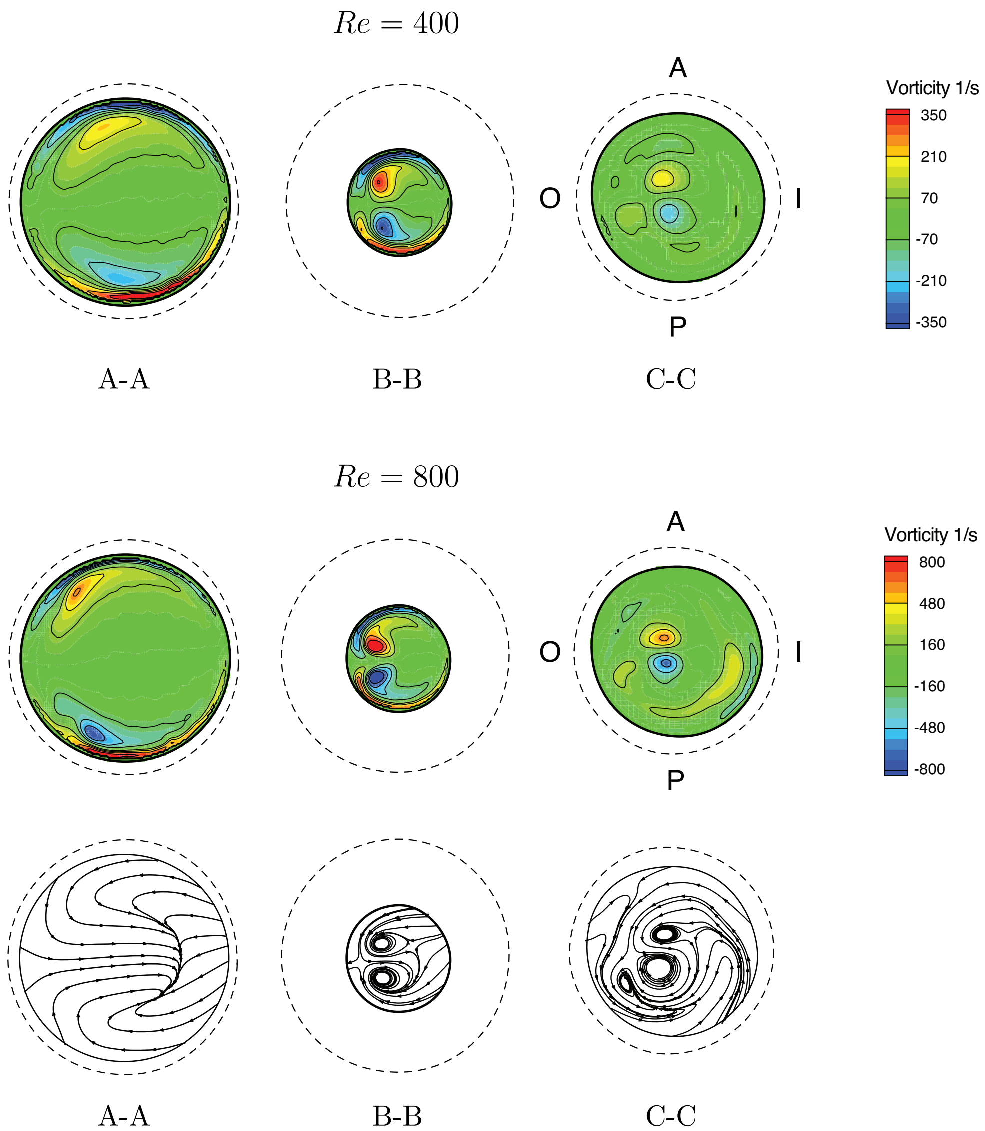

Figure 5.21 Secondary flow pattern in the stenosed carotid artery bifurcation for $Re = 400$ and 800: (top) vorticity magnitude, (bottom) sectional streamlines. Dashed lines indicate cross-section of the *healthy* bifurcation

served. At this point, streamwise vorticity increases to approximately five times of that in the *healthy* carotid model, indicating an increase in strength and tortuosity of the helicoidal flow structure. In the post-stenotic region, secondary velocity and streamwise vorticity decrease again. At this location, the vessel cross-section is somewhat asymmetric (due to manufacturing inaccuracies) and the flow is highly unstable resulting in an asymmetric secondary velocity field and the formation of a third vortex in the lower vessel half. Furthermore, the vessel expansion introduces an adverse pressure gradient, which results in flow separation and disturbance and a low pressure region along the inner sinus wall. Overall, the primary and secondary velocity fields for the two Reynolds numbers are broadly similar, but are more pronounced for $Re = 800$.

5.4.2 Wall Shear Stress

As expected, the 63% stenosis model is subject to very high WSS at the the stenosis neck and on both the inner and outer sinus wall as demonstrated in Figure 5.22. A small recirculation zone exists along the outer wall, which is largest for $Re = 800$ and a second WSS peak occurs at the distal location where the stenotic jet impinges on the outer vessel wall. Regions of low WSS and flow detachment are more pronounced along the inner bifurcation wall (Figure 5.22(b)). Flow separation occurs at the post-stenotic expansion and flow remains detached throughout the majority of the post-stenotic region. Along the distal inner wall, flow reattachment occurs somewhat earlier for $Re = 800$, which may be attributed to the stronger secondary flows and higher turbulence intensity. Overall however, WSS variations are similar irrespective of Reynolds numbers.

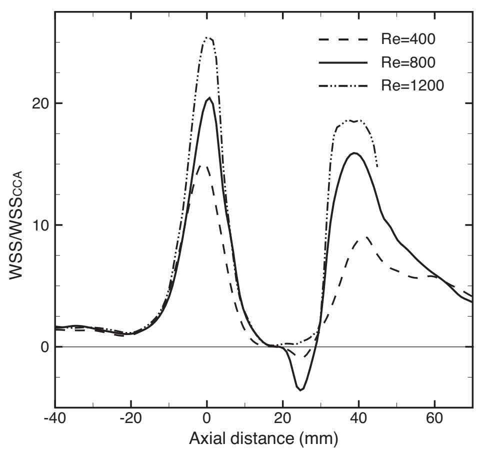

(a)

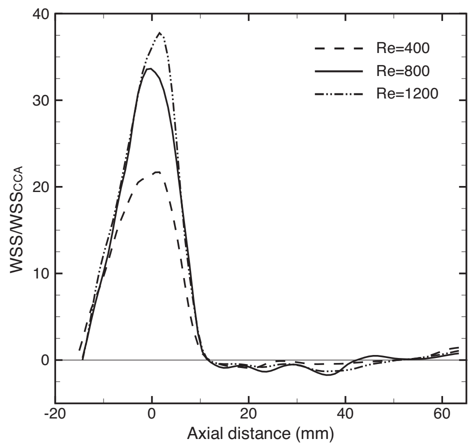

(b)

Figure 5.22 WSS in the 63% stenosed carotid bifurcation for different Reynolds numbers, $Re = 400$ and 800, (a) outer sinus wall, (b) inner sinus wall. Data are normalised by $\text{WSS}_{CCA} = 8Re\rho\nu^2/D^2$

In comparison with the idealised model, the stenosed model is subjected to high WSS peaks (> 60 Pa), which are localised largely at the stenosis throat and the outer post-stenotic wall. Conversely, a large low WSS region (< 2 Pa) exists for the stenosed model along the inner bifurcation wall (Figure 5.23). In the distal internal carotid artery, wall shear stresses are largely similar for both models. Furthermore, WSS in the external carotid branch is unaffected by the stenoses and is low and similar to the idealised model.

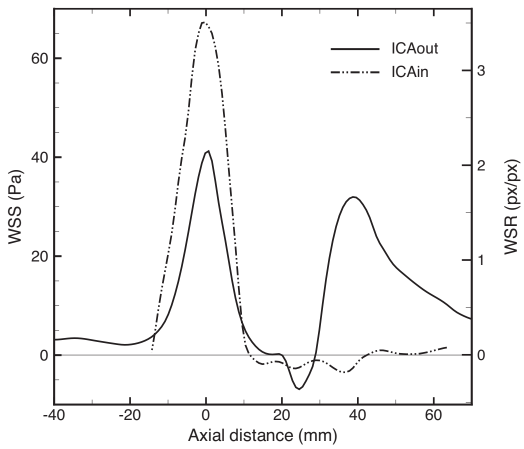

Figure 5.23 Dimensional WSS in the 63% stenosed carotid bifurcation at $Re = 800$

5.5 Discussion and Conclusion

There is a significant amount of literature that identifies the outer bifurcation walls and recirculation zones as regions that are most susceptible to the formation of atherosclerotic plaque [Chatzizisis et al., 2007; Malek et al., 1999; Zarins et al., 1983]. The current experimental model simulates the prevailing haemodynamic environment in the carotid artery under steady flow and shows a strong correlation between regions of low WSS, inlet flow conditions and the arterial geometry. Regions of low WSS imply impaired mass transport [Comerford and David, 2008] and reduced endothelial cell signaling [Plank et al., 2006], and have been directly linked to endothelial dysfunction and the subsequent onset of atherogenesis [Resnick et al., 2003; Traub and Berk, 1998]. In regions of low WSS and flow separation, local mass transfer to and from the wall is inhibited, resulting in reduced ATP concentration and increased LDL concentration at the endothelial surface. Furthermore, regions of low convective transport are prone to particle deposition and platelet aggregation, which is an important contributor to thrombosis formation.

Endothelial cells sense haemodynamic stimuli, which affects alterations in vascular function and in regions of un-disturbed flow, such as the common carotid artery, the vessel diameter adapts to the local flow environment to maintain shear stress levels at approximately 1.5 Pa [Traub and Berk, 1998]. In these areas, the endothelial cells are aligned with the mean flow direction and exhibit athero-protective phenotypes that suppress intimal thickening and plaque growth [Chatzizisis et al., 2007]. In contrast, in areas of low WSS (< 0.4 Pa) and reversed flow, endothelial cell signaling is reduced and the endothelium exhibits pro-atherogenetic phenotypes and becomes susceptible to plaque growth [Malek et al., 1999]. Low WSS leads to reduced WSS-induced nitric oxide (NO) synthesis, vascular smooth muscle cell proliferation, increased permeability of the endothelium and increased LDL uptake.

5.5.1 Idealised Model

Steady flow experiments in an idealised carotid artery bifurcation have identified areas that are subjected to low WSS, and hence, are most susceptible to endothelial dysfunction and disease. These are the outer walls of the internal and external carotid artery, and in particular the proximal locations. The extend of the pathological condition varies with Reynolds number and flow division ratio, however these regions always experience low WSS *relative* to the remaining arterial wall. Hence, these regions can be identified as 'hot spots' for the initiation of atherosclerotic plaque formation due to endothelial dysfunction. Regions of low and spatially varying WSS are more significant at higher Reynolds numbers, due to stronger secondary flows.

The inner bifurcation walls experience high shear stresses and are unlikely to be of significance for the onset of vascular disease. There is a possibility that the upper and lower walls of the bifurcation may also experience low WSS [Ding et al., 2001], and are hence prone to disease. This phenomena however, is highly dependent on the vessel curvature [Comerford et al., 2008]. Curvature effects can be significant in anatomically realistic vessels and are discussed in greater detail in the following Chapter 6 and 7.

The flow in the idealised carotid artery bifurcation exhibits a complex and three-dimensional motion with strong secondary flows. The results of this study therefore agree well with published data in similar idealised geometries [Ding et al., 2001; Marshall et al., 2004; Milner et al., 1998]. Fluid particles are deflected at the bifurcation apex to form a region of reversed, low momentum flow along the outer sinus wall. The formation and size of this region is largely dependent on the Reynolds number and the flow division ratio.

Secondary flow exhibits two counter-rotating vortices and their interaction with the main axial flow results in the formation of a three-dimensional heliocoidal flow structure. These findings are consistent with flow visualisation experiments in similar geometries [Ding et al., 2001; Motomiya and Karino, 1984]. The significance of the three-dimensional flow is its influence on flow separation and reattachment.

Along the outer carotid sinus wall, WSS is generally low and becomes negative at the separation or saddle points and positive again at the reattachment or nodal points, resultig in a high variation in spatial WSS. The results in the idealised model agree well with *in-vivo* research that has correlated regions of low time-averaged WSS and distributed flow (such as those found on the outer bifurcation walls) with the onset of cardiovascular disease [Asakura and Karino, 1990; Zand et al., 1999; Zarins et al., 1983; Ku et al., 1985b].

5.5.2 Stenosed Model

Carotid stenosis severity is commonly used as an indicator for assessing the risk of stroke. However, the majority of individuals with severe carotid artery disease never suffer a stroke, and strokes can even occur for mild or moderate stenosis [Steinman et al., 2000]. This suggests that there are factors other than stenosis severity which may be important in determining stroke risk.

This study investigated the flow pattern in a moderately to severely stenosed carotid artery bifurcation. The flow patterns in the stenotic carotid bifurcation model are composed of a helical Dean-type vortex, a velocity jet at the stenosis throat and post-stenotic flow recirculation. One of the main characteristics of stenotic flow is the presence of turbulence and vortex shedding downstream of the constriction. The extent of flow disturbance depends upon the flow conditions proximal to the stenosis and Reynolds number. In similar studies, Ahmed and Giddens [1983b,a] investigated steady flow through a symmetric constricted tube and Tan et al. [2008] performed numerical simulations in a stenosed carotid bifurcation. Both studies reported high WSS at the stenosis neck and intense velocity fluctuations downstream, and are in accordance with results from this work. Although it is intuitively obvious that the presence of a stenosis will invariably produce elevated shear stress, the time-dependent nature of platelet activation (by high shear) suggests that the post-stenotic flow environment may lead to increased residence time and may be relevant for platelet aggregation and thrombogenesis in these regions.

Several aspects of stenosis geometry vary within individuals, even for lesions with similar degree of stenosis. Lesions at the carotid bifurcation can occur with equal deposition of plaque on both side walls (axisymmetric plaque) or with plaque preferentially deposited on the outer wall, i.e., asymmetric plaque. Although, there is a tendency for asymmetric plaque development, both configurations exist. In a similar study to this, Steinman et al. [2000] have shown that post-stenotic flow also depends on plaque symmetry (or asymmetry) and stenosis severity. In all cases, flow separation always occurred along the inner bifurcation, and only size and location were dependent on plaque geometry. With regard to this study, the identified post-stenotic recirculation size and location and the spatial extent of elevated shear stress are key haemodynamic factors. The distribution pattern of low WSS is closely related to the development of atherosclerotic lesions [Ku et al., 1985b], and may lead to further plaque development downstream of the stenosis. On the other hand, regions of high WSS can lead to smooth muscle cell degeneration, platelet aggregation and thrombus formation, as well as plaque fissure and rupture [Slager et al., 2005].

5.5.3 Experimental - Numerical Comparison

With regard to the comparison between experimental and numerical data, a very good agreement is obtained for the primary and secondary velocity fields with maximal errors between 6.1% to 13.7%. For WSS, larger relative errors occurred in the carotid sinus and are caused by the low WSS magnitude in the error estimation (Equation 5.3). Likewise, normalised errors are rather low in this region with ϵ_{norm} between 0.9% and 9.8%. Absolute differences between CFD and iPIV WSS are 0.01-0.2 Pa in the carotid sinus and 0.78 Pa (ϵ_{rel} = 13.7%) in the distal internal carotid branch. Excellent agreement in WSS is obtained in the common carotid artery. In a similar study, Xiong and Chong [2007] investigated the flow in a distal end-to-side anastomosis and reported similar relative WSS errors of 14-85% and normalised errors of 2.8-21.3%. The present results are particularly encouraging, given the large range of wall shear rate (WSR) within the carotid sinus (i.e., -250 1/s $\leq$ WSR $\leq$ 2250 1/s).

Regarding the experimental WSS, two observations can be made. Firstly, a systematic underestimation of the experimental WSS is evident for high shear rates due to the low pass filtering in iPIV, and secondly, true differences in the three-dimensional flow structure exist in the carotid sinus between the CFD and PIV results. This is evidenced by the mismatch of flow separation and reattachment point in Figure 5.16(a).

The error sources in PIV are extensively discussed in Appendix F and can be divided into experimental and image processing uncertainties. In PIV, an area-averaged displacement is determined based on the assumption of a homogeneous tracer displacement within the interrogation volume. This is not always the case, and spatial velocity gradients and large out-of-plane velocity components greatly affect the accuracy of the cross-correlation function[5]. As a result, the signal-

[5]The current PIVCC algorithm utilises iterative correlation and window deformation techniques to compensate for such effects, but they can by no means be eliminated, see Chapter 3.4.1 for more detail

to-noise ratio decreases and velocity estimates are biased towards lower values. Hence, the experimental velocity fields have a higher uncertainty in areas with strong secondary flows and steep velocity gradient such as in the carotid sinus.

Experimental uncertainties include light reflections and optical noise at the model interface, which are caused by a slight mismatch in refractive index and tracer particle accumulation in stagnant and low momentum flow areas. As discussed in Chapter 4.2, this results in erroneous vector calculation, data drop out and adversely affects the WSS estimation with iPIV. Other experimental errors include mismatches in flow rate and viscosity, and hence Re due to measurement uncertainties and temperature changes in the working liquid.

Furthermore, differences in the geometric details of the experimental flow phantom and the numerical mesh can also give rise to errors. Although both models are created from the same data set, small differences in vessel diameter and curvature are introduced during the manufacturing process of the flow phantom ($\epsilon = 1.4\%$, Chapter 2.4). The main sources of numerical errors are numerical diffusion and discretisation errors, but are not discussed here in further detail.

Overall, the agreement between numerical prediction and measurement is satisfactory and percentage differences between the data are similar to the experimental and image processing errors.

5.5.4 Physiological Limitations

Finally, some physiological limitations of this study should be noted. The carotid bifurcation models used in this study, although based upon measurements from patient angiograms, are idealised. The models are axi-symmetric across the plane of the bifurcation and the vessels have circular cross section. For example, recent work by Milner et al. [1998], demonstrated that curvature effects can have a significant impact on the amount of secondary flow compared to idealised models. This in turn would impact both wall shear stress and flow recirculation. Furthermore, the assumptions of steady flow, rigid walls, and Newtonian blood properties are also likely to be physiologically limiting for the accurate modelling of carotid artery haemodynamics. Whilst the latter two assumptions are now widely accepted, the assumption of steady flow is still controversial. The time scale of one cardiac cycle (approx. 1sec) is considerably shorter than that of physiological processes relevant to atherogenesis, which is known to occur over time scales in the order of decades [Plank et al., 2006; Wiesner et al., 1997]. On the other hand, there is consensus for the correlation between endothelial dysfunction and temporally oscillating shear stress [Ku et al., 1985b; Zarins et al., 1983] as well as mean shear stress gradients [DePaola et al., 1993; LaMack and Friedman, 2007].

Therefore an investigation in the pulsatile nature of carotid blood flow in a patient specific geometry will be presented in the next Chapter 6 to assess the relation between time-averaged and steady flow haemodynamic metrics.

Chapter 6

Patient Specific Modeling[1]

This chapter presents velocity and WSS measurements in a physiologically realistic carotid artery model under steady and pulsatile flow conditions. The development of the physiological flow phantom from *in-vivo* MRI angiogram data together with a description of the physiological inlet waveform is presented in the first part. This is followed by a brief a description of the experimental setup and the developed piston pump to reproduce the physiological waveform *in-vitro*. The haemodynamic field is first analysed under steady flow conditions, before pulsatile effects are studied. The reconstructed model has an interesting geometric complexity that potentially provides more insight into the mechanisms of atherosclerosis within the human carotid artery. The analysis of time averaged and steady state WSS provides for an interesting comparison and conclusions regarding the applicability of the steady flow assumption are drawn. Furthermore, the pulsatile flow results illustrate the time-depended variation flow recirculation, secondary flows and WSS distribution. The chapter concludes with a discussion of some of the physiological implications and measurement constraints.

[1]The content of this chapter has in part been published in *Int. J. of Experimental and Computational Biomechanics*, 2009, Vol. 1, No. 2, pp.172-192, under the title:

Experimental investigation of carotid artery haemodynamics in an anatomically realistic model

N.A. Buchmann, M.C. Jermy and C.V. Nguyen

6.1 Introduction

This chapter implements the previously described modelling and measurement methodologies into an anatomically realistic geometry of the carotid artery bifurcation. The present study will focus on wall shear stress (WSS) characteristics under steady and pulsatile flow, as there are very few published studies concerning the measurement of these quantities in a realistic geometry. Idealised models of the carotid artery represent only a population average and tend to omit interesting flow features observed in *real* arteries [Milner et al., 1998].

A major focus of this study will be the application of the developed iPIV technique to an anatomically realistic geometry with physiological boundary conditions, i.e., inlet waveform. The geometry includes a non-uniform arterial wall and complex vessel curvature, and it will be interesting to observe how this will affect the WSS distribution and prevailing flow field. The incorporation of a physiological inlet waveform will provide for an interesting analysis of the primary and secondary flow field, flow recirculation and spatial distribution of WSS under different flow conditions. There is a strong correlation between endothelial dysfunction and temporally oscillating shear stress [Ku et al., 1985b; Zarins et al., 1983]. Therefore, it will be interesting to observe any differences between steady-state WSS and time-averaged WSS. Furthermore, WSS transients will be investigated to give insight into the oscillatory nature of the prevailing haemodynamics.

6.2 Methodology

6.2.1 Arterial Geometry and Boundary Conditions

The geometry of the carotid model is created from *in-vivo* MRI angiogram data of the left common (CCA,) internal (ICA) and external (ECA) carotid arteries of a healthy male volunteer. The cross-sectional image slices are acquired on a GE MR scanner (3.0T, Sigma) with a 2D *time-of-flight* (TOF) sequence. A total of 84 parallel image slices are obtained covering the bifurcation region about 100mm in length. Continuous 1.2mm thick slices are recorded with an in-plane resolution of 0.47mm, (Table 2.1). The image segmentation technique used for the 3D lumen reconstruction was developed by Moore [2008] and is discussed in Chapter 2.3.2. The resulting anatomically realistic carotid artery bifurcation is comprised of the common carotid artery and its bifurcation into the internal and external carotid artery and is shown in Figure 6.1.

The geometry exhibits some interesting variations, such as asymmetry and to some extent *secondary curvature* or non-planarity [Caro et al., 1996; Friedman and Ding, 1998]. The surface of the model exhibits true *in-vivo* characteristics. The wall includes topological variations, which lead to differences in cross-sectional area and asymmetry along the vessel axes. The vessel has a nominal common carotid artery diameter of 7.2mm and a bifurcation angle of approximately 40^o. The geometry is scaled to 2.8 times life size to allow for a higher effective spatial resolution during the velocity and WSS measurements and the transparent flow phantom is created as detailed in Chapter 2.4. The anatomically accurate flow phantom is shown in Figure 2.11.

Figure 6.2 details cross-sectional planes setup to observe secondary flow features and comprise the bifurcation region and the the carotid sinus. The

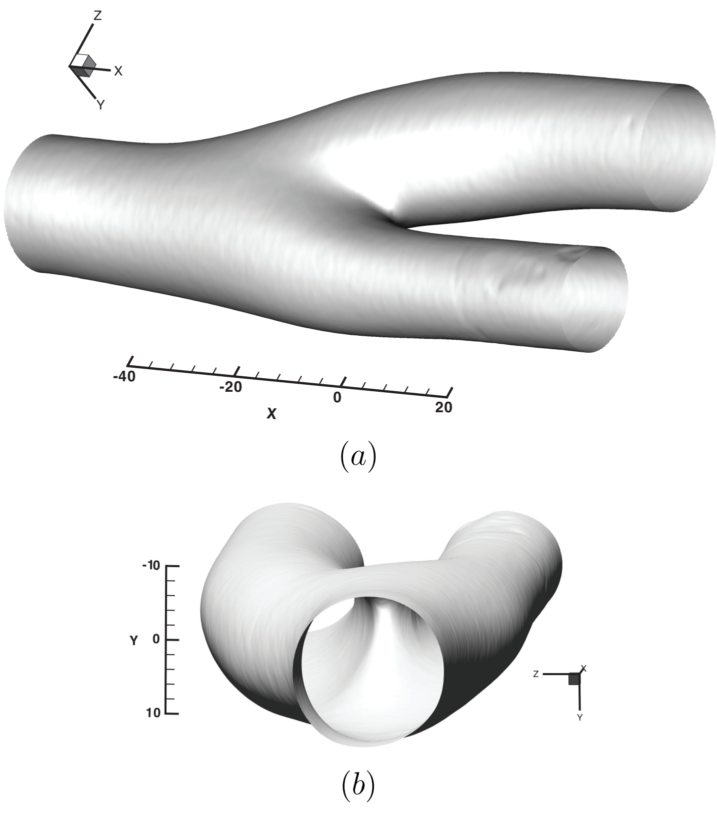

Figure 6.1 Reconstructed carotid artery geometry comprising the common carotid artery, internal and external carotid artery. (a) side view, (b) front view

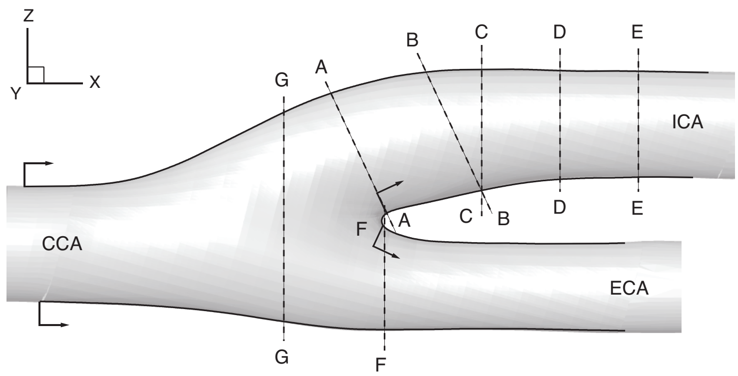

Figure 6.2 Locations of cross-sectional planes to observe secondary flow characteristics and WSS and the inner and outer bifurcation walls. Arrows indicate plot direction

geometry in this region exhibits asymmetry and secondary curvature, and the measurement planes are tightly spaced to capture the variations in vessel calibre. Information regarding WSS is detailed along lines on the inner and outer walls of the internal and external artery branch (Figure 6.2). The lines are located within the measurement (or bifurcation) plane, which is positioned symmetrically across the inlet diameter.

The time-dependent *in-vivo* flow rates in the same volunteer are determined with *Phase Contrast* (PC) MRI measurements. A detailed explanation of phase contrast MRI is given in Vlaardingerbroek and Boer [1996]. The basic principle is that a reversal of one of the magnetic field gradients causes a change in the MR signal, which is directly proportional to the blood velocity. Furthermore, gated *cine* PCMRI is used to obtain the variations in blood flow throughout the cardiac cycle.

Measurements are taken at locations approximately five common carotid diameters downstream and upstream of the bifurcation. The measurement planes are oriented perpendicularly to the vessel axis and only the axial velocity component is acquired with an encoding velocity[2] of 75mm/s. The recorded images are cardiac gated and a total of 30 recordings are equally spaced during one cardiac cycle. Additional recording parameters are give in Table 2.1.

[2]encoding Velocity V_{ENC} is the maximum velocity measurable by the MRI scanner. For the current GE 3.0T pixel velocity in cms^{-1} is one tenth of the pixel intensity and the dynamic intensity range is $-10V_{ENC} : +10V_{ENC}$

The resulting *cine* PCMRI scans consist of magnitude images, which contain information about the arterial lumen (similar to TOF data) and phase images with the embedded velocity information. Representative samples of the phase images for different time steps are shown in Figure 6.3(a) for the common carotid artery. The procedure to obtain the respective cardiac waveforms in the common, internal and external carotid artery is similar to that used in the 3D lumen reconstruction and is detailed in Moore [2008]. At each time step, the lumen cross-section is identified from the magnitude image. The mean velocity is calculated as the average pixel value in the phase image and the individual flow rates are computed as the mean velocity multiplied by the lumen area. The resulting waveforms for the common, internal and external carotid artery are shown in Figure 6.3(b). A closer inspection of the computed waveforms reveals a slightly lower flow rate for the combined outlet branches (i.e., ICA+ECA) compared to the inflow in the common carotid artery. This is for two reasons: first, further away from the bifurcation, the external artery branches multiple times, which makes it difficult to image the flow in all of the adjoining vessels. And secondly, closer to the bifurcation, measurement artifacts arise due to the complex flow structure, which introduce errors in the phase contrast MRI measurements [Milner et al., 1998].

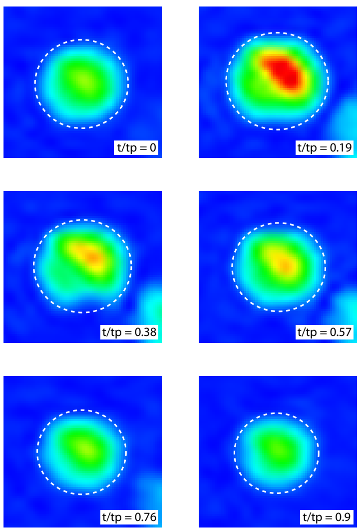

(a)

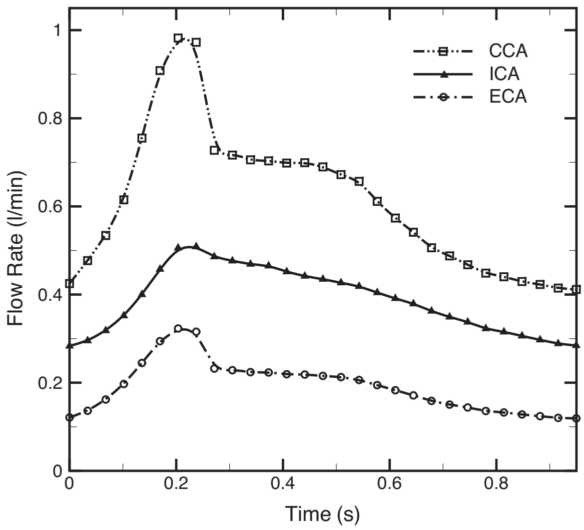

(b)

Figure 6.3 (a) Cine PCMRI phase intensity images of the left CCA at 6 discrete time steps. Note the asymmetric velocity profile, indicating the presence of undeveloped, helical flow in the CCA. Dashed lines indicate the approximate vessel cross-section. (b) Reconstructed cardiac flow wave in the CCA, ICA and ECA; (symbols) measured data, (lines) smooth data points

The phase images in Figure 6.3(a) show an asymmetric velocity profile in the common carotid artery, evidencing undeveloped, helical flow prior to the carotid bifurcation. A recent study by Moyle et al. [2006] demonstrated that the effects of secondary velocities in the inlet profile on spatial and temporal WSS are significantly smaller than the effect due to geometric variability. Furthermore, they conclude that the assumption of fully developed inlet flow is justified, if a sufficient entrance length of realistic geometry is modeled. In the present case, the physiological model extents approximately five vessel diameters upstream of the bifurcation, which is considered here to be of sufficient physiological entrance length.

6.2.2 Experimental Setup

Flow Facility

A schematic of the flow facility is shown in Figure 6.4 and consists of a steady flow loop and a computer controlled piston pump to provide oscillatory flow. A detailed description of the operation of the steady flow facility is provided in Chapter 5. Pulsatile flow at the test section is obtained by superpositioning of the steady and oscillatory flow component.

The computer controlled piston pump consists of a linear pneumatic actuator controlled by a proportional directional valve and connected to a hydraulic cylinder of diameter, $D = 20$ and length, $L = 250$mm as shown in Figure 6.5. It is important that the hydraulic piston follows the planned trajectory faithfully since any deviations would result in a misinterpretation of the investigated flow. To ensure accurate and repeatable motion of the hydraulic piston, feedback is provided by a linear encoder connected to the pneumatic cylinder and an electromagnetic flow meter at the test section entrance. Real time closed loop control of the piston pump is obtained with a LabView (National Instruments) motion control program stored on an Intel Pentium IV 2.6GHz desktop computer. The piston stroke and the cycle frequency can be adjusted independently such that any waveform and combination of Reynolds and Womersley number can be investigated. The piston pump can perform strokes up to 250mm at a frequency up to 1Hz.

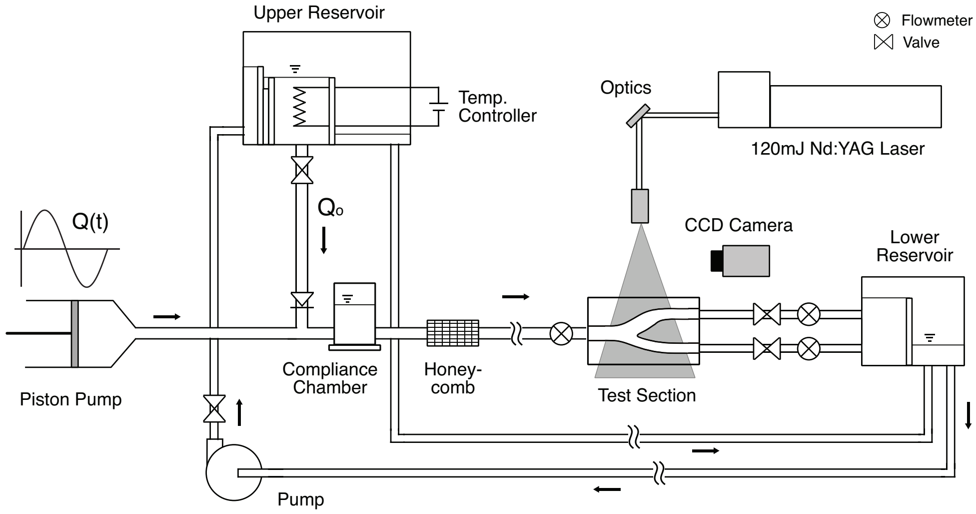

Figure 6.4 Schematic representation of the experimental facility showing the flow circuitry and the optical setup. Note the piston pump and compliance chamber. Pulsatile flow in the test section is achieved by super position of the steady Q_0 and oscillatory flow component $Q(t)$

One major concern in designing the oscillating flow pump is the potential for high frequency flow perturbations and attenuation of the wave propagation speed. In both cases, the effects on the inlet waveform would be undesirable and would contaminate the measurements. To minimise high frequency oscillations and sharp pressure waves, a positive pressure vessel (i.e., compliance chamber) is included downstream of the piston pump (Figure 6.4). The compliance chamber is charged with compressed air and stores kinetic flow energy while damping high frequency oscillations. Depending on the air pressure and air-to-liquid ratio, different damping ratios can be chosen. On the downside, the compliance chamber increases the phase lag and attenuates the flow amplitude. This is accounted for by the in-line electromagnetic flow meter (OPTIFLUX 2040 C, Krohne) installed at the test section inlet. The meter provides real-time flow wave information and is used for feed-back control to ensure the desired inlet waveform at the model inlet.

Both piston pump and model outlets are connected to straight pipes of length $L = 75D$ to ensure fully developed flow at the model entrance and exit. Note that in oscillating flow, the necessary entrance length to obtain fully developed flow reduces by almost 40% compared to steady laminar flow [Burgmann et al., 2009], and as such, the entrance length of the flow facility can be considered sufficient to obtain fully developed flow. The facility is operated with the refractive index matched working liquid composed of 39% water and 61% glycerin ($\nu = 10.2 \cdot 10^{-6}\text{m}^2/\text{s}$, $\rho = 1.15\text{g/cm}^3$ at 20^oC). Depending on the temperature/viscosity of the working liquid, the maximum achievable Reynolds and Womersley numbers are approximately 2500 and 8.3, respectively.

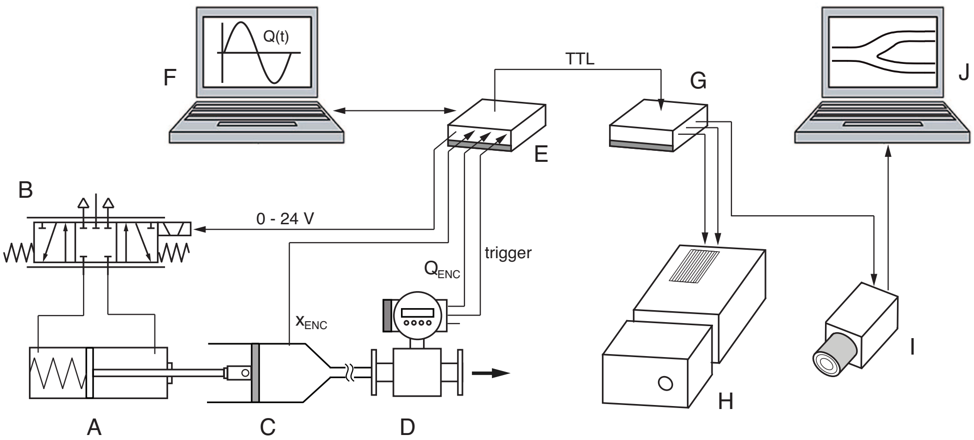

Figure 6.5 Schematic of the real-time control and data acquisition system: A) pneumatic actuator, B) proportional pneumatic valve, C) hydraulic cylinder, D) electromagnetic flow meter, E) real-time controller, F) control PC, G) pulse delay generator, H) Nd:YAG laser, I) CCD camera, J) camera control and data acquisition PC

PIV Measurements

The flow field and WSS in the carotid artery model is investigated with phase-locked PIV measurements. The PIV setup is similar to that used for the steady flow measurements and described in Chapter 5. The PIV recording system is synchronized to the piston stroke with the real-time controller and is initiated by a trigger signal from the electromagnetic flow sensor as detailed in Figure 6.5. On receipt of the trigger signal, the controller activates a pulse delay generator, which in turn synchronizes the laser pulses and the camera shutter. The acquired images are stored on an Intel Pentium III 1.33GHz desktop computer and consecutive image pairs are acquired at a rate of 14Hz or 43 image pairs per cycle. The time delay between the two laser pulses is adjusted in compliance with the flow field such that an optimal pixel displacement is achieved. Note that for oscillating flow, a compromise with respect to the detection accuracy during flow reversal and peak pixel displacement at peak systole is necessary.

Using the illustrated sequence, measurements can be acquired at any time during the cardiac cycle to perform an appropriate phase-averaging of the results.

To determine the global velocity field and WSS distribution, the recorded data are processed with the adaptive multigrid PIVCC and iPIV algorithms. The image processing parameters are similar to those used in the steady flow experiments and are detailed in Chapter 5 and Table 5.4. The image evaluation includes an initial interrogation window IW_0 of 64 pixel and two subsequent refinement steps and 75% window overlapping. Ensemble correlation averaging is used for the steady flow data, while for the pulsatile flow, time and phase averaged velocity and WSS fields are calculated. An extensive uncertainty discussion for the current experimental procedure is given in Appendix F and some measurement parameters are summarised in Table 6.1

Table 6.1 Overview of recording parameters

Field of view (mm)	120×100
Spatial resolution (mm)	1.96
Vector spacing (mm)	0.49
Dynamic range (px)	± 16
Vectors/sample ($-$)	15,600
No. of samples ($-$)	$100 - 450$
No. of cycles ($-$)	$15 - 100$

6.2.3 Description of the Measurement

For the unsteady flow experiments, the oscillatory flow component is obtained by Fourier decomposition of the measured cardiac waveform shown in Figure 6.3(b). The cardiac waveform is first sampled at discrete locations throughout the cycle and the individual Fourier coefficients are calculated to define the unsteady component, $q(t)$ as follows:

$$q(t) = \frac{A_o}{2} + \sum_{n}^{N} A_n \cos\left(\frac{2\pi n t}{T}\right) + \sum_{n}^{N} B_n \sin\left(\frac{2\pi n t}{T}\right) \tag{6.1}$$

where n represents the Fourier mode, N the maximum mode determined by the number of phase contrast MR images per cardiac cycle, and A_n and B_n the Fourier coefficients. Note that typically the first 8 Fourier coefficients contain 99% of the energy [Lou and Yang, 1992] and are listed in Table 6.2 for the waveform shown in Figure 6.6.

To provide the the time-dependent displacement input to the piston pump, the resulting Fourier series is integrated to $x(t) = \frac{1}{A}\int_0^T q(t)dt$, where A is the cross-sectional area of the piston.

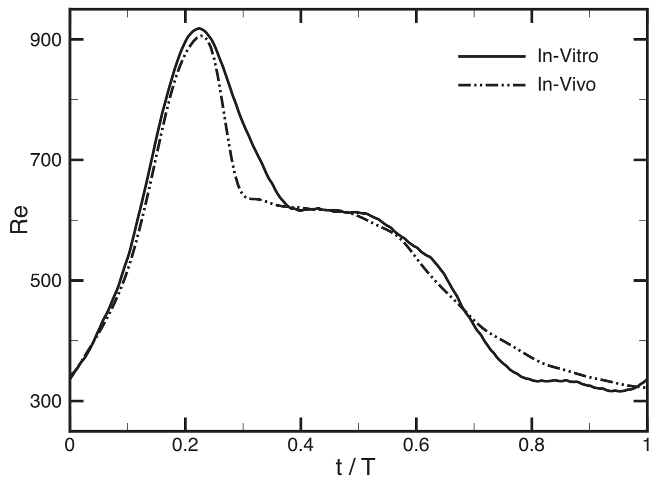

Figure 6.6 Pulsatile *in-vitro* and *in-vivo* inlet waveform

Once the unsteady component of the waveform is found, the inlet profile is obtained by superimposing the steady and oscillatory components to $Q(t) = q_0 + q(t)$. The resulting waveform at the inlet of the bifurcation model is displayed in Figure 6.6. Also shown in the *in-vivo* waveform in the common carotid artery as measured by phase contrast MRI. Some differences occur during early flow deceleration and at late diastole. Overall, the match between the two waveforms is satisfactory and the developed flow circuitry provides accurate and repeatable inflow conditions.

The dimensionless parameters describing the pulsatile flow are the Reynolds number, Re, the Womersley number, α and the pulsatility index, $\hat{u}/U_m$ and are defined in Equation 2.8 to 2.10. For the present cardiac waveform, mean and peak Reynolds numbers are 540 and 920, and $\alpha = 4.54$, translating to an *in-vitro* time period of approximately 3 seconds and a peak flow of 8.7l/min. The division of flow between the internal and external branch varies over the cardiac cycle, with a division of approximately 5:5 (ICA:ECA) during systole and 8:2 during early diastole (Figure 6.3(b)). Overall, the cycle averaged flow division accounts to approximately 7:3 (ICA:ECA) and is consistent with previous studies [Ku and Giddens, 1987]. Adjusting the flow circuitry to produce the averaged flow division ratio of 7:3 in the two outlet branches results in a very similar variation throughout the cardiac cycle to that observed *in-vivo*. Steady flow experiments are performed at inlet Reynolds numbers of 453, 540 and 704.

The velocity field is observed in the median plane of the bifurcation and cross-sectional planes in the internal and external carotid artery as detailed in Figure 6.2. Wall shear stress is observed in the median plane and along the inner and outer walls of the bifurcation. Results are presented for both, steady and pulsatile flow conditions. For the pulsatile flow simulations, instantaneous images are acquired at 43 different phases along the cardiac cycle and time, and phase averages are calculated from 15 and 100 recorded waveforms respectively.

Table 6.2 First 8 Fourier coefficients for the waveform shown in Fig. 6.6

n	0	1	2	3	4	5	6	7
A_n	11.152	-0.849	-0.621	-0.47	0.148	0.194	-0.071	-0.094
B_n	0	1.523	0.416	-0.381	-0.271	0.084	0.148	-0.025

coefficients in l/min

6.3 Steady Flow Results

6.3.1 Flow Characteristics

Steady flow in the physiological carotid artery model exhibits some very interesting phenomena and dynamics, including helicoidal and reversed flows. Helicoidal flow is formed in the bifurcation due to the vessel curvature and the herewith imposed secondary flow as already discussed in Chapter 5.3. The non-uniform and additional secondary curvature of the physiological model create very complex radial pressure gradients (due to centripetal acceleration) that vary over the vessel cross-sections and in streamwise direction. This leads to significantly more complex flow patterns than those observed in the idealised model, which are discussed in the following.

An interesting feature of the physiological model is the marked difference between the internal and external branch as seen in Figure 6.7. In the internal carotid artery, the axial velocity profiles are similar to the previous idealised model, with the high momentum fluid at the inner wall and the low momentum flow region at the outer sinus wall. In contrast to this, flow in the external carotid artery exhibits a stronger helicoidal motion and flow separation compared to the idealised model. The separated flow region forms relatively early in the bifurcation and increases in size towards the proximal external carotid artery. Reattachment occurs approximately $0.5D$ downstream of the bifurcation. The size and extent of the flow re-circulation changes with Reynolds number and is also likely to be affected by variations in flow division during the cardiac cycle. Overall, the prevailing steady flow field in the physiological model appears counter-intuitive compared with the idealised model, and it will be interesting to observe these differences under pulsatile flow conditions.

In contrast to the idealised models, in which the daughter arteries are circular and lie in a common plane, the present geometry has both in-plane and secondary curvature. These curvatures set up opposing pressure gradients to that caused by branching and lead to significantly different flow dynamics. Considering Figure 6.8, secondary flow streamlines evidence the vortical flow structure in the internal carotid artery.

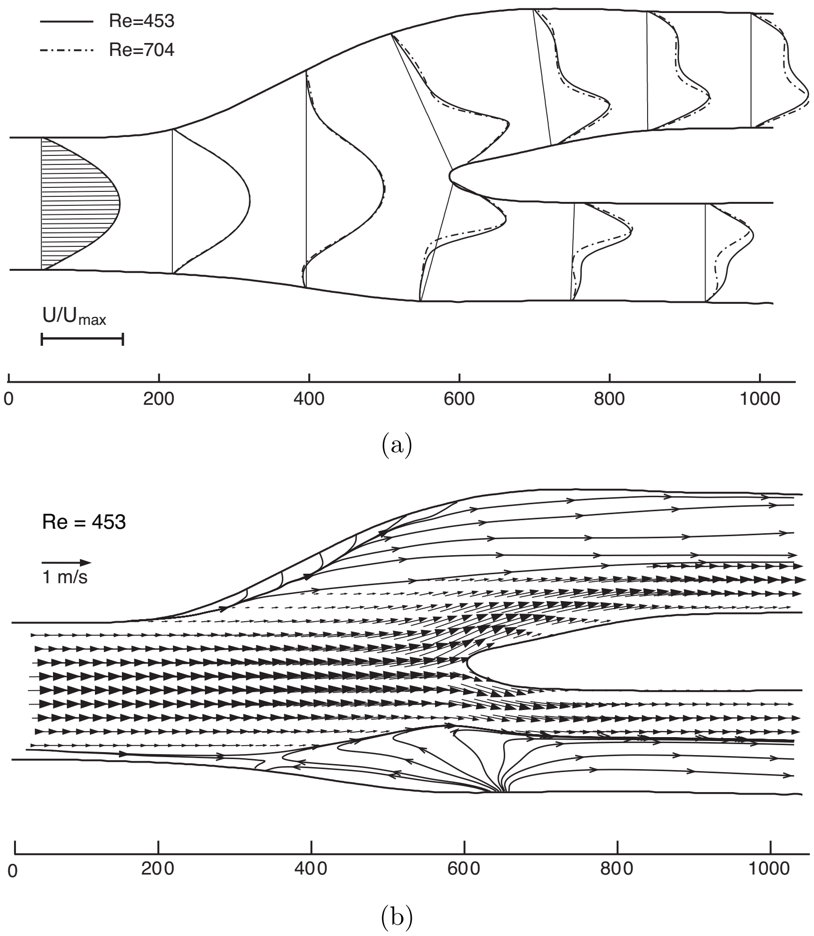

Figure 6.7 (a) Axial velocity profiles in the branching plane of the anatomical realistic carotid bifurcation model at different Reynolds numbers, $Re = 453$ and 704. (b) vector field and sectional streamlines in the the branching plane for $Re = 453$

At the proximal sinus, a pair of counter rotating vortices exist with the upper one being somewhat weaker. The strength of the lower vortex is driven by a stronger retrograde flow (deflected from the apex) in the posterior half of the vessel. Progressing into the internal artery (plane B-B), the vortices dissipate before a single vortex forms at the distal sinus (plane C-C). Rotation of this vortex is observed in plane C-C due to the secondary curvature and has also been observed by others [Moore et al., 1999; Papaharilaou et al., 2002]. This vortex rotates counter-clockwise along the streamwise axis and a second, unevenly matched, clock-wise rotating vortex forms in plane E-E. The vortices are pushed towards the inner wall primarily due to the in-plane straightening of the vessel, which results in a third vortex at the bottom of the vessel (posterior wall). A counter-clockwise movement the secondary flow exists and the resulting vortex pair is rotated nearly a full 90^o. This rotation can be attributed to vessel asymmetry and secondary curvature in this region. Note that measurements of the secondary flows in the external carotid artery are not possible due to constraints in the optical accessibility of the current flow phantom.

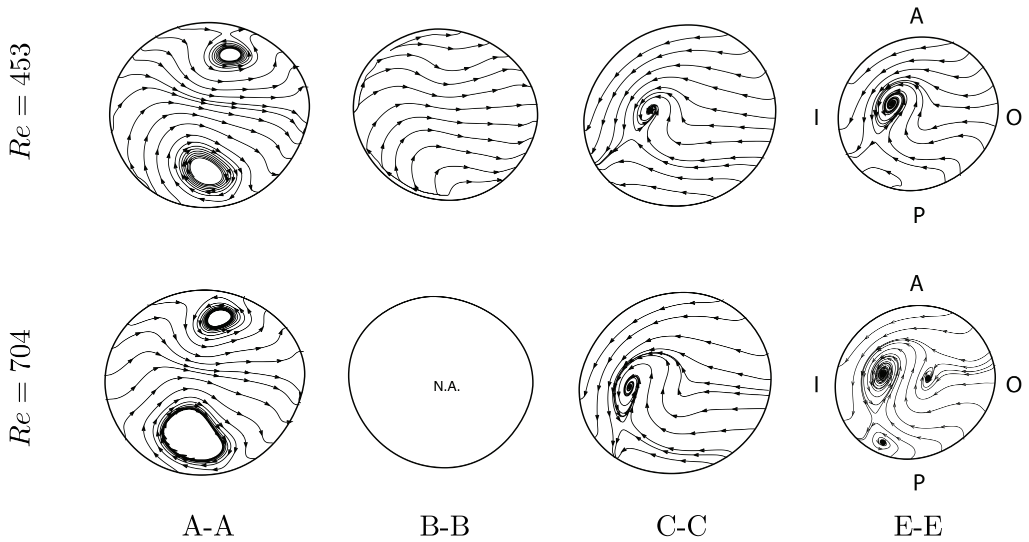

Figure 6.8 Secondary flow streamlines at Re = 453 (top) and Re = 704 (bottom) in the carotid sinus at the distal internal carotid branch. (I) inner, (O) outer, (A) anterior and (P) posterior wall. Note, measurements at B-B for Re = 704 were not possible due to experimental limitations

6.3.2 Wall Shear Stress

Similar to the idealised geometry, regions on the outer walls are subjected to low shear stress, while the inner bifurcation walls experience rather high WSS. This is directly related to the high momentum fluid being 'thrust' towards the flow divider walls as it is clearly evidenced in Figure 6.7. However, the detailed distribution of WSS along the outer walls is different to that in the idealised model, and is influenced by local variations in vessel curvature and surface topology. Additionally, the non-uniform vessel caliber leads to local flow acceleration and deceleration, which further alters the WSS distribution.

Figure 6.9(a) and 6.9(b) demonstrate variations in WSS consistent with the observed flow patterns, along the outer walls of the two daughter branches. The sharp decrease in WSS at the proximal location corresponds to flow separation and the small spatial variations seen in both distributions are due to local curvature variations. Overall, the shear environment in the external carotid artery is considerably weaker than in the internal artery and is dependent on Reynolds number and flow division. Although no flow recirculation occurs in the internal carotid artery, these differences will be interesting to observe under pulsatile conditions. Wall shear stress along the inner bifurcation walls is similar to the idealised model, with flow stagnation at the bifurcation apex and medium shear stress levels in the distal arteries (Figure 6.9(c)).

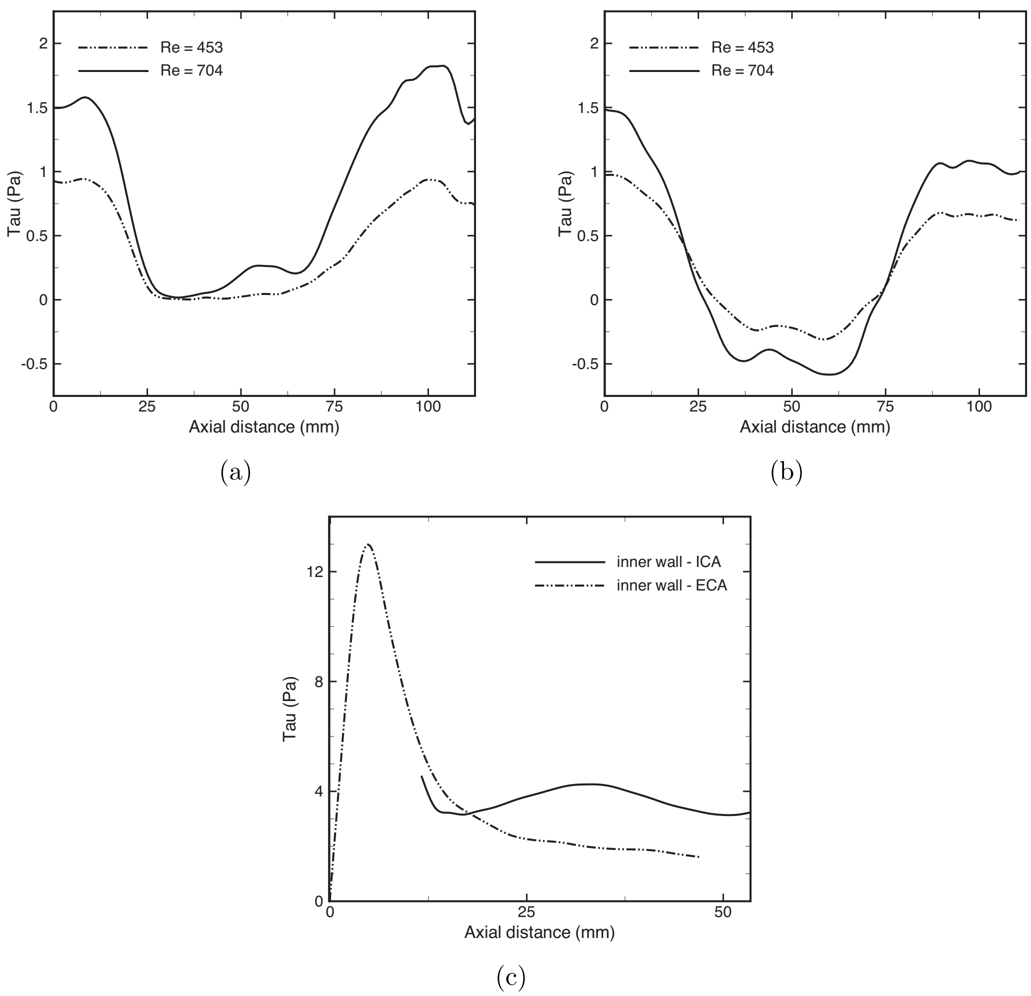

Figure 6.9 WSS in the anatomically realistic carotid bifurcation for different Reynolds numbers, $Re = 453$ and 704, (a) outer internal carotid artery wall; (b) outer external carotid artery wall; (c) inner bifurcation walls for $Re = 800$

6.4 Pulsatile Flow Results

In order to justify the assumption of steady flow conditions, an investigation into the pulsatile nature of carotid artery flow is necessary and presented in the following. This provides an understanding on how different flow conditions affect the formation of flow recirculation and spatial distributed WSS, and to observe the differences between steady-state WSS and time-averaged WSS. Furthermore, the oscillatory shear index (OSI) will give insight into the oscillatory nature of the prevailing haemodynamics.

6.4.1 Time Average

The time averaged wall shear stress (TAWSS) over the course of one cardiac cycle of period T is given by:

$$\text{TAWSS} = \frac{1}{T}\int_0^T \tau_w dt \tag{6.2}$$

where τ_w is the instantaneous WSS vector. An important time dependent WSS index is the oscillatory shear index (OSI) originally proposed by [Ku et al., 1985b]. This quantity provides fundamental information about the oscillatory nature of the prevailing haemodynamics and assesses the variational nature of the WSS vector with the time averaged WSS as follows:

$$\text{OSI} = \frac{1}{2}\left(1 - \frac{\tau_{mean}}{\tau_{mag}}\right) \tag{6.3}$$

where τ_{mean} represents the magnitude of the time averaged shear stress TAWSS and τ_{mag} the temporal mean of the WSS magnitude.

$$\tau_{mean} = \left|\frac{1}{T}\int_0^T \tau_w dt\right| \tag{6.4}$$

$$\tau_{mag} = \frac{1}{T}\int_0^T |\tau_w| dt \tag{6.5}$$

From the above definition, the OSI can vary between 0 and 0.5, where 0 corresponds to unidirectional flow and 0.5 indicates purely oscillatory flow. However, there are a number of issues associated with OSI, particularly its insensitivity to WSS magnitude.

Figure 6.10 provides a comparison between the steady ($Re = 540$) and time-averaged velocity field in the branching plane of the anatomically realistic carotid artery model. Very similar flow characteristics are observed for both experiments, with the time-averaged velocity field closely tracking the steady state results throughout the majority of the vessel. In the external carotid artery, however, some larger differences occur due to differences in secondary flow and the time-dependent growth of the recirculation zones.

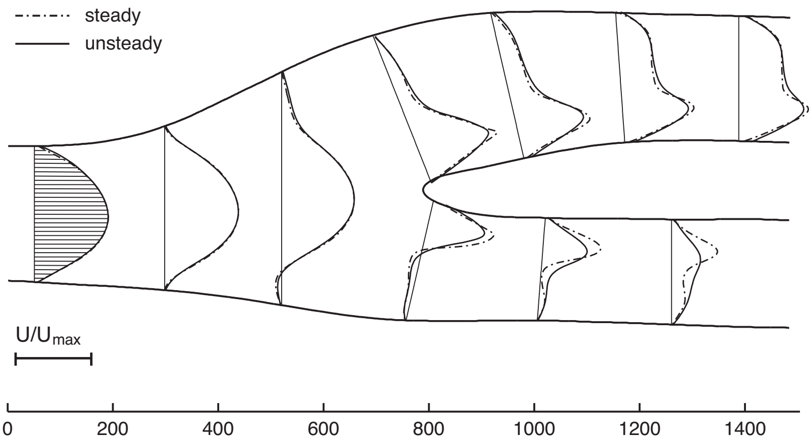

Figure 6.10 Time-averaged and steady state axial velocity profiles in the branching plane of the anatomically realistic carotid bifurcation model

Time averaged WSS is examined along the cut plane of the bifurcation outer walls and compared to the steady state WSS. A good match between TAWSS and steady WSS is obtained in the common carotid artery and the early bifurcation region. In the carotid sinus, TAWSS is slightly larger in the low momentum region (Figure 6.11(a)). The lower WSS under steady flow conditions is due to the standing low momentum region, which in unsteady flow is reduced during the systolic flow acceleration with uni-directional high momentum flow. To further understand the variations of instantaneous wall shear, Figure 6.11(b) plots the oscillatory shear index (OSI), which spikes in regions of low TAWSS. The primary contribution to this OSI is a brief period of flow separation induced by the adverse pressure gradient during the systolic deceleration phase. However, OSI is very low, indicating almost purely unidirectional flow along the outer sinus wall.

For the external branch, similar behaviour is observed with the TAWSS exhibiting very similar characteristics to the steady WSS in the common carotid artery and the bifurcation region. Sustained lower WSS over the cardiac cycle

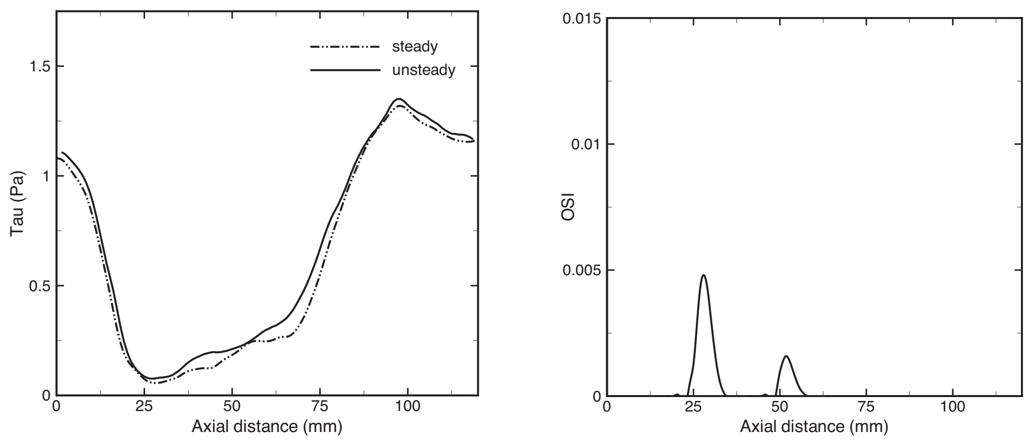

(a) (b)

Figure 6.11 Temporal WSS and related indices for the outer internal carotid artery wall: (a) Time-averaged WSS compared wit steady WSS; (b) Oscillatory shear index (OSI). Note that the OSI scale has been limited to 0.015, hence representing only a small oscillatory component

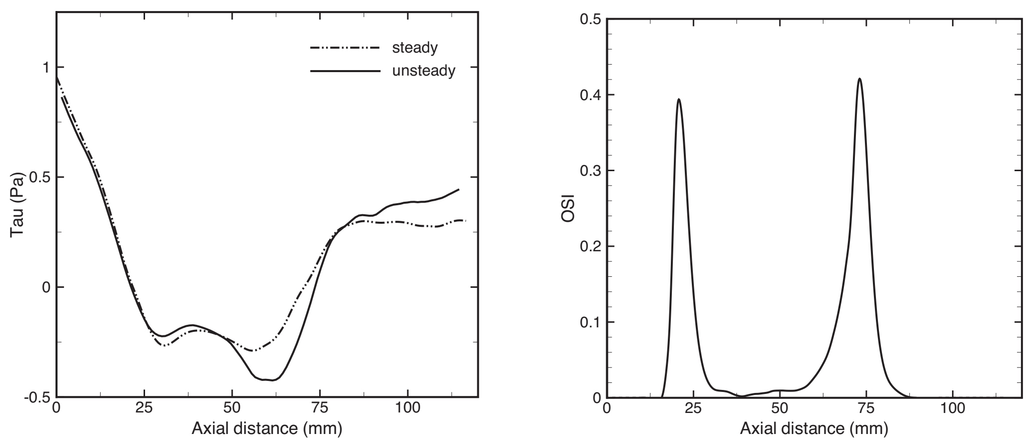

(a) (b)

Figure 6.12 Temporal WSS and related indices for the outer external carotid artery wall: (a) TAWSS compared wit steady WSS; (b) Oscillatory shear index (OSI)

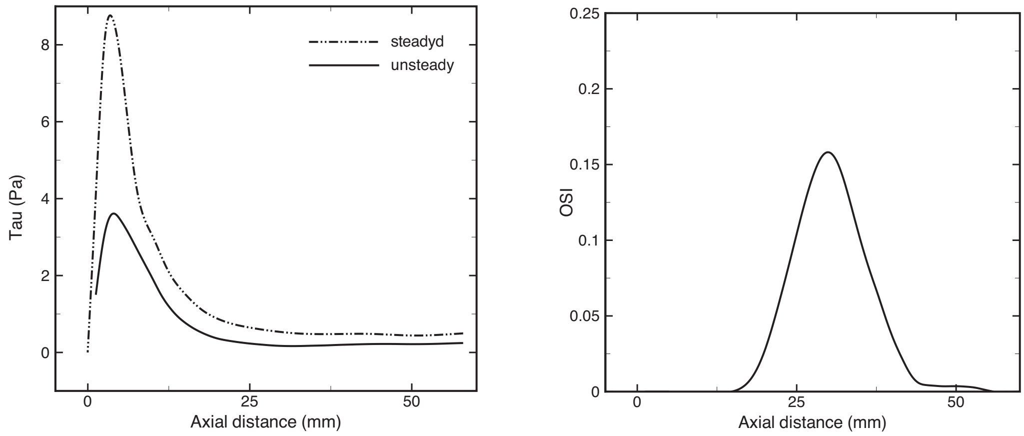

(a) (b)

Figure 6.13 Temporal WSS and related indices for the inner external carotid artery wall: (a) TAWSS compared with steady WSS; (b) Oscillatory shear index (OSI)

occurs in the low momentum region (proximal and distal) due to strong flow recirculation during systole (Figure 6.12(a)). In this part of the artery, WSS exhibits strong temporal variations (see later) due to the build-up of the adverse pressure gradient. Furthermore, WSS is highly oscillatory in this region with OSI ≈ 0.42 (where 0.5 corresponds to purely oscillatory), Figure 6.12(b). Maximum OSI occurs at flow separation and reattachment, while within the recirculation region, OSI and TAWSS are low.

Along the inner external carotid wall, TAWSS is significantly lower compared with steady WSS (Figure 6.13(a)). Again, the prevailing flow field in this region is very dynamic and exhibits periods of very low WSS (during diastole) and moderate WSS at systole, hence leading to a lower mean WSS. Additionally, WSS is somewhat oscillatory at the distal location as shown in Figure 6.13(b). The contribution to this oscillation is a short period of reverse flow on the inner bifurcation wall during peak systole (see Figure 6.18(c)).

The results suggest that there is a difference in WSS between pulsatile and steady flow conditions. This difference is quite small[3] in areas of uni-directional flow such as in the common carotid artery and the early bifurcation ($\leq 1\%$). In areas of disturbed and separated flow, this difference becomes larger with approximately 5% in the internal and 11% in the external carotid artery. Overall, spatial variations in TAWSS are in the range of -0.4 $-$ 1.3Pa on the outer walls and 0.1 $-$ 5.8Pa on the flow divider wall.

[3]based on the normalised error ϵ_{norm}, Equation 5.4

6.4.2 Transient

Axial Flow

Figure 6.14 details transient axial velocity profiles sampled at discrete time steps in the systolic and diastolic flow phase. As expected, the velocity profiles are skewed towards the inner walls, which varies in intensity throughout the cardiac cycle.

In the external carotid artery, a growth of the reversed low momentum flow region is observed during the systolic phase. This is also where the strong rotational flow is observed with counter rotating vortices at plane F-F (Figure 6.17). Reduced axial flow exists during the diastolic phase with the profile skewing towards the inner wall. At late diastole, axial velocity is almost stagnant due to the increased crossflow velocity and the dissipation of the vortical flow structure seen in Figure 6.17 (plane F-F).

In the internal carotid artery, axial velocity profiles are more consistent with the steady state velocity profiles. High velocities occur during the systolic phase with large velocity gradients on the inner wall and medium gradients on the outer sinus wall. At early flow acceleration, the low momentum flow region is at its smallest and continues to grow throughout the cardiac cycle. At late diastole, velocities near the outer wall are low (due to reduced volume flow) and WSS approaches zero (Figure 6.18), however, no flow separation occurs.

Contours of the instantaneous velocity for the x and y components (u, v) are shown in Figure 6.15 and 6.16 at several time steps during the cardiac cycle. The solid and dotted lines indicate positive and negative axial and lateral velocities. Flow in the internal carotid artery is predominantly uni-directional, while the external carotid artery exhibits significant flow recirculation in axial direction.

Significant lateral, i.e., vertical velocity fluctuations are only present in the external carotid artery. The results clearly show the presence of small scale structures and a weakly turbulent flow in the external carotid artery. In the internal carotid artery, the streamwise vortices (secondary flow) persist through the length of the branch and cardiac cycle, whilst in the external carotid artery, the vortices break down to smaller-scale structures as the flow develops axially. The reversed low momentum flow region (caused by retrograde flow deflected at the apex) penetrates deep into the external carotid artery at peak systole. This

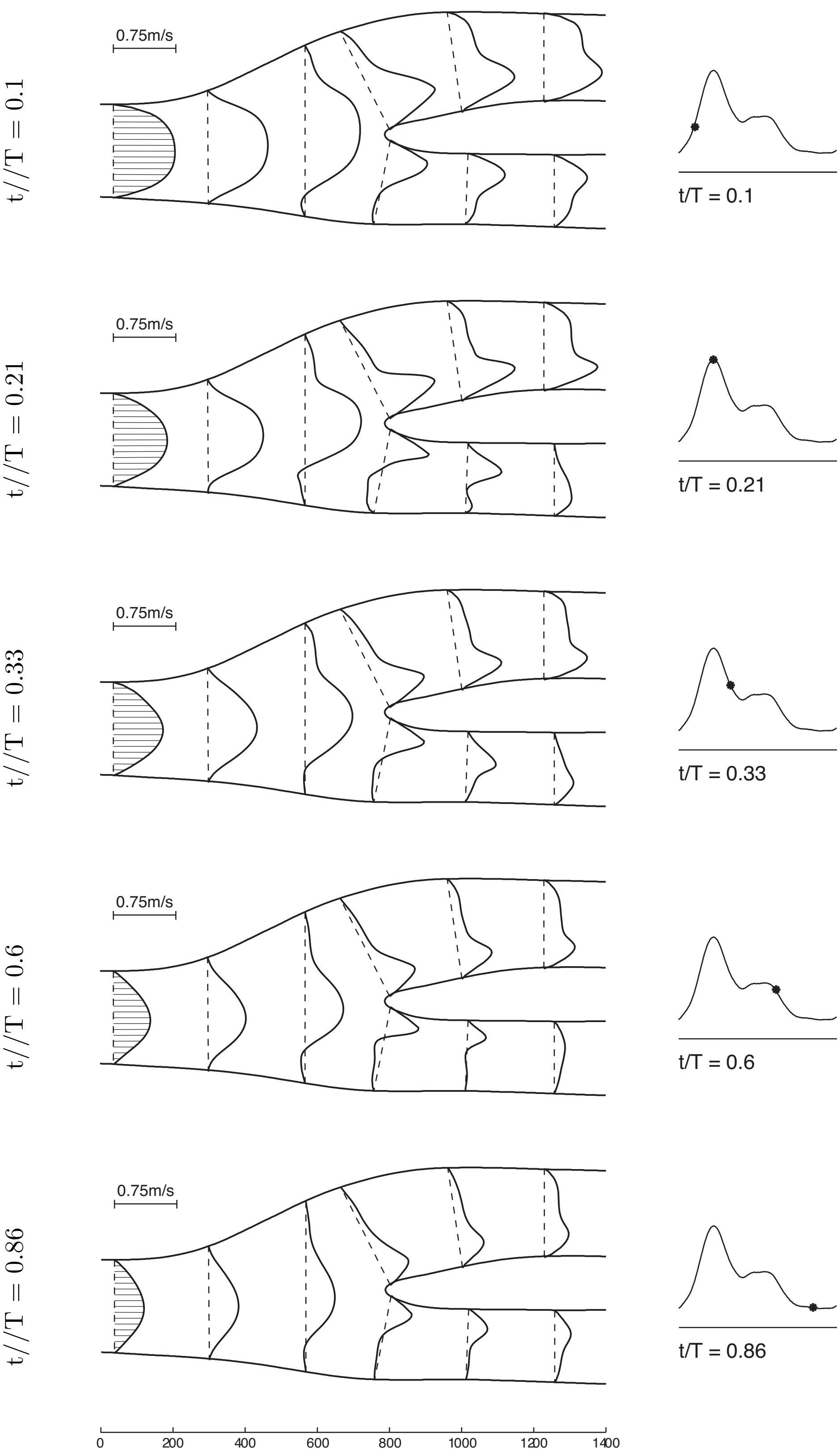

Figure 6.14 Instantaneous axial velocity profiles in the plane of bifurcation at t/T=0.1, t/T=0.21, t/T=0.33, t/T=0.6, t/T=0.86

causes an 'obstruction' to the main flow and vortex shedding occurs during peak and late systole. This instability is further promoted by the adverse pressure gradient developing during the flow deceleration phase. The wavelength of the velocity pertubation is approximately one vessel diameter, based on the lateral velocity contour (Figure 6.16). Towards the end of the cardiac cycle, the small scale structures dissipate and uniform flow is re-established in both branches.

Secondary Flow

To further assess the transient flow structure, Figure 6.17 presents secondary flow lines in the bifurcation region (plane G-G) and the proximal internal (plane A-A) and external (F-F) carotid artery.

At the bifurcation (plane G-G), secondary flow patterns exhibit four vortices located near the outer anterior and posterior walls. These vortices are counter-rotating and convect near wall fluid towards the vessel center. The vortices are at their strongest during flow acceleration. The vortices located near the external branch (left in Figure 6.17) are driven by secondary flow crossing over from the internal carotid branch (right to left in Figure 6.17). This is further amplified by the retrograde flow deflected at the bifurcation apex as detailed earlier. At peak systole ($t/T = 0.21$), the vortex strength reduces, while strong cross flows are sustained. During flow deceleration and diastole, the two vortices located at the anterior wall disappear almost completely, whilst the vortex pair near the posterior wall tends to increase.

Progressing into the internal and external carotid branch, the observed vortex pairs divide to yield the previously observed counter-rotating helicoidal flow structure. At the proximal external carotid artery (plane F-F), secondary flow patterns undergo transformation and exhibit strong temporal variations. This is due to the growth of the separated flow region and the observed flow instabilities at peak and late systole. Consistent with plane G-G, the vortex pair weakens at peak systole and moves closer to the vessel center. At early diastole ($t/T = 0.6$), the pair has converged to a single counter-clockwise rotating vortex and dissipates completely during the second flow deceleration phase at late diastole ($t/T=0.86$).

At the proximal internal carotid (A-A), secondary flow exhibits less temporal variations and is more consistent with the steady state results in this plane

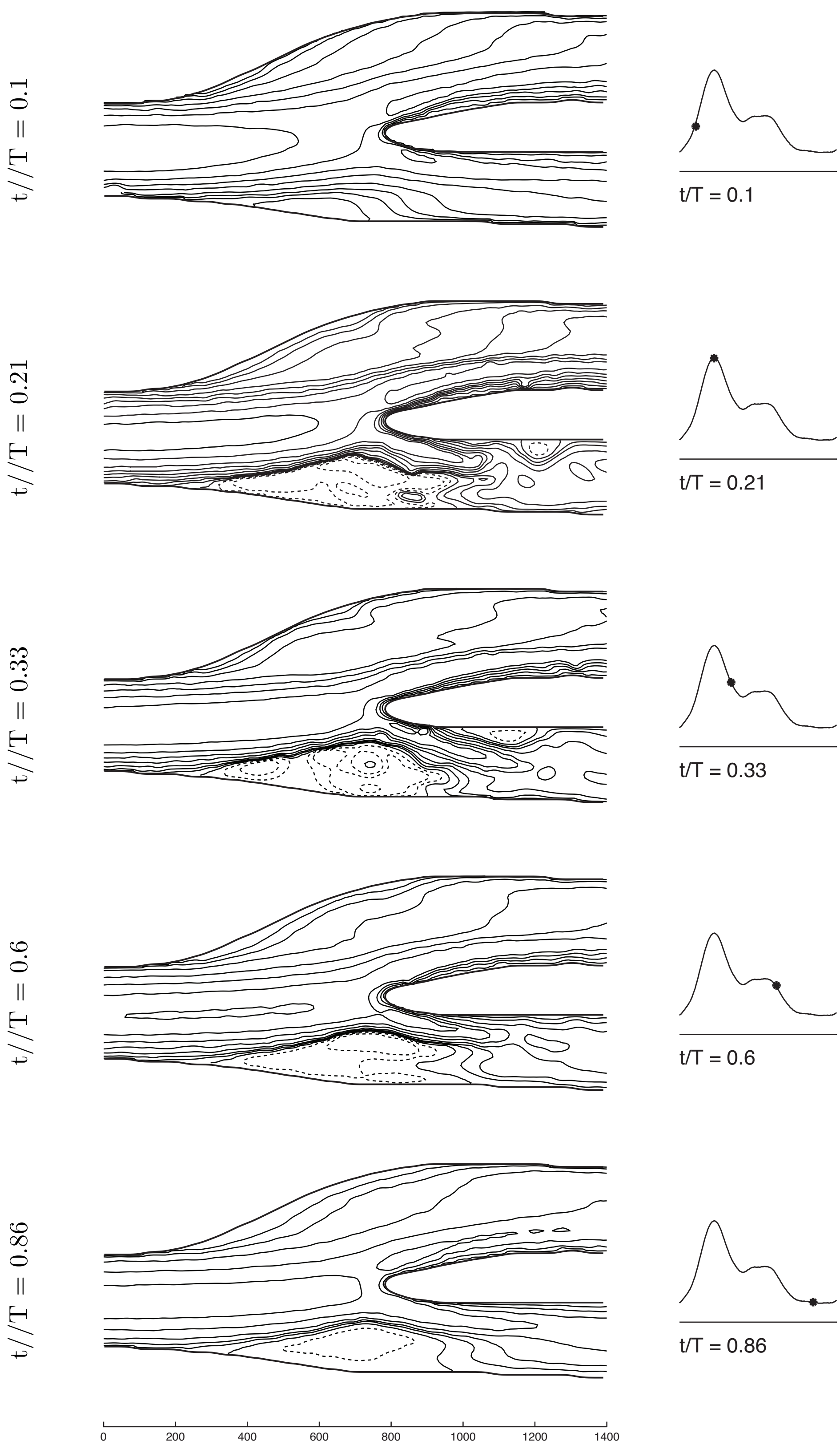

Figure 6.15 Instantaneous axial velocity contours in the plane of bifurcation at t/T=0.1, t/T=0.21, t/T=0.33, t/T=0.6, t/T=0.86: (solid) positive, (dashed) negative, contour: u = [-0.1:0.1:0.7] m/s

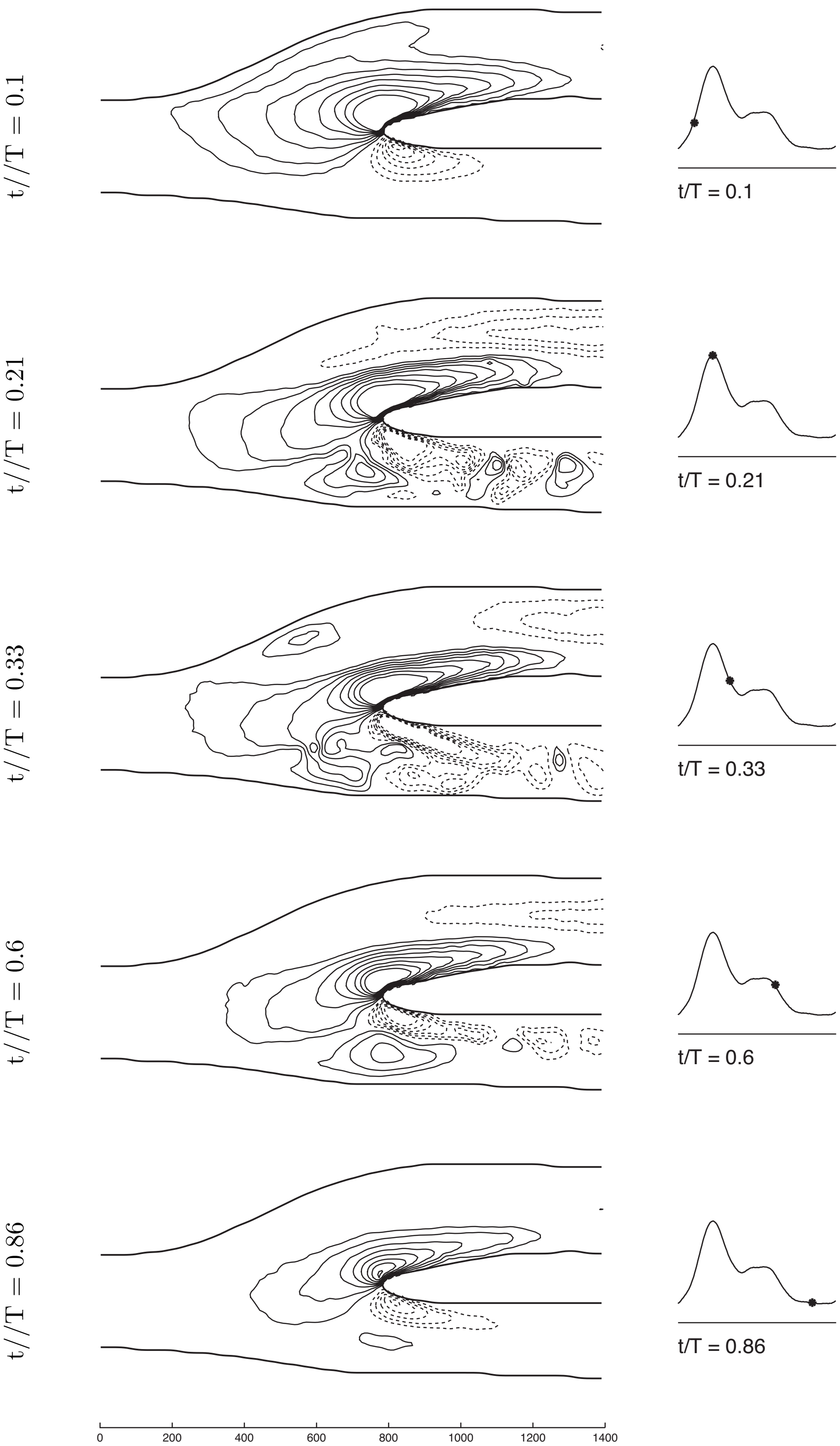

Figure 6.16 Instantaneous vertical velocity contours in the plane of bifurcation at t/T=0.1, t/T=0.21, t/T=0.33, t/T=0.6, t/T=0.86: (solid) positive, (dashed) negative, contour: v = [-0.15:0.025:0.2] m/s

(Figure 6.8). Overall, secondary flows are stronger compared with the external artery, which is due to the stronger in- and out-of-plane curvature and larger volume flow. The vortex near the anterior wall reaches its maximum strength at peak systole and is consistent with the observations in plane G-G, but weakens again throughout the remainder of the cardiac cycle. By contrast, the posterior vortex sustains its size and strength over the cardiac cycle, except at early systole ($t/T = 0.1$) where it matches the anterior vortex. At late diastole, both vortices rotate towards the inner wall (due to secondary curvature), thereby giving rise to a larger low momentum region along the outer sinus wall. This is consistent with the axial velocity profiles and the low WSS observed in this location.

Other locations sampled in the internal and external carotid branch exhibit very similar secondary flow characteristics. The observed transients are relatively small (except in the proximal external branch).

Wall shear Stress

Figure 6.18(a-c) presents transient WSS profiles at spatial locations specified in Figure 6.18(d). Location A, B and C progress along the outer external carotid wall in the separated flow region, whilst H is located at the inner wall where OSI is high. In the internal carotid branch, location F and G correspond to high shear regions, whilst D and E progress through the low momentum region along the outer wall. Note that the sampling locations B, E and D correspond to the respective cross-sectional planes F-F, A-A and G-G in Figure 6.17.

Evidently, strong temporal variations in WSS exist, which are very location specific. For example, in the common carotid and distal internal carotid artery (F,G), WSS follows the inlet waveform pattern closely with a sharp rise at systole and a decrease during diastole. In the separated flow region at location A (bifurcation), WSS is low and close to zero throughout the cardiac cycle. At peak systole ($t/T = 0.21$), WSS drops rapidly (Figure 6.14) due to the forward acceleration and the movement of the separation point upstream.

Strong reversed axial flow is experienced throughout the cardiac cycle at the proximal location (B) and shear stress is lowest amongst the observed locations, reaching values of approximately -1.4Pa during late systole. WSS in the separated flow region exhibits significant transients.

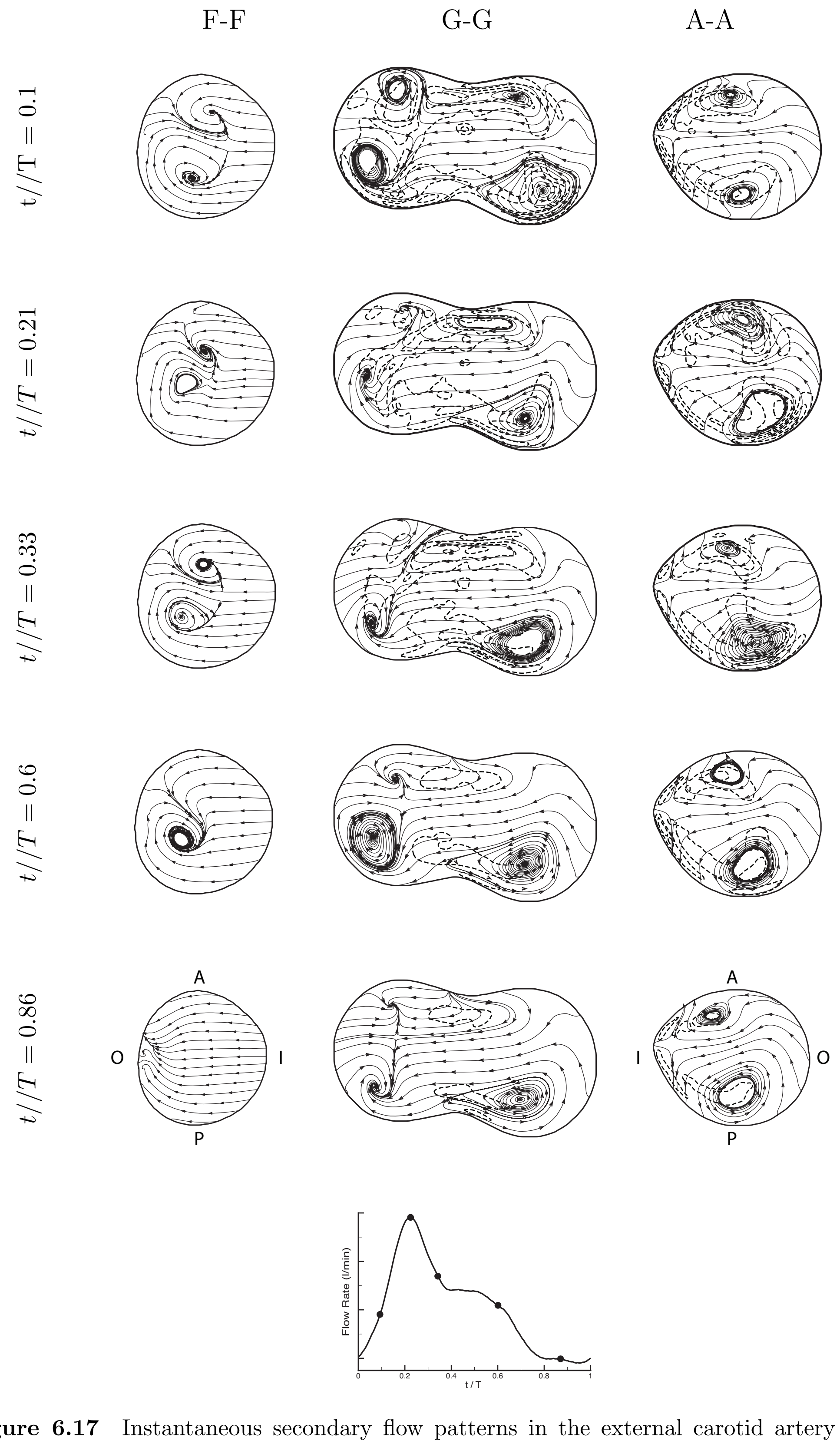

Figure 6.17 Instantaneous secondary flow patterns in the external carotid artery (F-F, left), bifurcation region (G-G, center) and internal carotid artery (A-A, right); t/T=0.1, t/T=0.21, t/T=0.33, t/T=0.6, t/T=0.86. Dashed lines indicate streamwise vorticity contours $\Omega_z = [-200 : 50 : 200]$

Along the inner wall (location H), a short period of flow separation exists at late systole. This is caused by the adverse pressure gradient during flow deceleration and the interaction between the axial and secondary flows.

As opposed to the outer external carotid artery wall, transient WSS and flow characteristics in the carotid sinus are less pronounced. WSS in the carotid sinus (location D and E) is low throughout the cardiac cycle with no observable flow separation. Flow in this region is predominantly uni-directional and variations in WSS follow the inlet waveform characteristics. The low momentum region near the outer wall is regularly 'washed out' due to strong secondary flows in the systolic flow phase.

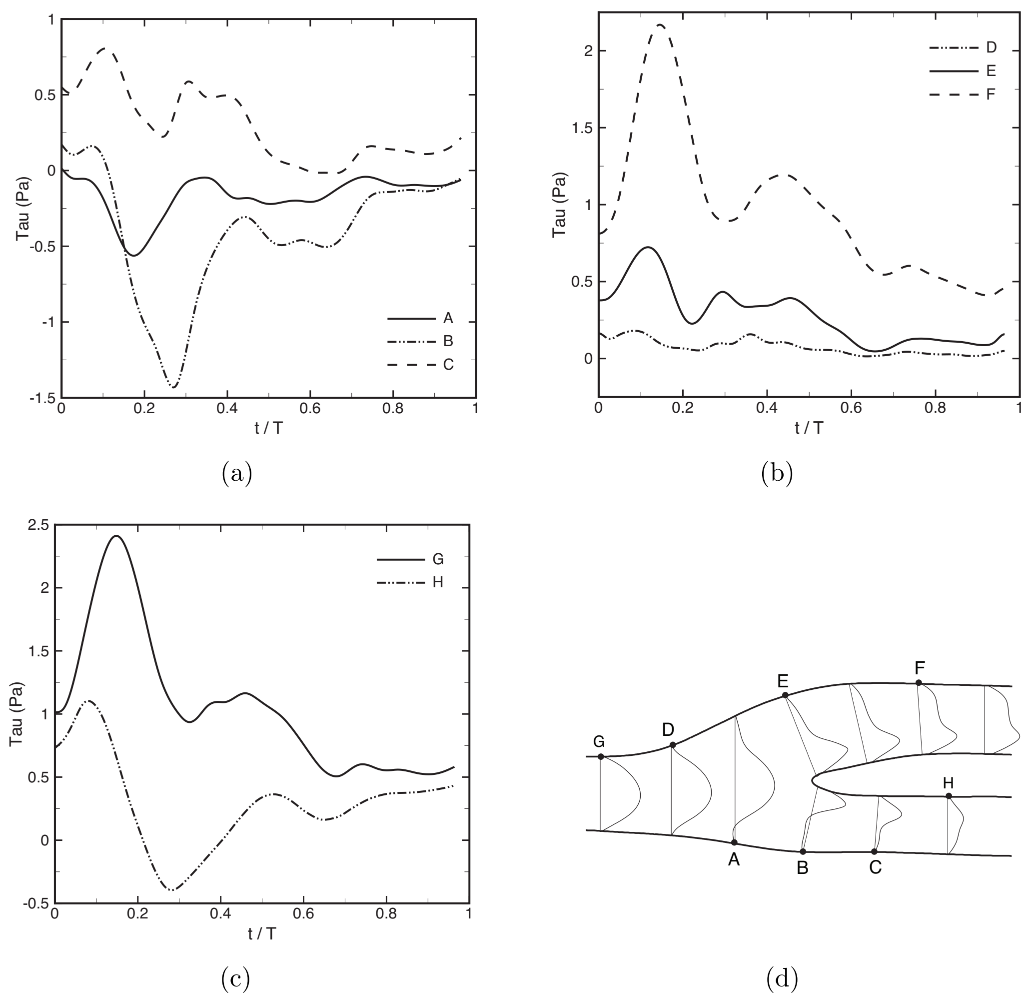

Figure 6.18 Walls shear stress transients: (a) external carotid artery, (b) internal carotid artery, (c) common and external carotid artery, (d) sampling locations on the bifurcation walls

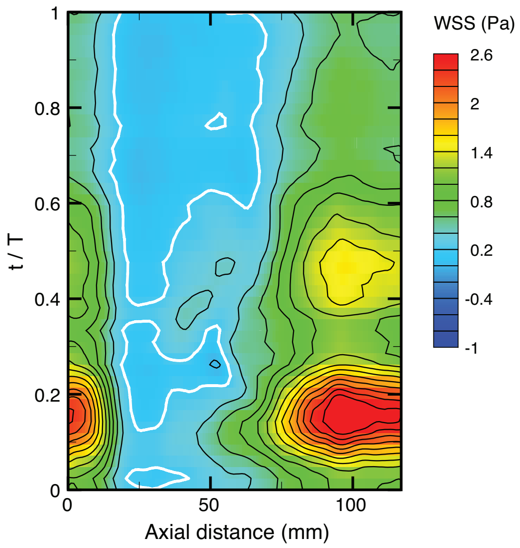

(a)

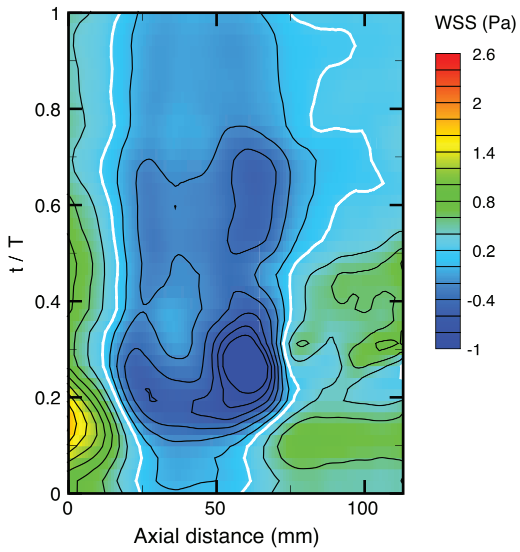

(b)

Figure 6.19 Time variation in WSS plotted along the outer wall of (a) the internal carotid artery and (b) the external carotid artery. White line indicates contours of WSS $\leq$ 0.15Pa. Data recorded every 0.07sec ($dt/T = 0.023$)

Referring to Figure 6.19, WSS sampled at other locations exhibit similar characteristics. The results show that transient characteristics are significant in regions of flow separation such as in the external carotid artery. These transients are caused by the growing, shrinking and directional change of the recirculation zone. In areas of unidirectional and low momentum flow, WSS may be low, however, temporal changes follow the inlet waveform. Figure 6.19 depicts the distribution of WSS along the outer walls throughout the cardiac waveform. Regions of low WSS are smallest at peak systole and increase towards the end of diastole (white contour line in Figure 6.19). The most significant transients occur along the proximal and distal outer external artery and in the distal internal carotid branch.

6.5 Discussion and Conclusion

Local haemodynamic factors are understood to influence the initiation and progression of atherosclerosis in the carotid artery [Caro, 2001; Chatzizisis et al., 2007; Ku et al., 1985b; Traub and Berk, 1998; Zarins et al., 1983] and numerous experimental studies have described local haemodynamics in models of the human carotid bifurcation under steady and pulsatile flow conditions. Despite the large body of research in this field, there are only few experimental studies that have implemented physiological boundary conditions (i.e., patient specific waveform) paired with an anatomically realistic carotid artery model [Liepsch, 2002; Bale-Glickman et al., 2003a]. Furthermore, detailed spatial and temporal WSS measurements under these conditions are still sparse.

Across the general population a large variety in carotid artery geometry exists [Ding et al., 2001; Thomas et al., 2005] and the local haemodynamic environment is largely influenced by the individual vessel geometry [Nguyen et al., 2008b; Perktold and Resch, 1990]. To accurately model this condition, the physiological model in this work is asymmetric with both in-plane and out-of-plane vessel curvatures. The application of the developed methodologies to this realistic model has provided for some very interesting and unexpected results. The most significant of these being the WSS and the underlying flow field in the external carotid artery branch. The branching artery, coupled with secondary curvature leads to locations of spatial and temporal varying WSS and complex asymmetric secondary flow patterns. Significant flow separation occurs in the external artery under both, steady and pulsatile flow conditions and in addition to the internal carotid artery may very well be at 'risk' of atherosclerotic plaque formation.

6.5.1 Physiological vs. Idealised Model

Regarding the comparison between the idealised (Chapter 5) and patient specific geometry the following observations can be made. Both ,the axial and secondary flow fields are markedly different from those observed in idealised models. This is caused by the non-planarity of the vessel, which leads to unmatched secondary flows that rotate along the circumferential direction along the vessel axis. These secondary flows evolve with time and lead to very complex helicoidal flow trajectories and significant flow separation in the external carotid artery not observed in the idealised model. The observation of recirculating flow and low WSS in the external carotid artery is not new and has previously been reported by Milner et al. [1998]. Also, the local curvature variations, particularly in the bifurcation region, lead to non-uniformity in WSS distribution along the outer internal and external carotid artery.

Overall, the current observations are consistent with previous numerical simulations [Perktold et al., 1998; Myers et al., 2001] that have studied curvature effects and their implication for atherosclerosis. Furthermore, the observed correlation between WSS and helicoidal flow structure (caused by curvature) in the current model also supports the the notation of a "geometric risk factor", [Friedman et al., 1983]

6.5.2 Steady vs. Pulsatile Flow

A comparison between steady and pulsatile flow has revealed some very interesting aspects. Regarding time-averaged quantities (i.e., velocity, WSS), only small differences between the steady and pulsatile flow experiments could be observed. The largest discrepancies occurred in the external carotid artery, where the flow exhibits significant transients and instabilities. This is further evidenced by the OSI, which is largest along the outer external carotid artery, indicating almost purely oscillatory WSS in this region. However, the mean WSS distributions are in reasonable agreement and it is hypothesised that in low Womersley number flow greater agreement will be obtained between steady and unsteady flow.

Differences in velocity and WSS are attributed to regions with large transients that occur over the cardiac cycle. For example, in the external carotid artery, the growth of low the momentum flow regions in the diastolic phase results in an 'artificial' constriction of the vessel lumen (see Fig. 6.15), which causes flow instabilities during the flow deceleration phase, similar to those observed in the stenotic model (Chapter 5). These flow instabilities propagate downstream, causing large temporal and spatial variations, including a short period of flow reversal at the inner wall. These perturbations are not present in the internal carotid artery branch at any time during the cardiac cycle.

6.5.3 iPIV Wall Shear Stress

Previously, the only other experimental studies in physiologically accurate geometries utilising PIV were the like of Bale-Glickman et al. [2003a,b] and Vétel et al. [2009], but did not provide detailed WSS measurements. Hence the novelty of this work is the measurement of detailed spatial and temporal WSS by means of iPIV. As discussed in Chapter 4, the iPIV technique provides a low uncertainty and performs superiorly compared to commonly used velocity differentiation. However, an underestimation, particularly for higher shear rates is expected (see Chapter 5.5) in the pulsatile flow measurements. As can be seen in Figure 6.14, the spatial wavelength of the near wall velocity profiles changes significantly during the cardiac cycle, meaning that the optimal Gaussian weighting parameter to obtain maximal amplitude response also changes over time. This has been ignored in the current analysis and the iPIV processing parameters are constant during the cardiac cycle and identical for the steady and pulsatile WSS measurements ($\sigma = 10$pixels, $M = 32$pixels).

In order to benchmark some of the results of this work, steady and time averaged WSS values are compared with previous studies (experimental and numerical) in Table 6.3. Under steady flow conditions in idealised geometries, minimal and maximal reported WSS values are in the range of 0.2 Pa to 12.4 Pa along the outer and inner internal carotid artery [Bharadvaj et al., 1982b; Ku and Giddens, 1987]. Under pulsatile flow, time-averaged minimal and maximal WSS in idealised models is between -2Pa and 14Pa [Perktold et al., 1991c,b; Marshall et al., 2004], while for physiologically realistic models, depending on location and vessel compliance, time-averaged WSS varies between 0.3Pa to 6Pa [Karner et al., 1999; Zhao et al., 2000]. Measured *in-vivo* WSS varies between 1.3Pa and 3.3Pa along the outer and inner internal carotid artery, respectively [Samijo et al., 1998].

The current results are in general agreement with those reported previously, with minimal and maximal steady WSS between -0.25Pa to 8.5Pa and minimal and maximal time-averaged WSS of 0.4Pa and 3.8Pa in the external carotid. Wall shear stress also exhibits large transients with a maximum of 2.6Pa and 1.5Pa and a minimum of 0.2Pa and -1.4Pa in the internal and external carotid artery, respectively. Thus, over the cardiac cycle, WSS along the outer walls exhibits peak-to-peak variation of up to 2.9Pa, which are almost twice the mean

Table 6.3 Internal carotid artery wall shear stress (WSS) values collected from literature. Values correspond to *min/max* WSS found along the inner and outer sinus wall if not indicated otherwise. Values are time-averaged in the case of pulsatile flow

	Author	Geometry	Q_I:Q_E	Method	outer wall		inner wall		Comments
					min	*max*	*min*	*max*	
In-vitro	This study	ideal.,steady	70:30	PIV	-0.47	4.03	1.14	9.96	*Re*=400,700
					-7.6	40.2	-4.09	68.0	stenosed, 800
		phys.,steady	70:30		0	1.81	1.12	9.8	453,703
		phys.,pulst.	70:30		0.1	1.35	0.12	3.84	
	Bharadvaj et al. [1982b]	ideal.,steady	70:30	LDV	-0.17	4.05	1.41	12.4	400,800
	Zarins et al. [1983]	ideal.,steady	70:30	LDV	-0.3	4.2	3.1	21.0	400,800
	Ku and Giddens [1987]	ideal.,steady	70:30	LDV	-0.2	4.0	1.4	12.3	400,800
		ideal.,pulst.			-1.3	4.9	1.0	10.9	
	Ding et al. [2001]	ideal.,pulst.	70:30	LDV	0.1	2.65			ICA side walls
In-silico	Perktold et al. [1991c,b]	ideal.,pulst.	70:30	CFD	-1.94	6.12	1.08	14.1	
					-1.92	6.18	1.16	12.8	non-Newt.
	Karner et al. [1999]	phys.,pulst.	n.a.	CFD	-0.5	2.1	2.2	6.0	compliant
	Zhao et al. [2000]	phys.,pulst.	75:25	CFD	0.3	1.55	0.6	2.55	
					0.3	1.3	0.6	1.7	compliant
	Marshall et al. [2004]	ideal.,pulst.	n.a.	CFD	0.1	1.8	1.1	6.8	
					0.2	4.1	0.0	8.0	stenosed
In-vivo	Samijo et al. [1998]	phys.	n.a	DUS	1.29 ± 0.24		3.33 ± 0.58		CCA
	Oshinski et al. [2006]	phys.	n.a	MRV	0.8 ± 0.41				CCA

Shear stress given in Pa

ideal.=idealised; phys.=physiologically realistic; pulst.=pulsatile flow; flow split = Q_I:Q_E; DUS=Doppler ultrasound, MRV=MR velocimetry physiological WSS of 1.5Pa in the common carotid artery.

Note, the range of WSS values reported in Table 6.3 is due to variations in detailed model geometry and inlet waveform. Also interesting to see, is that WSS in the physiological models is on average lower than that in the idealised models. This trend is also confirmed by the current results.

Chapter 7

3D-3C PIV Investigations of Carotid Artery Haemodynamics[1,2]

This chapter presents Stereo-PIV and tomographic PIV (Tomo-PIV) measurements of the three-dimensional flow structure and WSS in a physiologically accurate model of the human carotid artery bifurcation. The vascular geometry is reconstructed from patient-specific data and this chapter aims to demonstrate the feasibility of three-dimensional, three-component (3D-3C) measurements in such complex vascular geometries. The experimental setup and procedure is detailed in the first part before the 3D-3C Tomo-PIV technique is briefly introduced in the second part. This is followed by a detailed validation of the implemented methodology by comparing the Tomo-PIV results with Stereo-PIV measurements in the same model. Both techniques are then applied to acquire 3D-3C velocity fields and WSS data at multiple axial locations within the carotid artery model. The results indicate the presence of a complex and three-dimensional flow structure, with regions of flow separation and strong velocity gradients. The WSS distribution is markedly asymmetric confirming a complex swirling flow structure within the vessel. Additional Stereo-PIV measurements in the idealised geometry are presented in the last part of this chapter and reference to the results obtained in Chapter 5 is given.

---

[1]The content of this chapter has been accepted by *Experiments in Fluids*, under the title:

Tomographic Particle Image Velocimetry Investigation of the Flow in a Modelled Human Carotid Artery Bifurcation

N.A. Buchmann, C. Atkinson, M.C. Jermy and J. Soria

[2]The measurements presented in this chapter were mostely performed at the Laboratory for Turbulence Research in Aerodynamics and Combustion (LTRAC) at Monash University, Melbourne, Australia. The support of Prof. J. Soria is kindly acknowledged.

7.1 Introduction

In the previous two chapters, planar (2D-2C) PIV was used to characterise the steady and unsteady flow fields within the human carotid artery. From these investigations it has become evident that the prevailing haemodynamics are dominated by complex, three-dimensional flow motion. Therefore, to further investigate the complex flow field within the carotid artery, this chapter presents 3D-3C velocity and WSS measurements by utilising the developed Stereo-PIV technique and the most recently invented Tomo-PIV technique [Atkinson and Soria, 2009; Elsinga et al., 2006].

For detailed 3D flow investigations, several variations of the PIV technique exist and are commonly used in a variety of fluid flow applications. One technique that is widely used is Stereo-PIV [Prasad and Adrian, 1993] as it readily facilitates the measurement of the three-component velocity field on a single plane (2D-3C). While the 2D-3C Stereo-PIV system only provides six of the nine components of the velocity gradient tensor, it can be extend to a full 3D-3C system by performing multi-plane Stereo-PIV [Kähler, 2004]. An alternative and increasingly popular 3D-3C technique is tomographic PIV (Tomo-PIV) [Elsinga et al., 2006]. In Tomo-PIV, multiple instantaneous views of the seeded flow field are used to estimate the 3D intensity distribution. Subsequent 3D cross-correlation is then used to determine the corresponding 3D-3C velocity field. Beside the above methods, further 3D-3C techniques include holographic PIV [Soria and Atkinson, 2008], defocusing PIV [Willert and Gharib, 1992] and 3D-3C Particle Tracking Velocimetry [Boutsianis et al., 2009] and the interested reader is referred to the references provided for a more detailed discussion.

The reviewed work in Chapter 1 together with the findings from this work confirm the presence of three-dimensional flow structures within the carotid artery and their direct influence on the formation and progression of vascular disease. Yet, direct 3D-3C flow and shear stress measurements of such complex flows is still sparse. Some work in this direction has been undertaken by Vétel et al. [2009] who used multi-plane Stereo-PIV to describe the complex and coherent 3D structures within the carotid artery. Another study by Brunette et al. [2008] used a 2D-2C scanning technique with subsequent volume reconstruction of the flow field in a stenosed coronary artery. The scope of the present work is the investigation of the 3D-3C flow field by means of Tomo-PIV within a physiologically accurate model of the human carotid artery. Furthermore, this work demonstrates the application of this technique to a complex internal flow geometry.

7.2 Methodology

7.2.1 Arterial Geometry

The geometrical model of the carotid artery bifurcation is generated from post-mortem data using surface point reconstruction described in Chapter 2.3. The dissected vessel corresponds to that of a 71 year old deceased male [Goubergrits et al., 2002] and is depicted in Figure 7.1. The reconstructed geometry exhibits true *in-vivo* characteristics such as strong secondary curvature, non-planarity

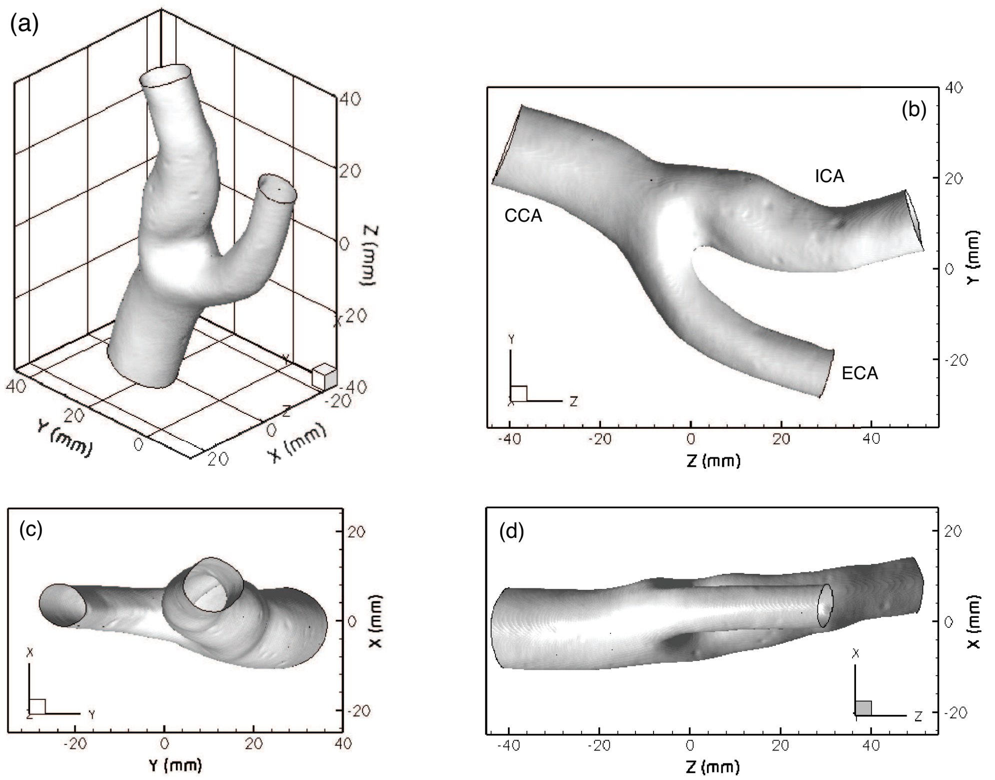

Figure 7.1 Illustrations of the physiological accurate carotid artery model: (a) isometric view; (b) front view; (c) top view and (d) side view

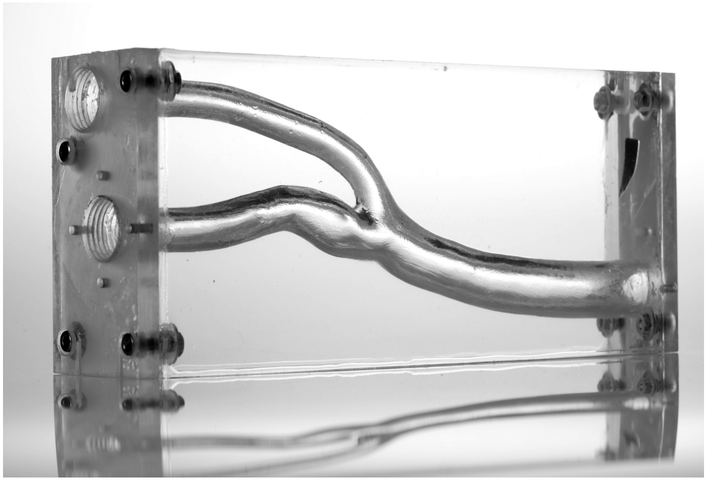

Figure 7.2 Silicone flow phantom of the patient specific carotid artery bifurcation

and topological surface variations. The nominal diameter measured at the common carotid artery (CCA) is approximately $7.2mm$ and the bifurcation angle between the internal (ICA) and external (ECA) carotid artery is about 40°. The transparent flow phantom is constructed using the process described in Chapter 2.4 and shown in Figure 7.2.

7.2.2 Experimental setup

The following section describes the experimental setup as well as the measurement and calibration procedure. The Stereo- and Tomo-PIV system are illustrated in Figure 7.3 and a summary of the relevant experimental parameters is given in Table 7.1.

Flow Facility

Flow measurements are conducted in a similar closed-loop flow facility described previously in Chapter 5. The flow phantom is connected to a system of rigid and flexible pipes to provide fully developed steady flow at the inlet of the flow phantom. Flow rates upstream and downstream of the test section are measured with an electromagnetic flow meter and two rotameters. Note, that the human carotid artery is part of a complex arterial system and as such the flow entering the carotid bifurcation will be influenced by the upstream geometry and the pulsatile nature of the flow. Thus, the real flow in the human arterial system cannot be considered fully developed nor steady and the above assumptions constitute a simplification of the real flow situation. Nevertheless, the chosen flow conditions adequately represent the mean flow condition as outlined in Chapter 2.

The rheological properties of the flowing blood are simulated with the aqueous glycerin mixture ($\mu = 12.7 mPa{\cdot}s$, $\rho = 1.15 g/cm^3$ at $20°C$). The refractive index match is verified by placing a regular grid behind the flow geometry and subsequent cross-correlation of the distorted and undistorted images and is within ±1% of the target index. This error is similar to the ±0.005 quoted by Burgmann et al. [2009] and is sufficiently small to reduce optical distortions at the model/liquid interface and to allow an undistorted view of the complex and convoluted flow passage.

Optical setup

Stereoscopic and tomographic PIV is used to measure the instantaneous 3D-3C velocity field in the carotid bifurcation model. The measurement plane or respective measurement volume is located in the $x - y$ plane perpendicular to the mean flow direction and allows to capture the flow velocities over the entire vessel cross section. The optical arrangement shown in Figure 7.3(a-b) is similar to that of Vétel et al. [2009] and is designed to take measurements at various cross-sectional planes with only one set of calibration data. For this purpose, the flow phantom is mounted on a micrometer stage, which facilitates precise translation in the $z-$direction ($\pm 5\mu m$). In order to perform orthogonal viewing of each camera, silicone viewing prisms are mounted on $x-$translation stages and positioned accurately with respect to the flow phantom (Figure 7.3(c)). In this way, the setup allows precise positioning of the flow phantom and viewing prisms in the respective streamwise and spanwise direction.

The Stereo-/Tomo-PIV setup consists of four PCO Pixelfly CCD cameras (1280×1024 pixel, $12 bit$), equipped with $55 mm$ focal length lenses and arranged in an angular configuration of 45° and 60° as shown in Figure 7.3(a). The Scheimpflug conditions, necessary to focus the image over the entire field of view, is satisfied by rotating the image plane with respect to the lens plane. Volume illumination is provided by two Spectra Physics 400mJ Nd:YAG lasers

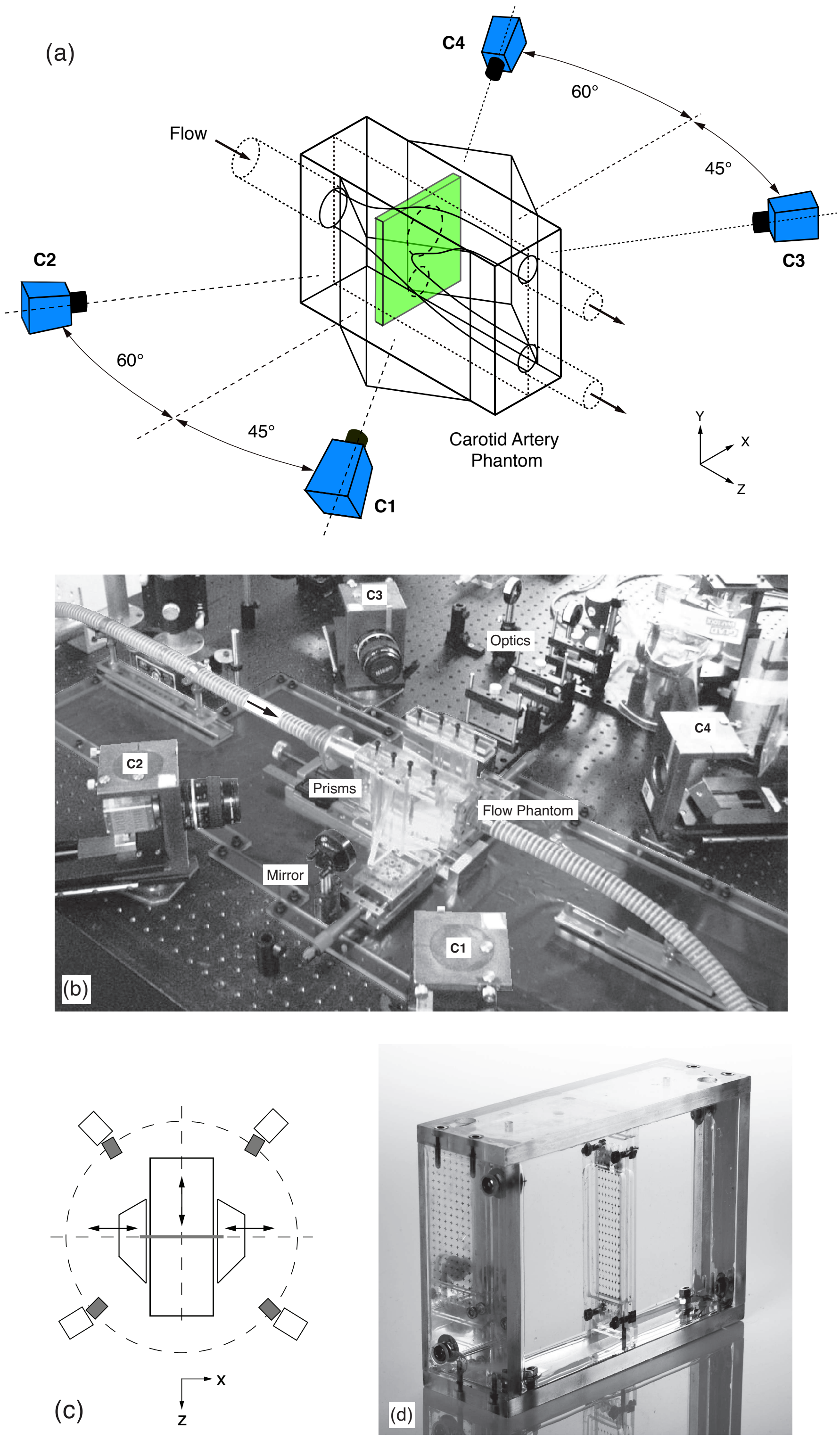

Figure 7.3 (a) Schematic of the optical arrangement showing camera and laser sheet position; (b) Flow circuitry and experimental setup with flow phantom, viewing prisms, optics and camera setup; (c) Translation of the flow phantom and the viewing prisms; (d) Calibration model with the calibration grid cast into the silicone. The grid comprises 8×17 markers with a $3.5mm$ grid spacing

Table 7.1 Overview of the relevant experimental parameters for the stereoscopic and tomographic PIV investigation

Arterial model	Inlet diameter	$20mm$
	Dimensions ($H \times W \times L$)	$100 \times 50 \times 250mm$
	Material	silicone, $n = 1.417$
Flow	Liquid	61% glycerin, 39% water
	Properties at $20°C$	$n = 1.417$, $\mu = 12.7mPa{\cdot}s$
		$\rho = 1.15g/cm^3$
	Re	339
	U_{max}	0.37m/s
Calibration model	Dimensions ($H \times W \times L$)	$100 \times 50 \times 250mm$
	Material	silicone, $n = 1.417$
	Grid spacing	$2.5 \times 2.5mm$
Seeding	Type	Hollow glass spheres
	Diameter	$20\mu m$
	Density	$1.1g/cm^3$
Laser	Type	Nd:YAG, dual cavity
	Max. energy	$400mJ$
	Pulse width	$5ns$
	Pulse separation	$750\mu s$
	Thickness	$1.0 - 6.0mm$
Camera	Type	CCD
	Resolution	1280×1024 pixel, 12bit
	Pixel size	$4.65 \times 4.65\mu m$
	Aquisition rate	$5Hz$
Image properties	Lens focal length	$55mm$
	Viewing angles	$\pm 45°$ and $\pm 60°$
	Lens aperture	$f = 5.6 - 8$
	Diffraction limit	$9.6\mu m$
	Image magnification	0.202
	Field of view	$35 \times 28mm$
	Maximum particle displacement	8-12 pixel

introduced through the side of the model and shaped into a sheet by a set of spherical and cylindrical lenses. The thickness of the light sheet varies according to the measurement between $1.0-6.0mm$. The time separation, Δt is $750\mu s$ for all experiments yielding a maximum particle displacement in the centre of the model of $u_{max} = 0.28mm$ or approximately 11.2 pixel. The flow is seeded with $20\mu m$ hollow glass spheres with a particle density, $\rho = 1.1g/cm^2$. Due to the smaller difference in refractive index between the glass spheres and the working liquid, larger seeding particles are required to provide adequate scattering intensity to each CCD array. The seeding density is adjusted to approximately $0.01ppp$. In order to remove differences in scattering efficiency due to the forward/backward scattering arrangement, a mirror is positioned at the end of the light pass to reflect the laser light back through the test section.

Camera calibration is performed using the method described in Appendix E.1 with the calibration target cast into a separate silicon phantom as shown in Figure 7.3(d). The calibration model is of identical size and manufactured together with the flow phantom to ensure identical optical properties. The only difference between the two models is the flow passage, which is filled with the refractive index matched working liquid. For the calibration, the flow phantom is substituted with the calibration model and the light sheet plane (volume) is aligned to the calibration grid. The target is translated through the light sheet thickness, from $z = -3mm$ to $z = 3mm$ in steps of $0.5mm$ and an uncertainty of $\pm 5\mu m$. Furthermore, a volume self-calibration analogue to that of Wieneke [2007] is applied for all measurements.

7.2.3 Verification of the experimental procedure

To verify the experimental procedure, initial measurements of a laminar and fully developed flow are conducted in a straight section upstream of the bifurcation. Laminar pipe flow is a good test case for investigating the measurement accuracy and is carried out here in the Stereo-PIV configuration. The measurements are conducted at a flow rate of $3.2l/min$ ($Re = 360$) and mean flow and RMS velocity fluctuations are calculated from 60 instantaneous velocity fields. The light sheet is approximately $1.2mm$ wide and the acquisition parameters correspond to those in Table 7.1.

Mean velocity profile

The mean streamwise velocity profile is depicted in Figure 7.4(a). The measured profiles along the $x-$ and $y-$direction closely agree with the theoretical solution. A slight asymmetry exists, which is caused by small disturbances such as a misalignment of the pipe segments or small curvature of the test section. The flow rate is calculated via integration of the instantaneous velocity field and averages to $3.17l/min$, which is in very good agreement with the prescribed flow rate of $3.2l/min$. Inherently, the flow rate (and Re) is affected by temperature variations of the working liquid (i.e., changes in viscosity), which in turn is kept constant to within $\pm 1°C$. Figure 7.4(b) shows that the flow rate remains almost constant over a long observation period with variations of less than $\pm 0.5\%$ during this time.

Calibration error

The measurement accuracy can be directly deduced from the in-plane velocity components, which is zero for a laminar, fully developed pipe flow. The movement of the viewing prisms during the calibration and measurement procedure inevitably introduce errors in the mapping function, which results in a bias in the measured in-plane velocity field [van Doorne and Westerweel, 2007]. Figure 7.5(a) shows the mean spanwise velocity component u_x along the spanwise (x) and vertical (y) direction before and after self-calibration is performed. Without self-calibration, a significant in-plane velocity component exists and its magnitude depends on the gradient of the out-of-plane velocity [van Doorne and Westerweel, 2007]. Near the centreline, the bias is almost zero, but increases gradually away from the centre (larger velocity gradients in u_z) and reaches up to 12% of the centreline velocity at approximately $x/D = 0.375$. Near the wall, the error becomes zero again, due to the no-slip condition. Volume self-calibration effectively reduces the bias error across the entire measurement plane to below 2% of the centreline velocity or approximately 0.16 pixel. The remaining in-plane velocity component can be attributed to the slight asymmetry observed in the mean velocity profile. Note that the vertical velocity component remains unaffected by the calibration error as the image is only distorted in spanwise direction.

Measurement noise

The measurement noise can be directly extracted from the RMS velocity fluctuation for steady flow and is shown in Figure 7.5(b) for u_x. The measurement noise in the centre of the pipe is approximately 1% of the centreline velocity (≈0.08 pixel) and progressively increases towards the wall (due to the higher ve-

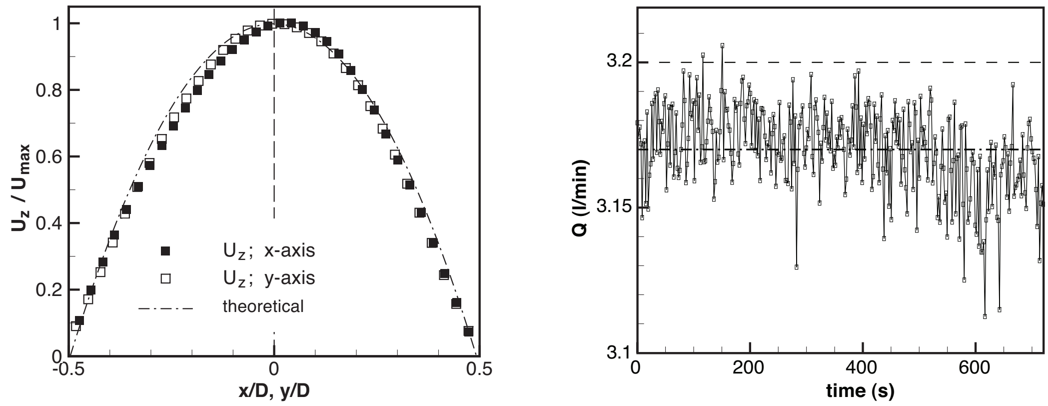

(a) (b)

Figure 7.4 Mean flow quantities: (a) velocity profile along the vertical and spanwise direction; (b) Flow rate vs. time computed from the instantaneous velocity fields

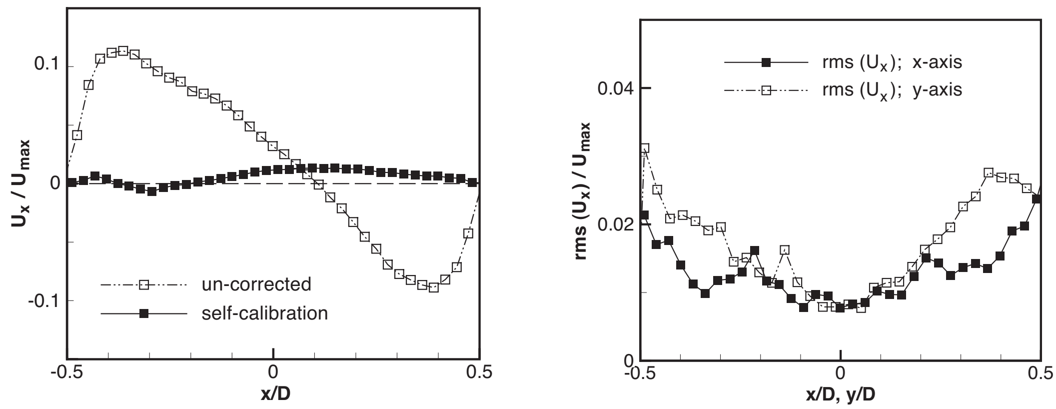

(a) (b)

Figure 7.5 Measurement accuracy: (a) Effect of the mapping accuracy on the measured in-plane velocity $u_z x$; (b) Vertical and spanwise velocity fluctuation, $rms(U_x)$

locity gradients) to values of about 3% or 0.24 pixel. This is in good agreement with the results from the numerical simulations in Chapter 3.5.

Beside the mapping and PIV procedure error, the above error estimates also include errors due to refractive index mismatch, position and alignment inaccuracies and variations in temperature and fluid viscosity as discussed in Appendix F. Overall, the accuracy of the experimental procedure is adequate for the current investigations. Although the present analysis is carried out for the Stereo-PIV system, similar conclusions can be drawn for the tomographic PIV measurements. To further elucidate this, Section 7.4 provides a detailed comparison between the Stereo-PIV and Tomo-PIV experiment.

7.3 A Description of Tomographic PIV

This section gives a brief overview of the tomographic PIV technique and the volume reconstruction technique used in this work. A more complete description of Tomo-PIV is available in Elsinga et al. [2006] and Atkinson and Soria [2009].

In Tomo-PIV, the seeded flow is illuminated with a thick laser light sheet and the 3D intensity distribution of the tracer particles is determined and subsequently cross-correlated to yield the 3D-3C velocity field. This process requires the reconstruction of the 3D intensity distribution from multiple instantaneous camera views via tomographic reconstruction techniques. The intensity recorded by each pixel P_i of the camera array represents the integration of the intensity along the pixel's line of sight s_i through the volume, which can be expressed as

$$P_i = \int_{s_i} I(x, y, z) ds_i \tag{7.1}$$

where $I(x, y, z)$ represents the intensity field of the recorded particle field. In order to reconstruct the 3D light intensities from the individual camera projections and hence solving Equation 7.1, an iterative correction of the intensity values at each point in the volume to satisfy the recorded projections is required. This is illustrated schematically in Figure 7.6.

To date, the most commonly used technique for solving Equation 7.1 in Tomo-PIV is the multiplicative algebraic reconstruction technique (MART) [Elsinga et al., 2006], which is well suited for the limited number of views typically available in fluid experiments and compared with other algebraic reconstruction techniques, provides better reconstruction quality in fewer iterations [Atkinson and Soria, 2007]. However, the MART algorithm requires long reconstruction times and large computer memory allocations, which makes the technique often unsuitable for standard desktop computing systems. An alternative to the above MART reconstruction is the multiplicative line-of-sight simultaneous correction reconstruction technique (MLOS-SMART) proposed by Atkinson and Soria [2009] and briefly explained in the following.

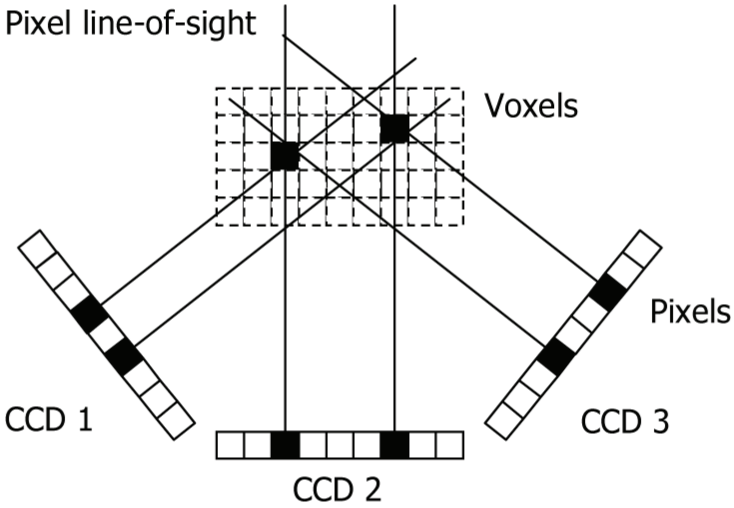

Figure 7.6 Schematic of multi-camera algebraic reconstruction technique. Filled voxels represent particle locations required to satisfy the filled pixels in each CCD recorded projection. Figure reproduced with permission from Atkinson and Soria [2007]

7.3.1 MLOS-SMART volume reconstruction

For a typical PIV experiment only 10-15 particle pairs per interrogation region are sufficient to obtain a valid displacement estimate [Keane and Adrian, 1992], the resulting volume fraction of the reconstructed particles should be less than 5%. This means that approximately 95% of the reconstructed volume will have a negligible intensity and can be excluded from the reconstruction process.

The MLOS-SMART technique takes advantage of this concept via a multiplicative line of sight (MLOS) approach to isolate the expected non-zero points from the reconstruction volume. This results in an initial estimate of the 3D particle intensity distribution, which contains the approximated particle intensities, but also ghost particles due to the non-uniqueness of the camera projections. In order to reduce the intensity of the ghost particles, the MLOS estimation is followed by an iterative voxel correction in the form of the simultaneous multiplicative algebraic reconstruction technique (SMART), which is only performed on the non-zero voxels.

The SMART technique is based on the same principles as the MART technique and the only difference is the method by which the correction is determined. SMART involves the simultaneous multiplicative correction of the non-zero voxel intensities in each iteration k, based on the product of the ratio of the recorded P_i to the projected $\sum_j W_{ij} I_j$ pixel intensities so that

$$I_j^{k+1} = I_j^k \prod_i^{N_i} \left[\left(\frac{P_i}{\sum_j W_{ij} I_j^k} \right)^{\mu W_{ij}} \right]^{1/N_i} \tag{7.2}$$

where N_i is the number of pixels that observe a given voxel j, W_{ij} the weighting of the individual pixel intensities and μ a relaxation to adjust the convergency of the iterative reconstruction.

Simulations by Atkinson and Soria [2009] for a 4 camera Tomo-PIV setup with a 0.05*ppp* seeding density, have shown that 40 iterations with the MLOS-SMART technique produce an equivalent reconstruction quality compared to 5 iterations with the standard MART algorithm. This corresponds to an increase in reconstruction speed for the MLOS-SMART of 5.5 times and a 15 times reduction in total memory requirements. Further comparison for a turbulent boundary layer experiment (0.01*ppp*) showed that as few as 10 MLOS-SMART iterations were sufficient to achieve a vector difference in the velocity fields which is within the experimental error of Tomo-PIV [Atkinson and Soria, 2009]. An example of the reconstructed three-dimensional particle volume is given in Figure 7.7(a) and the corresponding 3D-3C velocity field is illustrated in Figure 7.7(b) comprising a measurement volume of approximately $22 \times 24 \times 6\text{mm}^3$.

7.3.2 Calculation of wall shear stress

As discussed previously, WSS is an important haemodynamic parameter and directly related to the development and progression of vascular disease [Traub and Berk, 1998; Chatzizisis et al., 2007] and it is also a notoriously difficult quantity to determine experimentally (Chapter 4). Wall shear stress is estimated from the velocity gradient at or near the wall as:

$$\tau_{wall} = \mu \frac{\partial u}{\partial n}\bigg|_{wall} \tag{7.3}$$

where, n is the wall normal direction and $\partial u / \partial n|_{wall}$ the velocity gradient at the wall. To determine the WSS from the velocity field, it is necessary to compute Equation 7.3 in the vicinity of the model surface. In order to obtain the

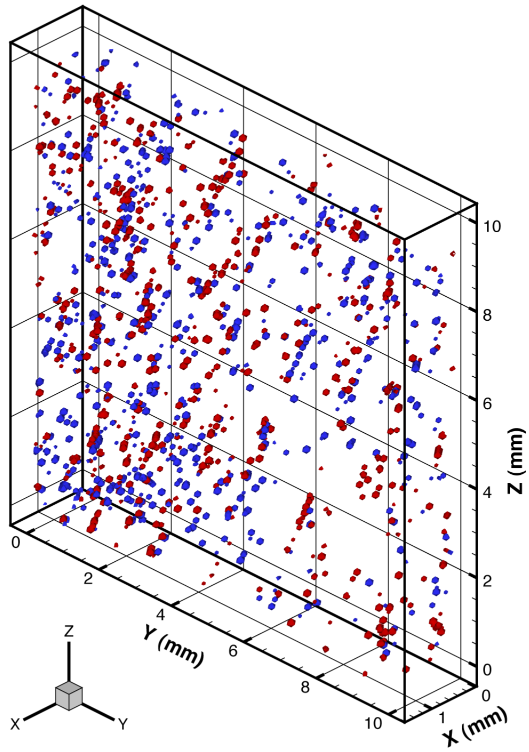

(a)

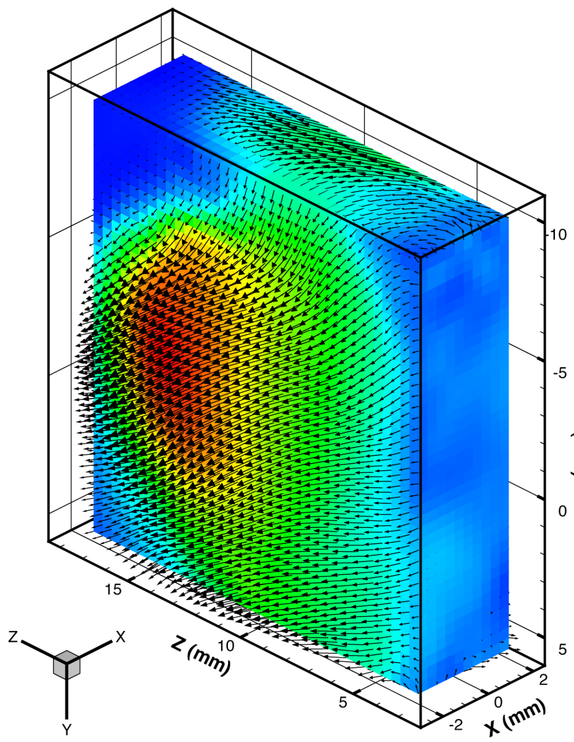

(b)

Figure 7.7 (a) Sub-volume of a reconstructed 3D particle intensity field. First and second exposure are labeled by blue and red particles, respectively. (b) Corresponding full 3D-3C velocity field of $22 \times 24 \times 6\text{mm}^3$ size

WSS values on an irregular three-dimensional surface, the vessel orientation has to be determined and a data transformation from the measurement coordinate system to a wall-parallel coordinate system is necessary. In the previous chapter, this was achieved with iPV for planar PIV data. However, in the present case this procedure is not straight forward due to the three-dimensionality and non-uniformity of the vessel surface. Therefore, an alternative procedure is applied here, where the vessel surface is mapped onto the measurement coordinate system and the shear stress is derived from the measured data via velocity field differentiation in a cartesian coordinate system.

As described in Section 2.4.3, an accurate surface description of the flow geometry is obtained by reconstruction of the recorded CT data. The idea of the following procedure is to merge this surface mesh with the 3D velocity data and to calculate the 3D shear stress distribution in cartesian coordinates, which can then be interpolated onto the surface mesh.
In detail, location markers embedded in the silicone flow phantom are used together with the camera mapping function to allow an accurate alignment of the two data sets. The accuracy by which this alignment can be performed depends primarily on the precision of reconstructed marker locations from the CT data (i.e., $\pm 0.28mm$) and the accuracy of the camera calibration (i.e., 1pixel or $25\mu m$ after self-calibration) and is estimated here to approximately $\pm 1.5\%$ of the vessel diameter or $\pm 0.3mm$.

In the cartesian coordinate system, the shear stress at a given point in the volume can be derived from the Cauchy stress tensor τ_{ij}, which for incompressible flow can be expressed as follows:

$$\tau_{ij} = p\delta_{ij} + \mu \left(\frac{\partial u_i}{\partial x_i} + \frac{\partial u_j}{\partial x_j} \right) \tag{7.4}$$

where p is the hydrostatic pressure and δ_{ij} the kronecka delta. The computation of the velocity derivatives in Equation 7.4 are performed through a least square fit of a second order regression of the following form to each velocity component in a $5 \times 5 \times 5$ neighbourhood,

$$\begin{aligned} U_i(x,y,z) &= a_0 + a_1 x + a_2 y + a_3 z + a_4 xy + a_5 xz \quad ... \\ &\quad + a_6 yz + a_7 x^2 + a_8 y^2 + a_9 z^2 \end{aligned} \tag{7.5}$$

The coefficient a_0 in Equation 7.5 corresponds to the fitted velocity at the point (x_0, y_0, z_0) and a_1, a_2, a_3 are the velocity gradients at that point in the respective $x-$, $y-$, and $z-$direction. The accuracy of the analytical velocity field differentiation has been discussed extensively in Chapter 4.2.

Substitution of Equation 7.5 into 7.4 allows to compute the principle 3D shear stress as $(\lambda_{max} - \lambda_{min})/2$, where λ_i are the eigenvalues of τ_{ij}. Finally, the shear stress (i.e., wall shear stress) on the model surface is obtained by a weighted inverse distance interpolation of the principle 3D shear stress onto the imported surface mesh.

The advantage of this method is that the shear stress is computed in the measurement coordinate system and no coordinate transformation to a system based on the local vessel geometry is necessary. The disadvantage, however, is that it only allows the computation of the WSS magnitude and any directional information of the WSS is lost. Recovering the sign of the WSS would again require knowledge of the wall normal coordinate system.

7.4 Comparison between Stereo- and Tomo-PIV

The accuracy of the Tomo-PIV technique is investigated by comparing velocity statistics and WSS distributions with Stereo-PIV measurements. The flow field is recorded in a plane in the internal carotid artery ($z = 2mm$) and the mean and RMS values are computed from an ensemble of 40 instantaneous realisations. The experimental conditions are listed in Table 7.1 with the light sheet thickness varying between $1.0 - 6.0mm$. Stereo-PIV results are obtained using only camera 1 and 2 (Fig. 7.3) and the $1mm$ thick light sheet.

The recorded images are pre-processed to remove the background intensity as required by the MLOS-SMART algorithm and to eliminate light reflection on the wall interface caused by small differences in refractive index. The image processing involves the subtraction of a mean intensity image, followed by a dynamic histogram filtering and a Gaussian smoothing (3×3) (Appendix C) to equalize the camera intensity differences caused by forward/backward scattering differences and/or laser profile variations. Due to the circular shape of the measurement volume, the recorded particle fields only occupy approximately 60-75% of the CCD array and a masking technique is applied to exclude the non-flow areas from the reconstruction process. Note, that the average seeding density of approximately $0.01ppp$ is retained throughout the image pre-processing.

Volume reconstruction is performed with 10 iterations of the MLOS-SMART technique and an initial solution, I_j^0 and relaxation parameter, μ of unity (Eq. 7.2). Depending on the light sheet thickness, the volume size varies between $880 \times 960 \times 64$ and $880 \times 960 \times 256$ voxels. The corresponding physical dimensions are $22mm \times 24mm \times \delta z$, with the light sheet thickness δz, a pixel-to-voxel ratio of about 1:1 and a discretisation of 40 voxles/mm. The volumes are reconstructed on a single core 2.8 MHz Intel processor with reconstruction times for $880 \times 960 \times 96$ voxels in the order of 6 minutes or 8.7 times faster than 5 MART iterations (excluding computation of the weighting matrix).

The 3D-3C velocity fields are calculated with an multi-pass FFT-based cross- correlation algorithm [Soria, 1996]. Interrogation volumes of 64^3 voxels with 75% overlap are used to provide fields of $52 \times 57 \times 13$ vectors. The calcu-

Table 7.2 Parameters for the Stereo- and Tomo-PIV analysis

Image pre-processing	mean intensity subtraction dynamic histogram filtering gaussian smoothing (3×3 pixel) masking of non-flow regions	
Volume reconstruction	Method	MLOS-SMART
	Particle density	$\approx 0.01ppp$
	# iterations	10
	I_j^0	1.0
	μ	1.0
	Discretisation	40 voxels/mm
	Size	$880 \times 960 \times 256$ voxel^3
		$22 \times 24 \times 13$ mm^3
Tomo-PIV analysis	Type	3D Multi-pass analysis
	# of passes	2
	Spatial resolution	$64 \times 64 \times 64$ voxel^3
		$1.6 \times 1.6 \times 1.6$ mm^3
	Grid spacing	16 voxel
		0.4 mm
	# vectors	$52 \times 57 \times 13$
Stereo-PIV analysis	Type	2D Multi-pass analysis
	# of passes	2
	Spatial resolution	64×64 pixel^2
		1.6×1.6 mm^2
	Grid spacing	16 pixel
		0.4 mm
	# vectors	52×57
Vector validation	max. displacement limit, normalised median test [Westerweel and Scarano, 2005]	

lated vectors are validated with the normalised median filter and a maximum displacement limit. Invalid vectors are replaced by a mean vector interpolation and typically amount to less than 5% of the total vector count. The use of smaller interrogation volumes is not possible due to the limited particle field density. Identical processing and vector discretisation is used for both the Stereo- and Tomo-PIV data. The Stereo-PIV images are analysed with the SPIVCC algorithm developed in Chapter 3.6. Furthermore, volume self-calibration is used for all measurements to minimise the errors due to light sheet miss-alignment. The most relevant analysis parameters are summarised in Table 7.2.

7.4.1 Velocity Fields

The instantaneous velocity distributions for light sheet thickness of 1.0, 3.0 and 6.0mm are shown in Figure 7.8 and as expected show a good qualitative agreement with the Stereo-PIV data. The results are presented in form of in-plane velocity vectors $[u_x, u_y]$ and out-of-plane velocity contours u_z. Both techniques clearly show a high velocity region in the centre of the vessel and a low velocity region on the outer wall (right in Fig. 7.8) with most of the in-plane flow directed towards the inner or flow divider wall (i.e., bottom). However, the Tomo-PIV results for the 3mm and 6mm light sheet indicated a slightly higher noise level.

To compare the results quantitatively, horizontal and vertical profiles of the mean and RMS fluctuations for the individual velocity components are extracted at the centre of the vessel (Figure 7.9). The mean profile of the u_z- and u_y- component demonstrate good overall agreement with some larger discrepancies

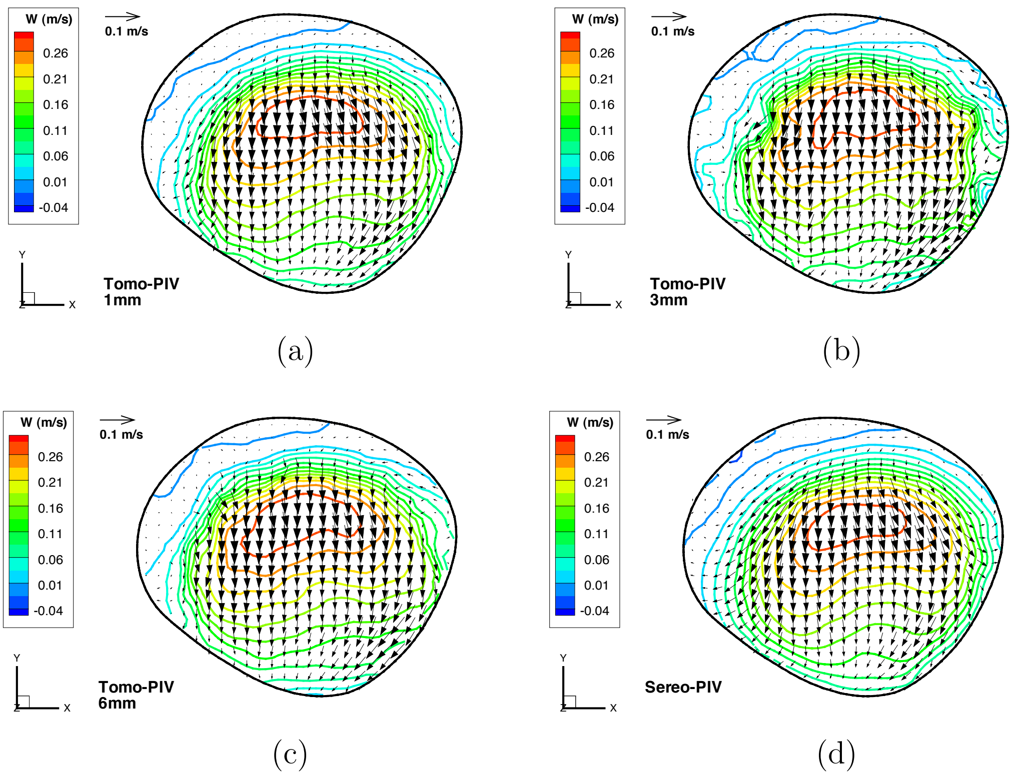

Figure 7.8 Comparison of instantaneous velocity fields: (a) Tomo-PIV, 1mm; (b) Tomo-PIV, 3mm; (b) Tomo-PIV, 6mm and (a) Stereo-PIV, 1mm

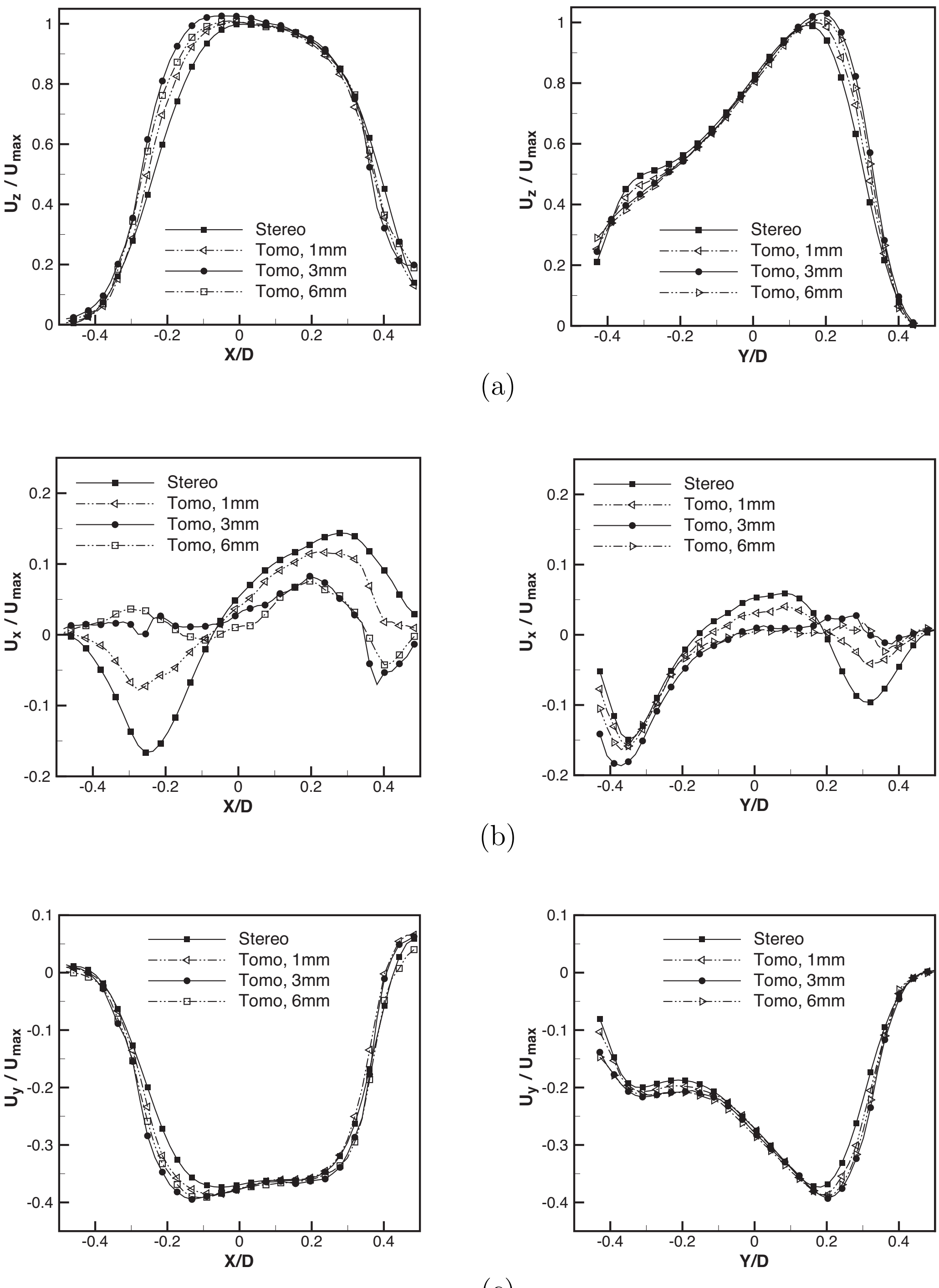

Figure 7.9 Mean velocity profiles in the centre of the vessel: (a) u_z; (b) u_x; (c) u_y along the horizontal (left) and vertical direction (right)

of about 10% (or ≈ 0.9 pixel) at locations with strong velocity gradients (i.e., $x/D = -0.2$ and $y/D = 0.3$). For the spanwise velocity component, u_x, larger differences occur, which may be explained by the perspective distortion along the camera axis in this direction. As demonstrated earlier, the in-plane velocity components are most susceptible to errors in the camera mapping function with the current results showing large variation in u_x for the different laser sheet thicknesses. Errors in the mapping function result in the reconstruction of ghost particles or no particles at all, both of which adversely affect the cross-correlation performance. Further volume self-calibration did not reduce the bias error any further.

In the present analysis, the steady state assumption directly allows an estimation of the measurement uncertainty from the computed RMS velocity fluc-

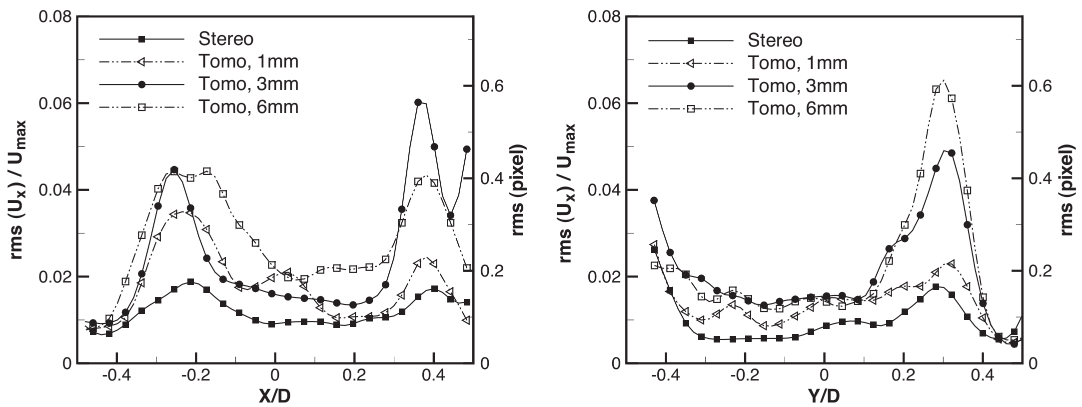

(a)

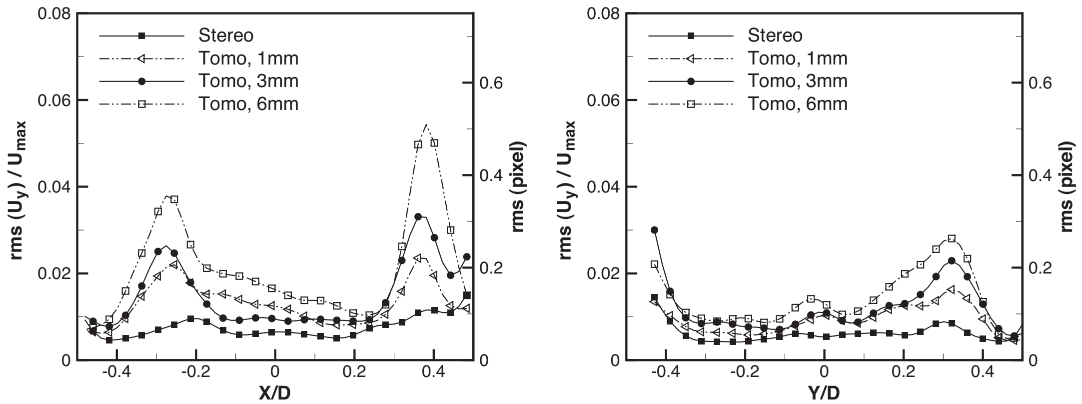

(b)

Figure 7.10 RMS velocity fluctuations in the centre of the vessel: (a) u_x; (b) u_y along the horizontal (left) and vertical direction (right) tuation shown in Figure 7.10. The RMS error for the Stereo-PIV data has been validated before (Section 7.2.3) and is within its expected values (i.e., $0.1 - 0.2$ pixels). For the Tomo-PIV data, an increase in RMS uncertainty can be observed for increasing light sheet thickness, which is consistent with earlier observations by Michaelis and Wieneke [2008]. Furthermore, the RMS error varies along the vessel cross-section with values of about $0.1 - 0.3$ pixels in the centre of the test section and an increase towards the vessel wall to up to 0.5 pixel and 0.6 pixel for u_y and u_x, respectively. Similar to the mean profiles, larger uncertainties are observed for u_x and along the $x-$axis. It is obvious that the RMS error is a function of the velocity gradient (both in- and out-of-plane components), which is small in the centre of the test section, but increases towards the vessel walls.

For traditional planar- and Stereo-PIV, well established theoretical and practical formulation for the RMS dependency on the velocity gradient exist. For example, Keane and Adrian [1992] recommend that the displacement difference across the interrogation region should be kept less than half the particle image diameter: $M|\Delta U|dt/d_p \leq 0.5$ and less than 3% of the interrogation size, $M|\Delta U|dt/W_x \leq 0.03$. Using Figure 7.12, the maximum gradient can be approximated to $du_z/dr = 0.09$ pixel/pixel, which for an interrogation size of 64 pixel and a particle image diameter of 3 pixel leads to $M|\Delta U|dt/d_p \approx 3$ and $M|\Delta U|dt/W_x \approx 9\%$. For these conditions, simulations in Chapter 3.5 indicated RMS values of about 1.0 pixel for $\approx 0.005ppp$. Although these considerations are currently only valid for planar-PIV, they may also have some general applicability in Tomo-PIV experiments.

Recently, Elsinga et al. [2009] have shown modulation effects of the velocity field due to the cross-correlation of ghost particles that occur in both exposures. While this effect occurs predominantly in areas of low flow velocities and small gradients, it reduces for larger gradients due to the de-correlation of ghost particles [Elsinga et al., 2009]. Conversely, the RMS uncertainty is expected to increase in theses cases due to a broadening or splitting of the correlation peak. For the present case, the RMS errors in the centre of the vessel are consistent with values quoted by Wieneke and Taylor [2006] for moderate velocity gradients of approximately $0.2 - 0.3$ pixel. Finally, it should be noted that the expected RMS error in the Stereo-PIV data is smaller due to the perspective viewing, i.e., smaller in-plane displacement and hence $du_x/dr \sim 1/\sqrt{2}du_z/dr$.

7.4.2 Wall shear stress

A comparison of the computed WSS distribution on the vessel surface is given in Figure 7.11. WSS is computed via Equation 7.4 and 7.5 for the $6mm$ thick light sheet and a grid spacing of $0.4mm$. Note, that the $5 \times 5 \times 5$ kernel used for the velocity gradient estimation is equal to the interrogation window size with 75% overlap. Hence, the spatial resolution of the cross-correlation and the WSS estimation are similar. For the Stereo-PIV, seven adjacent data planes spaced $1mm$ apart are combined to produce a 3D-3C data set with a grid spacing of $0.4mm$ in x and y and $1mm$ in $z-$direction. Likewise, the WSS distribution is determined with the above equations in a $5 \times 5 \times 3$ neighbourhood. A good qualitative agreement between the two methods exists with a low WSS region occurring at the outer vessel wall and medium to high shear stress along the side and inner walls. The Tomo-PIV data predict a slightly smaller low WSS region, whilst along the side walls, patches of higher shear stress occur.

Profiles of the mean shear stress distribution in the centre of the slice are shown in Figure 7.12 for the horizontal and vertical direction. A very good agreement is obtained in the centre of the vessel, while some deviation of the Stereo-PIV data occurs near the wall where the velocity gradients are larger. Additionally, The Stereo-PIV under-predicts the shear rate in these regions by

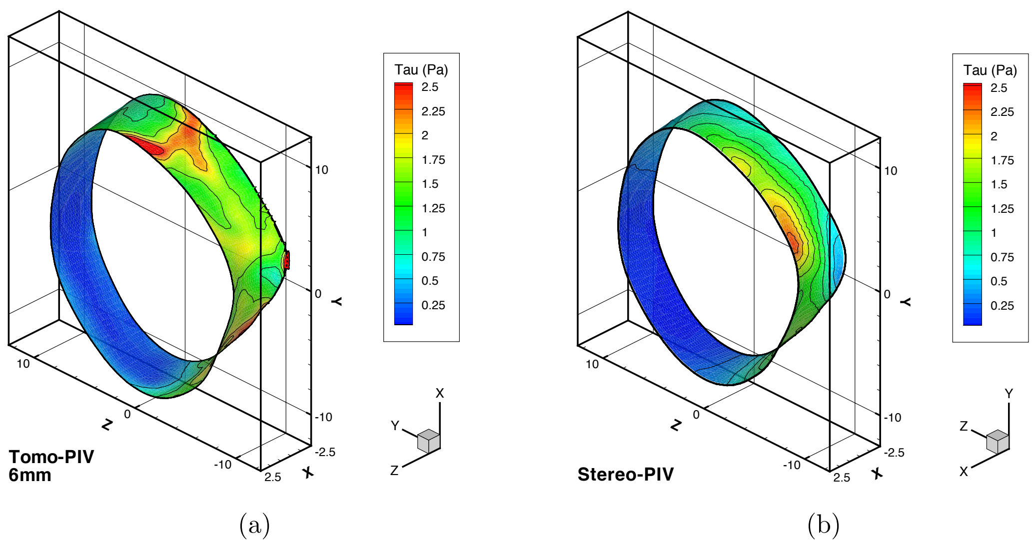

Figure 7.11 Wall shear stress contours: (a) Tomo-PIV, 6mm; (b) Stero-PIV from 7 consecutive planes, spaced $1mm$ apart

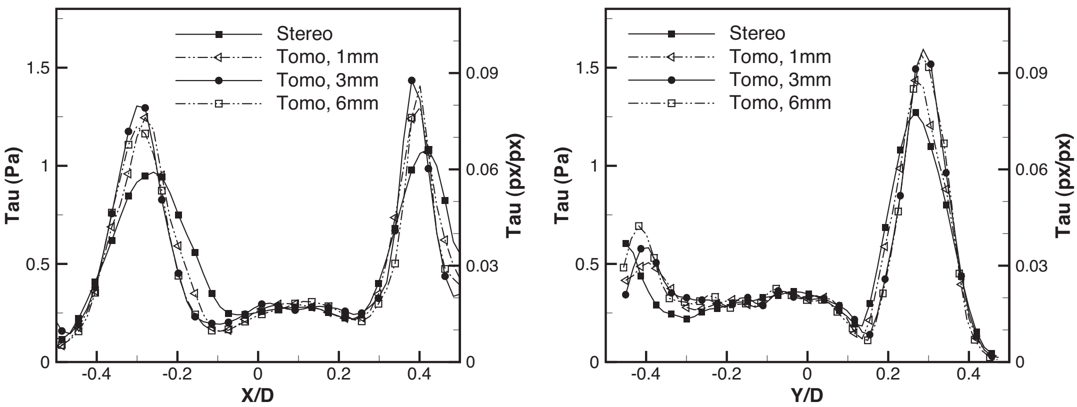

Figure 7.12 Mean shear stress profiles in the centre of the vessel and along the horizontal (left) and vertical direction (right)

approximately 25%. The maximal measured shear rates are in the order of $0.9 - 1.0$ pixel/pixel which corresponds to a displacement difference across the interrogation volume of approximately 6.0 pixels. Overall, however, the agreement between the two techniques is satisfactory and the observed differences can be attributed to the wider spacing of the Stereo-PIV data and a higher noise level in the Tomo-PIV data.

7.5 Tomographic PIV Results in a Patient Specific Geometry

In order to map the entire velocity field in the internal carotid artery and the bifurcation region, Tomo-PIV measurements are performed at several axial locations and subsequently combined. For this, the flow phantom is traversed in axial direction in steps of $5mm$ and a total of 10 measurement volumes with a $6mm$ light sheet are acquired. The cameras are calibrated only at the first and last measurement location, with volume self-calibration performed at each measurement location. The self-calibration indicates an initial particle based calibration error of typically 2-10 pixels, which for all measurement locations reduces to less than 1 pixel after four iterative corrections.

The Reynolds number corresponds to an average physiological flow rate of $Re = 339$ and remains constant within $\pm 0.5\%$ between the different measurement locations as shown in Figure 7.4(b). The division of flow in the two daughter branches is adjusted to 7:3 between the internal and external carotid artery.

The particle volumes are reconstructed with the MLOS-SMART technique with reconstruction parameters identical to those in Section 7.4. The particle images are reconstructed in a domain of $26 \times 27 \times 6$ mm or $1040 \times 1080 \times 240$ voxels. The reconstructed volumes are cross-correlated and subsequently averaged over 40 instantaneous realisations and combined to yield a 3D-3C velocity field of size $26mm \times 27mm \times 60mm$. From this, the WSS distribution is calculated with Equations 7.4 and 7.5.

7.5.1 3D Flow Field and Wall Shear Stress

Profiles of the streamwise velocity u_z together with velocity contours at selected cross-sections are shown in Figure 7.13(a). The flow is fully developed at the model entrance as shown in Figure 7.4(a). Near the bifurcation region (section i) the velocity profile is already skewed towards the outer wall due to the curvature of the main vessel upstream. After the vessel bifurcation (section ii and iii), a separated flow region forms along the outer internal carotid artery wall, which results in the formation of a complex 3D velocity profile. In this region, the flow

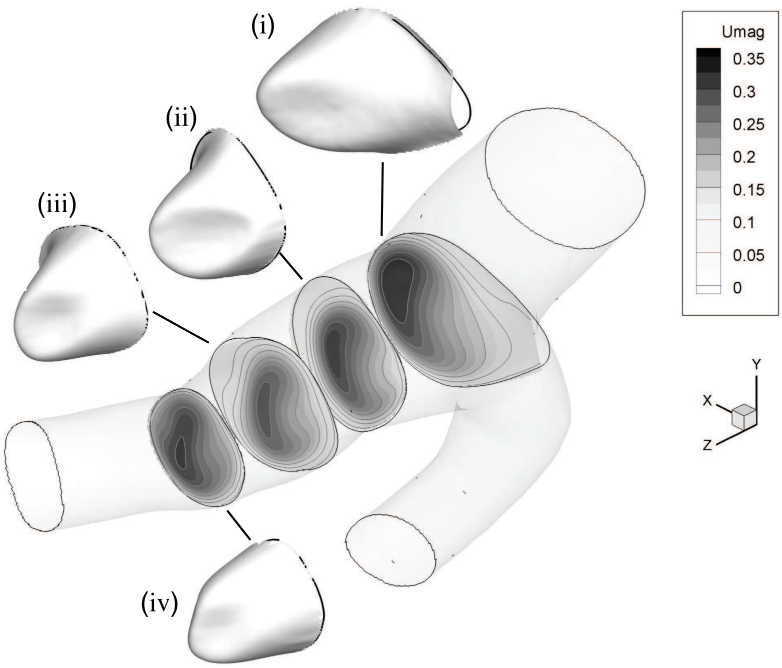

(a)

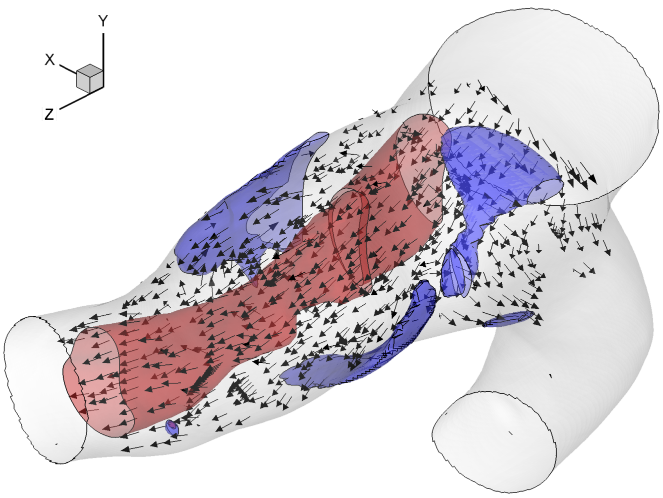

(b)

Figure 7.13 Velocity field in the carotid artery for $Re = 339$: (a) Profiles and contours of the streamwise velocity component $u_z z$ at different cross-sectional planes in the bifurcation and internal carotid artery; (b) Iso-surface of axial velocity extracted at $(u_z z/\overline{U} \geq 1.6)$, red and $(u_z z/\overline{U} \leq -0.1)$,blue overlaid by the vector field. For clarity only every 64^{th} vector is shown

is subjected to a strong centripetal acceleration (due to the vessel curvature) and is pushed towards the inner wall (i.e., flow divider wall). This creates a radial pressure gradient, which results in the re-distribution of the axial velocity and formation of a low momentum region along the outer wall. This can also be seen in the characteristic formation of the c-shaped iso-contours in Figure 7.8, which are typical for secondary flow development in curved pipes. Further downstream (section iv), the flow accelerates again and the velocity becomes more uniformly distributed due to a reduction in cross-sectional area in this region.

Figure 7.13(b) illustrates the measured vector field and iso-surfaces of the axial velocity. At the bifurcation, the flow is deflected into the internal and external carotid artery. A high velocity region exists in the centre of the vessel ($u_z z/\overline{U} \geq 1.6$) and several separated flow regions ($u_z z/\overline{U} \leq -0.1$) occur along the inner and outer wall as well as along the bifurcation region. The fluid is unable to remain attached in these regions due to vessel curvature, constantly changing surface topology and adverse pressure gradient.

Wall shear stress in the bifurcation region and the internal carotid artery is shown in Figure 7.14. A large low shear region forms along the outer wall, which extends around the circumference to the upper and inner wall and coincides with the separated flow region seen in Figure 7.13(b). Along the flow divider wall, shear stress levels are slightly higher compared to the outer wall with a peak in WSS near the bifurcation apex. High shear stress levels primarily exist at the proximal and distal outer wall and correspond to regions of strong vessel curvatures. The WSS distribution is noticeably asymmetric and has a spiraling or helical appearance, which closely follows the helical flow motion in direction and pitch.

Details of the WSS distribution along the lines A-D (Fig. 7.14) are presented in Figure 7.15. A maximum shear stress of approximately $2.5Pa$ occurs at the proximal and distal outer sinus wall (line D) and minimal stress levels exist throughout the internal carotid artery. The corresponding wall shear stress for the fully developed, parabolic inlet profile is $0.96Pa$.

7.5.2 Verification of Wall Shear Stress Estimates

In order to verify the proposed WSS method and particularly the alignment accuracy of the surface mesh with the velocity data, a simple test is performed. The surface mesh is purposely mis-aligned in the respective $x-$ and $y-$direction by $\pm 0.5mm$ and the WSS distribution is re-computed for each case and com-

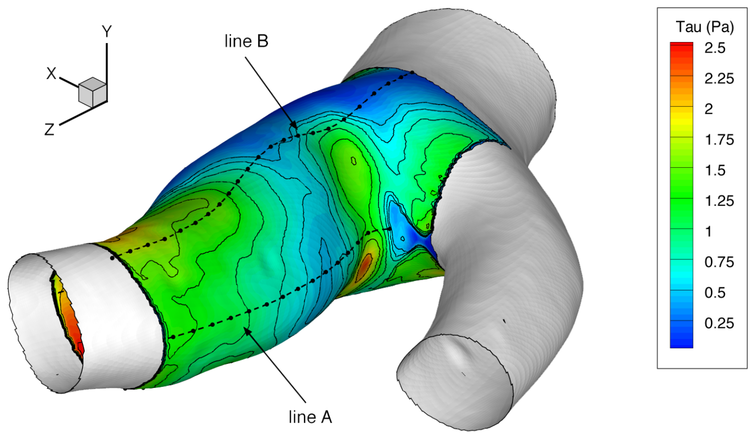

(a)

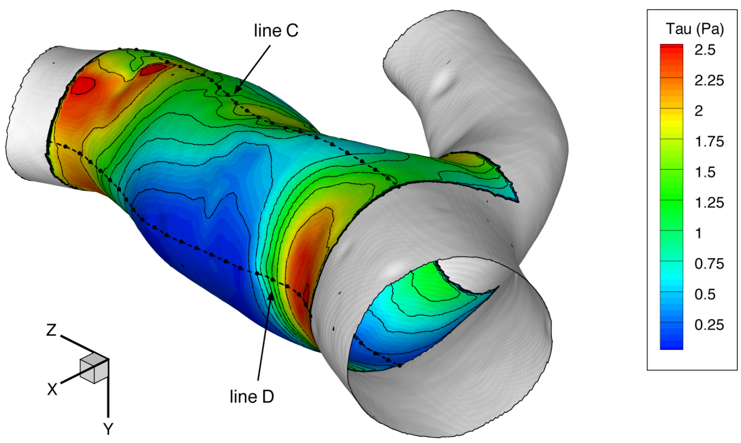

(b)

Figure 7.14 Wall shear stress in the bifurcation and the internal carotid artery: (a) inner/flow divider wall; (b) outer wall

pared to the original mesh alignment in form of surface distribution histograms (Figure 7.16). The original mesh has a homogeneous WSS distribution with two peaks corresponding to the mean level of approximately $1.01Pa$ and the low WSS region on the outer wall at $0.1Pa$. For the $-0.5mm$ displacement, the low WSS peak disappears and the distribution is slightly shifted to higher values, while for the $+0.5mm$ shift, the low WSS peak increases and the distribution follows the original one more closely. The WSS distributions for the different surface meshes are qualitatively very similar with mean WSS levels of $1.02Pa$ and $0.98Pa$ for the $+0.5mm$ and $-0.5mm$ displacements, respectively.

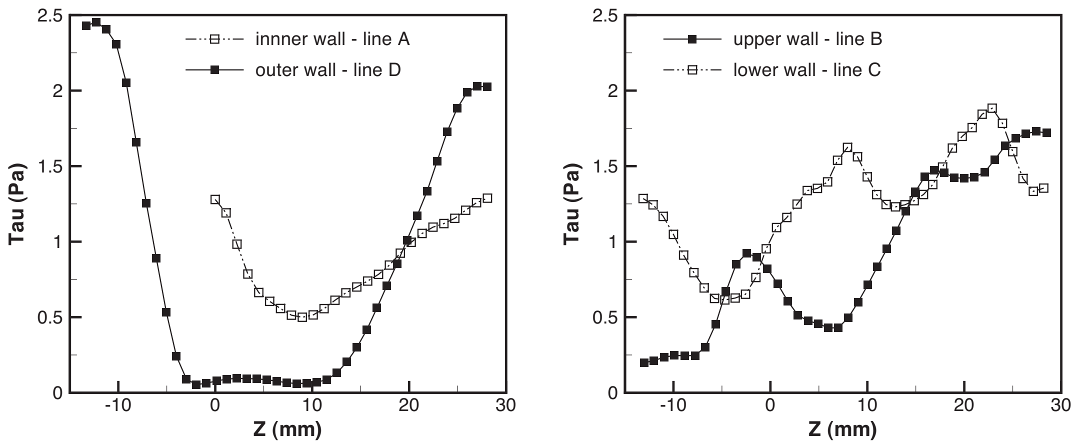

(a) (b)

Figure 7.15 Wall shear stress magnitude along the line A-D as indicated in Figure 7.14: (a) inner and outer wall; (b) upper and lower wall, $z = 0$ corresponds to the bifurcation apex

Also note, that the prescribed surface displacement of $\pm 0.5mm$ is larger than the expected alignment uncertainty of $\pm 0.3mm$. Overall, the variation in the computed WSS distributions due to a mis-alignment of the two data sets are expected to be low and the proposed technique is adequate for the current investigations. A further increase in accuracy can be achieved by improving the precision of the location markers in the silicone flow phantom.

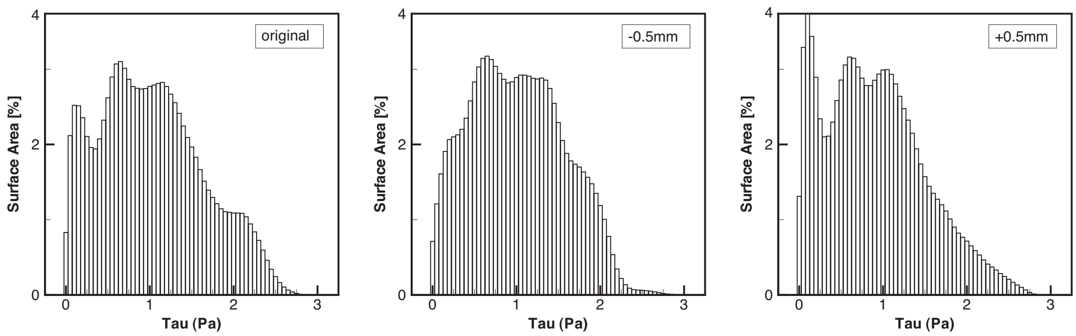

Figure 7.16 Histograms of the WSS surface distribution for the original surface mesh used in Fig. 7.14, (left) and the $x - y$ shifted meshes, (middle) and (right)

7.6 Stereo-PIV Results in the Idealised Geometry

Lastly, the 3D-3C flow field the idealised carotid artery bifurcation is investigated. The model geometry is identical to that used in Chapter 5 and the steady flow conditions correspond to a Reynolds number of $Re = 654$ and a flow division between internal and external carotid artery of 7:3.

The measurements are conducted using the Stereo-PIV configuration (i.e., camera 1 and 2) to acquire 2D-3C velocity fields at planes spaced 1mm apart in z-direction. A total of 100 image pairs are recorded per plane and a total of 54 planes (i.e., $z = -24 : 28$) are acquired, comprising the bifurcation and carotid sinus region. As before, the flow phantom is traversed in streamwise direction and the cameras are calibrated before and after the measurement, with subsequent self-calibration at each measurement plane.

The recorded Stereo-PIV images are processed with the SPIVCC algorithm developed in Chapter 3.6 using parameters equivalent to those in Table 7.2. Subsequently, the individual 2D-3C velocity fields are combined to produce a 3D-3C velocity volume with a grid spacing of $0.4 \times 0.4 \times 1$mm (or $52 \times 57 \times 54$ vectors). Wall shear stress is calculated using Equations 7.3 and 7.5.

7.6.1 3D Flow and Wall Shear Stress Characteristics

Both flow characteristics and WSS distribution in the idealised geometry have been described extensively in Chapter 5 where some interpretations of the three-dimensional flow structure has been provided. The following section is thought to complement and verify the previous observation and to extend those by adding valuable three-dimensional information, not provided by the planar PIV measurements previously.

Profiles of the streamwise velocity component, sampled at the spanwise planes A-A, B-B, C-C and D-D (see Fig. 5.4) are shown in Figure 7.17. These profiles exhibit the previously observed skewing towards the inner sinus wall and the low momentum flow regions along the outer wall. At location A-A and B-B, the regions of low or reverse flow (and hence low WSS) are confined to only a very small region along the outer wall near the vessel's centreline. Most

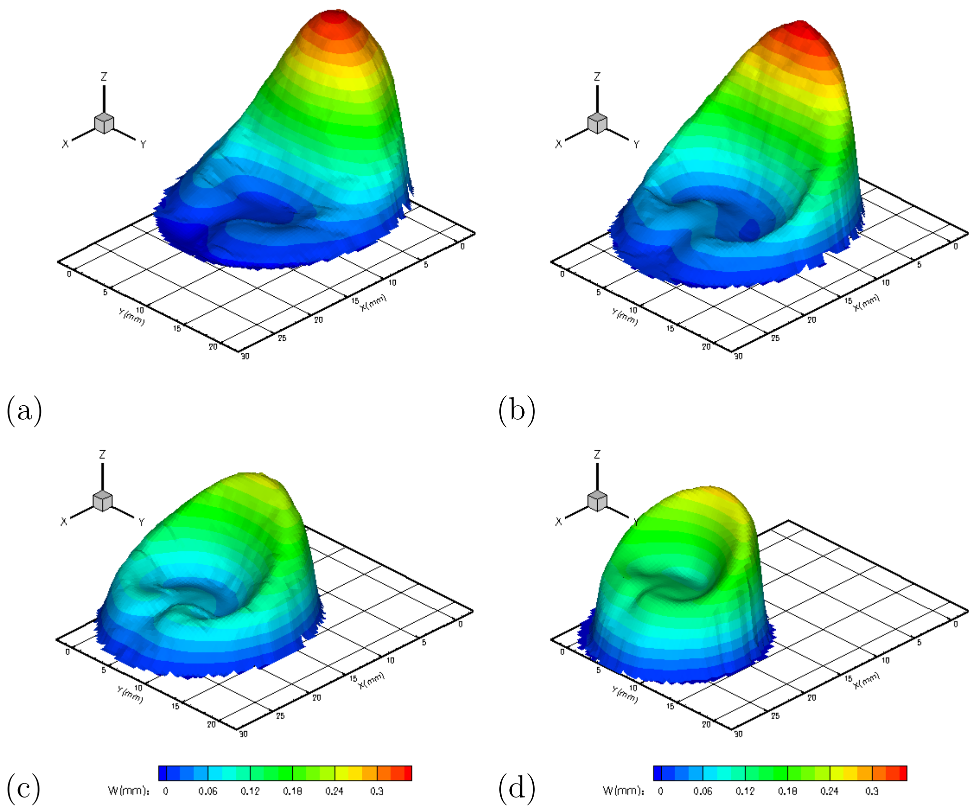

Figure 7.17 Profiles of axial velocity in the idealised carotid artery sinus sampled cross-sectional planes indicated in Fig. 5.4: (a) plane A-A; (b) plane B-B; (c) plane C-C; (d) plane D-D;

interestingly is the velocity lag in the centre of the vessel, which could not be observed in the planar PIV data. This lag in velocity is a direct consequence of the secondary flow patterns (i.e., Dean vortices) evolving within the carotid sinus. Further evidence of this is given by the characteristic 'c-shape' of the axial velocity component. Towards the distal part of the carotid sinus (plane C-C and D-D), the centreline velocity recovers and velocity profiles becomes more uniform again.

Three-dimensional streamlines together with a representation of the vortical flow structure are presented in Figure 7.18. The three-dimensional streamlines confirm the previously discussed heliocoidal flow structure within the carotid sinus. Close to the inner wall, streamlines follow the mean flow with little or no helicity, while closer to the outer wall, flow exhibits a strong swirling motion. Also, the deflection of the flow originating from outside the symmetry plane can clearly be seen at the apex. The vortical flow structure is investigated by means

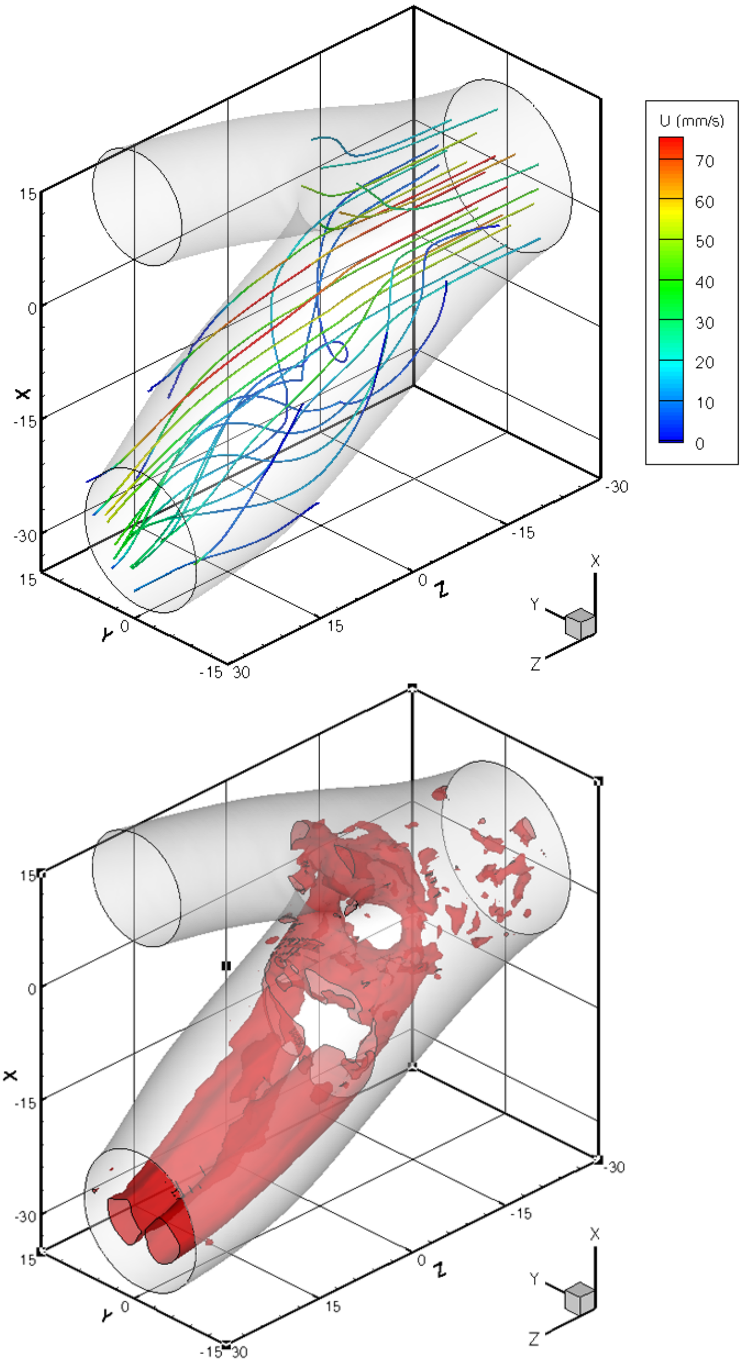

Figure 7.18 Three-dimensional flow topology in the idealised carotid sinus: (a) Streamlines colour-coded by velocity magnitude; (b) Vortex iso-contours as calculated by the Q-criterion (Q > 0)

of the vortex Q-criterion [Haller, 2005] and illustrated in Figure 7.18(b) for Q > 0. Two characteristic structures can be identified. First, a 'ring-shaped' structure, centred around the bifurcation apex, which is caused by the strong shear layer developing along the inner walls of the bifurcation. The second structure

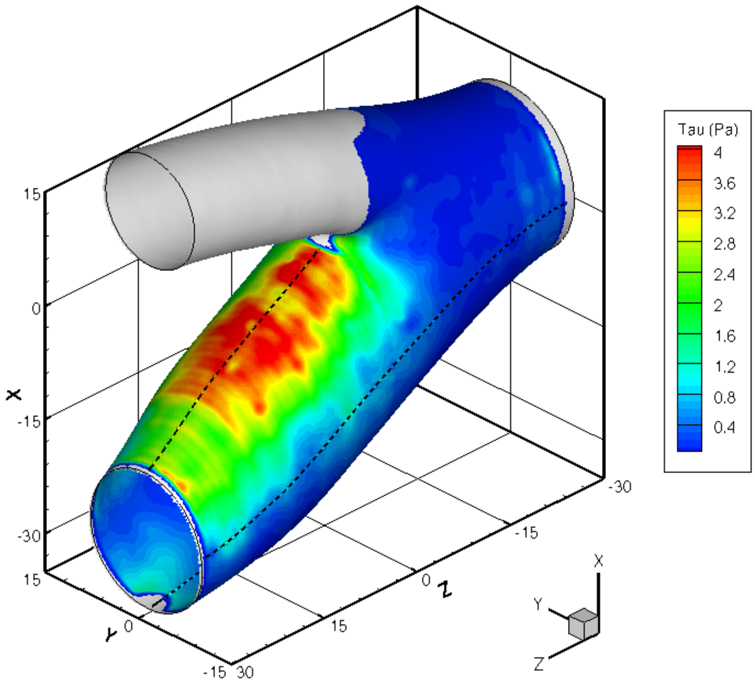

Figure 7.19 Three-dimensional wall shear stress in the idealised carotid sinus

is located along the outer sinus walls and is formed by the secondary vortices observed in the spanwise plane. These two vortex structures are symmetric (due to the symmetric geometry) and are counter-rotating.

The three-dimensional WSS distribution is depicted in Figure 7.19 and

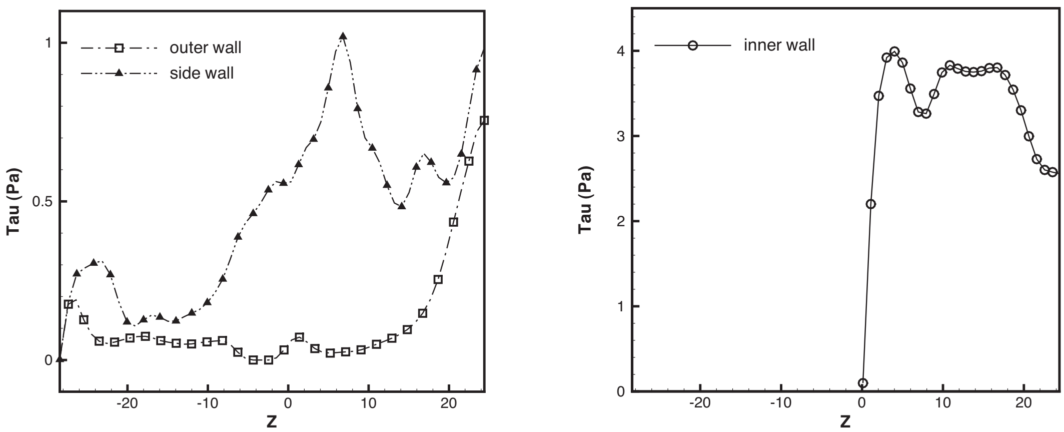

(a) (b)

Figure 7.20 Wall shear stress magnitude along the inner, outer and sidewalls in the idealised carotid sinus as indicated in Figure 7.19: (a) outer wall and sidewall; (b) inner wall. $z = 0$ corresponds to the bifurcation apex shows the high and low shear stress regions along the inner and outer sinus walls. Along the bifurcation sidewalls, WSS is also generally low, but matches that in the common carotid artery.

Profiles of WSS extracted along the inner, outer and sidewalls (dashed lines in Fig. 7.19) are given in Figure 7.20 and exhibit very similar characteristics to those shown in Figure 5.13. The WSS magnitude tends to be underestimated due to the limited spatial resolution in streamwise direction, but the general features are present. For example, along the outer sinus wall, the WSS distribution clearly the flow separation and reattachment characteristics (also see Fig. 5.12), while along the inner wall, the second WSS peak due to the adverse vessel curvature is clearly visible. For the sidewalls, WSS is initially low, but increases progressively towards the distal sinus.

7.7 Discussion and Conclusion

This chapter has presented Stereo- and Tomo-PIV measurements of the flow field and WSS in a physiologically accurate model of the human carotid artery. The model geometry was reconstructed from post-mortem data and reproduced in a scaled and transparent flow phantom. A refractive index matched working liquid consisting of a 39% aqueous glycerin mixture was used to enable distortion free viewing of the complex and convoluted flow passage. The experimental setup was designed such that multiple measurements at different cross-sections could be performed by simply traversing the flow phantom in streamwise direction without the need for re-calibrating the camera setup. The robustness and accuracy of the experimental procedure was assessed with preliminary Stereo-PIV measurements and was within $2-3\%$ of the maximum flow velocity.

Tomographic PIV was used to measure the 3D flow structure within the carotid artery model under steady inflow conditions. The experimental setup consisted of a four camera imaging system with a maximum angle between the viewing directions of 45 and 60 degrees. 3D volume reconstruction was performed with the MLOS-SMART technique [Atkinson and Soria, 2009] and subsequent 3D cross-correlation was carried out with an in-house algorithm.

The accuracy of Tomo-PIV was assessed experimentally based on the measurements in a single cross-sectional plane at light sheet thickness of 1.0, 3.0 and $6.0mm$. It was shown that both, RMS and bias error, are a function of the light sheet thickness and velocity gradient. The measurement uncertainty is shown to vary along the vessel cross-section with values of $0.1-0.3$ pixels ($\approx 2\%$) in the centre of the test section and up to 0.6 pixels ($\approx 5\%$) near the wall.

As indicated by Elsinga et al. [2009], the correlation of ghost particles can cause a displacement bias towards the mean value in cases of small displacements and small shear rates. This bias, however, decreases for increasing shear rates due to the de-correlation of ghost particles and may therefore not be the cause of the observed errors in the regions of high shear. In fact, the increase in RMS uncertainty in regions of high shear is more likely an artifact of the increased noise level in the cross-correlation operation. However, the current understanding of the velocity gradient effects in Tomo-PIV and particularly the role of ghost particles is still insufficient and further rigorous studies are needed.

For the present case, additional measurement uncertainties also arose from small miss-matches in refractive index, which causes non-linear distortions near the wall and deformed particle images. Overall, the current measurement uncertainties are in accordance with data from Wieneke and Taylor [2006] of approximately $0.2 - 0.3$ pixel for moderate velocity gradients.

In terms of physiological relevance, the current findings show that the prevailing haemodynamic environment in the carotid artery under steady flow conditions is strongly determined by the arterial geometry. The curvature and bifurcation of the vessel introduces a transverse pressure gradient, which leads to the formation of complex secondary flows and flow separation (Figure 7.8 and 7.13). The WSS distribution derived from the 3D velocity gradient tensor is noticeably asymmetrical and has a spiraling appearance, which closely follows the helical flow motion. These observations are in agreements with earlier flow visualisations [Ding et al., 2001; Zarins et al., 1983] and more recent PIV measurements [Bale-Glickman et al., 2003a; Vétel et al., 2009] in similar geometries.

The significance of the three-dimensional flow is its influence on flow separation and re-attachment and the thereof resulting spatial variation in WSS. Regions of low WSS imply impaired mass transport and reduced cell signaling and are directly linked to the onset of atherogenesis [Traub and Berk, 1998]. In regions of low WSS and flow recirculation, local mass transfer to and from the wall is disturbed, which leads to a lack in nutrients and increased particle deposition at the arterial wall. Endothelial cells, which line the arterial wall, sense haemodynamic stimuli and effect alterations in vascular function. Shear stress is particularly important in the regulation of vasodilation and constriction, cell metabolism and cell morphology [Traub and Berk, 1998; Zarins et al., 1983]. In regions with undisturbed flow such as the common carotid artery, physiological mechanisms maintain WSS within a narrow range of 1-2Pa and the endothelial cells exhibit athero-protective phenotypes that suppress plaque growth. In areas of low WSS ($< 0.4Pa$) and reversed flow, endothelial cells exhibit pro-atherogenetic phenotypes and become susceptible to plaque growth and disease [Chatzizisis et al., 2007].

The current steady flow experiments have identified areas of low WSS along the outer wall of the internal carotid artery. The extent of this region varies with Reynolds number and flow division ratio (see Chapter 5), but it always experiences low WSS relative to the remaining arterial wall. Hence, the outer wall can be identified as a 'hot spot' for the initiation of atherosclerotic plaque formation for this particular geometry. The inner bifurcation wall and sidewalls experience higher shear stress levels and are unlikely to be of significance for the onset of vascular disease.

In conclusion, Stereo- and Tomo-PIV measurement of the velocity field and WSS distribution in a complex internal flow geometry have been carried out successfully. The associated measurement errors were characterised by comparison with Stereo-PIV measurements and the current results provide a comprehensive insight into the three-dimensional flow organisation within the human carotid artery. It should, however, be noted that the assumption of steady flow is physiologically limiting and further studies should include the pulsatile nature of the carotid artery flow. Yet, the scope of the present study was to demonstrate the applicability of Stereo- and Tomo-PIV in a complex flow geometry and an extension of this methodology to include time-varying flow conditions is straight forward. (e.g., Chapter 6).

Chapter 8

Conclusion and Future Work

Atherosclerosis and related CVD have reached epidemic proportions worldwide. In particular the frequency of occurrence as well as the level of complications is rapidly growing for this chronic disease. Thus, the increasing incidents of major or fatal vascular syndromes are consuming a major and steadily increasing portion of worldwide healthcare costs for intervention and rehabilitation.

One of the key pathological factors leading to atherosclerosis is endothelial dysfunction, which amongst others is a direct response to the underlying haemodynamic environment. The investigation of arterial haemodynamics, both experimentally and numerically, has already lead to substantial advancements in the areas of pathology and intervention. However, important haemodynamic questions such as the role of the individual arterial geometry are still unanswered. With the advent of modern non-intrusive, full dimensional flow measurement technology, such as PIV, new insights into the structure and dynamics of the underlying haemodynamics can be obtained. However, such three-dimensional, full field *in vitro* studies are still non-existent.

This thesis aimed at developing such a measurement system for accurate full-field *in vitro* measurement of arterial haemodynamics. The research incorporated physiological modelling and engineering technologies to investigate the flow field in the human carotid artery. The outcomes provided novel and superior flow measurement technology and an in-depth analysis of the haemodynamic environment and the parameters affecting it.

8.1 Particle Image Velocimetry and Technological Outcomes

In chapter 3 and 4 the development of the PIV methodology used in this research to measure velocity and WSS fields in models of the human carotid artery was reported. The methodologies were rigorously derived and particular attention was given to the appropriate treatment of fluid/wall interfaces.

Near the wall, conventional PIV suffers from increased noise artifacts that cause data drop out and erroneous velocity estimates. These limitations in near wall PIV can be mitigated by appropriate vector relocation and mean intensity removal techniques. Nevertheless, a substantial measurement uncertainty remains in these cases, which is further compounded during the velocity gradient estimation. For this reason, interfacial PIV (iPIV) was developed to provide accurate and high resolution WSS and near wall velocity measurements along curved and irregular interfaces. This is obtained by directly evaluating the velocity gradient from the recorded particle images via 1D cross-correlations and subsequent weighted linear fit to the correlations peaks.

Additionally, the stereoscopic PIV technique was implemented in this thesis and 3D-3C flow and shear stress measurements were performed by means of the Stereo- and Tomo-PIV.

The accuracy and performance of the developed PIV methodologies was assessed by means of numerical simulations and experimental verification. Compared to traditional velocity field differentiation, iPIV reduces the measurement uncertainty by almost one order of magnitude, while at the same time improving the amplitude response. Under ideal conditions, measurement uncertainties in iPIV are between 1% and 5% (≈ 0.01 pixel/pixel) compared to an estimated uncertainty of 10 - 20% for the velocity field based operators. In the case of no-slip conditions, measured WSS is very sensitive to the interface locations, and as such great care needs to be taken when locating the wall interface.

Regarding the 2D-2C analysis, excellent agreement in performance was achieved compared with previously published data with an average measurement uncertainty of 0.05 to 0.1 pixel depending on flow, image and analysis characteristics.

8.2 Haemodynamic Modelling and Specific Outcomes

Steady Flow and Idealised Models

In Chapter 5, the steady flow and WSS fields in an idealised carotid artery model are investigated to quantify the basic fluid mechanic phenomena in the carotid artery bifurcation and more precisely in the carotid sinus. Additionally, a stenosed bifurcation model was investigated and interesting differences between the *healthy* and *diseased* bifurcation geometry were observed. Lastly, the measurements were complimented by numerical simulations, primarily aimed to validate the experimental WSS measurements.

A major physiological simplification in this chapter was the assumption of steady flow conditions, which was deemed reasonable on the basis of previous research. Although the opposite was proven in the subsequent chapter, the steady flow assumption provided a useful first step to test and validate the experimental procedure and to provide a basic description of carotid artery haemodynamics under various conditions.

Steady flow in the carotid sinus is characterised by skewed velocity profiles, strong secondary flows and spatially varying WSS. In particular, a region of retrograde flow exists along the outer sinus wall, setting up a low momentum, low WSS region. Additionally, strong three-dimensional heliocoidal flow trajectories exist due to the interaction of the secondary and main axial flow. The extend of the observed phenomena varies with Reynolds numbers and flow division ratio. Overall, the steady flow results in the *healthy* carotid bifurcation model confirmed previous experimental and numerical observations and extended those by applying PIV to acquire detailed maps of the spatial flow and WSS distribution.

A comparison with numerical simulations revealed an excellent agreement between the two techniques with some smaller differences in WSS along the outer sinus wall. These differences were mainly attributed to experimental and numerical errors as well as differences in the three-dimensional flow structure caused by small variations in the individual vessel geometry.

The investigated symmetrical stenosed bifurcation model revealed very different flow pattern, with high momentum flow and WSS at the stenotic throat and flow separation and low WSS in the post stenotic region. Furthermore, flow instabilities, low Reynolds number turbulence and unsteady WSS was observed, which were not present in the *healthy* geometry.

The key haemodynamic factors identified is this chapter are the spatial extent of high and low WSS regions and the size and location of flow recirculation in the idealised carotid artery bifurcation. Regions of low WSS are directly linked to the development of atherosclerosis (see Chapter 5), while high WSS can lead to smooth muscle cell degeneration, thrombus formation and plaque rupture.

Pulsatile Flow and Physiological Models

In order to provide some *in vivo* significance to the present work, a similar study to the one in Chapter 5 was implemented for an anatomically realistic geometry in Chapter 6. This was primarily motivated by the the previous observations and the general lack of experimental work in this area. The patient specific geometry was reconstructed from MRI data and exhibited true *in vivo* characteristics that lead to very complex flow structures.

In contrast to the studies in the idealised model, the results of this chapter demonstrated that the previous investigations lacked crucial physiological details to sufficiently represent true *in vivo* flow conditions. The secondary flows, caused by out-of-plane curvature and changes in vessel calibre were responsible for regions of the vasculature subjected to large spatial and temporal variations in WSS. This was evident in both, steady and pulsatile experiments, but was particularly notable under pulsatile conditions were regions of low WSS and reversed axial flow existed, which were not seen under steady flow conditions.

Velocity and WSS transients, observed over the course of a cardiac cycle were 'generally' negligible (they followed the inlet waveform) in the majority of the vessel, except along the outer external carotid artery where significant transients were observed during systolic acceleration. In this region, strong flow separation caused an 'artificial' constriction of the vessel lumen, giving rise to strong WSS transients and velocity perturbations downstream. These disturbances dissipated towards the end of the cardiac cycle and WSS and velocity profiles followed the inlet waveform again. The transient behaviour was further evidenced by the oscillatory shear index (OSI). Although some differences were exhibited between steady and unsteady flow, these differences were within a reasonable tolerance (5%-11%) and spatial variations seemed to be more significant.

The incorporation of physiological flow conditions, coupled with an anatomically realistic model has provided some interesting results. The most significant of these was WSS and the underlying flow field in the external carotid artery. The current results support the notation of a 'geometric risk factor'. There are some reports in literature that suggest that the individual geometry is the largest pathogenetic risk factor, while others suggest a myriad of factors including flow division and waveform. This may also depend on the type of bifurcation that exists at different locations within the vasculature.

Three Dimensional Flow Measurements

Chapter 7 presented Stereo- and Tomo-PIV measurements of the flow structure and WSS in a physiological accurate model of the human carotid artery bifurcation. This was the first study of its kind and the only other similar work is that of Vétel et al. [2009] who conducted Stereo-PIV measurements.

The vascular geometry was reconstructed from patient-specific post-mortem data and steady flow measurements were conducted to demonstrate the feasibility of Tomo-PIV in complex three-dimensional interior geometries. The implemented methodology was validated by comparing the results with Stereo-PIV measurements in the same facility. In Tomo-PIV, the measurement uncertainty increased for increasing light sheet thickness and increasing velocity gradients, and were typically within ±2% of the maximum velocity (or ±0.2 pixel) near the centre of the vessel and within ±5% (±0.6 pixel) near the vessel wall. The technique was applied to acquire 3D-3C velocity field data at multiple axial locations within the carotid artery model, which were combined to yield the flow field and WSS in a volume of approximately $26mm \times 27mm \times 60mm$. Shear stress was computed from the velocity gradient tensor and a method for inferring the WSS distribution on the vessel wall was elucidated.

The results indicated the presence of a complex and three-dimensional flow structure, with regions of flow separation and strong velocity gradients. The three-dimensional WSS distribution was markedly asymmetric, confirming a complex swirling flow structure within the vessel. A comparison of the measured WSS with Stereo-PIV data returned an acceptable agreement with some differences in WSS magnitude. Furthermore, 3D-3C measurement in the idealised geometry revealed excellent agreement with the earlier measurements in Chapter 5.

8.3 Future Work

This work has established a novel and versatile PIV methodology for *in vitro* investigation of arterial haemodynamics. The developed methodologies were tested and verified for the current experimental conditions and applied to a number of physiological relevant flow cases. To extend the current investigations and add further value to the research field, future work should aim to progress the current methodology to even more accurately reproduce the true *in vivo* conditions. This goal could be achieved by implementing models and measurement methodologies along the lines given below.

Blood Flow Modelling

From a experimental modelling perspective there is a reasonable amount of work that could be implemented over and above what has already been done.

Vessel Compliance

For example, one interesting extension of the current methodology and a further increase in realistic modelling would be the introduction of arterial compliance to study the effects of transient behaviour coupled with wall movement (i.e., fluid-structure interaction). Although vessel compliance has been shown to be of secondary importance in the carotid artery, it may well have a large significance in other parts of the vasculature and pathological conditions such as cerebral or abdominal aneurysms.

For the present modelling methodology, there are a number of obstacles to overcome, which include the manufacturing of elastic, thin wall flow phantoms as well as an automated detection of the vessel wall, which is necessary for WSS measurements. While the development of transparent elastic models is partially documented in the literature, the latter remains a simple implementation problem.

Furthermore, by combining materials of different properties, complex models can be constructed to simulate the different layers of the human blood vessel and/or represent vascular plaques, which are known to have different material properties. Some of the recent advancements in this area made by the author and his colleagues include the investigation of the time-dependent flow field in an elastic pipe [Geoghegan et al., 2009].

Non-Newtonian Rheology

Another extension to the current modelling methodology would be the introduction of Non-Newtonian fluid properties to accurately model the shear thinning properties of blood. The main arguments given in the justification for treating blood flow as a Newtonian fluid is the fact that at high shear rates blood approaches a Newtonian behaviour. Strictly speaking, this assumption is only true for mean shear rates in the centre of the vessel (i.e., average velocity/artery diameter) where bulk flow velocities are high. However, in the wall vicinity where local shear rates are low and vary with both space and time this assumption is violated. In these cases, the Newtonian assumption will lead to different outcomes in the local velocity field (e.g., flow separation and recirculation) and WSS distribution.

However, for the carotid artery, literature suggests that these differences may be small and therefore Non-Newtonian rheology was ignored in the present work. Nevertheless, to verify this hypothesis subsequent work should include the Non-Newtonian rheology, particularly when investigating fluid structure interaction, as little is yet known about the interaction between wall motion, blood rheology and WSS.

The implementation of Non-Newtonian rheology in the current methodology is unfortunately not straightforward and requires further dynamic scaling considerations, particularly when using scaled models. Another milestone towards implementing Non-Newtonian rheology would have to be the development of a new transparent and refractive index matching liquid that accurately represents the shear-thinning properties. Additionally, blood is also viscoelastic, which is of relevance in unsteady flows.

Further Physiologically relevant Conditions

Probably most relevant for future investigations would be the study of more physiological and pathological relevant conditions such as diseased vessels, aneurysms or other disease prone configurations. The current research has provided the key instruments necessary for detailed *in-vitro* modelling and measurement of vascular haemodynamics and subsequent research is now charged with using these tools for further investigation and exploration.

At this point, it should be noted that the availability of such patient specific data (i.e., vessel geometry, waveform, ect.) had been limited in the past and new collaborated research approaches have to be thought of to expand future research in this direction. For example, anatomically realistic models, paired with Non-Newtonian rheology and wall distensibility bear great potential for future investigations into haemodynamics and its role in the development of vascular disease. Additionally, these most realistic models can be used for the planning of surgical interventions and the development of new surgical procedures and technologies.

In parts, this has already been demonstrated by the author and his colleagues, who have successfully constructed a 1.5 times scaled model of the human nasal cavity and respiratory tract, suitable for PIV measurements and surgical intervention [Spence et al., 2009].

Wall Shear Stress and Related Measurements

Interfacial PIV

The interfacial PIV technique has proven its capability as an alternative mean of accurately measuring WSS in PIV. However, there are still some open questions relating to the measurement accuracy and amplitude response in particular. In order to use the iPV technique across a range of applications, future work has to include a further rigorous performance assessment under a wider range of experimental conditions exceeding those presented here. These could include relevant test cases with well known solutions such as oscillating pipe flow, turbulent boundary layer flow or flow over a backward facing step.

Furthermore, the technique's adverse sensitivity to the spatial velocity wavelength can be improved. For example, shear rates in in carotid sinus vary significantly and as such, the WSS estimation is not always carried out with the optimal iPIV parameters. Hence, future work should investigate the possibility of an adaptive gaussian weighting method. Such a procedure should aim to optimise the shear stress amplitude response, while keeping the RMS noise at a minimum by using knowledge of the spatial wavelength of the velocity profile closest to the wall.

Further developments related to iPIV could also be in the direction of an automated procedure to accurately identify the wall interface and consequently to reduce the associated errors in wall sensitivity.

It should also be noted that the current iPIV technique is based on planar image data and only provides a 2D projection of the three-dimensional WSS tensor. Thus, the current WSS results are only a lower bound of the true three-dimensional shear stress. An extension of the current technique to include stereoscopic imaging is straight forward and could be done along the lines of the work presented by Nguyen and Wells [2006b].

Turbulence Measurements

The results from Chapter 5 and 6 demonstrated the existence of flow instabilities and low Reynolds number turbulence in some cases. The investigation of these phenomena was limited in the current research due to the lack of sufficient data samples to compute converged turbulence statistics. Valuable insight to these phenomena can be added in future studies by increasing the data sampling rate ($O > 1000$) and/or by using high-speed imaging. The latter may be particularly well suited in cases of unsteady flows paired with complex and or diseased vessel geometries, which were shown to introduce flow instabilities and turbulence. Additionally, the role of turbulence and its correlation to disease pathology also deserves further investigation.

Fluid-Structure Interaction

The developed 2D-3C and 3D-3C PIV methodologies can also be used to investigate fluid structure interaction in the case of elastic wall models. Very similarly to PIV, small tracer particles can be attached to the model surface and their 3D locations can for example be reconstructed by a similar approach to that of tomographic reconstruction. Then using a surface triangulation procedure similar to that in Section 2.3, the 3D vessel surface can be recovered in space and time. Knowing the deformation of the vessel surface, with respect to a nominal level, surface stress and strain can easily be extracted. Furthermore, using tracer particles with different light scattering properties (e.g., fluorescent particles), both, the fluid and structure measurements could be carried out simultaneously.

Lastly, a new implementation of the current analysis algorithm in C^{++} language should be considered for the future. The current implementation uses Matlab (Mathworks Inc., 2008), which on the one hand offers a very user-friendly platform, but on the other hand is very inefficient for computing large data sets. For example, evaluating one image pair (1600 $\times$ 1200 pixel^2) with the current PIVCC method requires approximately 120 seconds compared to only 16 seconds with an equivalent C^{++} version. These considerations are particularly useful when dealing with large data sets such as from Stereo-PIV or time-resolved measurements where the time required for data processing can be reduced substantially.

In conclusion, the presented thesis has provided the basic tools for a physiological accurate modelling of arterial haemodynamics. The current knowledge in arterial modelling and PIV measurement technology has been expanded throughout this thesis, but is by no means complete. Further research, whether concerned with biological modelling or other fluid flow applications should aim to progress into the indicated directions in order to add valuable contributions to the according research fields.

Appendix A

Refractive Index Matching

Liquid	a	$b(10^{-3})$	c	e	$f(10^3)$	g	s
water	1.377	-0.2		-13.12	1.831	1.0	0.17
aqueous NaI	1.351	-0.291	0.365				
aqueous sucrose	1.325		0.198				
d-limonene	1.607	-0.5		-5.78	-0.219	0.85	0.84
diethyl phthalate	1.619	-0.4		-13.77	2.768	1.18	0.244
methyl salicylate	1.673	-0.5		-6.644	0.28	1.18	0.36
mineral oil	1.575	-0.4		-12.38	2.546	0.82	0.652
ethanol	1.477	-0.4		-11.74	1.48	0.79	0.302
glycerin	1.456	-0.2		-20.53	6.04	1.26	0.119

Table A.1 Empirical parameters of the refractive index, dynamic viscosity and density for selected liquids.

Appendix B

Particle Size Distribution

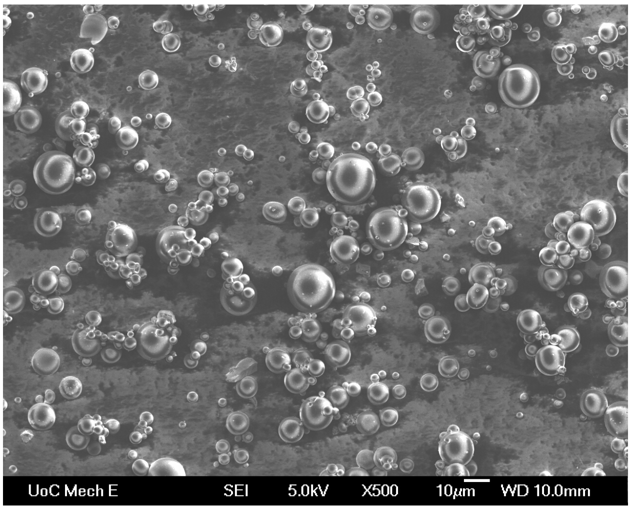

Figure B.1 Photograph of the 10μm hollow glass spheres under the electron microscope. The seeding particles show a good sphericity

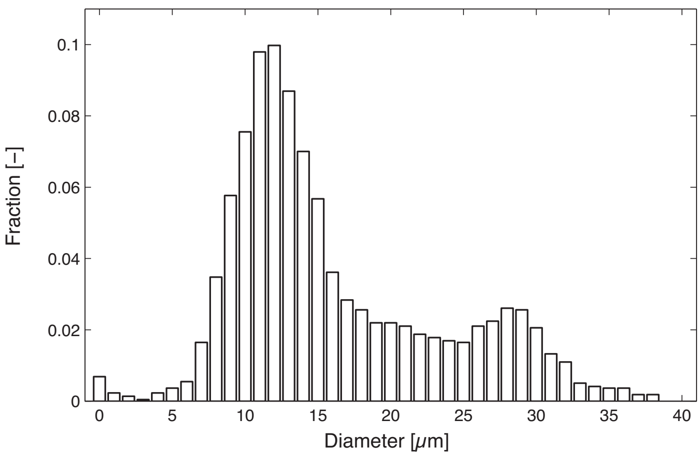

Figure B.2 Particle size distribution; mean diameter, $\bar{d}_p = 16.2\mu$m

Appendix C

Image Pre-Processing

PIV recordings also contain image noise due to the recording device and laser light reflections from solid objects or interfaces present in the measurement plane. This can greatly degrade the signal to noise ratio, which reduces the number of valid vector detections. In order to improve the image quality the following appendix presents a variety of image pre-processing methods developed in this research and commonly used in PIV image pre-processing.

In theory, the image grey level I can be expressed as a summation of background camera noise N, reflections R and the scattered particle light I_p.

$$I(x, y) = N(x, y) + R(x, y) + I_p(x, y) \tag{C.1}$$

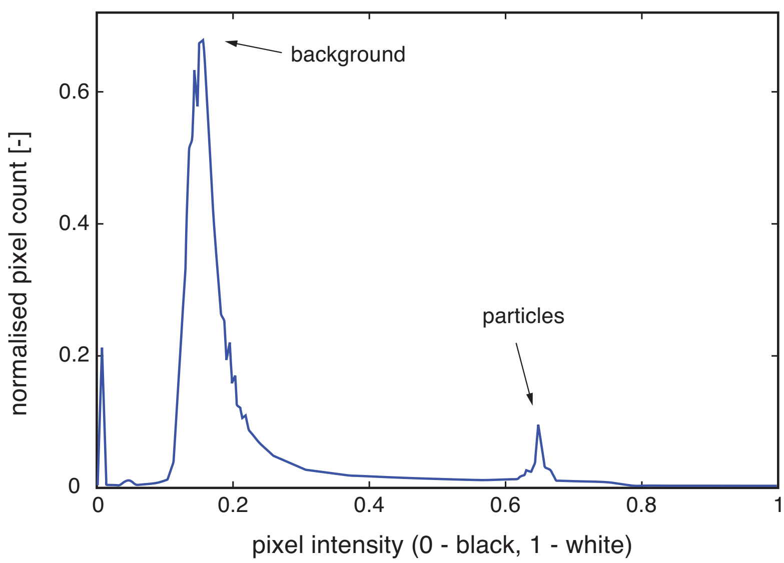

Figure C.1 Intensity Histogram of an ideal digital PIV image

Figure C.1 shows the intensity histogram of a typical image recording which contains two distributions, one belonging to the background intensity and the other to the actual particle images. In many cases, however, these two distributions are not as distinct as shown in Figure C.1 and often overlap, making it difficult to distinguish the particles from the background.

The process of image pre-processing aims to isolate the distribution of the particle images and to remove background noise and stationary reflections. This results in an improved signal to noise ratio and consequently a higher probability of a valid displacement detection.

C.1 Background Subtraction

A typical single exposed PIV image from the current set of experiments and its corresponding histogram is shown in Figure C.2. The Histogram shows three distinctive intensity distributions. The first and third peak in the histogram are specific to the current recording setup and correspond to the no-flow region (i.e., black region) and interface reflections on the model wall. The central peak contains the merged particle intensities and background noise as expressed in Equation C.1. The particle intensity distribution is embedded in the tail of the second histogram peak as it is indicated by its asymmetry.

A simple concept to remove the background noise and light reflections is to perform a time-average *image subtraction* as suggested by Wereley et al. [2002]. In this procedure, a model of the background intensity, I_o is obtained from the average of the acquired frame sequence. Because the particles are randomly distributed and are assumed to move quickly through the object plane, they will not appear on the background model. As a consequence, the averaged image only contains stationary noise and reflections. The modelled background is then subtracted from each individual image, allowing a better differentiation of the particle patterns. Alternatively, the background model can also be constructed by taking the pixel intensity minimum of the ensemble of the recordings [Wereley et al., 2002] or in the cases of image to image intensity variations, a time-dependent background calculated by a moving average is possible.

An example of such an averaged background image, calculated from 100 instantaneous recordings is shown in Figure C.3 and contains the stationary

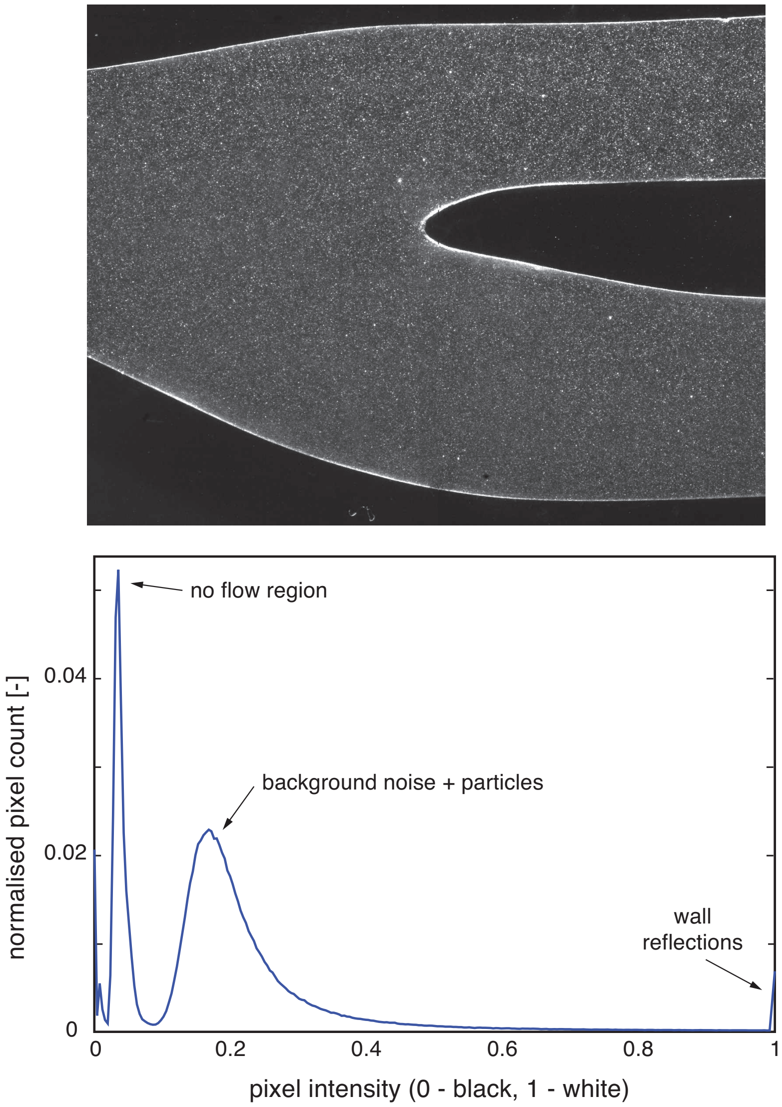

Figure C.2 Single exposed PIV image and its corresponding histogram for the current experimental data

light reflections and background noise. However, due to the intensity averaging, the mean image also contains a significant amount of actual particle images as can be seen in the overlapping histograms in Figure C.2 (bottom). Subtracting the mean image from the instantaneous image in this particular case would result in loss of information. Likewise, the use the minimum image results in an underestimate of the background noise (Figure C.3).

Therefore, the background subtraction procedure is expressed as a thresholding operation in which only pixel intensities above the threshold level are assigned as pixels belonging to the image. Stitou and Riethmuller [2001] propose a local threshold based on the decomposition of the image intensity into a mean (*) and a fluctuating part. The mean contribution of the image noise and light reflections is determined from the background model I_0, while the intensity fluctuations can be determined from the variance of the image intensity I within the image sequence. With this, the local threshold T is expressed as:

$$T(x, y) = I_0^*(x, y) + k \cdot rms(I(x, y)) \tag{C.2}$$

where $rms(I_o(x, y)) \sim rms(N(x, y))$. The parameter k is chosen so that for a pixel with an intensity higher than the local threshold, the probability of being noise is negligible. Stitou and Riethmuller [2001] estimated a value of k of about 4.2. However, the proper choice of k depends on whether the mean or minimum background model are used as can be deduced from Figure C.3. In practice, this means that when using the mean background image, k should be chosen negative and vice versa, when using the minimal image. The actual value of k depens on the background model, the experimental setup and the image quality and has to be found individually for each experiment.

Figure C.4 shows the image from Figure C.2 after subtracting the mean background image and $k = -1.5$. The stationary reflections on the model interface have been removed nearly completely and the low intensity background noise has been reduced. This results in an improvement in the particle image contrast as can be seen by the two intensity peaks in the image histogram.

C.2 Dynamic Histogram Filter

Another image pre-processing method is *dynamic histogram stretching* wherein the intensity range of the output image is stretched to a prescribed upper and lower threshold value. The thresholds are computed dynamically for each image from the individual histograms by excluding a certain number of pixels (in %) from the upper and lower end of the histogram. The technique accounts for image to image (or pulse to pulse) intensity fluctuations and to some extend equalises the contribution of the individual particle images to the correlation signal.

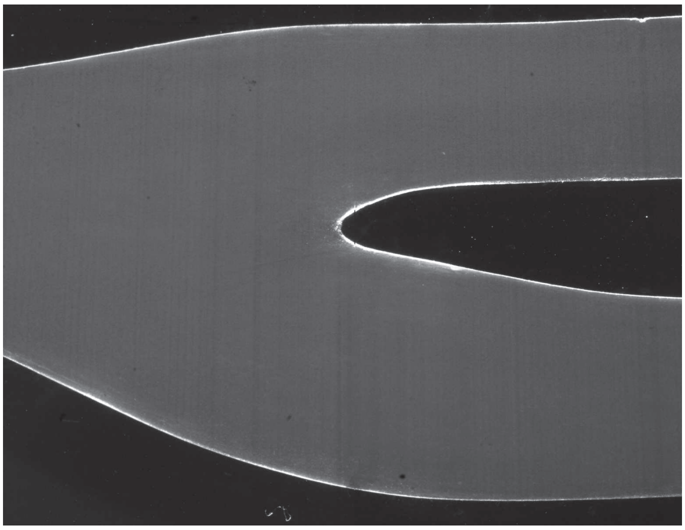

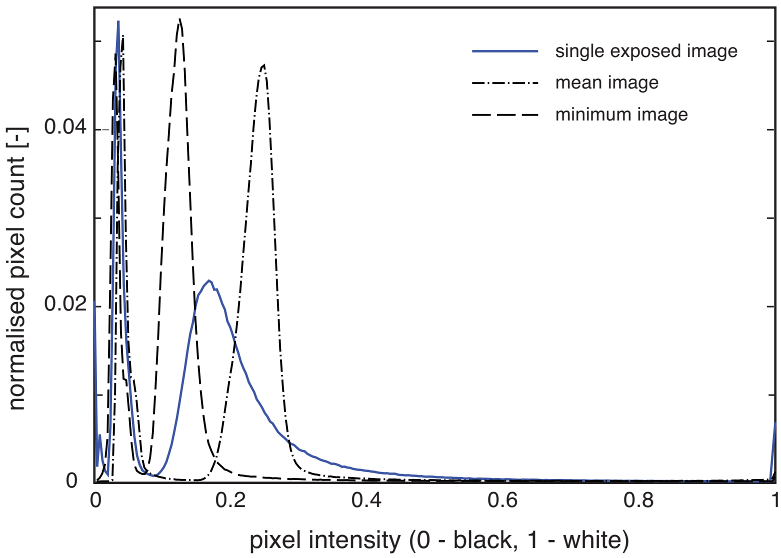

Figure C.3 (top) Mean background image computed from 100 instantaneous recordings; (bottom) Histograms for the instantaneous, mean and minimum image corresponding to Figure C.2

The histogram stretching technique is an alternative to the thresholding method in Equation C.2. Compared to the background subtraction, dynamic histogram stretching does not rely on a user-defined threshold value (which is the same for each image), but dynamically adjusts the threshold levels for each instantaneous image. However, the method can not remove stationary reflections and only operates on the lower and upper end of the image histogram. In the case of stationary reflection, a background subtraction becomes mandatory and dynamic histogram stretching can be supplementary to further enhance the image contrast.

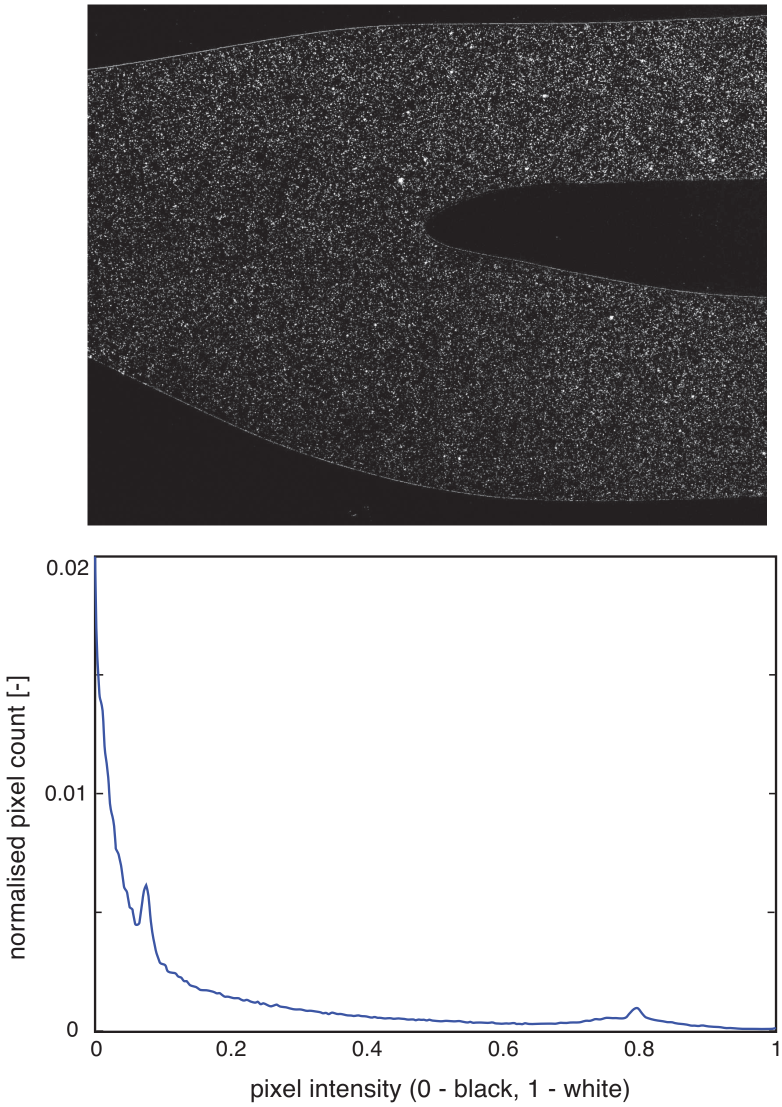

Figure C.4 The processed image histogram of Figure C.2 after subtracting the mean image in Figure C.3, $k = -1.5$

An example of the histogram stretching is given in Figure C.5 for a turbulent boundary layer flow. Light reflections at the boundary are already removed with a mean image subtraction ($k = 0$). The dynamic thresholds are determined based on the 2% and 98% margin of the image histogram. The histograms for the image in figure A.5 before and after dynamic histogram stretching are shown in Figure C.6. The dynamic histogram stretching stretches the intensity histogram and shifts the distribution towards zero pixel intensity. Furthermore, the dynamic histogram operation separates the particle image intensities distribution from the background noise and thus further increases the image contrast.

Instantaneous vector fields obtained from a PIV analysis of the image pairs in Figure C.5 before and after dynamic histogram stretching are shown in Figure C.7. The results clearly demonstrate the effectiveness of image preprocessing in enhancing the image contrast and increase the signal-to-noise ratio. Spurious vectors due to stationary light reflections and background noise are reduced and the vector fidelity increases from 87% to more than 99% for the presented data.

C.3 Image Smoothing

Finally, image filtering can be applied by convolving the recorded images with a *Gaussian* or *mean* filter kernel. This *low-pass filtering* removes high frequency noise (i.e. CCD noise) and results in the widening of the correlation peak and thus, an improved sub-pixel peak fitting. *Low-pass filtering* can also reduce peak-locking in cases of under-sampled image recordings, but also increases the measurement uncertainty. Typical filter kernels are 3×3 or 5×5 pixel^2 in size.

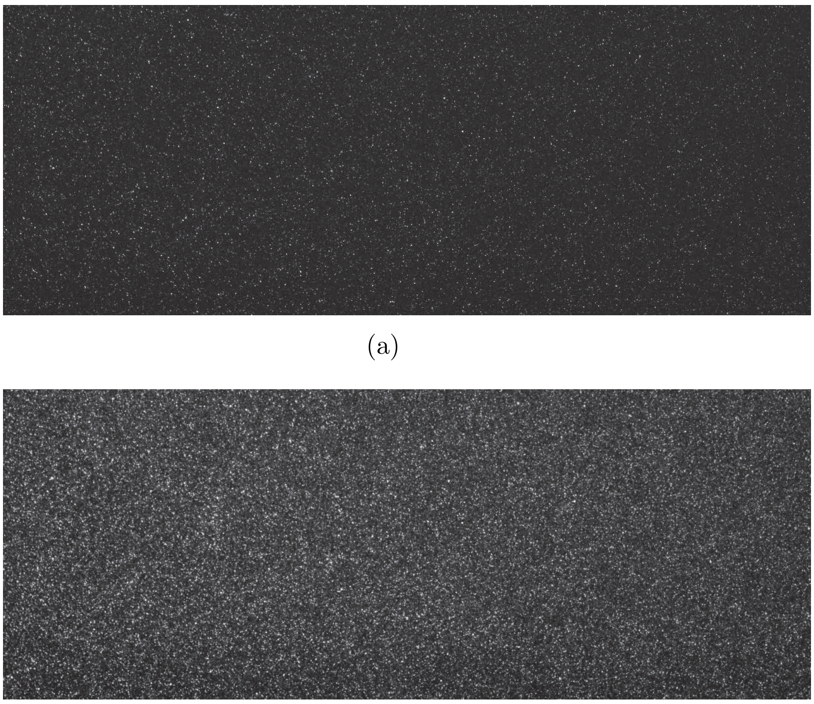

(a)

(b)

Figure C.5 (a) instantaneous raw image with mean image subtracted ($k = 0$) to remove light reflections; (b) same image after dynamic histogram stretching [0.2:0.98]

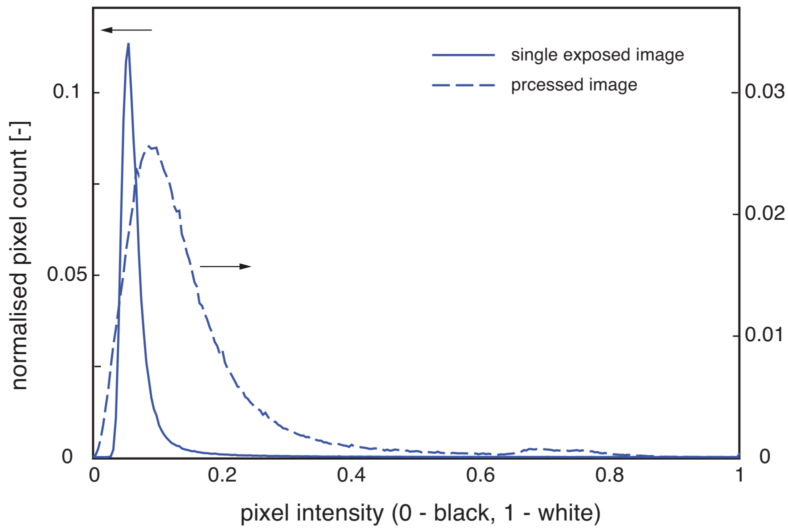

Figure C.6 Intensity histogram for the instantaneous images in Figure C.5

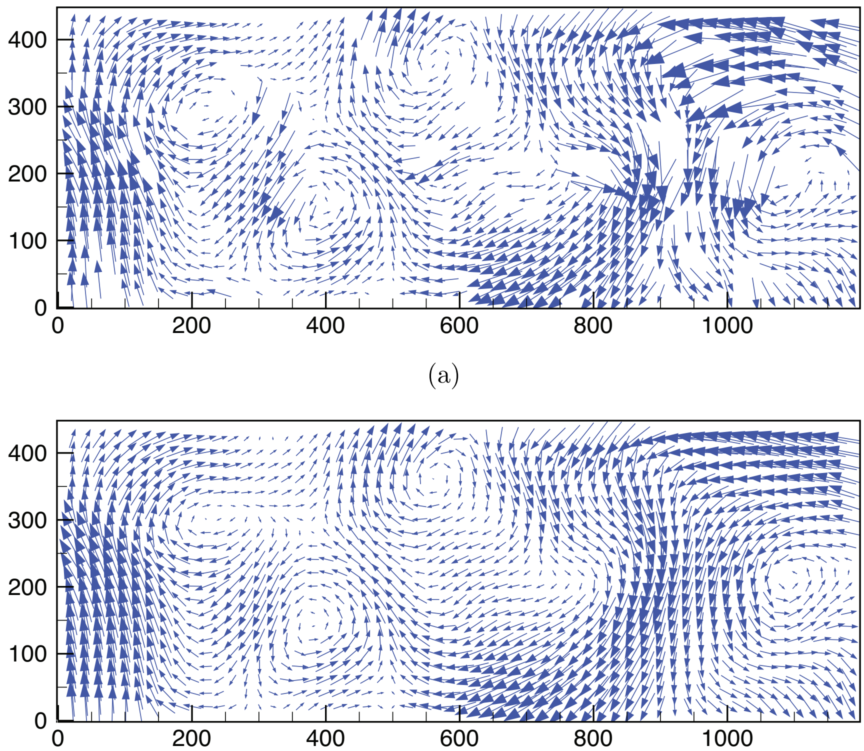

(a)

(b)

Figure C.7 Instantaneous velocity field obtained from an image pair (a) before and (b) after image pre-processing. The invalid vectors are not shown for clarity

Appendix D

Measurement Accuracy

D.1 Error Definition

In PIV the overall measurement accuracy is a combination of a variety of aspects ranging from image acquisition all the way to image evaluation methods. The current section is devoted to the analysis of the contributing factors in the digital evaluation of the PIV recording. The total error of a single displacement vector ϵ_{tot} can be decomposed into a bias error ϵ_{bias} and a random error ϵ_{rms} or measurement uncertainty

$$\epsilon_{tot}^2 = \epsilon_{bias}^2 + \epsilon_{rms}^2 \tag{D.1}$$

Every displacement vector is associated with a systematic bias error inherent to the analysis method and some degree of random error or measurement uncertainty $\pm\epsilon_{rms}$. The individual errors are defined as follows:

$$\epsilon_{bias} = \overline{\Delta x} - \Delta x_a \tag{D.2}$$

where Δx_a is the known displacement and $\overline{\Delta x}$ is the arithmetic mean of the measured displacements Δx_i defined as

$$\overline{\Delta x} = \frac{1}{N}\sum_{i=1}^{N} \Delta x_i \tag{D.3}$$

The RMS error is expressed as

$$\epsilon_{rms} = \sqrt{\frac{1}{N}\sum_{i=1}^{N}(\Delta x_i - \overline{\Delta x})^2} \tag{D.4}$$

D.2 Synthetic Particle Image Generation

An important part of the the Monte Carlo based measurement error estimation is the generation of adequate synthetic particle images. The generated images have to provide known characteristics, such as particle diameter, shape, spatial density, and image depth amongst others. For the simulations presented in this work, the individual particle images are described with an Gaussian Intensity profile as proposed by Raffel et al. [1998].

$$I(x,y) = I_o exp\left[\frac{-(x-x_o)^2-(y-y_o)^2}{1/8d_p^2}\right] \quad \text{(D.5)}$$

where the particle is centered at (x_o, y_o). The particle image diameter, d_p is defined by the e^{-2} intensity value of the Gaussian distribution, which by definition contains 95% of the scattered light (i.e., two standard deviations). The particle intensity, I_o is a function of the particles' z position within the light sheet. For a light sheet centered at $z = 0$ and with a Gaussian intensity distribution, I_o is given as [Raffel et al., 1998]:

$$I_o(z) = qexp\left[-\frac{z^2}{1/8\Delta z_o^2}\right] \quad \text{(D.6)}$$

where again, Δz_o is defined as the e^{-2} intensity waist and q as the scattering efficiency. For a top-hat intensity profile, the above relation simplifies to $I_o(z) = q$ within the light sheet ($z \leq \pm\frac{1}{2}\Delta z_o$) and $I_o(z) = 0$ otherwise.

The particle image is generated at random location (x_1, y_1, z_1) within the three-dimensional light volume illustrated in Figure D.2. For simplicity, the magnification factor between object and image plane is chosen as unity. The particle peak intensity is specified according to the light sheet intensity profile. The integration of Equation D.5 onto the pixel array is approximated with a two-dimensional discrete Gaussian kernel. To generate the second exposure, the generated particle image is translated by a *virtual* flow to produce the new location (x_2, y_2, z_2) for which a new particle intensity distribution is calculated. This procedure is repeated until the desired particle seeding density C (ppp, particle per pixel) is reached.

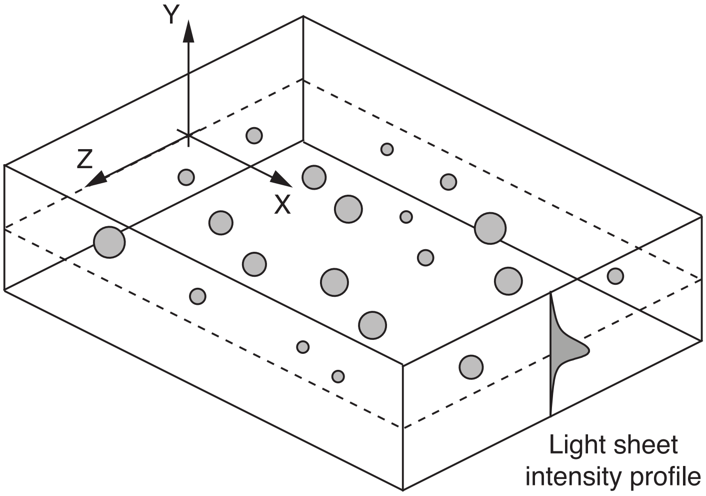

Figure D.1 Schematic of synthetic particle image generation. 3D volume containing the light sheet and randomly distributed particles. Figure adapted from Raffel et al. [1998]

Different types of artificial images are used in this work and are illustrated in Figure D.2. Synthetic images of type I consists of particles with a constant mean diameter, d_p, which are randomly distributed in a light sheet with a top-hat intensity profile. The image background is at zero pixel intensity and the seeding density varies between $C = 1/16 - 1/64$ ppp. Type II images consist of particles with a normally distributed diameter (e.g., $d_p = 2$ pixel, $\sigma_{dp} = 0.5$) in a Gaussian intensity light sheet and additional image noise in form of a mean and fluctuating intensity level. Type II image are thought to more realistically simulate real particle image recordings. Lastly, type III images are produced by adding light reflections and flare to type II image to simulate the wall interface. All image types are quantised to 8 bits and the particle intensities are integrated over a virtual sensor with a fill factor of 1.0.

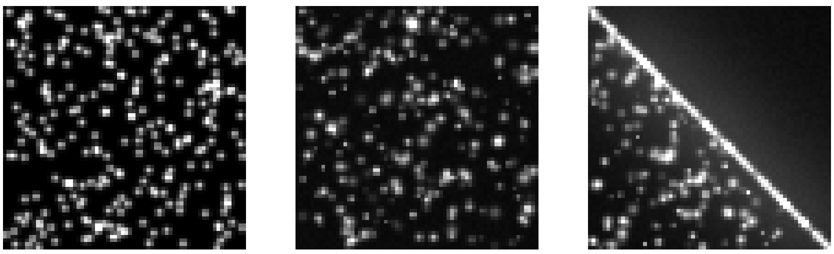

(a) (b) (c)

Figure D.2 Synthetic images: (a) Type I, d_p=2pixel, top-hat light sheet; (b) Type II, d_p=2pixel, σ_{dp}=0.5, Gaussian light sheet, 4% (σ=±2%) background noise; (c) Type III, similar to type II with wall reflection and flare added

D.3 Results

Displacement Error - Peak Locking

Figure D.3 (a) and (b) illustrate the bias and RMS as a function of the imposed particle image shift and different particle image diameters for the discrete window shift method (DWS). Note the occurrence of the peak locking phenomena on the one pixel intervals. The bias error reaches a minimum at a particle image diameter of approximately 1.5 pixel, whereas the RMS error indicates an optimal particle size of about 2 pixel. This is consistent with Raffel et al. [1998].

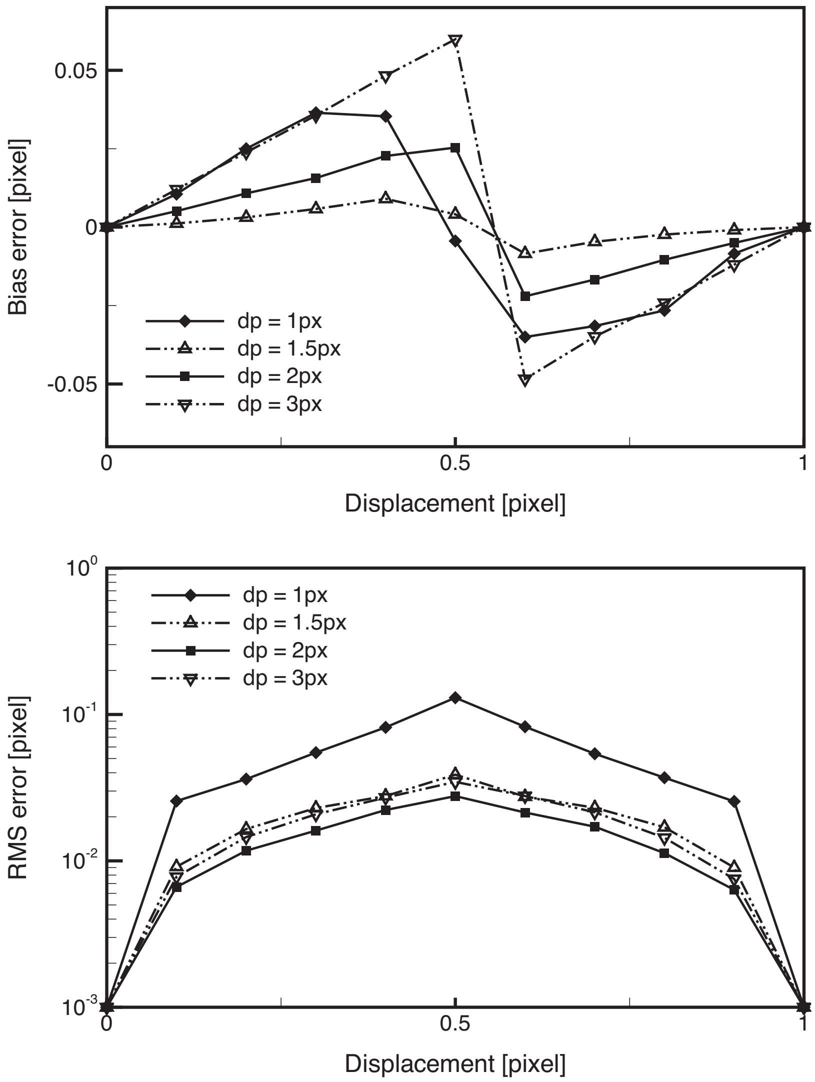

Figure D.3 Bias (a) and RMS (b) error for the discrete window shift and different particle image sizes. Simulation parameter: $C = 1/32$, $d_p = [1, 1.5, 2, 3]$ pixel, 32×32 pixel, no noise

For smaller particles, both, RMS and bias error increase significantly, whereas for larger particles (> 3 pixel) only the displacement bias increases, while the RMS uncertainty remains low.

Effect of Background Noise

The effect of random background noise is demonstrated in Figure D.4. The bias error increases almost proportionally with the noise level to up to 0.12 pixel for $10 \pm 5\%$ background noise. Additionally, some peak locking effects are present, which are not observed for the 0% noise case. Likewise, the image noise affects

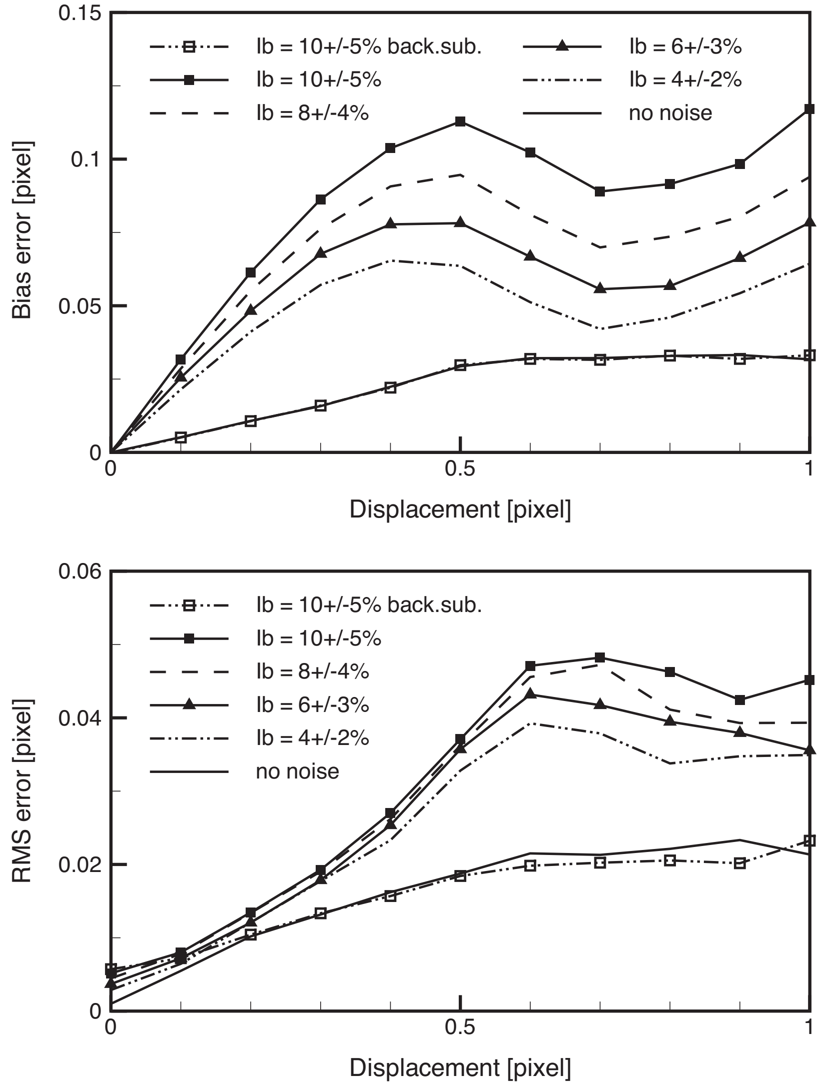

Figure D.4 Bias error as a function of particle image shift and various amounts of background noise. Simulation parameter: $C = 1/32$, $d_p = 2$ pixel, 32×32 pixel the RMS uncertainty which increases to about 0.05 pixel. If a background subtraction is applied prior to the cross-correlation, both, bias and RMS error reduce again.

Effect of Particle Image Density

The particle image density, N_I also affects the measurement uncertainty as shown in Figure D.5. As N_I increases, more particles contributed to the cross-correlation product and hence the signal strength and measurement certainty improves. Likewise, a reduction in N_I has a diminishing effect on the cross-

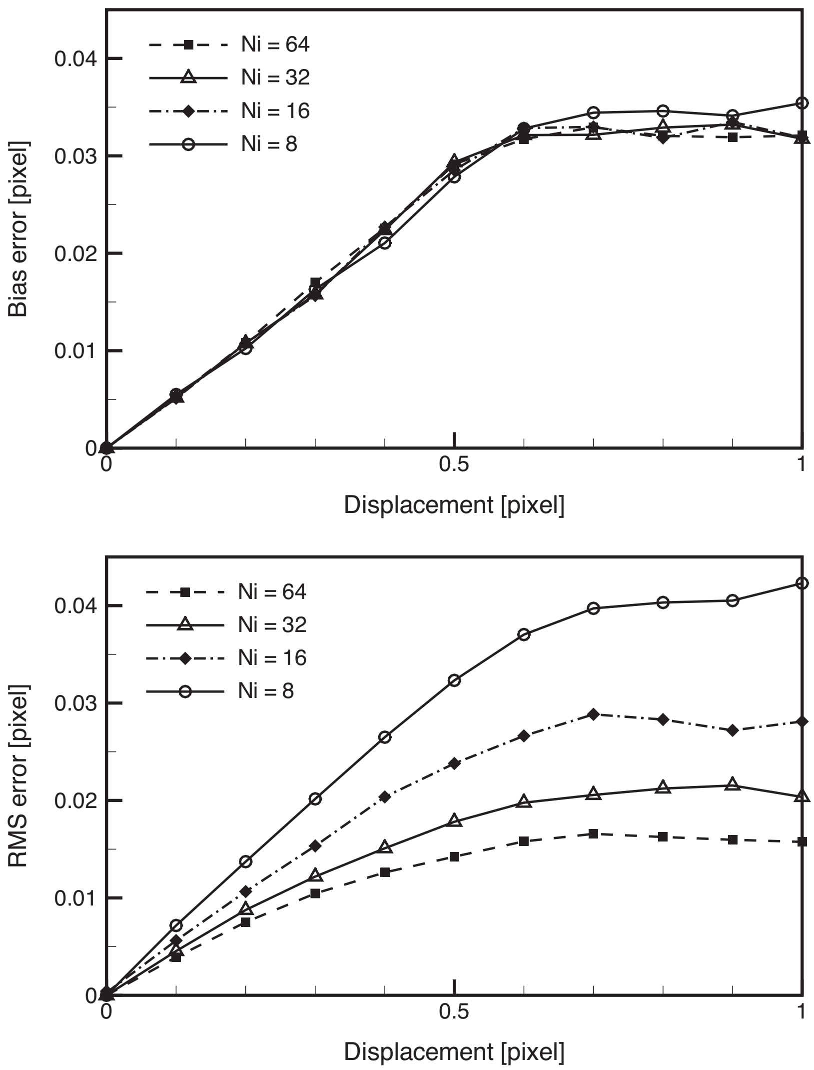

Figure D.5 Bias (a) and RMS (b) error as a function of particle image shift and particle image density N_I. Simulation parameter: $d_\tau = 2$ pixel, 32×32 pixel, no noise correlation peak and consequently, the RMS uncertainty increases (Figure D.5(b)). Furthermore, for low particle image densities, the probability of a valid displacement detection decreases [Keane and Adrian, 1990], which can result in spurious or ambiguous displacement vectors. Interestingly, for any given interrogation size, the bias error appears to be unaffected by changes in N_I.

Effect of Displacement Gradients

Figure D.6 shows the RMS error for an imposed velocity gradient $\partial u/\partial y$ and different interrogation methods versus the imposed particle displacement. For the continuous window deformation method with three iterations (CWD3) the measurement uncertainty remains below 0.01 pixel for shear rates of up to $\partial u/\partial y$=1.0. In contrast, the RMS error increases more significantly up to 0.1-0.2 pixel for the discrete window shift technique (DWS). Furthermore, the RMS uncertainty is no longer zero at integer locations for both cases and tends to become constant and independent of the particle displacement and velocity gradient.

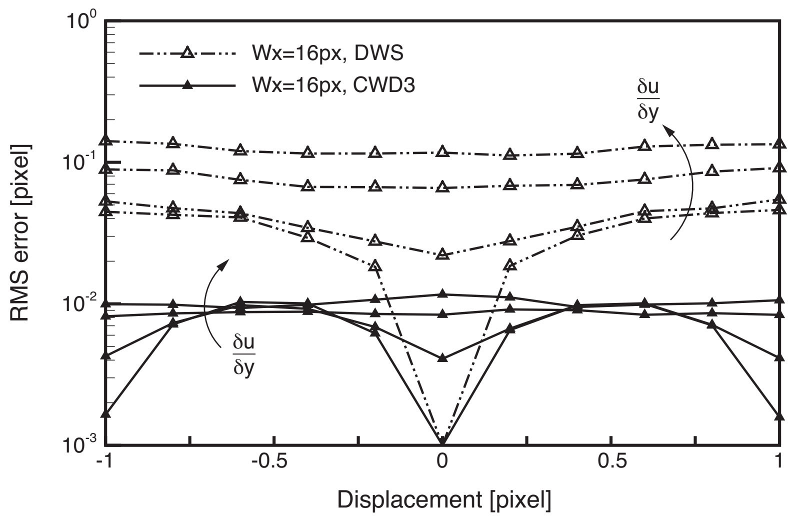

Figure D.6 RMS uncertainty for the discrete window shift (DWS) and continuos window distortion (CWD) method versus particle displacement and increasing velocity gradients. Simulation parameters: $d_p = 2$ pixel, $N_I = 16$ ppw, $\partial u/\partial y = [0, 0.2, 0.6, 1]$ pixel/pixel

Appendix E

A Description of Stereo-PIV

The basic principles of stereoscopic particle image velocimetry (SPIV) are discussed in this appendix. A description of the angular-offset stereo-PIV technique in this thesis is presented. Details of the camera calibration and three component velocity reconstruction utilised here, are provided.

E.1 Stereo-PIV Principle

The theory of stereo-PIV is introduced based on excellent reviews by Prasad [2000]; Lawson and Wu [1999, 1997b]; Prasad and Adrian [1993]; Wieneke [2005] and Willert [1997, 2006]. Conventional planar PIV suffers from two deficiencies. First, the out-of-plane velocity component is lost and the resulting vector field is a 2D projection in the object plane of the three component velocity field. Second, the measured in-plane components are contaminated by the local non-zero out-of-plane component. This perspective error is proportional to the relative magnitude of the out-of-plane component to the in-plane component ($\Delta z/\Delta x$). Stereoscopic imaging eliminates both of theses shortcomings through the use of a second camera and simultaneous off-axis viewing. Two basic viewing configurations exist [Prasad, 2000]. In the angular-displacement or angular-offset method, the two cameras are orientated in a non-orthogonal manner towards the object plane. This configuration is used in this thesis and an example of the setup is given in Figure 3.13. The second configuration is the so-called translation method and uses two cameras whose axis are orthogonal to the light sheet plane and parallel to each other.

A typical problem of the angular offset configuration is that the object plane is no longer parallel to the lens plane. This results in a variable magnification across the image plane and subsequently image distortion. Furthermore, focusing across the entire measurement plane becomes difficult due to the variable magnification. Increasing the depth of field (Equation 3.7) can improve the ability to focus and can be achieved by decreasing the lens aperture (i.e., increasing $f^{\#}$). Decreasing the aperture, however, requires a higher laser intensity to adequately illuminate the particles in the object plane. When the camera angle is increased, the required depth of field also increases, which further amplifies the problem of insufficient depth of field.

This problem can be overcome by satisfying the so-called Scheimpflug condition, which can be achieved by rotating the lens plane with respect to the image plane as shown in Figure 3.13. As a result, the object plane, image plane and principle lens plane intersect at a common point and it is possible to focus the entire image plane [Prasad and Jensen, 1995].

Furthermore, significant radial distortions occur in liquid flow applications due to the mis-match in refractive index between the surrounding air and the silicon interface [Prasad and Adrian, 1993]. This causes an astigmatism and adversely affects the ability to focus across the image plane. This problem is further exacerbated by viewing through thick walls such as in the present configuration. In order to orientate the line of sight from each camera orthogonal to the air-silicone interface, viewing prisms can be used as shown in Figure 3.13. The viewing prisms are manufactured in silicone and thus have the same refractive index as the flow phantom. The prisms are located symmetrically with respect to the stereo-cameras and the angle subtended by the inclined wall of the prism to the original interface is equal to the camera angle Φ. This corrects radial distortions and allows to focus over the entire image plane (i.e., satisfying the Scheimpflug condition).

E.2 2D-3C Velocity Field Reconstruction

As a result of the off-axis viewing configuration of the angular-offset stereo-PIV setup, a square region in the object plane appears as a trapezoid in the image plane (e.g., Figure E.1). To correct for this distortion several calibration and reconstruction techniques exist for stereo-PIV and are, for example, summarised in Lin et al. [2008]; Prasad [2000] and Willert [2006]. Generally these techniques can be categorised as follows [Prasad, 2000]:

1. two-dimensional calibration-based reconstruction
2. three-dimensional calibration-based reconstruction
3. geometric reconstruction techniques

The geometric reconstruction method requires accurate knowledge of the experimental setup and imaging system (i.e., focal distance, camera angle, nominal magnification, ect.). Furthermore, this method does not adequately account for non-linearities such as lens distortion and is not able to account for variations from one experiment to the next. The inaccuracy of the geometric reconstruction method increases from the center towards the outer edges of the image, and hence, any results from the cross-correlation analysis can also be expected to be inaccurate in these regions. As a result, a three-dimensional calibration-based reconstruction method is adopted in this research. In this method, the mapping function is determined via an in-situ calibration procedure previously described by Soloff et al. [1997]. This technique does not rely on the accurate knowledge of the imaging system or experimental setup and is able to account for any known and unknown distortions encountered in the real experiment.

In order to obtain the three-component vector field from the individual 2D-2C vector field (one for each camera) via the calibration-based reconstruction, the following three procedures exist in the literature [Prasad, 2000; Wieneke, 2005]:

1. Computation of the 2D-2C field on a regular grid for each camera (image space) and subsequent interpolation onto a regular grid in object space to calculate the 2D-3C vector field in object coordinates.
2. Dewarping of the recorded images into object space and computation of the 2D-2C and subsequent 2D-3C vector field at the correct object coordinates.

3. Computation of 2D-2C vectors in image space at locations corresponding to the correct object position and subsequent 2D-3C vector reconstruction in object space.

The implementation of the first method is straight forward, however, the vectors are not computed at the correct world position and interpolation of the 2D-2C vector field onto a common grid is necessary. Depending on the interpolation scheme, false or inaccurate vectors can greatly affect the accuracy of the final 2D-3C vector field. Alternatively, method 2 and 3 compute the 2D-2C vector field at the correct object coordinates and an undesired error propagation due to vector interpolation is avoided. Method 2 requires an additional sub-pixel image interpolation, which, together with the sub-pixel interpolation necessary for the multi-pass window deformation scheme, leads to added image degradation and computational increase. This however, can be reduced if both steps are combined as demonstrated by Wieneke [2005]. The last method requires no vector or image interpolation at all, but has the disadvantage that the size and shape of the interrogation windows differ between the two cameras due to the perspective viewing. In this research, method 3 is implemented for the 2D-3C vector field reconstruction and discussed in more detail in the following sections.

E.2.1 Calibration

The purpose of the camera calibration is to determine how positions in the object (i.e., measurement) plane are mapped to locations in the image plane according to Equation E.1. In order to do this, it is necessary to acquire images of a calibration target, whose location in physical space is known accurately. In this work, a method similar to that of Soloff et al. [1997] is used wherein calibration data at different z locations parallel to the object plane are acquired. The calibration data are used to calculate the relationship between the 3D object coordinates $\underline{x}$ and the 2D image coordinates $\underline{X}$ for each camera. The advantage of this method is that it allows the particle displacement to be measured without any need for geometric reconstruction.

$$\underline{X} = F\underline{x} \tag{E.1}$$

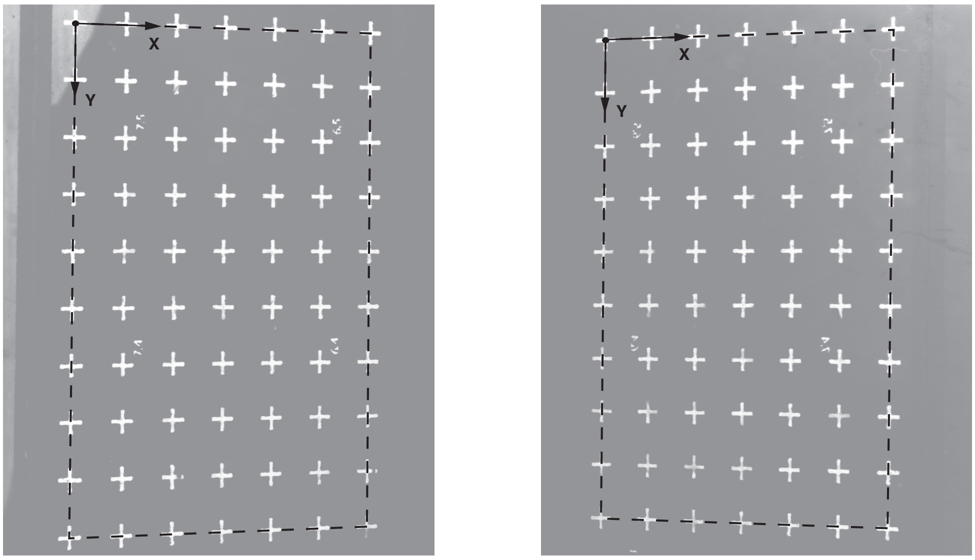

(a) (b)

Figure E.1 Calibration images taken from the left (a) and right (b) camera under an angle of ±45 degrees

The calibration target consists of a flat plate with a number of crosses as calibration markers. The markers are evenly spaced on a Cartesian grid with their location and size chosen so that the markers occupy the entire field of view of the cameras. Before the calibration images are acquired, a coordinate system in both, the object and image plane has to be defined. This is typically done by assigning the coordinate origin to the top left calibration marker and taking the respective $x-$ and $y-$ directions to the left and downwards as shown in a typical calibration image in Figure E.1.

Once the calibration images are acquired, the location of the calibration markers with respect to the coordinate origin is determined with a template matching scheme as described below.

Firstly, a template of the calibration image is created by approximating the locations of the calibration markers. The template and calibration image are then correlated using two-frame image correlation similar to PIV. The sub-pixel location of the image markers is determined with the two-dimensional Gaussian fit in Equation 3.16. An example of the identified calibration marker, marker template and resulting cross-correlation function is shown in Figure E.2. Once the image locations of the calibration markers are found, the 19 coefficients of the mapping function in Equation E.2 are determined with a least-squares procedure and the known locations in object space.

The accuracy of the coefficients is primarily dependent on the accuracy of the image marker locations. The mapping error is a measure for this accuracy and is discussed further in appendix F. The effect of camera self-calibration to improve the image to object mapping is detailed in Willert [1997] and Wieneke [2005] and implement in the current SPIVCC algorithm as disparity correction.

E.2.2 3C Velocity Reconstruction

The calibration data is used to calculate the mapping function, F, with a least-squares approach. Thus, it is important to have an adequate number of calibration makers distributed over the entire measurement volume. The least-squares approach was found to provide easy implementation and very good results since the distortions, as can be inferred from Figure E.1 are practically linear. Equation E.2 shows the mapping function F, which has a cubic dependency in the in-plane directions, x and y and a quadratic dependency in the out-of-plane direction, z. The exponent of the out-of-plane variable in F is at best one less than the number of planes required for calibration. This equation adequately tracks any barrel distortions and non-uniform magnification effects and accurately resolves the mapping function with minimal residual error [Soloff et al., 1997]. Others references (see Prasad [2000] for more detail) have used higher orders for the out-of-plane direction, but have found little or no significant increase in the accuracy of the reconstructed velocity field. In general, there exists a unique mapping function for each camera perspective.

$$
\begin{aligned}
F &= a_0 + a_1 x + a_2 y + a_3 z + a_4 x^2 + a_5 xy + a_6 y^2 + a_7 xz \\
&\quad + a_8 yz + a_9 z^2 + a_{10} x^3 + a_{11} x^2 y + a_{12} xy^2 + a_{13} y^3 \\
&\quad + a_{14} x^2 z + a_{15} xyz + a_{16} y^2 z + a_{17} xz^2 + a_{18} yz^2 \qquad \text{(E.2)}
\end{aligned}
$$

The process of reconstructing the three velocity components from the individual 2D-2C velocity fields follows the following procedure:

The calibration target is traversed in z-direction through the measurement volume in discrete steps of typically 1mm. Images of the calibration target are

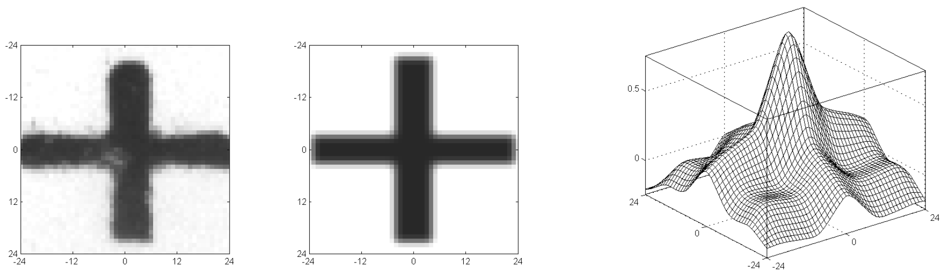

(a) (b) (c)

Figure E.2 Determination of calibration grid locations by cross-correlating sub-images (48 × 48pixel) with a synthetic template; (a) original grey-level image, (b) synthetic cross-template, (c) cross-correlation function

acquired at a minimum of three different z locations with each camera. Afterwards, the target is removed and 2D PIV images are recorded.
Using the calibration images, the individual calibration coefficients are determined with Equation E.2 for each camera. The region where both camera views overlap is determined and is used to create a uniform grid in the object plane to determine the vector location in physical space. The vector locations are projected onto each camera (i.e., image space) and the recorded images are interrogated at these positions with the multigrid PIVCC technique described in Chapter 4. The results are two 2D-2C vector fields of the projected in-plane velocity components with the vectors located at the mapped object coordinates.

To calculate the three component displacement field, Equation E.3 is obtained from a Taylor expansion of Equation E.1 and subsequent volume averaging over the calibrated interrogation volume [Soloff et al., 1997]. In Equation E.3, $F^c_{i,j}$ is the gradient tensor $\partial F_i/\partial x_j$, where c represents each camera, i the image coordinates $(i = 1, 2)$ and j the object coordinates $(j = 1, 2, 3)$.

$$\underline{\Delta X} = F^c_{i,j}\underline{\Delta x} \tag{E.3}$$

To solve for the fluid displacement, Equation E.3 is augmented to form the set of four linear equations in expression E.4. With four equations and only three unknown variables, Equation E.4 is over determined and can easily be solved using a least-squares approach for Δx, Δy and Δz. The subscripts 1 and 2 denote the first and second camera, respectively.

$$\begin{bmatrix} \Delta X^1 \\ \Delta Y^1 \\ \Delta X^2 \\ \Delta Y^2 \end{bmatrix} = \begin{bmatrix} F^1_{11} & F^1_{12} & F^1_{13} \\ F^1_{21} & F^1_{22} & F^1_{23} \\ F^2_{11} & F^2_{12} & F^2_{13} \\ F^2_{21} & F^2_{22} & F^2_{23} \end{bmatrix} \begin{bmatrix} \Delta x \\ \Delta y \\ \Delta z \end{bmatrix} \tag{E.4}$$

For the purpose of this thesis, the existing PIVCC analysis algorithm was extended to perform the above steps. A flow chart of the resulting SPIVCC algorithm is shown in Figure 3.14 and includes the object to image mapping, the iterative multigrid analysis and the subsequent 2D-3C velocity reconstruction. A separate algorithm was developed for the camera calibration step (i.e., Equation E.2).

Appendix F

Experimental Error Analysis

This Appendix contains an overview of possible sources in the experimental procedure and the PIV data analysis. In section F.1 the errors associated with the stereo-PIV measurements are analysed. Section F.2 presents the mapping and residual errors for the camera calibration procedure and in section F.3 estimates are made for the total velocity error in planar and stereo PIV. The analysis is concluded with an estimation of the uncertainty of the experimental procedure.

F.1 Stereo-PIV Error Validation

In the present work, an angular offset configuration with Scheimpflug condition is utilised for the stereoscopic PIV measurements. In-house software is used to compute the 2D vector field containing all three velocity component u, v and w. The performance and accuracy of the stereo-PIV apparatus and software is tested in this section using a solid body translation experiment similar to that of Parker et al. [2004].

F.1.1 Procedure

The camera setup and calibration procedure used in the solid body experiment is similar to that discussed in Chapter 7. The experiment involves the translation of a particle image by an know distance and recording of the particle pattern. The recorded images are processed using the stereo PIVCC algorithm and the results are compared to the known displacement. To simulate high density seeding particles, a sheet of 150 grit sandpaper is attached to a micrometer traverse as illustrated in Figure F.1. The sandpaper is illuminated with diffused light from a 240W halogen lamp and provides excellent contrast and signal to noise ratio. An angular configuration 45^o degree is utilised and the particle images are recorded on 800×1200 pixel frames. A distorting medium is placed between the cameras and the object plane to simulate optical distortion similar to that in the real experiments.

The particle pattern mounted onto a two-axis XZ-traverse and accurately displaced by 1mm in the x and z direction. This corresponds to an image displacement of approximately $13 - 14$ pixels and is comparable to that obtained from the real PIV measurements. For each case a reference and a displaced image are acquired for correlation with the stereo PIVCC algorithm described in Chapter 3. The displacement field is computed for an interrogation window of 64×64 pixel with a 50% overlap and no vector validation.

F.1.2 Results

The statistical results from the resolved displacement in the three principle directions are shown in Table F.1. The mean and RMS errors are calculated from a total of 10 measurements and averaged over the entire measurement plane ($N = 5400$) using Equation D.3 and D.4. The uncertainty in the translation of the particle pattern is $\pm 5\mu$m. The RMS error in the x, y and z displacement is a function of the direction of motion and includes the PIV displacement error

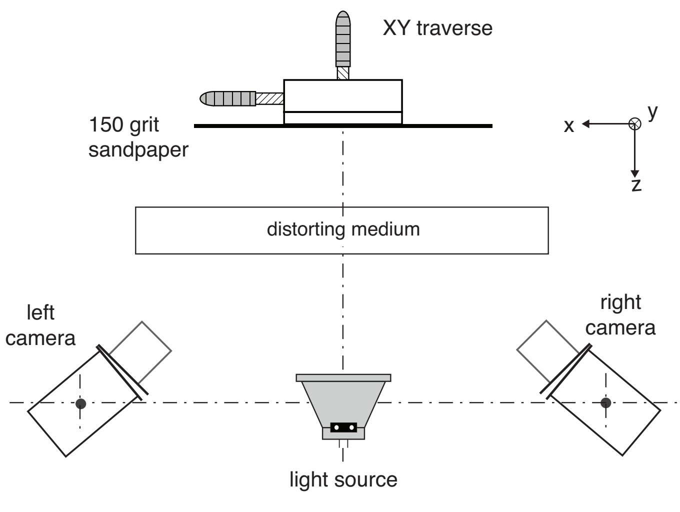

Figure F.1 Schematic of the solid body translation experiments

Table F.1 SPIV errors from solid body measurements

Traverse	Mean (μm)	RMS (μm)
0mm xyz displacement		
Δx	0.28	0.36
Δy	0.25	0.29
Δz	0.32	0.42
1mm x displacement		
Δx	999.2	3.1
Δy	1.5	1.2
Δz	5.2	4.2
1mm z displacement		
Δx	1.6	2.1
Δy	1.5	1.9
Δz	997.2	2.2

(Section D.1), interpolation errors, calibration and target grid spacing errors, and traversing errors.

For the 1mm displacement the measurement results show a total error of 0.4% and 0.5% or 3.9μm and 5μm in the x and z directions respectively. The errors due to a displacement in y direction was not assessed, but are typically in the same order as in x direction [Willert, 1997]. The ratio between in-plane and out-of-plane error is approximately one and consistent with the theoretical $1/tan(\alpha)$ relation [Lawson and Wu, 1997a], which for the present case ($\alpha = 45^o$) is equal to one. The RMS errors for Δx, Δy, and Δz are low for the 0mm xyz displacement and range between 1.2 and 3.1μm in the case of the 1mm displacement. The probability density function of the bias error is presented in Figure F.2. The error is distributed normally with a standard deviation equal to the RMS error in Table F.1. The errors are relatively small compared to the imposed displacement and the error distribution appears to be lightly skewed towards negative values. Any deviation from a zero mean value in the individual components may be attributed to inaccuracies in the mechanical translation system [Fouras et al., 2007].

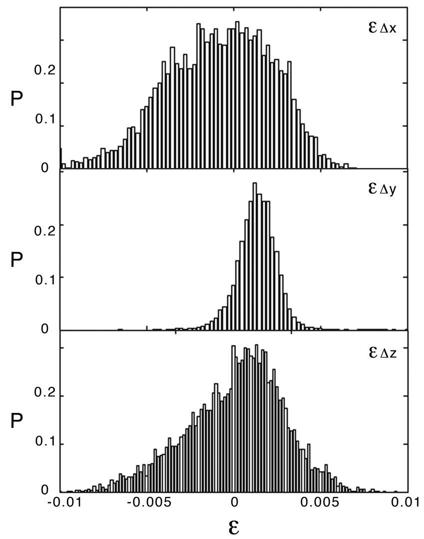

(a)

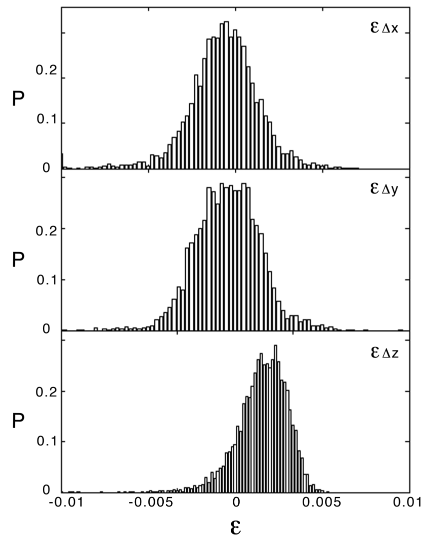

(b)

Figure F.2 Probability density function of error $\epsilon_{\Delta \underline{x}}$ in the measured displacement components: (a) 1mm x displacement; (b) 1mm z displacement

The difference between the measured and the actual displacement can be expressed as following

$$\epsilon_{\Delta \underline{x}} = \Delta \underline{x}_i - \Delta \underline{x}_a \tag{F.1}$$

where $\Delta \underline{x_i}$ is the measured displacement in all three directions and $\Delta \underline{x_a}$ the true displacement of 1.000mm. The fluctuating component $\epsilon'_{\Delta \underline{x}}$ with respect to the mean error $\overline{\epsilon_{\Delta \underline{x}}}$ (Eq.D.3) is calculated as

$$\epsilon'_{\Delta \underline{x}} = \epsilon_{\Delta \underline{x}} - \overline{\epsilon_{\Delta \underline{x}}} \tag{F.2}$$

Figure F.3 shows the error fluctuation with removed bias error for the displacements in x and z direction, respectively. The iso-contours indicate the distribution of the error over the calibrated measurement area of approximately 50mm $\times$ 40mm. The greatest measurement errors occur in the out-of-plane displacement Δz, while for Δy the errors are the smallest. Generally the errors are larger for the x displacement compared to the z displacement. The distribution of the fluctuating error appears random, expect for Δx and Δz for the x translation case. Here the errors appear to be correlated in some areas, which might be attributed to the 50% overlapping factor used in the interrogation analysis. Overall, the error distributions are consistent with previously reports [Fouras et al., 2007; Soloff et al., 1997; Willert, 1997]

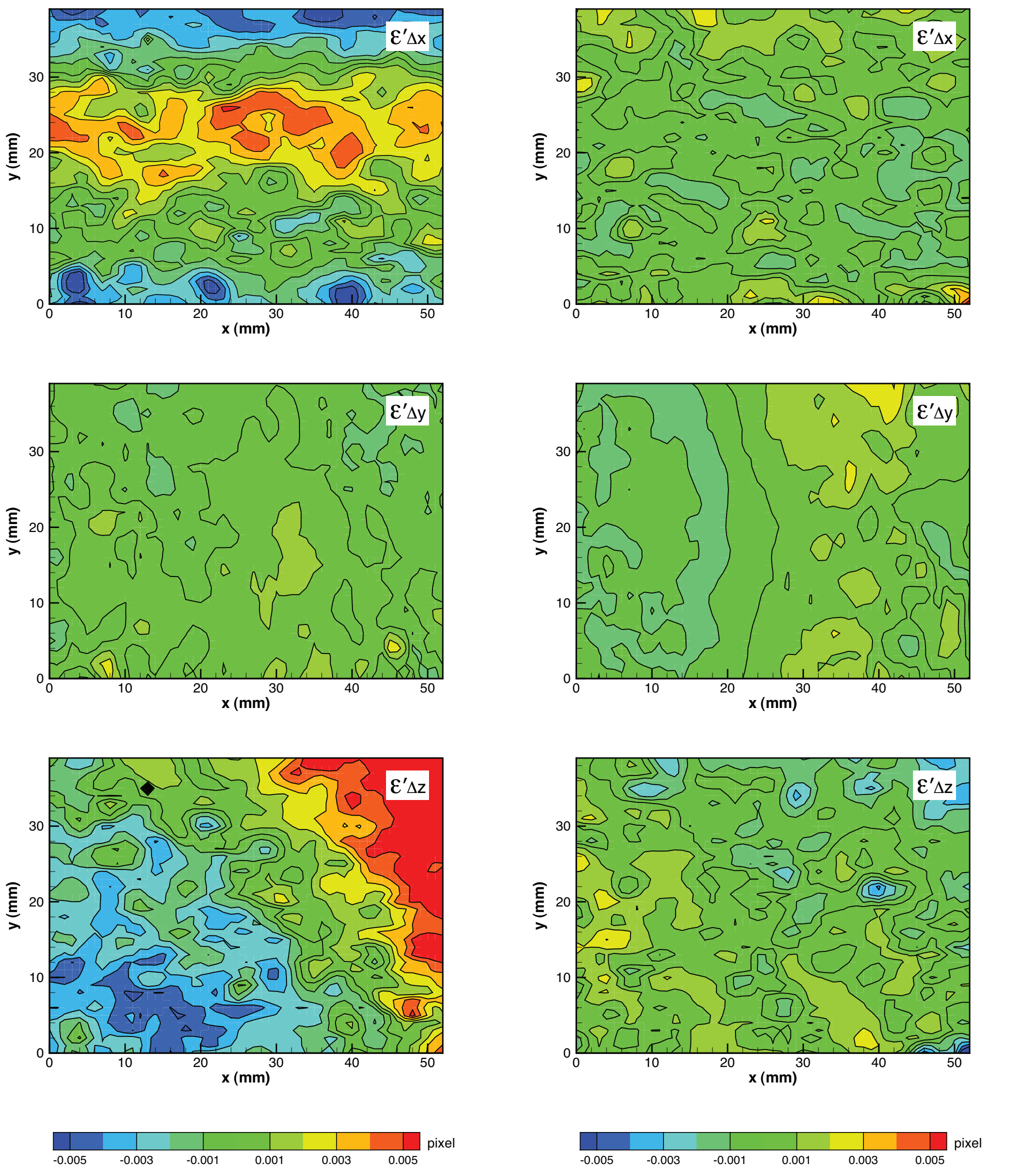

Figure F.3 Fluctuating component of the error $\epsilon_{\Delta\underline{x}}$ (mm) between the true displacement in object space and its computed value in the image plane: (top) $\epsilon'_{\Delta x}$; (center) $\epsilon'_{\Delta y}$; (bottom) $\epsilon'_{\Delta z}$; (left) 1mm x displacement; (right) 1mm z displacement. Any bias error has been removed.

F.2 Evaluation of the Mapping Error

In stereo-PIV the accuracy of the calculated 3D vector field depends on the accuracy of the individual 2D measurements and the calibration procedure. The accuracy of the fluid to image mapping function can be estimated by using the calibration function to map the calibration marker locations from fluid to image space and then comparing them to the marker locations actually recorded for each calibration image. This is referred to as the mapping error. Table F.2 shows the RMS mapping error and maximal total error for the left and right camera. The largest recorded RMS error is 0.21 pixel for the left camera X location, which corresponds to a nominal RMS error of 0.0156mm in the object plane. The largest absolute mapping error is measured for the same camera at 0.85 pixel or 0.0663mm in object coordinates. Due to the angular viewing configuration the image back-projection stretches the image in horizontal direction by a factor of approximately 1.4 ($\sim\sqrt{2}$) with respect to the vertical direction. As a result, the measurement uncertainties in the x direction are comparably larger.

The RMS mapping error is not only influenced by the ability of the least-square polynomial (Eq. E.2) to fit the calibration data, but also by the accuracy with which the image locations of the calibration markers are detected. Prasad et al. [1992] has shown that the random error for locating particle image centroids is in the order of 5-10% of the particle image diameter. In the current analysis the calibration marker have a characteristic size of approximately 9 pixel. The maximum error associated with the least-square fit is approximately 0.85 pixel (Tab.F.2) or 9.4% of the calibration marker size. Hence, the accuracy of the curve fit and the marker centroid location are comparable, from which it can be concluded that the third-order polynomial is adequate to represent the image distortion in the current experiments.

Table F.2 Total and RMS mapping error

	RMS Error		Max. absolute Error	
	(px)	(mm)	(px)	(mm)
Left Camera X	0.21	0.0156	0.85	0.0663
Left Camera Y	0.161	0.0086	0.437	0.0232
Right Camera X	0.193	0.0127	0.706	0.0465
Right Camera Y	0.165	0.0081	0.36	0.0176

F.3 Evaluation of the Velocity Error

There are several contributors to the total velocity error in PIV measurements. Some of which are inadequate particle seeding (poor or excessive), which can result in increased random errors as shown in Section D or poor selection of the time delay between laser pulses, which can cause in-plane particle loss or unresolved displacements. While these parameter can be adjusted for each experiment they may also adversely affect the spatial and dynamical resolution of the measurement. Other sources of errors are image and camera noise and in- and out-of-plane velocity gradients which greatly affect the ability of the cross-correlation algorithm to accurately detect the displacement peaks. A comprehensive discussion of error sources in digital PIV is presented in Huang et al. [1997] and Raffel et al. [1998]. In addition to the errors introduced during the digital image evaluation discussed in Section D, the total velocity error is also caused by experimental uncertainties and is comprised of a bias and a random error component. Experimental bias can be caused by optical distortion and refractive index mis-match or incorrect setup of the experimental apparatus, while random errors are caused by large velocity gradients and image noise and are associated with the statistical uncertainty of the measured displacement.

The total uncertainty in one component of the 2D velocity field obtained from conventional PIV measurements can be expressed by Equation F.3 and is comprised of the displacement uncertainty, a calibration or scale uncertainty, and a temporal uncertainty.

$$\epsilon_u^2 = \left(\frac{\delta_u}{u}\right)^2 = \left(\frac{\delta_{\Delta X}}{\Delta X}\right)^2 + \left(\frac{\delta_{scale}}{scale}\right)^2 + \left(\frac{\delta_{\Delta t}}{\Delta t}\right)^2 \tag{F.3}$$

The scale error, δ_{scale} is the error in determining the image magnification or calibration and for example can be inferred from the mapping error in Section F.2. This error is typically very small (less than 1%) since the calibration is performed over the entire measurement area. The timing error, $\delta_{\Delta t}$ between the successive particle images is also typically less than 1% for the current experiments with $\Delta t = 500 - 2600\mu$s. The error in the measured displacement, $\delta_{\Delta X}$ is related to the minimum resolvable displacement of the correlation algorithm. For the current PIVCC algorithm this error is 0.1 pixel and is referenced to the maximum displacement encountered in the the experiment (typically $8-12$ pixel). Based on Equation F.3 the total error for one velocity component, ϵ_u arising from the PIV measurements is 1.32%

Planar PIV (2D-PIV) is unable to resolve the out-of-plane velocity component and a additional error in the in-plane component exists due to perspective projection [Prasad, 2000]. This error can be up to 10% and strongly depends on the out-of-plane velocity gradients and flow three-dimensionality. In SPIV, this perspective error is removed, while the displacement accuracy still depends on the accuracy of the individual planar velocity fields. Assuming a constant displacement error $\delta_{\Delta X} = \delta_{\Delta Y}$ for both directions and cameras, Prasad [2000] gives the following relation between the true 2D3C displacement error $\delta_{\Delta \underline{x}}$ and the displacement error $\delta_{\Delta \underline{X}}$ of a single camera.

$$\begin{aligned} \delta_{\Delta x} &\approx \frac{1}{\sqrt{2}} \left[\frac{1}{M}\right] \delta_{\Delta X} \qquad \text{for } x = 0 \\ \delta_{\Delta y} &\approx \frac{1}{\sqrt{2}} \left[\frac{1}{M}\right] \delta_{\Delta Y} \qquad \text{for } y = 0 \end{aligned}$$

and the ratio between the in-plane and out-of-plane error is given by Lawson and Wu [1997a] as

$$\frac{\delta_{\Delta z}}{\delta_{\Delta x}} = \frac{1}{\tan \alpha} \qquad \text{for } x = 0, y = 0$$

For a angular-offset stereoscopic systems the above relations are valid in the image center where $x = y = 0$ and for a nominal magnification M. The absolute value of the in-plane error is smaller than the corresponding error for a single camera due to the contribution of two cameras. The out-of-plane error is a function of the stereo angle, α and increases for decreasing viewing angles. For a angular configuration of $\alpha = 45^o$ the out-of-plane and in-plane errors are of equal magnitude.

F.3.1 Experimental Error Validation

In order to determine the accuracy of the experimental procedure and the hydraulic flow circuitry, 2D-PIV *in-situ* measurements are performed in a straight pipe at a flow rate of $8.73l/min$ ($Re = 853$). Results are compared to the analytical solution for fully developed pipe flow and are shown in Figure F.4. A slight underestimation of the velocity near the upper wall $r/D = 0.5$ can be seen. Also shown is the vorticity distribution, computed from the velocity field via central differences, which for fully developed pipe flow is equal to the radial velocity gradient du/dr. The analytical solution is $du/dr = 2U_{max}r/R^2$. The biasing of the measured velocity gradient towards lower values at the wall ($r = \pm R$) is inherent to conventional planar PIV [Tsuei and Savas, 2000], but can be mitigated for example by shifting the vector position to the fluid centroid (Chapter 4.2.2) or by the current iPIV technique.

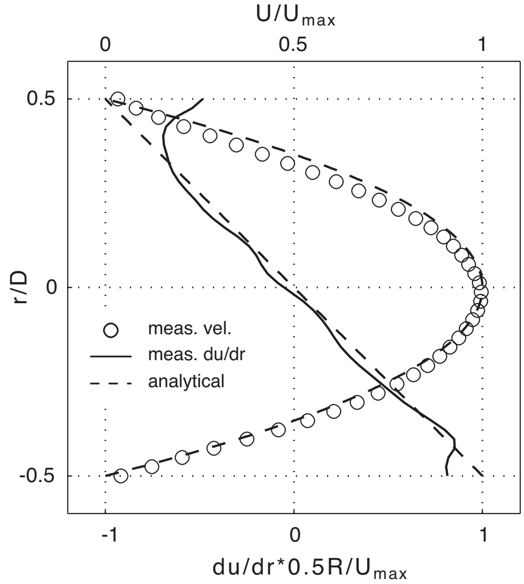

Figure F.4 Axial velocity (circle) and velocity gradient (solid line) profile and its analytical solutions (dashed lines) measured in a straight segment of the common carotid artery at approximately $2.5D$ upstream of the bifurcation

The velocity profiles are measured at two stations and the flow rates are calculated according to Equation F.4

$$Q = \frac{2\pi}{N} \sum_{i=1}^{N} U \cdot \Delta \tag{F.4}$$

where U is the velocity magnitude, N the number of velocity vectors across the pipe diameter and Δ the vector spacing. The calculated flow rates amount to 8.48 l/min and 8.51 l/min and deviate from the prescribed flow rate by of 2.9% and 2.5%, respectively. The actual flow rate is measured with an uncertainty of 1.3% by measuring the weight of the liquid collected within a specific time interval.

Using a PIVCC error of 0.1 pixel of the calculated displacement, the expected velocity error for the current setup with magnification of 1.24^{-4} and time delay of $1300\mu s$ is 0.0095m/s or approximately 2% of the mean velocity. Uncertainties in the light sheet position can also incur velocity errors. For example, a misalignment of the light sheet by half the sheet thickness (i.e. 1mm) outside the symmetry plane would results in an underestimation of the centerline velocity by 1% for a fully-developed flow profile.

Lastly, as shown in Chapter 2.5, there exists a strong temperature dependency of the working liquid and its kinematic viscosity. At a working temperature of 20^{o}C, temperature variations in the order of $\pm 0.5^{o}$C lead to an error in kinematic viscosity of approximately 1.9%. Combined with the above error in flow rate, the total error in Reynolds number can be estimated to $\pm 2.3\%$. Overall, the hydraulic errors are comparable to the total PIV velocity error of 1.32% estimated with Equation F.3.

Appendix G

Differential Operators

This appendix summarises the mathematical formulation of the different discrete and analytical differential operators analysed in Section 4.2.3. A comprehensive summary and additional operator note listed here can be found in Durst et al. [1996]; Foucaut and Stanislas [2002]; Fouras and Soria [1998]; Raffel et al. [1998] amongst others.

G.1 Discrete Operators

In the following, the differential operators are characterised in terms of the velocity grid spacing Δx, the random velocity error σ_u and the error amplification coefficient ϵ. The individual a_i and α_i are obtained from Foucaut and Stanislas [2002] and are summarised in Table G.1. The error amplification coefficient, ϵ is estimated via Monte Carlo simulations of a sinusoidal velocity profile, corrupted with 2% measurement noise and is also listed in Table G.1.

For a *forward difference* scheme, the gradient at the wall (j=1) can be obtained as follows:

$$\left.\frac{\partial u}{\partial x}\right|_{j=1} = \frac{1}{a\Delta x}\sum_{i=1}^{n} a_i(u_{j+1} - u_j) + \sum_{i=n+1}^{\infty} \alpha_i \frac{\Delta x^{i-1}}{i!}\left.\frac{\partial^i u}{\partial x^i}\right|_j + \epsilon\frac{\sigma_u}{\Delta x} \tag{G.1}$$

In order to evaluate the shear gradient at the wall by means of centered differences, the velocity field is extended across the interface by reflecting and reversing its direction to obtain a symmetric velocity profile, i.e., $u_{j+1} = -u_{j-1}$

[Tsuei and Savas, 2000]. This additionally imposes the no-slip condition and simplifies the expression for the n order *centered difference* scheme as follows:

$$\left.\frac{\partial u}{\partial x}\right|_{j=1} = \frac{1}{a\Delta x}\sum_{i=1}^{n/2} 2a_i u_{j+1} + \sum_{i=n+1}^{\infty} \alpha_i \frac{\Delta x^{i-1}}{i!}\left.\frac{\partial^i u}{\partial x^i}\right|_j + \epsilon\frac{\sigma_u}{\Delta x} \tag{G.2}$$

In the present work, a second and sixth order centered difference (CD2, CD6) operator and a first order forward difference (FD) scheme are investigated.

An improvement in accuracy can be obtained by using the *Richardson extrapolation*, which is computed as a linear combination of second order centered differences at different data spacings $\Delta x, 2\Delta x, 4\Delta x$ and $8\Delta x$.

$$\left.\frac{\partial u}{\partial x}\right|_{j} = \frac{1}{a}\sum_{i=1,2,4,8} a_i \frac{u_{j+1}}{i\Delta x} + \sum_{i=n+1}^{\infty} \alpha_i \frac{\Delta x^{i-1}}{(n+i)!}\left.\frac{\partial^i u}{\partial x^i}\right|_j + \epsilon\frac{\sigma_u}{\Delta x} \tag{G.3}$$

Depending on the objective, the coefficients a_i can either be optimised to minimise the truncation error via Taylor expansion or to minimise the noise amplification ϵ via a least square method [Foucaut and Stanislas, 2002]. Two fourth order scheme were investigated in this study, one with optimisation of the truncation error (RE4) and the other with minimisation of the noise term (RE4*). Also note that the standard second and fourth order Richardson extrapolation are mathematically equivalent to the second and fourth order central difference scheme.

A third group of differential operators are *least square* (LS) methods, which are optimised for small noise amplification and are mathematically similar to the centered differences.

G.2 Analytical Operators

The two analytical differential operators tested in this work are based on a third and fifth order polynomial interpolation (PL3, PL5) of the following form:

$$u(y) = a_0 + \sum_{i=1}^{n} a_i y^i + \delta u_j \tag{G.4}$$

where $\delta u_j = u(y = j) - \tilde{u}_j$ is the difference between the fitted and measured velocity and which is proportional to the velocity measurement uncertainty, i.e., $\delta u_j = \epsilon\sigma_u$ [Fouras and Soria, 1998].
Hence, the velocity gradient at the wall ($j = 0$) is given as:

$$\left.\frac{\partial u}{\partial x}\right|_{y=0} = a_1 + \epsilon\frac{\sigma_u}{\Delta x} \tag{G.5}$$

where ϵ is equal to 0.51 and 7.9 for the third and fifth order polynomial, respectively. The coefficient a_1 is determined via a least squares fit of Equation G.4 using $n + 1$ data points.

Table G.1 Characteristics of different discrete derivative operators of order n. Data taken from Foucaut and Stanislas [2002], * indicates noise optimisation

n	a	a_1	a_2	a_3	a_4	a_8	α_{n+1}	ϵ
Forward Differences:								
1	1	1	0	0	0	0	1	1.41
Centered Differences:								
2	2	1	0	0	0	0	1	0.71
4	12	8	-1	0	0	0	4	0.95
6	60	45	-9	1	0	0	36	1.08
Richardson Extrapolation:								
4	3	4	-1	0	0	0	1	0.95
4*	1239	272	1036	0	0	-69	214.5	0.334
Least Squares:								
2	10	1	2	0	0	0	3.4	0.316

References

Adler, K. and Bruecker, C. (2007). Dynamic flow in a realistic model of the upper human lung airways. *Experiments in Fluids*, 43(2):411–423.

Adrian, R. J. (1997). Dynamic ranges of velocity and spatial resolution of particle image velocimetry. *Measurement Science & Technology*, 8:1393–1398.

Adrian, R. J. (2005). Twenty years of particle image velocimetry. *Experiments in Fluids*, 39(2):159 – 169.

Adrian, R. J. and Yao, C.-S. (1984). Development of pulsed laser velocimetry (plv) for measurement of turbulent flow. In *Symposium on Turbulence, Proceedings of the Eighth Symposium on Turbulence.*, pages 170–186.

Ahmed, S. A. and Giddens, D. P. (1983a). Flow disturbance measurements through a constricted tube at moderate reynolds numbers. *Journal of Biomechanics*, 16(12):955–963.

Ahmed, S. A. and Giddens, D. P. (1983b). Velocity measurements in steady flow through axisymmetric stenoses at moderate reynolds numbers. *Journal of Biomechanics*, 16(7):505–516.

Amili, O., Law, K. H., and Soria, J. (2009). Wall shear stress measurements using a novel shear stress sensor. In *8th International Symposium on Particle Image Velocimetry, Melbourne, Australia.*

Anandarajah, K., Hargrave, G. K., and Halliwell, N. A. (2006). Digital particle image velocimetry: Partial image error (PIE). *Journal of Physics: Conference Series*, 45:174–185.

Asakura, T. and Karino, T. (1990). Flow patterns and spatial distribution of atherosclerotic lesions in human coronary arteries. *Circulation Research*, 66(4):1045–1066.

Aspert, N., Santa-Cruz, D., and Ebrahimi, T. (2002). MESH: Measuring Errors between Surfaces using the Hausdorff distance. In *IEEE International Conference on Multimedia and Expo*, volume I-II of *Proceedings of the IEEE International Conference on Multimedia and Expo 2002 (ICME)*, pages 705–708.

Astarita, T. and Cardone, G. (2005). Analysis of interpolation schemes for image deformation methods in PIV. *Experiments in Fluids*, 38(2):233–243.

Atkinson, C. and Soria, J. (2009). An efficient simultaneous reconstruction technique for tomographic particle image velocimetry. *Experiments in Fluids*, 47(4):553–568.

Atkinson, C. H. and Soria, J. (2007). Algebraic reconstruction techniques for tomographic particle image velocimetry. In *Proceedings of the 16th Australasian Fluid Mechanics Conference, Gold Coast, Australia.*

Bale-Glickman, J., Selby, K., Saloner, D., and Savas, O. (2003a). Experimental flow studies in exact-replica phantoms of atherosclerotic carotid bifurcations under steady input conditions. *Journal of Biomechanical Engineering*, 125(1):38 – 48.

Bale-Glickman, J., Selby, K., Saloner, D., and Savas, O. (2003b). Physiological flow studies in exact-replica atheroslerotic carotid bifurcation. *American Society of Mechanical Engineers, Bioengineering Division (Publication) BED*, 55:57 – 58.

Ballyk, P. D., Steinman, D. A., and Ethier, C. R. (1994). Simulation of non-Newtonian blood flow in an end-to-side anastomosis. *Biorheology*, 31(5):565–86.

Barbato, J. E. and Tzeng, E. (2004). Nitric oxide and arterial disease. *Vasclular surgery*, 40:187–193.

Berger, S. A. and Jou, L.-D. (2000). Flows in stenotic vessels. *Annu. Rev. Fluid Mech*, 32:347 – 382.

Berger, S. A., Talbot, L., and Yao, L. S. (1983). Flow in curved pipes. *Annu. Rev. Fluid Mech*, 15:461 – 512.

Bharadvaj, B. K., Mabon, R. F., and Giddens, D. P. (1982a). Steady flow in a model of the human carotid bifurcation. 1 - Flow visualization. *Journal of Biomechanics*, 15(5):349 – 362.

Bharadvaj, B. K., Mabon, R. F., and Giddens, D. P. (1982b). Steady flow in a model of the human carotid bifurcation. 2 - Laser-doppler anemometry measurements. *Journal of Biomechanics*, 15(5):363 – 378.

Botnar, R., Rappitsch, G., Beat Scheidegger, M., Liepsch, D., Perktold, K., and Boesiger, P. (2000). Hemodynamics in the carotid artery bifurcation:: a comparison between numerical simulations and in vitro MRI measurements. *Journal of Biomechanics*, 33(2):137–144.

Boutsianis, E., Guala, M., Olgac, U., Wildermuth, S., Hoyer, K., Ventikos, Y., and Poulikakos, D. (2009). CFD and PTV steady flow investigation in an anatomically accurate abdominal aortic aneurysm. *Journal of Biomechanical Engineering*, 131(1).

Brunette, J., Mongrain, R., Laurier, J., Galaz, R., and Tardif, J. C. (2008). 3D flow study in a mildly stenotic coronary artery phantom using a whole volume PIV method. *Medical Engineering & Physics*, 30(9):1193–1200.

Buchmann, N., Yamamoto, M., Jermy, M., and David, T. (2010). Particle image velocimetry (piv) and computational fluid dynamics (cfd) modelling of carotid artery haemodynamics under steady flow: A validation study. *Journal of Biomechanical Science and Engineering*, 5(4):421–436.

Buchmann, N. A. (2005). Experimental modelling of aerosol particles within lung bifurcations. Master's thesis, von Karman Institute for Fluid Dynamics and Technische Universität Darmstadt.

Buchmann, N. A. and Jermy, M. C. (2007). Particle image velocimetry measurements of blood flow in a modeled carotid artery bifurcation. In *Proceedings of the 16th Australasian Fluid Mechanics Conference, Gold Coast, Australia.*

Buchmann, N. A., Nguyen, C. V., Wells, J. C., and Jermy1, M. (2008). In-vitro wall shear stress measurements using interfacial particle image velocimetry (IPIV). In *14th Int Symp. on Applications of Laser Techniques to Fluid Mechanics, Lisbon, Portugal.*

Budwig, R. (1994). Refractive index matching methods for liquid flow investigations. *Experiments in Fluids*, 17(5):350–355.

Burgmann, S., Große, S., Schröder, W., Roggenkamp, J., Jansen, S., Gräf, F., and Büsen, M. (2009). A refractive index-matched facility for fluid–structure interaction studies of pulsatile and oscillating flow in elastic vessels of adjustable compliance. *Experiments in Fluids*, DOI 10.1007/s00348-009-0681-y.

Bushberg, J. T., Seibert, J. A., Leidholt, E. M., and Bonne, J. M. (2001). *The Essential Physics of Medical Imaging*. Lippincot Willams and Wilkins, 2nd edition.

Caro, C. G. (2001). Vascular fluid dynamics and vascular biology and disease. *Mathematical Methods in the Applied Sciences*, 24(17-18):1311 – 1324.

Caro, C. G., Doorly, D. J., Tarnawski, M., Scott, K. T., Long, Q., and Dumoulin, C. L. (1996). Non-planar curvature and branching of arteries and non-planar-type flow. *Proceedings of the Royal Society A: Mathematical, Physical and Engineering Sciences*, 452(1944):185–197.

Carter, K., Anderson, C., Hacket, M., Feigin, V., Barber, P., Broad, J., and Bonita, R. (2006). Trends in ethnic disparities in stroke incidence in auckland, new zealand, during 1981 to 2003. *Stroke*, 37(1):56–62.

Chatzizisis, Y. S., Coskun, A. U., Jonas, M., Edelman, E. R., Feldman, C. L., and Stone, P. H. (2007). Role of endothelial shear stress in the natural history of coronary atherosclerosis and vascular remodeling: Molecular, cellular, and vascular behavior. *Journal of the American College of Cardiology*, 49(25):2379–2393.

Cho, Y. I. and Kensey, K. R. (1991). Effects of the non-newtonian viscosity of blood on flows in a diseased arterial vessel. part 1: Steady flows. *Biorheology*, 28(3-4):241–62.

Chong, C. K., Rowe, C. S., Sivanesan, S., Rattray, A., Black, R. A., Shortland, A. P., and How, T. V. (1999). Computer aided design and fabrication of models for in vitro studies of vascular fluid dynamics. *Proceedings of the Institution of Mechanical Engineers, Part H (Journal of Engineering in Medicine)*, 213(H1):1–4.

Cieslicki, K. and Ciesla, D. (2005). Investigations of flow and pressure distributions in physical model of the circle of willis. *Journal of Biomechanics*, 38(11):2302 – 2310.

Comerford, A. and David, T. (2008). Computer model of nucleotide transport in a realistic porcine aortic trifurcation. *Annals of Biomedical Engineering*, 36(7):1175–1187.

Comerford, A., Plank, M. J., and David, T. (2008). Endothelial nitric oxide synthase and calcium production in arterial geometries: An integrated fluid mechanics/cell model. *Journal of Biomechanical Engineering*, 130(1).

Davies, P., Reidy, M. A., Goode, T. B., and Bowyer, D. E. (1976). Scanning electron microscopy in the evaluation of endothelial integrity of the fatty streak lesion of atherosclerosis. *Atherosclerosis*, 25:125–130.

Davies, P. F. (2000). Spatial hemodynamics, the endothelium, and focal atherogenesis - a cell cycle link? *Circulation Research*, 86(2):114–116.

Davignon, J. and Ganz, P. (2004). Role of endothelial dysfunction in atherosclerosis. *Circulation*, 109:27–32.

Dean, W. R. (1928). LXXII. The stream-line motion of fluid in a curved pipe (second paper). *Philosophical Magazine Series 7*, 5(30):673 — 695.

DeBakey, M., Lawrie, G., and Glaeser, D. (1985). Patterns of atherosclerosis and their surgical significance. *Annals of Surgery*, 201(2):115–131.

Delnoij, E., Westerweel, J., Deen, N. G., Kuipers, J. A. M., and van Swaaij, W. P. M. (1999). Ensemble correlation PIV applied to bubble plums rising in a bubble column. *Chemical Engineering Science*, 54:5159–5171.

DePaola, N., Gimbrone, M., Davies, P., and Dewey, C. (1993). Vascular endothelium responds to fluid shear stress gradients. *Arteriosclerosis, Thrombosis, and Vascular Biology*, 13(3):465.

Dey, T. K. (2007). *Curve and Surface Reconstruction: Algorithms with Mathematical Analysis*. Cambridge University Press, Cambridge.

Ding, Z., Wang, K., Li, J., and Cong, X. (2001). Flow field and oscillatory shear stress in a tuning-fork-shaped model of the average human carotid bifurcation. *Journal of Biomechanics*, 34(12):1555 – 1562.

Doorly, D., Taylor, D. J., Franke, P., and Schroter, R. C. (2008). Experimental investigation of nasal airflow. *Proceedings of the Institution of Mechanical Engineers, Part H (Journal of Engineering in Medicine)*, 222(H4):439–53.

Doyle, B., Morris, L., Callanan, A., Kelly, P., and Vorp, D. (2008). 3D reconstruction and manufacture of real abdominal aortic aneurysms: From CT scan to silicone model. *Journal of Biomechanical Engineering*, 130.

Dring, R. P. (1982). Sizing criteria for laser anemometry particles. *Journal of fluids engineering*, 104(1).

Durst, F., Kikura, H., Lekakis, I., Jovanović, J., and Ye, Q. (1996). Wall shear stress determination from near-wall mean velocity data in turbulent pipe and channel flows. *Experiments in Fluids*, 20(6):417–428.

Elkins, C. J. and Alley, M. T. (2007). Magnetic resonance velocimetry: Applications of magnetic resonance imaging in the measurement of fluid motion. *Experiments in Fluids*, 43(6):823–858.

Elsinga, G., Adrian, R., van Oudheusden, B., and Scarano, F. (2007). Tomographic-PIV investigation of a high reynolds number turbulent boundary layer. In *7th International Symposium on Particle Image Velocimetry, Rome, Italy.*

Elsinga, G., Westerweel, J., Scarano, F., and Novara, M. (2009). On the velocity of ghost particles. In *8th International Symposium on Particle Image Velocimetry, Melbourne, Australia.*

Elsinga, G. E., Scarano, F., Wieneke, B., and van Oudheusden, B. W. (2006). Tomographic particle image velocimetry. *Experiments in Fluids*, 41(6):933–947.

FarField Technology (2004). *FastRBF Toolbox, MATLAB Interface.* FarField Technology Ltd.

Fatemi, R. S. and Rittgers, S. E. (1994). Derivation of shear rates from near-wall lda measurements under steady and pulsatile flow conditions. *Journal of Biomechanical Engineering*, 116(3):361 – 368.

Fischer, P. F., Loth, F., Lee, S. E., Lee, S.-W., Smith, D. S., and Bassiouny, H. S. (2007). Simulation of high-reynolds number vascular flows. *Computer Methods in Applied Mechanics and Engineering*, 196(31-32):3049–3060.

Foucaut, J., Miliat, B., Perenne, N., and Stanislas, M. (2004). Characterization of different PIV algorithms using the europiv synthetic image generator and real images from a turbulent boundary layer. In *Particle Image Velocimetry: Recent Improvements*. Springer-Verlag Berlin-Heidelberg.

Foucaut, J. M. and Stanislas, M. (2002). Some considerations on the accuracy and frequency response of some derivative filters applied to particle image velocimetry vector fields. *Measurement Science & Technology*, 13:1058–1071.

Fouras, A., Dusting, J., and Hourigan, K. (2007). A simple calibration technique for stereoscopic particle image velocimetry. *Experiments in Fluids*, 42(5):799–810.

Fouras, A. and Soria, J. (1998). Accuracy of out-of-plane vorticity measurements derived from in-plane velocity field data. *Experiments in Fluids*, 25(5-6):409–30.

Frayne, R., Holdsworth, D., Gowman, L., and Rickey, D. (1992). Computer-controlled flow simulator for MR flow studies. *J Magn Reson Imaging*, 2:605 – 612.

Friedman, M., Hutchins, G., Bargeron, C., Deters, O., and Mark, F. (1981). Correlation between intimal thickness and fluid shear in human arteries. *Atheroslcerosis*, 39:425–436.

Friedman, M. H., Deters, O. J., Mark, F. F., Brent Bargeron, C., and Hutchins, G. M. (1983). Arterial geometry affects hemodynamics : A potential risk factor for atherosclerosis. *Atherosclerosis*, 46(2):225–231.

Friedman, M. H. and Ding, Z. (1998). Variability of the planarity of the human aortic bifurcation. *Medical Engineering & Physics*, 20(6):469–472.

Friedman, M. H. and Giddens, D. P. (2005). Blood flow in major blood vessels - modeling and experiments. *Annals of Biomedical Engineering*, 33(12):1710–1173.

Friedman, M. H., Kuban, B. D., Schmalbrock, P., Smith, K., and Altan, T. (1995). Fabrication of vascular replicas from magnetic resonance images. *Journal of Biomechanical Engineering*, 117(3):364–6.

Geoghegan, P., Jermy, M., Buchmann, N., Spence, C., and Freitag, T. (2009). Experimental investigation of flow in a compliant tube using particle image velocimetry. In *8th International Symposium on Particle Image Velocimetry, Melbourne, Australia*.

Gijsen, F. J. H., Allanic, E., van de Vosse, F. N., and Janssen, J. D. (1999a). Influence of the non-newtonian properties of blood on the flow in large arteries: Unsteady flow in a 90 degree curved tube. *Journal of Biomechanics*, 32(7):705 – 713.

Gijsen, F. J. H., Palmen, D. E. M., van der Beek, M. H. E., van de Vosse, F. N., van Dongen, M. E. H., and Janssen, J. D. (1996). Analysis of the axial flow field in stenosed carotid artery bifurcation models - LDA experiments. *Journal of Biomechanics*, 29:1483–1489.

Gijsen, F. J. H., van de Vosse, F. N., and Janssen, J. D. (1999b). Influence of non-Newtonian properties of blood on the flow in large arteries: Steady flow in a carotid bifurcation model. *Journal of Biomechanics*, 32(6):601 – 608.

Gimbrone, M. A. (1999). Vascular endothelium, haemodynamic forces and atherogenesis. *Am. J. Pathology*, 115:1–5.

Gimbrone, M. A., Topper, J., Nagel, T., Anderson, K., and Garcia-Cardena, G. (2000). Endothelial dysfunction, hemodynamic forces, and atherogenesis. *Ann NY Acad. Sci.*, 902:230–239.

Goubergrits, L., Affeld, K., Fernandez-Britto, J., and Falcon, L. (2002). Geometry of the human common carotid artery. a vessel cast study of 86 specimens. *Pathology - Research and Practice*, 198(8):543–551.

Goubergrits, L., Wellnhofer, E., Kertzscher, U., Affeld, K., Petz, C., and Hege, H.-C. (2009). Coronary artery wss profiling using a geometry reconstruction based on biplane angiography. *Annals of Biomedical Engineering*, 37(4):682 – 691.

Gray, J. D., Owen, I., and Escudier, M. P. (2007). Dynamic scaling of unsteady shear-thinning non-newtonian fluid flows in a large-scaled modeld of a distal anastomosis. *Experiments in Fluids*, 43:535–546.

Große, S., Burgmann, S., and Schröder, W. (2008). Time-resolved piv measurements of oscillating flow in a non-collapsing flexible pipe. In *Proceedings of the 14th Int Symp. on Applications of Laser Techniques to Fluid Mechanics, Lisbon, Portugal*.

Gui, L. and Wereley, S. T. (2002). A correlation-based continuous window-shift technique to reduce the peak-locking effect in digital PIV image evaluation. *Experiments in Fluids*, 32(4):506–517.

Gui, L., Wereley, S. T., and Kim, Y. H. (2003). Advances and applications of the digital mask technique in particle image velocimetry experiments. *Measurement Science & Technology*, 14:1820–1828.

Guyton, A. C. and Hall, J. E. (2000). *Textbook of Medical Physiology*. W.B. Saunders Company.

Haller, G. (2005). An objective definition of a vortex. *Journal of Fluid Mechanics*, 525:1–26.

Hart, D. (1999). Super-resolution piv by recursive local-correlation. *Journal of Visualization*, 10.

He, X. and Ku, D. N. (1996). Pulsatile flow in the human left coronary artery bifurcation: average conditions. *Journal of Biomechanical Engineering*, 118:74–82.

Helleloid, G. T. (2001). On the computation of viscosity-shear rate temperature master curves for polymeric liquids. *Morehead Electronic Journal of Applicable Mathematics*, 1.

Hochareon, P., Manning, K. B., Fontaine, A. A., Tarbell, J. M., and Deutsch, S. (2004). Wall shear-rate estimation within the 50cc Penn State artificial heart using particle image velocimetry. *Journal of Biomechanical Engineering*, 126(4):430 – 437.

Hoeks, A. P. G., Samijo, P. J., and Reneman, R. S. (1995). Assessment of wall shear rate in humans: an ultrasound study. *Journal of Vascular Investigation*, 1(3):108–117.

Honkanen, M. and Nobach, H. (2005). Background extraction from double-frame piv images. *Experiments in Fluids*, 38(3):348 – 362.

Hopkins, L. M., Kelly, J. T., Wexler, A. S., and Prasad, A. K. (2000). Particle image velocimetry measurments in complex geometries. *Experiments in Fluids*, 29:91–95.

Huang, H., Dabiri, D., and Gharib, M. (1997). On errors of digital particle image velocimetry. *Measurement Science & Technology*, 8(12):1427 – 1440.

Huang, H. T., Fiedler, H. E., and Wang, J. J. (1993). Limitation and improvement of piv partii. *Experiments in Fluids*, 15(4):263–273.

Ives, D. D. and Zacharias, R. M. (1987). Conformal mapping and orthogonal grid generation. In *23rd AIAA Joint Propulsion Conference, San Diego*.

Kähler, C., Scholz, U., and Ortmanns, J. (2006). Wall-shear-stress and near-wall turbulence measurements up to single pixel resolution by means of long-distance micro-piv. *Experiments in Fluids*, 41(2):327–341.

Kähler, C. J. (2004). Investigation of the spatio-temporal flow structure in the buffer region of a turbulent boundary layer by means of multiplane stereo piv. *Experiments in Fluids*, 36(1):114–130.

Karner, G., Perktold, K., Hoferm, M., and Liepsch, D. (1999). Flow characteristics in an anatomically realistic compliant carotid artery bifurcation model. *Computer Methods in Biomchanics and Biomedical Engineering*, 2(3):171–185.

Karri, S., Charonko, J., and Vlachos, P. P. (2009). Robust wall gradient estimation using radial basis functions and proper orthogonal decomposition (pod) for particle image velocimetry (piv) measured fields. *Measurement Science & Technology*, 20(4):DOI:10.1088/0957–0233/20/4/045401.

Keane, R. D. and Adrian, R. (1993). Theory and simulation of particle image velocimetry. *Proceedings of SPIE*.

Keane, R. D. and Adrian, R. J. (1990). Optimization of particle image velocimeters. part i. double pulsed systems. *Measurement Science & Technology*, 1(11):1202 – 1215. Particle Image Velocimeters;.

Keane, R. D. and Adrian, R. J. (1992). Theory of cross-correlation analysis of piv images. *Applied Scientific Research*, 49(3):191–215.

Kim, H.-B., Hertzberg, J. R., and Shandas, R. (2004). Development and validation of echo piv. *Experiments in Fluids*, 36:455–462.

Ku, D. and Giddens, D. (1983). Pulsatile flow in a model carotid bifurcation. *Arteriosclerosis, Thrombosis, and Vascular Biology*, 3(1):31–39.

Ku, D. N. (1997). Blood flow in arteries. *Annu. Rev. Fluid Mech*, 29(1):399 – 434.

Ku, D. N. and Giddens, D. P. (1987). Laser doppler anemometer measurements of pulsatile flow in a model carotid bifurcation. *Journal of Biomechanics*, 20:407–421.

Ku, D. N., Giddens, D. P., Phillips, D. J., and Strandness, D. E. (1985a). Hemodynamics of the normal human carotid bifurcation: In vitro and in vivo studies. *Ultrasound in Medicine & Biology*, 11(1):13 – 26.

Ku, D. N., Giddens, D. P., Zarins, C. K., and Glagov, S. (1985b). Pulsatile flow and atherosclerosis in the human carotid bifurcation. positive correlation between plaque location and low oscillating shear stress. *Arteriosclerosis, Thrombosis and Vascular Biology*, 5(3):293 – 302.

LaMack, J. A. and Friedman, M. H. (2007). Individual and combined effects of shear stress magnitude and spatial gradient on endothelial cell gene expression. *AJP - Heart and Circulatory Physiology*, 293(5).

Lawson, N. J. and Wu, J. (1997a). Three-dimensional particle image velocimetry: Error analysis of stereoscopic techniques. *Measurement Science & Technology*, 8(8):894 – 900. Stereoscopic particle image velocimetry;.

Lawson, N. J. and Wu, J. (1997b). Three-dimensional particle image velocimetry: Experimental error analysis of a digital angular stereoscopic system. *Measurement Science & Technology*, 8(12):1455 – 1464. Stereoscopic particle image velocimetry (PIV);Bicubic spline interpolation;.

Lawson, N. J. and Wu, J. (1999). Three-dimensional particle image velocimetry: A low-cost 35 mm angular stereoscopic system for liquid flows. *Optics and Lasers in Engineering*, 32(1):1 – 19. Three-dimensional particle image velocimetry (PIV);Angular stereoscopic imaging;.

Lecordier, B., Lecordier, J. C., and Trinite, M. (1999). Iterative sub-pixel algorithm for the cross-correlation PIV measurements. In *International Workshop on PIV'99, Santa Barbara, CA*.

Lecordier, B. and Trinite, M. (2004). Advanced PIV algorithms with Image Distortion Validation and Comparison using Synthetic Images of Turbulent Flow. In *Particle Image Velocimetry: Recent Improvements*. Springer-Verlag Berlin-Heidelberg.

Lee, S.-W., Antiga, L., and Steinman, D. A. (2009). Correlations among indicators of disturbed flow at the normal carotid bifurcation. *Journal of Biomechanical Engineering*, 131(6):061013–7.

Lee, S.-W., Smith, D. S., Loth, F., Fischer, P. F., and Bassiouny, H. S. (2007). Numerical and experimental simulation of transitional flow in a blood vessel junction. *Numerical Heat Transfer, Part A: Applications*, 51(1):1–22.

Lee, S.-W. and Steinman, D. A. (2007). On the relative importance of rheology for image-based cfd models of the carotid bifurcation. *Journal of Biomechanical Engineering*, 129(2):273–278.

Lei, M., Kleinstreuer, C., and Truskey, G. A. (1995). Numerical investigation and prediction of atherogenic sites in branching arteries. *Journal of Biomechanical Engineering*, 117(3):350–357.

Lesniak, B., Kaluzynski, K., Liepsch, D., and Palko, T. (2002). The discrimination of stenosed carotid bifurcation models with smooth and irregular plaque surface. part i. laser and ultrasonic doppler flow studies. *Medical Engineering & Physics*, 24(5):309 – 318.

Libby, P. (2001). *Heart Disease: A Textbook of Cardiovascular Medicine*. W.B. Saunders Company.

Libby, P., Ridker, P. M., and Maseri, A. (2002). Inflammation and atherosclerosis. *Circulation*, 105:1135–1143.

Liepsch, D. (2002). An introduction to biofluid mechanics - basic models and applications. *Journal of Biomechanics*, 35(4):415 – 435.

Liepsch, D. and Moravac, S. (1984). Pulsatile flow of non-Netonian fluid in distensible models of human arteries. *Biorheology*, 21:571–86.

Liepsch, D., Pflugbeil, G., Matsuo, T., and Lesniak, B. (1998). Flow visualization and 1- and 3-D laser-Doppler-anemometer measurements in models of human carotid arteries. *Clinical Hemorheology and Microcirculation*, 18:1–30.

Lin, J., Foucaut, J.-M., Laval, J.-P., Pérenne, N., and Stanislas, M. (2008). Assessment of different SPIV processing methods for an application to near-wall turbulence. In *Particle Image Velocimetry: New Developments and Recent Applications*, pages 191–221. Springer-Verlag Berlin-Heidelberg.

LoGerfo, F., Nowak, M., Quist, W., Crawshaw, H., and Bharadvaj, B. (1981). Flow studies in a model carotid bifurcation. *Arteriosclerosis, Thrombosis and Vascular Biology*, 1(4):235–241.

Lou, Z. and Yang, W.-J. (1992). Biofluid dynamics at arterial bifurcations. *Critical Reviews in Biomedical Engineering*, 19(6):455–493.

Lourenco, L. and Krothapalli, A. (1995). On the accuracy of velocity and vorticity measurements with PIV. *Experiments in Fluids*, 18(6):421–428.

Lowe, M. L. and Kutt, P. H. (1992). Refraction through cylindrical tubes. *Experiments in Fluids*, 13(5):315–320.

Luff, J. D., Drouillard, T., Rompage, A. M., Linne, M. A., and Hertzberg, J. R. (1999). Experimental uncertainties associated with particle image velocimetry (PIV) based vorticity algorithms. *Experiments in Fluids*, 26(1):36–54.

Malek, A. M., Alper, S. L., and Izumo, S. (1999). Hemodynamic shear stress and its role in atherosclerosis. *JAMA: The Journal of the American Medical Association*, 282(21):2035–2042.

Marshall, I., Zhao, S., Papathanasopouloua, P., Hoskinsa, P., and Xub, X. Y. (2004). MRI and CFD studies of pulsatile flow in healthy and stenosed carotid bifurcation models. *Journal of Biomechanics*, 37:679–687.

Maxey, M. R. and Riley, J. J. (1983). Equation of motion for a small rigid sphere in a non-uniform flow. *Phys. of Fluids*, 26(4):883–889.

McConalogue, D. J. and Srivastava, R. S. (1968). Motion of fluid in a curved tube. *Proceedings of the Royal Society A: Mathematical, Physical and Engineering Sciences*, 307:37 – 53.

Meinhart, C. D., Wereley, S. T., and Santiago, J. G. (2000). A PIV algorithm for estimating time-average velocity fields. *Journal of Fluids Engineering*, 122.

Melling, A. (1997). Tracer particles and seeding for particle image velocimetry. *Measurement Science & Technology*, 8(12):1406 – 1416.

Meyers, J. (1991). Generation of particles and seeding. In *von Karman Institute for Fluid Dynamics, Lecture Series - Laser Velocimetry, Belgium.*

Meynart, R. (1983). Instantaneous velocity field measurements in unsteady gas flow by speckle velocimetry. *Appl. Optics*, 22(4):535–540.

Michaelis, D. and Wieneke, B. (2008). Comparison between tomographic PIV and stereo PIV. In *14th Int. Symp on Applications of Laser Techniques to Fluid Mechanics, Lisbon, Portugal.*

Miller, P., Danielson, K., Moody, G., Slifka, A., Drexler, E., and Hertzberg, J. (2006). Matching index of refraction using a diethyl phthalate/ethanol solution for in vitro cardiovascular models. *Experiments in Fluids*, 41(3):375–381.

Milner, J., Moore, J. A., Rutt, B. K., and Steinman, D. A. (1998). Hemodynamics of human carotid artery bifurcations: computational studies with models reconstructed from magnetic resonance imaging of normal subjects. *Journal of Vascular Surgery*, 28(1):143–156.

Moore, J. A., Steinman, D. A., Prakash, S., Johnston, K. W., and Ethier, C. R. (1999). A numerical study of blood flow patterns in anatomically realistic and simplified end-to-side anastomoses. *Journal of Biomechanical Engineering*, 121(3):265–272.

Moore, S. (2008). *Computational 3D Modelling of Hemodynamics in the Circle of Willis*. VDM Verlag Dr. Mueller.

Motomiya, M. and Karino, T. (1984). Flow patterns in the human carotid artery bifurcation. *Stroke*, 15(1):50–56.

Moyle, K. R., Antiga, L., and Steinman, D. A. (2006). Inlet conditions for image-based CFD models of the carotid bifurcation: Is it reasonable to assume fully developed flow? *Journal of Biomechanical Engineering*, 128(3):371–379.

Myers, J. G., Moore, J. A., Ojha, M., Johnston, K. W., and Ethier, C. R. (2001). Factors influencing blood flow patterns in the human right coronary artery. *Annals of Biomedical Engineering*, 29(2):109–120.

Narrow, T. L., Yoda, M., and Abdel-Khalik, S. I. (2000). A simple model for the refractive index of sodium iodide aqueous solutions. *Experiments in Fluids*, 28(3):282 – 283.

Nguyen, C. V., Nguyen, T. D., and Wells, J. C. (2006). Sensitivity of piv/interface gradiometry to estimate wall position. *Journal of Visualization*, 26(2).

Nguyen, C. V., Nguyen, T. D., Wells, J. C., and Nakayama, A. (2008a). "interfacial piv": Velocity interpolation near curved walls. In *13th Int. Symposium on Flow Visualization, Nice, France.*

Nguyen, C. V., Nguyen, T. D., Wells, J. C., and Nakayama, A. (2010). Interfacial PIV to resolve flows in the vicinity of curved surfaces. *Experiments in Fluids*, 48(4):577 – 587.

Nguyen, C. V. and Wells, J. C. (2006a). Development of PIV/interface gradiometry to handle low tracer density and curved walls. In *Proceeding of FEDSM2006, ASME Joint U.S - European Fluids Engineering Summer Meeting.*

Nguyen, C. V. and Wells, J. C. (2006b). Direct measurement of fluid velocity gradients at a wall by PIV image processing with stereo reconstruction. *Journal of Visualization*, 9(2):199–208.

Nguyen, K. T., Clark, C. D., Chancellor, T. J., and Papavassiliou, D. V. (2008b). Carotid geometry effects on blood flow and on risk for vascular disease. *Journal of Biomechanics*, 41(1):11–19.

Nguyen, T. T., Biadillah, Y., Mongrain, R., Brunette, J., Tardif, J.-C., and Bertrand, O. F. (2004). A method for matching the refractive index and kinematic viscosity of a blood analog for flow visualization in hydraulic cardiovascular models. *Journal of Biomechanical Engineering*, 126(4):529 – 535.

Nobach, H., Damaschke, N., and Tropea, C. (2005). High-precision sub-pixel interpolation in particle image velocimetry image processing. *Experiments in Fluids*, 39:299–304.

Nobach, H. and Honkanen, M. (2005). Two-dimensional gaussian regression for sub-pixel displacement estimation in particle image velocimetry or particle position estimation in particle tracking velocimetry. *Experiments in Fluids*, 38:511–515.

Ootaki, Y., Kamohara, K., Akiyama, M., Zahr, F., Kopcak, Jr., M. W., Dessoffy, R., and Fukamachi, K. (2005). Phasic coronary blood flow pattern during a continuous flow left ventricular assist support. *European Journal of Cardio-Thoracic Surgery*, 28(5):711–716.

Oshinski, J., Curtin, J., and Loth, F. (2006). Mean-average wall shear stress measurements in the common carotid artery. *Journal of Cardiovascular Magnetic Resonance*, 8(5).

Palmen, D. E. M., Gijsen, F. J. H., van de Vosse, F. N., Janssen, J. D., and van Dongen, M. E. H. (1993). Lda measurements in a non-stenosed and a stenosed model of the carotid artery bifurcation. *Proceedings of SPIE - The International Society for Optical Engineering*, 2052:219 – 226.

Papaharilaou, Y., Doorly, D., and Sherwin, S. (2002). The influence of out-of-plane geometry on pulsatile flow within a distal end-to-side anastomosis. *Journal of Biomechanics*, 35(9):1225 – 1239.

Parker, K., Ellenrieder, v. K., , and Soria, J. (2004). Stereoscopic PIV measurements of the flow past a circular cylinder at reynolds number 15000. In *15th Australasian Fluid Mechanics Conference, Sydney, Australia*.

Perktold, K., Hofer, M., Rappitsch, G., Loew, M., Kuban, B. D., and Friedman, M. H. (1998). Validated computation of physiologic flow in a realistic coronary artery branch. *Journal of Biomechanics*, 31(3):217–228.

Perktold, K., Peter, R., Resch, M., and Langs, G. (1991a). Pulsatile non-Newtonian blood flow in three-dimensional carotid bifurcation models. a numerical study of flow phenomena under different bifurcation angles. *Journal of Biomedical Engineering*, 13(6):507 – 515.

Perktold, K. and Rappitsch, G. (1995). Computer simulation of local blood flow and vessel mechanics in a compliant carotid artery bifurcation model. *Journal of Biomechanics*, 28(7):845–856.

Perktold, K. and Resch, M. (1990). Numerical flow studies in human carotid artery bifurcations. basic discussion of the geometric factor in atherogenesis. *Journal of Biomedical Engineering*, 12(2):111 – 123.

Perktold, K., Resch, M., and Florian, H. (1991b). Pulsatile non-newtonian flow characteristics in a three-dimensional human carotid bifurcation model. *Journal of Biomechanical Engineering*, 113(4):464–75.

Perktold, K., Resch, M., and Peter, R. O. (1991c). Three-dimensional numerical analysis of pulsatile flow and wall shear stress in the carotid artery bifurcation. *Journal of Biomechanics*, 24(6):409 – 420.

Perry, A. and Chong, M. (1987). A description of eddying motions and flow patterns using critical-point concepts. *Annu. Rev. Fluid Mech*, 19:125–155.

Perry, A. E. and Chong, M. (1994). Topology of flow patterns in vortex motions and turbulence. *Applied Scientific Research*, 53:357–374.

Perry, R. H. and Chilton, C. H. (1973). *Chemical Engineers' Handbook*. McGraw-Hill Kogakusha, 5th edition.

Plank, M. J., Wall, D. J., and David, T. (2006). Atherosclerosis and calcium signalling in endothelial cells. *Progress in Biophysics and Molecular Biology*, 91(3):287–313.

Poelma, C., Mari, J., Foin, N., Tang, M. X., Krams, R., Caro, C., Weinberg, P., and Westerweel, J. (2009). 3D Flow reconstruction using ultrasound piv. *Experiments in Fluids*, (DOI 10.1007/s00348-009-0781-8).

Poelma, C., Vennemann, P., Lindken, R., and Westerweel, J. (2008). In vivo blood flow and wall shear stress measurements in the vitelline network. *Experiments in Fluids*, 45(4):703–713.

Prasad, A., Adrian, R., Landreth, C., and Offutt, P. (1992). Effect of resolution on the speed and accuracy of particle image velocimetry interrogation. *Experiments in Fluids*, 13(2):105–116.

Prasad, A. K. (2000). Stereoscopic Particle Image Velocimetry. *Experiments in Fluids*, 29(2):103 – 116.

Prasad, A. K. and Adrian, R. J. (1993). Stereoscopic particle image velocimetry applied to liquid flows. *Experiments in Fluids*, 15(1):49–60.

Prasad, A. K. and Jensen, K. (1995). Scheimpflug stereocamera for particle image velocimetry in liquid flows. *Appl. Optics*, 34(30):7092–7099.

Raffel, M., Willert, C. E., and Kompenhans, J. (1998). *Particle Image Velocimetry - A Practical Guide*. Springer-Verlag Berlin-Heidelberg.

Rappitsch, G. and Perktold, K. (1996). Pulsatile albumin transport in large arteries: A numerical simulation study. *Journal of Biomechanical Engineering*, 118(4):511–519.

Rayz, V., Berger, S., and Saloner, D. (2007). Transitional flows in arterial fluid dynamics. *Computer Methods in Applied Mechanics and Engineering*, 196:3043–3048.

Reneman, R. S., Arnold, T. A., and Hoeks, P. (2006). Wall shear stress – an important determinant of endothelial cell function and structure – in the arterial system in vivo. *Journal of Vascular Ressearch*, 43:251–269.

Resnick, N., Yahav, H., Shay-Salit, A., Shushy, M., Schubert, S., Zilberman, L. C. M., and Wofovitz, E. (2003). Fluid shear stress and the vascular endothelium: for better and for worse. *Progress in Biophysics and Molecular Biology*, 81(3):177–199.

Rindt, C. C. M. and Steenhoven, A. A. V. (1996). Unsteady flow in a rigid 3-d model of the carotid artery bifurcation. *Journal of Biomechanical Engineering*, 118(1):90–96.

Roesgen, T. (2003). Optimal subpixel interpolation in particle image velocimetry. *Experiments in Fluids*.

Ross, R. (1999). Atherosclerosis – An Inflammatory Disease. *The New England Journal of Medicine*, 340(2):115–126.

Ross, R. and Glomset, J. A. (1976). The pathogensis of atherosclerois. *The New England Journal of Medicine*, 295:369–377.

Ruan, X., Song, X., and Yamamoto, F. (2001). Direct measurement of the vorticity field in digital particle images. *Experiments in Fluids*, 30:696 – 704.

Ruwet, V., Corieri, P., Theunissen, R., Ma, B., Riethmuller, M., and Darquenne, C. (2008). Fow of aerosol in 3D alveolated bifurcations: experimental measurements by Particle Image Velocimetry and Particle Tracking Velocimetry. In *Proceedings of the 14th Int Symp. on Applications of Laser Techniques to Fluid Mechanics, Lisbon, Portugal*.

Samijo, S. K., Willigers, J. M., Barkhuysen, R., Kitslaar, P. J. E. H. M., Reneman, R. S., Brands, P. J., and Hoeks, A. P. G. (1998). Wall shear stress in the human common carotid artery as function of age and gender. *Cardiovascular Research*, 39:515–522.

Scarano, F. (2000). *Particle Image Velocimetry and Application - Investigation of Coherent Structures in Turbulent Shear Flows*. PhD thesis, von Karman Institute for Fluid Dynamics, Universita degli Napoli "Federico II".

Scarano, F. (2002). Iterative image deformation methods in PIV. *Measurement Science & Technology*, 13:R1–R19.

Scarano, F. and Riethmuller, M. L. (1999). Iterative multigrid approach in PIV image processing with discrete window offset. *Experiments in Fluids*, 26(6):513–523.

Scarano, F. and Riethmuller, M. L. (2000). Advances in iterative multigrid PIV image processing. *Experiments in Fluids*, 29(7):S051–S060.

Schrijer, F. and Scarano, F. (2006). On the stabilization and spatial resolution of iterative piv interrogation. In *13th Int Symp on Applications of Laser Techniques to Fluid Mechanics, Lisbon, Portugal*.

Schrijer, F. and Scarano, F. (2008). Effect of predictor–corrector filtering on the stability and spatial resolution of iterative piv interrogation. *Experiments in Fluids*, 45(5):927–941.

Schröder, A. and Willert, C. (2008). *Particle Image Velocimetry: New Developments and Recent Applications.* Springer-Verlag Berlin-Heidelberg.

Seeley, R. R., Stephens, T. D., and Tate, P. (2003). *Anatomy and physiology.* McGraw- Hill, Boston, 6th edition.

Shelby, J. E. (2005). *Introduction to glass science and technology.* Royal Society of Chemistry, 2nd edition.

Shinneeb, A. M., Bugg, J. D., and Balachandar, R. (2004). Variable threshold outlier identification in PIV data. *Measurement Science & Technology*, 15(9):1722–1732.

Slager, C., Wentzel, J., Gijsen, F., Schuurbiers, J., van der Wal, A., van der Steen, A., and Serruys, P. (2005). The role of shear stress in the generation of rupture-prone vulnerable plaques. *Nature Clinical Practice Cardiovascular Medicine*, 2:456–464.

Soloff, S. M., Adrian, R. J., and Liu, Z. C. (1997). Distortion compensation for generalized stereoscopic particle image velocimetry. *Measurement Science & Technology*, 8(12):1441–1454.

Soria, J. (1996). An investigation of the near wake of a circular cylinder using a video-based digital cross-correlation particle image velocimetry technique. *Experimental Thermal and Fluid Science*, 12(2):221–233.

Soria, J. (2006). Particle image velocimetry - application to turbulence studies. In *Lectures notes on Turbulence and Coherent Structures in Fluid, Plasma and non-linear media, Chapter 7.*

Soria, J. and Atkinson, C. (2008). Towards 3c-3d digital holographic fluid velocity vector field measurement—tomographic digital holographic piv (tomo-hpiv). *Measurement Science & Technology*, 19(7).

Spence, C., Buchmann, N., and Jermy, M. (2009). Flow field in the human nasal cavity with nasal high flow therapy from stereoscopic PIV measurements. In *8th International Symposium on Particle Image Velocimetry, Melbourne, Australia.*

Stanislas, M., Kopenhans, J., and Westerweel, J. (2000). *Particle Image Velocimetry: Progress Towards Industrial Application*. Kluwer Academic Publisher, Dordrecht.

Stanislas, M. and Monnier, J. C. (1997). Practical aspects of image recording in particle image velocimetry. *Measurement Science & Technology*, 8(12):1417 – 1426.

Stanislas, M., Okamoto, K., and Kaehler, C. (2004). *Particle Image Velocimetry: Recent Improvements Proceedings of the EUROPIV 2 Workshop held in Zaragoza, Spain*. Springer-Verlag Berlin-Heidelberg.

Stary, H. C., Chandler, A. B., Dinsmore, R. E., Fuster, V., Glagov, S., Insull, William, J., Rosenfeld, M. E., Schwartz, C. J., Wagner, W. D., and Wissler, R. W. (1995). A definition of advanced types of atherosclerotic lesions and a histological classification of atherosclerosis : A report from the committee on vascular lesions of the council on arteriosclerosis, american heart association. *Circulation*, 92(5):1355–1374.

Steinman, D., Poepping, T., Tambasco, M., and Rankin, R. (2000). Flow patterns at the stenosed carotid bifurcation: Effect of concentric versus eccentric stenosis. *Annals of Biomedical Engineering*, 28(415-423).

Steinman, D. A. and Taylor, C. A. (2005). Flow imaging and computing: Large artery hemodynamics. *Annals of Biomedical Engineering*, 33(12):1704–1709.

Stitou, A. and Riethmuller, M. L. (2001). Extension of PIV to super resolution using PTV. *Measurement Science & Technology*, 12:1398–1403.

Tan, F. P. P., Soloperto, G., Bashford, S., Wood, N. B., Thom, S., Hughes, A., and Xu, X. Y. (2008). Analysis of flow disturbance in a stenosed carotid artery bifurcation using two-equation transitional and turbulence models. *Journal of Biomechanical Engineering*, 130(6).

Tang, D., Yang, C., Mondal, S., Liu, F., Canton, G., Hatsukami, T. S., and Yuan, C. (2008). A negative correlation between human carotid atherosclerotic plaque progression and plaque wall stress: In vivo mri-based 2d/3d fsi models. *Journal of Biomechanics*, 41(4):727–736.

Tateshima, S., Murayama, Y., Villablanca, J. P., Morino, T., Takahashi, H., Yamauchi, T., Tanishita, K., and Vinuela, F. (2001). Intraaneurysmal flow dynamics study featuring an acrylic aneurysm model manufactured using a computerized tomography angiogram as a mold. *J. of Neurosurg.*, 95(6):1020–1027.

Taylor, C. A. and Draney, M. T. (2004). Experimental and computational methods in cardiovascular fluid mechanics. *Annu. Rev. Fluid Mech*, 36:197–231.

Thalmann, M., Schima, H., Wieselthaler, G., and Wolner, E. (2005). Physiology of continuous blood flow in recipients of rotary cardiac assist devices. *The Journal of Heart and Lung Transplantation*, 24(3):237–245.

Theunissen, R., Buchmann, N., Corieri, P., Riethmuller, M., and Darquenne, C. (2006). Experimental investigation of aerosol deposition in alveolar lung airways. In *13th Int. Symp. on Applications of Laser Techniques to Fluid Mechanics, Lisbon, Portugal.*

Theunissen, R., Scarano, F., and Riethmuller, M. (2008). On improvement of PIV image interrogation near stationary interfaces. *Experiments in Fluids*, 45(4):557–572.

Thevenaz, P., Blu, T., and Unser, M. (2000). Interpolation revisited. *Medical Imaging, IEEE Transactions*, 19(7):739–758.

Thomas, J. B., Antiga, L., Che, S. L., Milner, J. S., Hangan Steinman, D. A., Spence, J. D., Rutt, B. K., and Steinman, D. A. (2005). Variation in the carotid bifurcation geometry of young versus older adults: Implications for geometric risk of atherosclerosis. *Stroke*, 36(11):2450–2456.

Thurston, G. B. (1979). Rheological parameters for the viscosity viscoelasticity and thixotropy of blood. *Biorheology*, 16(3):149–162.

Traub, O. and Berk, B. C. (1998). Laminar shear stress: Mechanisms by which endothelial cells transduce an atheroprotective force. *Arteriosclerosis, Thrombosis, and Vascular Biology*, 18(5):677–685.

Tsuei, L. and Savas, O. (2000). Treatment of interfaces in particel image velocimetry. *Experiments in Fluids*, 29:203 – 214.

van Doorne, C. W. H. and Westerweel, J. (2007). Measurement of laminar, transitional and turbulent pipe flow using stereoscopic-PIV. *Experiments in Fluids*, 42:259–279.

van Dyke, M. (1978). Extended stokes series: laminar flow through a loosely coiled pipe. *Journal of Fluid Mechanics*, 86(1):129–145.

Vennemann, P., Lindken, R., and Westerweel, J. (2007). In vivo whole-field blood velocity measurement techniques. *Experiments in Fluids*, 42:495–511.

Vétel, J., Garon, A., and Pelletier, D. (2009). Lagrangian coherent structures in the human carotid artery bifurcation. *Experiments in Fluids*, (DOI 10.1007/s00348-009-0615-8).

Vlaardingerbroek, M. and Boer, J. (1996). *Magnetic Resonance Imaging*. Springer-Verlag Berlin-Heidelberg.

Walburn, F. J. and Stein, P. D. (1981). Velocity profiles in symmetrically branched tubes simulating the aortic bifurcation. *Journal of Biomechanics*, 14(9):601 – 611.

Weast, R. C. (1988). *Handbook of chemistry and physics*. CRC Press, 69th edition.

Wereley, S. T., Gui, L., and Meinhart, C. D. (2002). Advanced algorithms for microscale particle image velocimetry. *AIAA Journal*, 40(6).

Westerweel, J. (1993). *Digital particle image velocimetry – Theory and application*. PhD thesis, Delft University, Delft, Netherlands.

Westerweel, J. (1994). Efficient detection of spurious vectors in particle image velocimetry data. *Experiments in Fluids*, V16(3):236–247.

Westerweel, J. (1997). Fundamentals of digital Particle Image Velocimetry. *Measurement Science & Technology*, 8(12):1379 – 1392.

Westerweel, J. (2008). On velocity gradients in PIV interrogation. *Experiments in Fluids*, 44(5):831–842.

Westerweel, J., Dabiri, D., and Gharib, M. (1997). The effect of a discrete window offset on the accuracy of cross-correlation analysis of digital piv recordings. *Experiments in Fluids*, V23(1):20–28.

Westerweel, J., Geelhoed, P. F., and Lindken, R. (2004). Single-pixel resolution ensemble correlation for micro-PIV applications. *Experiments in Fluids*, 37:375–384.

Westerweel, J. and Scarano, F. (2005). Universal outlier detection for PIV data. *Experiments in Fluids*, 39(6):1096 – 1100.

Wieneke, B. (2005). Stereo-PIV using self-calibration on particle images. *Experiments in Fluids*, 39(2):267 – 280.

Wieneke, B. (2007). Volume self-calibration for stereo-PIV and tomographic-PIV. In *7th International Symposium on Particle Image Velocimetry, Rome, Italy.*

Wieneke, B. and Taylor, S. (2006). Fat-sheet PIV with computation of full 3D-strain tensor using tomographic reconstruction. In *13th Int. Symp on Applications of Laser Techniques to Fluid Mechanics, Lisbon, Portugal.*

Wiesner, T. F., Berk, B. C., and Nerem, R. M. (1997). A mathematical model of the cytosolic-free calcium response in endothelial cells to fluid shear stress. *Proceedings of the National Academy of Sciences of the United States of America*, 94(8):3726–3731.

Willert, C. (1997). Stereoscopic digital particle image velocimetry for application in wind tunnel flows. *Measurement Science & Technology*, 8(12):1465–1479.

Willert, C. E. (2006). Assessment of camera models for use in planar velocimetry calibration. *Experiments in Fluids*, 41:135–143.

Willert, C. E. and Gharib, M. (1991). Digital particle image velocimetry. *Experiments in Fluids*, 10(4):181–193.

Willert, C. E. and Gharib, M. (1992). Three-dimensional particle imaging with a single camera. *Experiments in Fluids*, 12(6):353–358.

Womersley, J. R. (1955). Method for the calculation of velocity, rate of flow and viscous drag in arteries when the pressure gradient is known. *The Journal of Physiology*, 127(3):553–563.

Xiong, F. L. and Chong, C. K. (2007). PIV-validated numerical modeling of pulsatile flows in distal coronary end-to-side anastomoses. *Journal of Biomechanics*, 40(13):2872–2881.

Xu, X. and Collins, M. (1990). A review of the numerical analysis of blood flow in arterial bifurcations. *Proc. Inst. Mech. Eng. H*, 204(4):205–216.

Yedavalli, R. V., Loth, F., Yardimci, A., Pritchard, W. F., Oshinski, J. N., Sadler, L., Charbel, F., and Alperin, N. (2001). Construction of a physical model of the human carotid artery based upon in vivo magnetic resonance images. *Journal of Biomechanical Engineering*, 123(4):372–376.

Young, D. F. and Tsai, F. Y. (1973). Flow characteristics in models of arterial stenoses. ii. unsteady flow. *Journal of Biomechanics*, 6(5):547–559.

Zand, T., Hoffman, A. H., Savilonis, B. J., Underwood, J. M., Nunnari, J. J., Majno, G., and Joris, I. (1999). Lipid deposition in rat aortas with intraluminal hemispherical plug stenosis. a morphological and biophysical study. *American Journal of Pathology*, 155(1):85–92.

Zarins, C., Giddens, D., Bharadvaj, B., Sottiurai, V., Mabon, R., and Glagov, S. (1983). Carotid bifurcation atherosclerosis. quantitative correlation of plaque localization with flow velocity profiles and wall shear stress. *Circulation Research*, 53(4):502–514.

Zhang, J.-M., Chua, L. P., Ghista, D. N., Zhou, T.-M., and Tan, Y. S. (2008). Validation of numerical simulation with piv measurements for two anastomosis models. *Medical Engineering & Physics*, 30(2):226–247.

Zhao, S. Z., Papathanasopoulou, P., Long, Q., Marshall, I., and Xu, X. Y. (2003). Comparative study of magnetic resonance imaging and image-based computational fluid dynamics for quantification of pulsatile flow in a carotid bifurcation phantom. *Annals of Biomedical Engineering*, 31(8):962–971.

Zhao, S. Z., Xu, X. Y., Hughes, A. D., Thom, S. A., Stanton, A. V., Ariff, B., and Long, Q. (2000). Blood flow and vessel mechanics in a physiologically realistic model of a human carotid arterial bifurcation. *Journal of Biomechanics*, 33(8):975 – 984.

Publications arising from this Research

Journal Articles

[1] N.A. Buchmann, C. Atkinson, M. Jermy, and J. Soria. Tomographic particle image velocimetry investigations of the flow in a modelled human carotid artery bifurcation. *Experiments in Fluids*, accepted, 2010.

[2] C.J.T. Spence, N.A. Buchmann, M.C. Jermy and S.M. Moore. Stereoscopic PIV measurements of flow in the nasal cavity with high flow therapy. *Experiments in Fluids*, DOI 10.1007/s00348-010-0984-z, 2010.

[3] N.A. Buchmann, M. Yamamoto, M.C. Jermy and T. David. Particle Image Velocimetry and Computational Fluid Dynamics Modelling of Carotid Artery Haemodynamics under Steady Flow: A Validation Study. *J. of Biomechanical Science and Engineering*, 4(5):421-436, 2010.

[4] N.A. Buchmann, M. Jermy, and C. Nguyen. Experimental investigation of carotid artery haemodynamics in an anatomically realistic model. *Int. J. Experimental and Computational Biomechanics*, 1(2):172192, 2009.

Conference Proceedings

[1] N.A. Buchmann and M.C. Jermy. Transient flow and shear stress measurements in an anatomical model of the human carotid artery. *In 15th Int. Symp on Applications of Laser Techniques to Fluid Mechanics*, Lisbon, Portugal, 2010.

[2] Callum J. T. Spence, Nicolas A. Buchmann, and Mark C. Jermy. Pulsatile flow in the nasal cavity with high flow therapy measured by stereoscopic PIV. *In 15th Int. Symp on Applications of Laser Techniques to Fluid Mechanics*, Lisbon, Portugal, 2010.

[3] Patrick H. Geoghegan, Nicolas A. Buchmann, Mark C. Jermy, David Nobes, Callum J.T. Spence, and Paul D. Docherty. SPIV and image correlation measurements of surface displacement during pulsatile flow in models of compliant, healthy and stenosed arteries. *In 15th Int. Symp on Applications of Laser Techniques to Fluid Mechanics*, Lisbon, Portugal, 2010.

[4] N. A. Buchmann, C. Atkinson, M. C. Jermy, and J. Soria. In-vitro investigation of three-dimensional carotid artery haemodynamics by tomographic particle image velocimetry. *In World Congress on Medical Physics and Biomedical Engineering*, Vol. 25/IV, Munich, Germany, 2009.

[5] N. A. Buchmann, C. Atkinson, M. C. Jermy, and J. Soria. Tomographic-PIV investigation of the three- dimensional flow structure in the human carotid artery. *In 8th International Symposium on Particle Image Velocimetry*, Melbourne, Australia, 2009.

[6] P. Geoghegan, M. Jermy, N. Buchmann, C. Spence, and T. Freitag. Experimental investigation of flow in a compliant tube using particle image velocimetry. *In 8th International Symposium on Particle Image Velocimetry*, Melbourne, Australia, 2009.

[7] C. Spence, N. Buchmann, and M. Jermy. Flow field in the human nasal cavity with nasal high flow therapy from stereoscopic PIV measurements. *In 8th International Symposium on Particle Image Velocimetry*, Melbourne, Australia, 2009.

[8] N. A. Buchmann, C. Atkinson, M. C. Jermy, and J. Soria. Three-dimensional in-vitro measurements of carotid artery haemodynamics. *In Fourth Asian Pacific Conference on Biomechanics*, Christchurch, New Zealand, 2009.

[9] P. Geoghegan, M. Jermy, N. Buchmann, C. Spence, and T. Freitag. Experimental investigation of flow in compliant tubes to validate numerical models of aneurysms. *In Fourth Asian Pacific Conference on Biomechanics*, Christchurch, New Zealand, 2009.

[10] C. Spence, N. Buchmann, and M. Jermy. Upper airway stereoscopic particle image velocimetry measurements with high-flow nasal cannula. *In*

Fourth Asian Pacific Conference on Biomechanics, Christchurch, New Zealand, 2009.

[11] M. Jermy, N. Buchmann, C. Spence, C. Nguyen, and T. David. PIV of human blood and upper airway flow in scaled models. *In Fifth Australian Conference on Laser Diagnostics in Fluid Mechanics and Combustion*, Perth, Australia, 2008.

[12] N. A. Buchmann, C. V. Nguyen, J. C. Wells, and M. Jermy. In-vitro wall shear stress measurements using interfacial particle image velocimetry (iPIV). *In 14th Int. Symp. on Applications of Laser Techniques to Fluid Mechanics*, Lisbon, Portugal, 2008.

[13] N. A. Buchmann and M. C. Jermy. Blood flow measurements in idealised and patient specific models of the human carotid artery. *In 14th Int Symp. on Applications of Laser Techniques to Fluid Mechanics*, Lisbon, Portugal, 2008.

[14] N.A. Buchmann, M. Jermy, and C. Spence. In-vitro imaging of blood flow in human carotid arteries. *In 13th Int. Symposium on Flow Visualization*, Nice, France, 2008.

[15] C.J.T. Spence, N.A. Buchmann, and M.C. Jermy. Particle image velocimetry measurements of nasal cavity flow with high flow humidified nasal interface. *In 13th Int. Symposium on Flow Visualization*, Nice, France, 2008.

[16] N. A. Buchmann and M. C. Jermy. Particle image velocimetry measurements of blood flow in a modeled carotid artery bifurcation. *In Proceedings of the 16th Australasian Fluid Mechanics Conference*, Gold Coast, Australia, 2007.

[17] N. A. Buchmann, M. C. Jermy, and T. David. Experimental investigation of blood flow in the brain by means of particle image velocimetry - a preliminary study. *In Proceedings of the Fifth International Conference on Fluid Mechanics*, Shanghai, China, 2007.

About the Author

Nicolas Alexander Buchmann was born on January 3, 1979 in Friedrichshafen, Germany, After finishing secondary school in 1998, he attend the German Military Service until 1999, before starting his Master degree in Mechanical Engineering at the Darmstadt University of Technology in Germany, which he completed in 2006 under the supervision of Prof. C. Tropea.
Subsequently, he spend 7 Month at the Von Karman Institute for Fluid Dynamics in Belgium as a graduate student to work on a project involving measurements of human airway flow using Particle Image and Particle Tracking Velocimetry.

In April 2006, he took up a PhD position at the Canterbury University, New Zealand under the supervision of Dr. Mark Jermy and Prof. Tim David to work in an interdisciplinary field comprising various aspects of biomechanical engineering and experimental fluid mechanics. His main focus was the development of a Particle Image Velocimetry system for haemodynamic *in vitro* studies of arterial blood flow. The results of his research are presented in this thesis. During this time, he was awarded with two full-time postgraduate scholarships by the University of Canterbury and the New Zealand Ministry of Education as well as the Royal Society R.H.T Bates Award for his achievements in interdisciplinary research.
In 2008, he worked at Monash University, Australia together with Prof. Julio Soria to develop a new technique for three-dimensional flow measurements in complex arterial models. He returned back to New Zealand in 2009 to complete his PhD thesis.

Currently, Nicolas Buchmann holds a position as a Research Fellow at the Department of Mechanical Engineering, Monash University were he works on the experimental investigation of wall-bounded and free-surface turbulent shear flows and the development of new optical and laser based flow diagnostics.